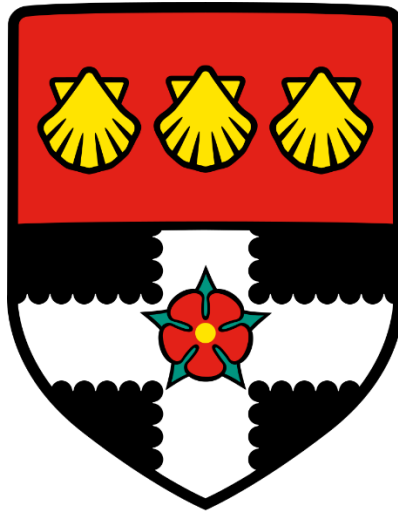


UNIVERSITY OF READING

Department of Meteorology



**Surface roughness parameters in cities:
improvements and implications for wind-
speed estimation**

Christoph William Kent

A thesis submitted for the degree of Doctor of Philosophy

February 2018

Declaration

I confirm that this is my own work and the use of all material from other sources has been properly and fully acknowledged.

Christoph William Kent

Abstract

The surface aerodynamic roughness parameters of the zero-plane displacement (z_d) and roughness length (z_0) can be critical for wind-speed estimates in the atmospheric boundary layer. In urban areas, the numerous sources and sinks of momentum makes it challenging to assign appropriate values for z_d and z_0 . The objective of this PhD is to improve the understanding of z_d and z_0 in urban environments, especially for wind-speed estimates when flow is free from roughness-element wakes.

Nine methods are applied to determine z_d and z_0 at three sites in central London (UK), demonstrating the inter-method variability leads to a wide range of values. Wind-speed estimates using the roughness parameters and five wind-speed profile methods are compared to Doppler lidar observations up to 200 m (approximately 10 times the average building height) above the canopy. Estimates with roughness parameters determined from morphometric methods (i.e. based upon surface geometry) which directly incorporate roughness-element height variability are consistently most accurate.

A morphometric method is developed to calculate z_d and z_0 that accounts for both buildings and vegetation. The method captures the directional and seasonal variability of roughness with vegetation and improves the accuracy of wind-speed estimates.

Due to the challenge of obtaining urban morphology and roughness parameters for cities globally, three satellite-derived global digital elevation models (GDEMs) are assessed using benchmark elevation datasets. It is concluded that empirical corrections to the most accurate GDEM (TanDEM-X) can improve the parameter accuracy and associated wind-speed estimates.

Acknowledgements

I would firstly like to thank my supervisor, Prof. Sue Grimmond, whom has been a source of motivation, enthusiasm, guidance and support throughout my doctoral studies. No matter the time of day, location in the world or other commitments, Prof. Grimmond has always found time to have weekly (or more) meetings and provide feedback upon my research. I am thankful to my industry supervisor Dr. David Gatey, who despite becoming a father to two children over the course of my studies and working full-time in London, has made himself available for weekly meetings, providing feedback upon my research and traveling to Reading. I am thankful to my co-supervisor Prof. Janet Barlow who in addition to attending weekly meetings, has provided valuable insight to the work, encouraging me to think more critically about analysis and results.

I would like to thank the many co-authors who have contributed to this work, with whom I have greatly enjoyed working with. I have learnt a great deal from each co-author and hope the collaboration will continue. I would specifically like to thank: Dr. Simone Kotthaus for the processing and provision of observations in central London (UK), as well as all of those involved in the daily operations of the London Urban Meteorology Observatory (LUMO); Dr. Christos Halios and Prof. Janet Barlow for providing Doppler lidar data; Dr. Helen Ward for use of observations in Swindon (UK); Prof. Jinkyu Hong, Keunmin Lee and Je-Woo Hong for use of observations in Seoul (Republic of Korea); Dr. Fredrik Lindberg for the time and effort spent assisting with the implementation of the research in the open source UMEP plugin for QGIS.

I am very grateful for the feedback, as well as insightful and probing questions from Dr. Omduth Coceal and Dr. Sylvia Bohnenstengel. I am also grateful for discussions regarding the work with Duick Young, Marco Giometto and Prof. Keith Morrison, with Prof. Morrison suggesting use/application for the TanDEM-X data. I am thankful to Prof. Jianguo Tan and Prof. Shiguang Miao for hosting my research visits to the Shanghai Institute of Meteorological Science and Beijing Institute of Urban Meteorology, respectively, as well as their many colleagues I worked with during my time there. Thank you to Dr. Babatunde Abiodun of University of Cape Town and all of those at the Climate Systems Analysis Group (CSAG), who initiated my interest in atmospheric science.

A special thank you is for my English and South African family and friends for their continuous support and encouragement. The greatest thanks is to my Fiancé Claire Reid, whom I got engaged to just over a year ago. Throughout my studies Claire has offered more than words can do justice.

This work is funded by a NERC CASE studentship in partnership with Risk Management Solutions (NE/L00853X/1) and Newton Fund/Met Office CSSP China. Observations used in these analyses were funded from NERC ClearfLo (KCL and Reading), EUf7 BRIDGE, H2020 UrbanFluxes EPSRC ACTUAL, KCL and University of Reading, the Korean Meteorological Administration Research and Development Program (KMIPA2015-2063) and the Global Ph.D. Fellowship Program (NRF-2015H1A2A1030932). The TanDEM-X data research grant: DEM_URBAN1021 (with assistance from Thomas Busche and Wieke Heldens, DLR) are gratefully acknowledged, as is the support with the provision with benchmark GIS datasets: Danilo Mizuta (Sao Paulo Municipality), The Tokyo Metropolitan Geographic Information System Data for Urban Planning.

Contents

Abstract.....	3
Acknowledgements.....	4
Contents.....	6
Table of Figures.....	11
Table of Tables.....	23
Chapter 1. Research overview.....	29
1.1 Motivation for research.....	29
1.2 Objectives.....	30
1.3 Thesis outline.....	31
Chapter 2. Background.....	33
2.1 The urban boundary layer (UBL).....	33
2.2 Describing flow in the atmospheric boundary layer.....	34
2.2.1 Reynolds decomposition, stresses and the friction velocity.....	34
2.2.2 The vertical profile of wind speed in the neutral atmospheric boundary layer.....	35
2.2.3 Monin-Obukhov Similarity Theory.....	38
2.2.4 Source area modelling.....	40
2.3 Aerodynamic roughness parameters.....	42
2.3.1 The state of the art.....	42
2.3.2 Morphometric methods – determining z_d and z_0 from surface geometry.....	45
Chapter 3. Evaluation of urban local-scale aerodynamic parameters: implications for the vertical profile of wind speed and for source areas.....	49
3.1 Introduction.....	49
3.2 Background.....	51
3.2.1 The urban boundary layer and logarithmic wind law.....	51
3.3 Determination of aerodynamic parameters in urban areas.....	52
3.3.1 Reference-based methods.....	52
3.3.2 Morphometric methods.....	52
3.3.2.1 Relations between aerodynamic parameters and roughness-element form.....	52
3.3.2.2 Morphometric method application in urban areas.....	53
3.3.3 Anemometric methods.....	58
3.4 Methods.....	59
3.4.1 Site description.....	59
3.4.2 Observations.....	60

3.4.3	Determination of aerodynamic parameters	62
3.4.3.1	Flow diagram illustrating framework of analysis	62
3.4.3.2	Anemometric determination of aerodynamic parameters	63
3.4.3.3	Morphometric determination of aerodynamic parameters	64
3.5	Results	65
3.5.1	Zero-plane displacement (z_d)	65
3.5.1.1	z_d determined by anemometric methods	65
3.5.1.2	z_d determined by morphometric methods	66
3.5.2	Aerodynamic roughness length (z_0)	69
3.5.2.1	z_0 determined by anemometric methods	69
3.5.2.2	z_0 determined by morphometric methods	69
3.5.3	Comparison between anemometric and morphometric aerodynamic parameters	70
3.5.4	Reference-based approach	72
3.6	Independent method assessment – wind-speed profile extrapolation.....	73
3.7	Source area modelling using the morphometric methods	75
3.8	Conclusions	77
	Appendix 3.A: Methods to calculate z_d and z_0 from the literature	80
	Appendix 3.B: Turbulence data at London sites	81
	Appendix 3.C: Sensitivity of source area model iterative procedure to initial estimates of z_d and z_0	84
	Appendix 3.D: Tutorial for using the source area footprint model for roughness calculations in UMEP.....	87
Chapter 4.	Assessing methods to extrapolate the vertical wind-speed profile from surface observations in a city centre during strong winds	93
4.1	Introduction	93
4.2	Describing the boundary layer wind speed using surface observations.....	95
4.2.1	The logarithmic wind law	96
4.2.2	Adapted power law profile	97
4.2.3	The Deaves and Harris profile.....	97
4.2.3.1	Equilibrium model.....	98
4.2.3.2	Non-equilibrium model.....	98
4.2.4	The Gryning profile.....	100
4.2.5	Vertical extrapolation of the surface wind speed.....	100

4.3	Aerodynamic roughness parameters.....	101
4.4	Observations	102
4.5	Results.....	104
4.5.1	Controlled comparison of the wind-speed profile methods.....	104
4.5.2	Upwind surface variability.....	105
4.5.2.1	Upwind surface variability at KCL.....	105
4.5.2.2	Influence of the upwind surface variability on the wind-speed profile.....	108
4.5.3	Internal parameters used in the wind-speed profile methods.....	109
4.5.4	Variability of observed wind speeds	111
4.5.5	Comparison of observed and estimated wind-speed profiles	113
4.6	Conclusions	117
	Appendix 4.A: Implementation of DH_v for estimating the wind-speed profile.....	119
Chapter 5.	Aerodynamic roughness parameters in cities: inclusion of vegetation	121
5.1	Introduction	121
5.2	Methodology.....	122
5.2.1	Macdonald et al. and Kanda et al. morphometric methods	122
5.2.2	Considering vegetation	123
5.2.3	Parameter determination and method development	126
5.2.4	Demonstration of impact.....	127
5.3	Results.....	129
5.3.1	Geometric parameters.....	129
5.3.2	Aerodynamic parameters.....	130
5.3.3	Influence of considering vegetation upon wind-speed estimates.....	134
5.4	Conclusions	136
Chapter 6.	Aerodynamic roughness variation with vegetation: analysis in a suburban neighbourhood and a city park	139
6.1	Introduction	139
6.2	Methodology.....	141
6.2.1	Site description and observations.....	141
6.2.2	Surface elevation database and differentiation between buildings and vegetation	142
6.2.3	Calculation of aerodynamic roughness parameters	146
6.3	Results.....	150
6.3.1	Impact of roughness elements on observational data	150

6.3.2	Land cover and geometry surrounding the sites	152
6.3.3	Aerodynamic parameters.....	154
6.3.3.1	Seoul Forest Park (SFP).....	154
6.3.3.2	Swindon (SWD).....	157
6.3.3.3	Similarities in aerodynamic parameter analysis between the sites.....	159
6.3.4	Implications for wind-speed estimation	160
6.4	Conclusions	163
Chapter 7. Urban morphology parameters from global digital elevation models: implications for aerodynamic roughness and for wind-speed estimation.....		165
7.1	Introduction	165
7.2	Elevation databases	167
7.2.1	Digital elevation model terminology.....	167
7.2.2	Global digital elevation models (GDEMs)	168
7.2.3	Previous assessment of GDEMs in urban areas	170
7.3	Methodology.....	171
7.3.1	Dataset comparison	171
7.3.2	Extraction of ground heights from the GDEMs.....	175
7.3.3	Polynomial function fitting.....	175
7.4	Results.....	176
7.4.1	Comparison 1: ASTER, SRTM and TanDEM-X in London, UK	176
7.4.2	Comparison 2: TanDEM-X in five cities	180
7.4.2.1	Comparison to benchmark data.....	180
7.4.2.2	Empirical correction of parameters	182
7.4.2.3	Assessment of empirical corrections for an independent location	186
7.5	Wind-speed estimates using the DEMs	187
7.6	Discussion of GDEM comparison	190
7.7	Conclusions	191
Appendix 7.A: The assessed global digital elevation models (GDEMs)		194
7.A.1	Advanced Spaceborne Thermal Emission and Reflection Radiometer (ASTER)	194
7.A.2	Shuttle Radar Topography Mission (SRTM)	194
7.A.3	TanDEM-X	194
Appendix 7.B: Pixel-to-pixel comparisons of global and benchmark DEMs		199
7.B.1	Comparison 1: ASTER, SRTM and TanDEM-X in London.....	199
7.B.2	Comparison 2: TanDEM-X in five cities	202

Appendix 7.C: Polynomials between benchmark and TanDEM-X model parameters.....	208
Appendix 7.D: Empirical relations between geometric parameters.....	209
Appendix 7.E: Urban morphology parameters for five global cities.....	212
Chapter 8. Conclusions	217
8.1 Research summary.....	217
8.2 Major conclusions	217
8.3 Limitations of analysis and possibilities for future work	223
References.....	227

Table of Figures

Figure 2.1: Idealised structure of the urban boundary layer (UBL), adapted from Fernando (2010). The outer layer is located above the surface layer, which is comprised of the sublayers: urban canopy layer (UCL), roughness sublayer (RSL) and inertial sublayer (ISL) 33

Figure 2.2: Logarithmic wind-speed profile (black dots) estimated above an urban surface showing the zero-plane displacement (z_d) and aerodynamic roughness length (z_0) (lines). Eq. 2.7 is used with: $z_d = 15$ m, $z_0 = 2$ m, $u_* = 1$ m s⁻¹ and $\kappa = 0.4$ 37

Figure 2.3: Source area for turbulent flux measurements at a central London site (yellow circle). The probable source area for the cumulative contribution to 80% of the total flux is calculated with the Kormann and Meixner (2001) model, using the median meteorological conditions of the fastest 25% of winds in 2014 (30-min averages), inputs are: standard deviation of the lateral wind velocity (σ_v) = 1.97 m s⁻¹; Obukhov length (L) = - 1513 m; friction velocity (u_*) = 0.94 m s⁻¹; wind direction 210°; zero-plane displacement (z_d) assumed = 30 m and aerodynamic roughness length (z_0) assumed = 2 m. The relative contribution of two-dimensional source area weightings are overlain upon building footprints > 2 m, assuming a measurement height (z_m) of: **(a)** 50.30 m and **(b)** 55.33 m (increase in z_m of 10%). For each source area, one-dimensional transects (red dashed lines in **(a)** and **(b)**) are shown for the: **(c)** along-wind wind direction (210°) and **(d)** cross-wind direction at the distance of maximum upwind relative contribution..... 42

Figure 2.4: Plan area of **(a)** buildings > 2 m and **(b)** buildings and vegetation > 2 m in central London, UK. Elevation database source: Lindberg and Grimmond (2011a)..... 44

Figure 2.5: Lateral cross section of flow approaching idealised arrays of roughness elements with heights that are **(a)** homogeneous and **(b)** heterogeneous. The mutual sheltering of roughness elements is exemplified, in addition to the unsheltered frontal areas of roughness elements, which exert a drag force (F_D) upon the flow and contribute to the shear stress (ρu_*^2 , Eqs. 2.5 and 2.6) in the inertial sublayer (figure not to scale)..... 47

Figure 3.1: Zero-plane displacement (z_d) and aerodynamic roughness length (z_0) normalised by average roughness-element height (H_{av}) for the morphometric methods assessed (Table 3.1), assuming roughness elements with: **(a, b)** homogeneous and **(c, d)** heterogeneous heights. Geometric parameters used are informed by the built surroundings within 1000 m of the KSSW site (Table 3.3): **(a, b)**: $H_{av} = 20$ m, maximum height (H_{max}) = 20 m and standard deviation of heights (σ_H) = 0 m; **(c, d)**: $H_{av} = 20$ m, $H_{max} = 117$ m, $\sigma_H = 11$ m. In both cases, frontal area index (λ_f) and plan area index (λ_p) are varied from 0 to 1, note λ_f can become larger than 1. The *Mac* method is shown for square (*Sq*) and staggered (*St*) arrays. Real cities limits are based on

Grimmond and Oke (1999). Curves shown may extend beyond the extent to which the model was originally developed.....57

Figure 3.2: Location of measurement sites KSK, KSS and KSSW at King’s College London (KCL) (see text for details) **(a)** within Greater London, UK (inset); **(b)** building heights surrounding the sites (major features labelled), red dashed lines indicate 250, 500, 750 and 1000-m radii from the KSSW site (black point); and **(c)** 250 m surroundings of KCL. (Photography source: Google imagery, 2014)..... 60

Figure 3.3: Flow diagram of the determination of aerodynamic parameters at the London sites using anemometric (*A*), reference (*R*) and morphometric (*M*) methods 63

Figure 3.4: Application of the temperature variance (TVM) and wind variance (WVM) anemometric methods at the KSSW site to determine z_d during unstable conditions ($-6.2 \leq z'/L \leq -0.05$), with $z_d = 30$ m used to define stability. Results shown are 30-min observations (points) of the scaled: **(a)** standard deviation of temperature (σ_T/T^*) and **(b)** vertical wind velocity (σ_w/u^*) by wind direction; and **(c)** frequency of unstable conditions for 10° bins. Non-linear fit (line) to observations for **(d)** TVM (Eq. 3.20) and **(e)** WVM (Eq. 3.21), with RMSE; **(f)** Solution for z_d (10° sectors) for the TVM (red solid line) and WVM (blue dashed line) 66

Figure 3.5: Comparison of anemometric (lines and shading) and morphometric (points) methods to determine the **(a, b, c)** zero-plane displacement (z_d) and **(d, e, f)** aerodynamic roughness length (z_0) (note $\ln y$ axis) surrounding the three assessed sites (Fig. 3.2). For anemometric methods, z_d is the median solution of the temperature variance (TVM, solid line) and wind variance (WVM, dashed line) methods, respectively, applied to 30-min observations during unstable conditions ($-6.2 \leq z'/L \leq -0.05$) for 10° sectors. The range (shading) represents all possible solutions by varying z_d used for stability definition from 0 to measurement height. z_0 is the median (lines) and upper and lower quartile (shaded) of the eddy-covariance method (Eq. 3.23) during neutral conditions ($|z'/L| \leq 0.05$) for each 10° sector using z_d from the TVM and WVM, respectively. Morphometric methods use geometry weighted by the final iterated footprint for each 30-min observation (Sect. 3.4.3.3) for the same stability conditions as anemometric methods, however, z_d in z'/L is determined by the respective morphometric method for each observation. Background shading is in directions where the River Thames is located (blue) and where turbulence data indicates disturbance (red). For method abbreviations see Tables 3.1 and 3.2..... 68

Figure 3.6: Root-mean-square error (RMSE) analysis of the aerodynamic parameters determined using the morphometric and anemometric methods for each 30-min period of observations at each site (smaller symbols) and for all observations (larger symbols). The RMSE

for z_d is plotted against root-mean-square geometric error (RMSGE) for z_0 (Eq. 3.24). The z_d is for unstable conditions ($-6.2 \leq z'/L \leq -0.05$ with z_d in z'/L for each morphometric method) and z_0 is for neutral conditions ($|z'/L| \leq 0.05$, with z_d in z'/L for each morphometric method). See Tables 3.1 and 3.2 for method abbreviations..... 72

Figure 3.7: Variation of mean hourly wind speed with height (33 profiles, see text for selection): **(a)** mean of extrapolated profiles (Eq. 3.25) with locally determined aerodynamic parameters from the KSS site (triangle) and each 30-m lidar gate (points). **(b)** Median (points) difference (U_{diff}) between observed (U_{obs}) and extrapolated (U_{ext}) wind speeds at 30-m lidar gates. Whiskers are the 5th, 25th, 75th and 95th percentiles. Lidar gates are shaded G1 – G3 (G1 = 126 – 156 m, mid-point = 141 m). See Tables 3.1 and 3.2 for method abbreviations 75

Figure 3.8: Integrated annual 80% source areas at the: **(a, b)** KSSW, **(c)** KSS and **(d)** KSK sites, normalised for the observation period (Table 3.3, from 30-min averaged observations, Sect. 3.3.2.2). Source areas are determined using the Kormann and Meixner (2001) analytical footprint model with aerodynamic parameters from the **(a, c, d)** *Mho* and **(b)** *Mac* morphometric methods. Cumulative source areas are shaded with 10% contours demarcated (black lines). Map units are metres..... 76

Figure 3.B1: **(a)** Aerodynamic drag coefficient ($C_{DU} = (u_*/\bar{U}_z)^2$), and turbulence intensities in the **(b)** longitudinal ($TI_u = \sigma_u/\bar{U}_z$), **(c)** transverse ($TI_v = \sigma_v/\bar{U}_z$) and **(d)** vertical ($TI_w = \sigma_w/\bar{U}_z$) wind directions, for all 30-min observations during neutral conditions (black dots) at the KSSW site. Neutral conditions are $|(z_m - z_d)/L| \leq 0.05$ (L is Obukhov length, $z_m = 50.3$ m and z_d is the average of the Millward-Hopkins (2011) and Kanda et al. (2013) morphometric methods for each time period (Fig. 3.5) (morphometric method z_d selected based upon wind-speed estimate accuracy, Fig. 3.7). The median each 5° wind direction is shown (red line). \bar{U}_z is the average wind speed, u_* is the friction velocity and $\sigma_u, \sigma_v, \sigma_w$ are the standard deviations of the longitudinal, transverse and vertical velocity components of the wind. Background shading is in directions where the River Thames is located (blue) and where turbulence data indicates disturbance (red)..... 81

Figure 3.B2: As for Fig. 3.B1, but for the KSS site ($z_m = 48.9$ m) 82

Figure 3.B3: As for Fig. 3.B1, but for the KSK site ($z_m = 38.8$ m)..... 83

Figure 3.C1: Sensitivity to the initial zero-plane displacement (z_d) and aerodynamic roughness length (z_0) when using the iterative procedure (Sect. 3.4.3.3), with the Kormann and Mexiner (2001) source area model and **(a, b)** Kanda et al. (2013) or **(c, d)** Macdonald et al. (1998) morphometric methods. The initial range of z_d and z_0 ‘test cases’ (initial input, blue dashed line: Miz_d and Miz_0 in Fig. 3.3) is shown with the z_d and z_0 result of each test case, after each iteration. See text for meteorological input and ‘Test case’ parameter selection..... 85

Figure 3.C2: Solution of iterative procedure (Sect. 3.4.3.3) for **(a)** zero-plane displacement (z_d) and **(b)** aerodynamic roughness length (z_0) (note $\ln y$ axis) for all 30-min observations in 2014 at the KSSW site. Roughness parameters are calculated using the Kanda et al. (2013) morphometric method and the iterative procedure is initiated with roughness parameters (i.e. Miz_d and Miz_0 in Fig. 3.3) from: (i) first-order estimates (gold points), or (ii) open country values (red points). Background shading: directions of River Thames (blue) and where turbulence data indicates disturbance (red)..... 86

Figure 4.1: Operation of the Deaves and Harris non-equilibrium wind-speed profile method (DH_v) as applied in this work. A source area footprint model is applied at pre-defined vertical increments (height: z_i m) above the reference site. The source area for each respective height (SA_r , SA_1 and SA_n) is used to determine representative roughness parameters (z_d and z_0), which are subsequently used to calculate local friction velocities ($u_{*,r}$, $u_{*,1}$, $u_{*,n}$). The effective wind-speed profile for each ‘layer’ (depth z_i m) is then calculated (using Eq. 4.5) with the appropriate roughness transition correction ($K_{x,1}$, $K_{x,n}$) (ESDU 2002). Subscripts are: ‘ r ’ reference (i.e. from the reference site observations), ‘1’ representative of the first calculations performed z_i m above the reference site, and ‘ n ’ for the n^{th} calculation (performed at $n \times z_i$ m above the reference height) 99

Figure 4.2: Location of the King’s College London (KCL) measurement sites in **(a)** Greater London (black outline), United Kingdom. **(b)** Ground height for the 20 km x 20 km around KCL. Building heights > 2 m in the surrounding: **(c)** 4 km and **(d)** 500 m. Sector divisions 1 – 5 in **(b)** and **(c)** are manually defined based upon upwind surface characteristics (see Sect. 4.5.2). Elevation data source: Lindberg and Grimmond (2011a) 103

Figure 4.3: Controlled comparison of the wind-speed profile extrapolated from 50 m using the different methods assessed (Sect. 4.2), normalised by a reference wind speed (U_{ref}) of 10 m s^{-1} . The profiles are extrapolated with roughness parameters characteristic of the study site determined by the **(a)** Kanda et al. (2013) and **(b)** Macdonald et al. (1998) morphometric methods. Profile abbreviations: *PL* – power law; *LOG* – logarithmic wind law; *DH_e* – Deaves and Harris equilibrium model; *DH_v* – Deaves and Harris non-equilibrium model; *GR* – Gryning et al. (2007). See text for the values used during the extrapolation 104

Figure 4.4: **(a)** Zero-plane displacement (z_d) and **(b)** aerodynamic roughness length (z_0) (note $\ln y$ axis), determined from source areas calculated in 25 m vertical increments above the KSSW site (colour indicates different heights). For the 251 hourly periods assessed, observations from the KSS site are used with the Kormann and Meixner (2001) footprint model from the KSSW position (Fig. 4.2) at the heights indicated, with the Kanda et al. (2013) morphometric method

to determine z_d and z_0 (Sect. 3.4.3.3 methodology). The five directional sectors (dashed lines, 1-5) for analysis (Table 4.1) are indicated 107

Figure 4.5: Mean of extrapolated wind-speed profiles in sector 1 ($n = 36$) using the DH_e method (black line) and DH_v method with height increment (z_i) = 50 m (blue line) and $z_i = 25$ m (red line). For the DH_v method, the extent of the upwind surface considered is dictated by the source area calculated at 200 m, which is altered to 150 m for comparison (green line). The 30 m wind gates used from lidar observations during this work are shaded G1 – G3 (G1=126 – 156 m, mid-point = 141 m) 109

Figure 4.6: For each hourly period assessed in sector 1 ($000^\circ - 045^\circ$ wind direction from the KSSW site): **(a)** friction velocity calculated internally to the DH_e model ($u_{*,calc}$) and from observations at the KSS site and ($u_{*,obs}$), **(b)** gradient height (h) determined internally to the DH_e model and the mixing layer height determined from observations (H_{ML} , average of two observation methods, see text). Subscripts K and M refer to use of the Kanda et al. (2013) and Macdonald et al. (1998) aerodynamic roughness parameters during calculations, respectively 110

Figure 4.7: Mean wind-speed profiles extrapolated using the Deaves and Harris equilibrium model (DH_e) for all hourly periods assessed in sector 1 ($n = 36$). The profiles are extrapolated using parameters calculated internally to the model ($calc$) and from observations (obs). Subscripts K and M indicate use of Kanda et al. (2013) and Macdonald et al. (1998) aerodynamic roughness parameters, respectively. The mean observed wind speed at 49 m by a sonic anemometer and 30 m wind gates of the lidar are shown with whiskers to indicate the minimum and maximum observed wind speeds. The 30-m lidar gates are shaded G1 – G3, with mid-points: G1 = 141 m, G2 = 171 m and G3 = 201 m 111

Figure 4.8: For all observations ($n = 245$): **(a)** average (points) and minimum/maximum (whiskers) observed wind speed at 49 m and 30 m gates of the Doppler lidar (shaded G1 – G3). Wind speed observed at: **(b)** 49 m (U_{49}) and the first gate of the lidar (U_{G1}), and **(c)** U_{G1} and the second (U_{G2} , circles) and third (U_{G3} , triangles) gates of the lidar, with a 1:1 relation (dashed line). Points circled in magenta are referred to in text. Data are selected through the filtering process outlined in Sect. 4.4 and coloured by wind direction (see Table 4.1 for sector definitions) 113

Figure 4.9: Distribution of hourly wind speed differences (U_{diff}) between observed (U_{obs}) and extrapolated (U_{ext}) wind speeds at heights corresponding to 30 m lidar gates (Gates shaded G1 – G3) ($U_{diff} = U_{ext} - U_{obs}$). Points are the median and whiskers are the 5th, 25th, 75th and 95th percentiles. The analysis is stratified into directional sectors (rows), labelled S1, S3, S4, S5 (see Table 4.1 for directions). Differences shown are using **(a – d)** Kanda et al. (2013) and **(e – h)**

Macdonald et al. (1998) roughness parameters. Profile abbreviations: *PL* – power law; *LOG* – logarithmic wind law; *DH_e* – Deaves and Harris equilibrium model, *DH_v* – Deaves and Harris non-equilibrium model; *GR* – Gryning et al. (2007) 114

Figure 4.A1: As for Fig. 4.5, but including *DH_v* profiles with $z_l = 10$ m and maximum source area calculation height of 200 m (purple line). For clarity, the comparative profile with $z_l = 25$ m and maximum source area calculation height of 150 m (green line in Fig. 4.5) is removed.....120

Figure 5.1: Relation between the drag coefficient of porous roughness elements (C_{Dv}) and porosity (P_{3D}), data from: Hagen and Skidmore (1971) (HA); Wilson (1985) (WI); Seginer (1975) (SG); Grant and Nickling (1998) (GN); Bitog et al. (2011) (BI), Guan et al. (2000) (GU00) and Guan et al. (2003) (GU03). Lines are relations from Guan et al. (2003) (GU_{wb}, Eq. 5.6) and Guan et al. (2000) (GU_{it}, Eq. 5.7) 125

Figure 5.2: Study areas representative of: **(a)** city centre with low vegetation (CC_lv), **(b)** city centre with similar building and vegetation heights (CC_hv), **(c)** suburban with low vegetation (Sb_lv), **(d)** a suburban with taller vegetation (Sb_hv) and **(e)** an urban park (Pa). Source areas determined using the iterative methodology in Sect. 3.4.3.3, rotated into the wind direction (210°). Colour indicates roughness-element type and hue its height (see key)..... 129

Figure 5.3: Logarithmic wind-speed profiles (using Eq. 5.1) from $z = z_d + z_0$ to $z = 100$ m, using z_d and z_0 determined for five study areas: **(a)** city centre with low vegetation (CC_lv), **(b)** city centre with similar building and vegetation heights (CC_hv), **(c)** a suburb with low vegetation (Sb_lv), **(d)** a suburb with taller vegetation (Sb_hv) and **(e)** a park (Pa). Wind speed at the bottom of the profile ($z_d + z_0$) is assumed 0 m s^{-1} and friction velocity (u_*) 0.94 m s^{-1} throughout the profile. Wind speeds are normalised by u_* (U_z/u_*). Aerodynamic parameters are determined are using the Kanda et al. (2013) (*Kan*) and Macdonald et al. (1998) (*Mac*) morphometric methods (different colours) for each study area, considering buildings only (solid line), including vegetation with leaf-off porosity (short dashed line) and leaf-on porosity (long dashed line) (values in Table 5.2). Note different x scale on **(e)** 135

Figure 6.1: View from the: **(a-d)** Seoul Forest Park (SFP) and **(e-f)** Swindon (SWD) measurement locations, with approximate directions 142

Figure 6.2: Classification of buildings and vegetation for the **(a-e)** Seoul Forest Park and **(f-h)** Swindon site (yellow triangles) surroundings: **(a, f)** aerial photograph; **(b)** manual land cover classification; **(c)** building digital surface model (BSM, red) and canopy digital surface model (CDSM, green) from manual technique; **(d)** vegetation mask from analysis of RGB colour bands in **(a)**; **(e)** BSM and CDSM from automated technique; **(g)** building footprints and, **(h)** BSM and CDSM using building footprint mask. Magenta circles are referred to in text. Map units are

metres. Data sources: aerial imagery – Seoul city aerial image service centre, Digimap 2017; elevation data – see Table 6.2; building footprints – Ordnance Survey 2014 145

Figure 6.3: All 30-min observations during neutral conditions (black dots) at the **(a-d)** Seoul Forest Park (SFP) and **(e-h)** Swindon (SWD) sites: **(a, e)** aerodynamic drag coefficient ($C_{DU} = (u_*/\bar{U}_z)^2$), and turbulence intensities in the **(b, f)** longitudinal ($TI_u = \sigma_u/\bar{U}_z$), **(c, g)** transverse ($TI_v = \sigma_v/\bar{U}_z$) and **(d, h)** vertical ($TI_w = \sigma_w/\bar{U}_z$) wind directions. Neutral conditions are $|(z_m - z_d)/L| \leq 0.05$ (L is Obukhov length, $z_m = 12.2$ m at SFP and 12.5 m at SWD, z_d is assumed as $H_{av} = 8$ m at SFP and 4.5 m at SWD). Red line is the median for each 5° wind direction. \bar{U}_z is the average wind speed, u_* is the friction velocity and $\sigma_u, \sigma_v, \sigma_w$ are the standard deviations of the longitudinal, transverse and vertical velocity components of the wind 151

Figure 6.4: Source area climatology of the Swindon site (SWD) modelled using the Kormann and Meixner (2001) source area model for the months of June, July and August (Leaf-on) in 2011 and 2012. Source areas are modelled using aerodynamic parameters from the **(a)** Kanda et al. (2013) and **(b)** Macdonald et al. (1998) morphometric methods. The 80% cumulative source area weights for each 30-min average of observations are integrated and normalised by the sum of all weightings ($n = 8787$). Source areas overlain upon buildings (black) and vegetation (green) > 2 m. Map units: metres 153

Figure 6.5: Median aerodynamic parameters determined for 10° wind sectors surrounding Seoul Forest Park site (SFP). Seasons (columns) are: leaf-on (June, July, August) and leaf-off (December, January, February). *Anemometric methods:* TVM (temperature variance, Rotach 1994); WVM (wind variance, Toda and Sugita 2003), with the range of solutions (shading) provided from varying constants used during application of the methods and initial z_d used to define stability (Sect. 6.3.2). *Morphometric methods:* *Kan* (Kanda et al. 2013); *Mac* (Macdonald et al. 1998) applied using the Kormann and Meixner (2001) footprint model for all 30-min observations, with $10^{\text{th}}/90^{\text{th}}$ percentile for each 10° sector shaded. z_d is for unstable conditions ($-6.2 \leq z'/L \leq -0.05$, with $z' = z_m - z_d$ and L the Obukhov length) and z_0 is for neutral conditions ($|z'/L| \leq 0.05$). For morphometric method stability definition, z_d in z'/L is determined by the respective morphometric method. Insufficient neutral conditions for southerly winds during leaf-off vegetation state means no morphometric z_0 is reported here 155

Figure 6.6: Comparison of anemometric (lines and shading) and morphometric (points) methods to determine the **(a)** zero-plane displacement (z_d) and **(b)** aerodynamic roughness length (z_0) (note $\ln y$ axis) surrounding the Swindon site (Fig. 6.2f). For anemometric methods, z_d is the median solution of the temperature variance (TVM) and wind variance (WVM) methods, applied to 30-min observations during unstable conditions ($-6.2 \leq z'/L \leq -0.05$, with $z' = z_m - z_d$ and L the

Obukhov length) for 10° sectors. The range (shading) represents all possible solutions by varying z_d used for stability definition and varying constants used in the methods. z_0 is the median (lines) and upper and lower quartile (shaded) of the eddy-covariance method, during neutral conditions ($|z'/L| \leq 0.05$) for each 10° sector, using z_d from the TVM and WVM, respectively. Less than 10 observations in the 110° sector means no values are reported here. The morphometric methods: *Kan* (Kanda et al. 2013); *Mac* (Macdonald et al. 1998) are for each source area during the same conditions as the anemometric methods, applied considering vegetation (subscript *bv*) and for buildings only (subscript *b*). For the morphometric method stability definition, z_d in z'/L is determined by the respective morphometric method..... 158

Figure 6.7: Observed (U_{obs}) and estimated (U_{est} , Eq. 6.10) wind speeds for each 30-min period (at the SWD site) using the Kanda et al. (2013, *Kan*) and Macdonald et al. (1998, *Mac*) morphometric methods, considering both buildings and vegetation (subscript *bv*) and only buildings (subscript *b*). Data are binned from lowest wind speed in groups of 1250 (30-min) data points. Median (points) and 5th and 95th percentiles shown. The root-mean-square error then mean absolute error ($m s^{-1}$) (between U_{est} and U_{obs}) are given in the legend 162

Figure 6.8: As for Fig. 6.7, but for wind directions between: **(a)** 210° – 240° and **(b)** 030° – 090°. Each point represents a 30-min period of observations (data are not binned) 162

Figure 7.1: Different digital elevation models (DEMs) and terminology used: **(a)** digital surface model (DSM) and digital terrain model (DTM), **(b)** roughness-element surface model (RESM = DSM – DTM), **(c)** building digital surface model (BSM) and **(d)** canopy digital surface model (CDSM). From **(b)** to **(c)** or **(d)** requires land cover information. GIS examples are: **(e)** DSM, **(f)** DTM, **(g)** mask of pixels which are in the BSM (black) and CDSM (green) for a 4 km x 4 km area in central London, UK (map units: km). Surface elevation database details: Lindberg and Grimmond (2011a)..... 167

Figure 7.2: Work flow for processing the global digital elevation models (GDEMs) and for comparison to benchmark data. For abbreviations see Fig. 7.1. For comparison 2, only pixels within the global urban footprint (GUF) mask ‘settlement layer’ are retained (Esch et al. 2017), indicated with ‘UF’ prefix: UFDSM – urban footprint digital surface model = ground + surface feature heights within the GUF; UFDTM – urban footprint digital terrain model = ground heights within the GUF; UFRESM – urban footprint roughness-element surface model = roughness-element heights within the GUF 172

Figure 7.3: Procedure to determine morphology parameters from a directional sector of a 1 km x 1 km grid square in central London: **(a)** roughness-element surface model (black = buildings, green = vegetation) overlain with 45° sector representing northerly wind direction (red shading);

(b) roughness-element heights within directional sector for calculation; **(c)** parameter calculation from idealised roughness elements 174

Figure 7.4: **(a)** Greater London (black demarcation), with the 20 km x 20 km study area (magenta) and a central area (red) with meteorological equipment (Sect. 7.5). The digital surface model (ground + roughness-element heights, DSM) of the **(b)** benchmark is shown, with DSMs from the **(c)** ASTER, **(d)** SRTM, and **(e)** TanDEM-X (with water mask applied [white]) and **(f – h)** their respective differences from the benchmark DSM. Map units: **(a)** degrees (WGS84) and **(b-h)** km 177

Figure 7.5: Comparison between parameters determined from the GDEMs and benchmark data for eight directional sectors of 1 km grid-squares in the 20 km x 20 km central London area (Fig. 7.4). For the comparisons, parameters in the benchmark dataset are divided into bins (x-axis, not inclusive of upper value labelled) and the distributions of parameters calculated by the GDEMs in the corresponding locations are shown for each bin (left y-axis). Whiskers are the 1st and 99th percentiles. Note, ideal distributions would be within the grey shaded areas. The percentage frequency of benchmark values within each bin are also shown (right y-axis, red line). Parameter calculation, abbreviations and units: Fig. 7.3c 179

Figure 7.6: A 1 km grid-square in central London: **(a-d)** digital surface model (DSM), **(e-h)** digital terrain model extracted using the Sect. 7.3.2 methodology with a 5 x 5-pixel moving window and **(i-l)** roughness-element surface model (RESM) (rows) derived from the: benchmark, TanDEM-X, ASTER and SRTM datasets (columns). Magenta circles are referred to in text (Sect. 7.5). Map units: km 180

Figure 7.7: Digital surface models of downtown New York from the **(a)** benchmark and **(b)** TanDEM-X data. Only buildings and ground heights are included in the benchmark data. The global urban footprint (GUF) mask (Esch et al. 2017, see text) is applied to the TanDEM-X model. Map units: km 181

Figure 7.8: Geometric parameters determined for five cities based on 1 km grid-squares (8 directional sectors per grid, Fig. 7.3) from benchmark [BM] and TanDEM-X [TDX] datasets. All data points are shown for average ground height ($H_{av,grid}$). For the other parameters, each city's data are binned (5 m for H_{av} and σ_H ; 10 m for H_{max} ; 0.1 for λ_p and λ_f) with the median (point) and interquartile range (whiskers) per bin shown. Polynomial fits use all city-specific data for each parameter (coloured lines). See Sect. 7.3.3 for 'multi-city' fit method and text for explanation of fits in **(f)**. For equation, error and data range of each fit see Appendix 7.C. Parameter calculation, abbreviations and units: Fig. 7.3c 182

Figure 7.9: Zero-plane displacement (z_d) [m] and aerodynamic roughness length (z_0) [m] (note log axis), calculated using the Kanda et al. (2013) morphometric method for five cities based on 1 km grid-squares (8 directional sectors per grid, Fig. 7.3) from benchmark [BM] and TanDEM-X [TDX] datasets. All data points are shown in **(b)** and elsewhere data are binned per city (10 m for z_d ; 1 m for z_0) with the median (point) and interquartile range (whiskers) per bin shown. Parameters are calculated with TanDEM-X geometry which is: **(a, b)** uncorrected; **(c, d)** corrected with multi-city relations (Fig. 7.8, Table 7.C1); and **(e, f)** corrected with city-specific relations (Fig. 7.8, Table 7.C1). Note, the multi-city relation is used to correct λ_f in all cases, with Eq. 7.3 used to estimate corrected values of $\lambda_f < 0.08$ (see discussion in text). Data point errors given in Table 7.4 184

Figure 7.10: Parameters derived from the benchmark and TanDEM-X data (directly/uncorrected and corrected with suggested method, see text) for New York (mean of 1 km grid-squares from 8 sectors, Fig. 7.3). Map units: km. Parameter calculations, abbreviations and units: Fig. 7.3c. Maps for other cities are included in Appendix 7.E 185

Figure 7.11: Land surface information in New York using TanDEM-X products. The water mask is used with the GUF mask (Esch et al. 2017) to indicate impervious and pervious surfaces ('settlement' and 'non-settlement' layer, respectively). For analysis of actual land cover in each mask, see Appendix 7.A. Map units: km 186

Figure 7.12: Independent assessment site of corrections to the TanDEM-X derived parameters – Slough, UK: **(a)** aerial image; **(b)** benchmark building footprints (OS MasterMap® Topography Layer – Building Height Attribute, Ordnance Survey 2014) used to mask heights derived from the 1 m resolution EA composite lidar data (UK Environment Agency 2017); and, **(c)** TanDEM-X roughness-element heights within the global urban footprint mask (UFRESM) (Esch et al. 2017) from which parameters are calculated. The central 3 km x 3 km area is shown for the **(d)** benchmark data and **(e)** TanDEM-X. Map units: km. Upper left corner coordinates (WGS84, UTM30N): $x = 661100.66$, $y = 5712952.10$ 187

Figure 7.13: Parameters derived from benchmark [BM] and TanDEM-X [TDX] data for (i) the independent assessment site, Slough (Fig. 7.12, circles here) (Sect. 7.4.2.3) and (ii) the wind-speed application site, central London (Fig. 7.6, triangles here) (Sect. 7.5). TanDEM-X parameters are: uncorrected (black and red symbols) and corrected (using the London-fit and multi-city procedure for λ_f (see text), blue and green symbols). Each point is one of eight 45° directional sectors within a 1 km grid-square – see Fig. 7.3 for parameter calculations, abbreviations and units 189

Figure 7.14: Hourly mean observed and estimated wind-speed for strong wind conditions above a central London site (Fig. 7.6). Profiles when wind is from: **(a)** all directions ($n = 245$), and **(b)** $000^\circ - 045^\circ$ ($n = 36$). Observed wind speed is the average (point) and 5th and 95th percentiles (whiskers) at 49 m (sonic anemometer) and at three 30 m gates (shaded G1 – G3) by Doppler lidar. Estimated wind speed is with roughness parameters determined from different DEMs (coloured lines): SRTM, ASTER, uncorrected TanDEM-X (TDX) (Fig. 7.13, red triangles), TanDEM-X with geometry corrected (TDX_{cor}) (Fig. 7.13, green triangles), and benchmark (BM). Roughness parameters are calculated for 45° sectors with a 500-m fetch (e.g. Fig. 7.3a), except for BM_{SAFM}, which uses source area calculations. See text for more details 190

Figure 7.A1: TanDEM-X meta-information layers for the 20 km x 20 km study area in central London (Fig. 7.4): **(a)** coverage map (COV); **(b)** consistency mask (COM); **(c)** height error map (HEM); and, **(d)** water mask (WAM). **(e-g)** Distribution of absolute elevation differences between pixels in the benchmark and TanDEM-X digital surface models for the value(s) in each meta-information layer (x-axis). Whiskers are the 1st and 99th percentiles. **(h)** Water mask derived from the OS MasterMap[®] topography layer (Ordnance Survey 2010). Databases are re-sampled to 4 m pixel resolution for comparison. White circles in **(b)** and **(c)** are referred to in text. Map units: km..... 196

Figure 7.A2: Land cover information in **(a)** central London and **(b)** New York. For London, the OS MasterMap[®] topography layer (Ordnance Survey, 2010) is complimented with building and vegetation height information from the Lindberg and Grimmond (2011a) database, ‘other vegetation’ refers to shrubs (< 2 m) and grasses. For New York, the New York City Landcover (2010) is used (Department of Parks and Recreation 2017), the ‘tree canopy’ layer is assumed to correspond to ‘vegetation > 2 m’ and ‘other impervious’ refers to roads, railroads and other paved surfaces 197

Figure 7.A3: Pixels classified as: **(a)** ‘settlement’ and **(b)** ‘non-settlement’ in the global urban footprint (GUF) mask (Esch et al. 2017) in central London. Land cover masks derived from the OS MasterMap[®] topography layer (Ordnance Survey 2010), comprising of: **(c)** built or paved surfaces and **(d)** tress, grasses, shrubs and water. Map units: km 198

Figure 7.A4: Percentage of pixels in the ‘settlement’ and ‘non-settlement’ layers of the global urban footprint (GUF) mask (Esch et al. 2017) compared to land cover information in **(a)** central London study area (Fig. 7.A2a) and **(b)** New York (Fig. 7.A2b). For land cover source and classes see Fig. 7.A2. All databases are resampled to 4 m pixel resolution for comparison 198

Figure 7.B1: Comparison between pixels in the benchmark and assessed global digital elevation models for the: **(a)** digital surface model (DSM), **(b)** digital terrain model (DTM) extracted with

a 5 x 5-pixel moving window and **(c)** roughness-element surface model (RESM). In **(c)** the additional RESM assessed (TanDEM-X2) is from subtracting the benchmark DTM from the TanDEM-X DSM. For the comparisons, pixels in the benchmark dataset are divided into 10 m bins (x-axis, not inclusive of upper value labelled) and the distribution of heights in the corresponding GDEM pixels are shown for each bin (left y-axis). Whiskers are the 1st and 99th percentiles. Note, ideal distributions would be within the grey shaded areas. The percentage frequency of benchmark pixels within each bin are also shown (right y-axis, red line). For count/percentage of pixels in each height bin and root-mean-square errors from the benchmark data, see Tables 7.B1, 7.B2 and 7.B3 for the DSM, DTM and RESM, respectively..... 200

Figure 7.B2: As for Fig. 7.B1b, but for a comparison between pixels in the benchmark dataset and pixels of the digital terrain models (DTMs) extracted from the TanDEM-X dataset. The DTMs are extracted as outlined in Sect. 7.3.2 varying the width of the moving window by the indicated pixels (colours). Counts and error results are provided in Table 7.B2c 201

Figure 7.B3: As for Fig. 7.B1, but for benchmark data in five cities compared to the TanDEM-X model with the global urban footprint mask (Esch et al. 2017) applied: **(a)** urban footprint digital surface model (UFDSM), **(b)** urban footprint digital terrain model (UFDTM) and **(c)** urban footprint roughness-element surface model (UFRESM). UFDTMs are extracted using Sect. 7.3.2 method with a 5 x 5-pixel moving window, except for New York (7 x 7-pixel). For count/percentage of pixels in each height bin and root-mean-square errors from the benchmark data see Tables 7.B4, 7.B5 and 7.B6 for the UFDSM, UFDTM and UFRESM, respectively 203

Figure 7.D1: Polynomial relations between geometric parameters determined from the benchmark data (buildings only, represented by subscript b). Polynomial fits use all city-specific data for each parameter (coloured lines) and the ‘multi-city’ polynomial is by Sect. 7.3.3 method. Auckland is dashed, as a lack of benchmark data building footprints mean the global urban footprint mask (Esch et al. 2017) is used to retain buildings only (see main text). Kanda et al. (2013) relations (Eqs. 7.D1 – 7.D3) are also shown (Kan). Each point is one of eight 45° directional sectors within a 1 km grid-square and is coloured by the average building height ($H_{av,b}$) in that 1 km grid-square. Table 7.D1 has the equation, error and data range of fits. Parameter calculation, abbreviations and units: Fig. 7.3c 210

Figure 7.E1: As for Fig. 7.10, but for Sao Paulo..... 212

Figure 7.E2: As for Fig. 7.10, but for Tokyo..... 213

Figure 7.E3: As for Fig. 7.10, but for Greater London..... 214

Figure 7.E4: As for Fig. 7.10, but for Auckland..... 215

Table of Tables

Table 2.1: The expected effect of atmospheric stability upon the wind-speed profile. Q_H is the turbulent sensible heat flux, L is the Obukhov length (Eq. 2.8) and ζ is the Monin-Obukhov stability parameter (Eq. 2.9). (Monin-Obukhov (1954), their Fig. 1 has diagrammatic representation) 39

Table 3.1: Morphometric methods assessed (rows) with their required geometric parameters (columns). Morphometric method abbreviations: *RT* – Rule of thumb (Grimmond and Oke 1999), *Rau* – Raupach (1994), *Bot* – Bottema and Mestayer (1998), *Mac* – Macdonald et al. (1998), *Mho* – Millward-Hopkins et al. (2011), *Kan* – Kanda et al. (2013). Geometric parameters: H_{av} – average roughness-element height, λ_p – plan area index, λ_f – frontal area index, H_{max} – maximum roughness-element height, σ_H – standard deviation of roughness-element heights 54

Table 3.2: Anemometric methods used to calculate the **(a)** zero-plane displacement (z_d) and **(b)** aerodynamic roughness length (z_0) with their respective meteorological variables and required stability condition. *Methods:* TVM – temperature variance method (Rotach 1994), WVM – wind variance method (Toda and Sugita 2003), EC – eddy covariance method (Grimmond et al. 1998). Variables: z – measurement height, z_d – zero-plane displacement, L – Obukhov length, u_* – friction velocity, \bar{U}_z – mean horizontal wind speed at height z , σ_w – standard deviation of vertical velocity component, σ_u – standard deviation of horizontal velocity component, σ_T – standard deviation of temperature, T^* – temperature scale 58

Table 3.3: Characteristics of the measurement sites within a 1-km fetch: **(a)** sensor heights: metres above ground level, river position: bearing of the most northern point of the north bank, **(b)** geometric parameters and **(c)** surface cover 62

Table 3.4: Characteristics of the annual source area (80%) for each site (Fig. 3.8). **(a)** geometric parameters and **(b)** surface cover. See Tables 3.1 and 3.3 for measurement time periods and method/ geometry abbreviations 77

Table 3.A1: Methods in the literature (ordered by date) to calculate the zero-plane displacement (z_d) and aerodynamic roughness length (z_0) from **(a)** morphometric and **(b)** anemometric data with the stability conditions required. Methods used in this study are indicated (*) and have their abbreviation used in the Reference column 80

Table 4.1: Directional sectors used for analysis with the number of hourly profiles. Upwind surface characteristics around the KSSW site (see Fig. 4.2b, c and Fig. 4.4) are used for the classification, based on the wind direction observed in the first usable Doppler lidar gate (mid-point = 141 m) 106

Table 5.1: Geometric parameters determined for: all roughness elements; vegetation only; and buildings only, in the five study areas (Fig. 5.2). H_{av} , H_{max} and σ_H are the average, maximum and standard deviation of roughness-element heights (in metres), respectively, λ_p is plan area index and λ_f is frontal area index. Subscripts: *v* for vegetation, *b* for buildings, *l-on* for leaf-on and *l-off* for leaf-off 132

Table 5.2: Aerodynamic parameters determined using the Macdonald et al. (1998, *Mac*) and Kanda et al. (2013, *Kan*) morphometric methods in the five study areas (Fig. 5.2). Parameters are determined for buildings only and for all roughness elements (both buildings and vegetation), with leaf-on (*l-on*) and leaf-off (*l-off*) vegetation 132

Table 5.3: Percentage difference in aerodynamic parameters calculated using the **(a)** Macdonald et al. (1998, *Mac*) and **(b)** Kanda et al. (2013, *Kan*) morphometric methods from Table 5.2, between: buildings (*x*) and all roughness elements (*y*) assuming a leaf-on porosity (*b, l-on*); buildings (*x*) and all roughness elements (*y*) assuming a leaf-off porosity (*b, l-off*) and for all roughness elements assuming a leaf-on (*x*) or leaf-off porosity (*y*) (*l-on, l-off*). Percentage difference = $\frac{|x-y|}{(x+y)/2} \times 100$ 133

Table 5.4: Percentage difference in aerodynamic parameters calculated using the Macdonald et al. (1998, *Mac*) (*x*) or Kanda et al. (2013, *Kan*) (*y*) morphometric methods from Table 5.2, for buildings only and all roughness elements assuming a leaf-on porosity (*l-on*) and leaf-off porosity (*l-off*). Percentage difference = $\frac{|x-y|}{(x+y)/2} \times 100$ 133

Table 6.1: Site observation meta-data. Heights are metres above ground level. *(Stewart and Oke 2012) 143

Table 6.2: Source and accuracy of surface elevation databases used at the Seoul Forest Park (SFP) and Swindon (SWD) measurement sites..... 144

Table 6.3: Constants ($C_1 - C_d$) for application of the temperature variance (TVM) and wind variance (WVM) anemometric methods (Eq. 6.1 and 6.2). For all observations, extensive flat homogeneous terrain is reported. Kaimal and Finnigan (1994) and Toda and Sugita (2003) are after synthesis of coefficients from various studies. At the SWD site, the Choi et al. (2004) constants are not applied, as they predict the scaled σ_T and σ_w to be much larger and smaller than observations, respectively, meaning z_d solutions are consistently zero. *constants obtained from $\sigma_T/T_* = C_1(1 - C_2[(z - z_d)/L])^{\frac{1}{3}}$ 147

Table 6.4: Characteristics within a 300-m radius of the Seoul Forest Park site by direction (45° sectors, ±22.5° of the stated direction): **(a)** Land cover and **(b)** Geometry of roughness elements > 2 m. ‘Other’ land cover is predominantly comprised of a water works (with few roughness

elements > 2 m), which cannot be classified from aerial imagery. Geometry abbreviations: H_{av} – average height, H_{max} – maximum height, σ_H – standard deviation of heights, λ_p – plan area index, λ_f – frontal area index 152

Table 6.5: Roughness-element characteristics in the source areas modelled during leaf-on conditions at SWD using the **(a)** Kanda et al. (2013, *Kan*) and **(b)** Macdonald et al. (1998, *Mac*) morphometric methods (Fig. 6.4) for all observations ($n = 8787$) and in the specified north-easterly (NE) ($n = 911$) and south-westerly (SW) ($n = 2045$) directions. Geometry abbreviations: H_{av} – average height, H_{max} – maximum height, σ_H – standard deviation of heights, λ_p – plan area index, λ_f – frontal area index. Cover is the weighted percentage of pixels in the source area which are in the BSM for buildings and CDSM for vegetation 154

Table 7.1: Summary of the global digital elevation models used in this work 169

Table 7.2: Source and extent of the benchmark data used in comparison 2 (Fig. 7.2). Benchmark datasets downloaded during March 2017. Symbols: ✓ = available from source, - = not available, C – created. Maps of spatial extent provided in Fig. 7.10 (New York) and Appendix 7.E..... 173

Table 7.3: Geometric parameters x and y used during polynomial function fitting (Eq. 7.2). Polynomial fits are between geometric parameters derived from the: **(a)** TanDEM-X [TDX] and benchmark [BM] elevation data (i.e. fitting stage (i) in Fig. 7.2) and **(b)** benchmark parameters considering buildings only (represented by subscript b) (i.e. fitting stage (ii) in Fig. 7.2). Parameter calculation, abbreviations and units: Fig.7.3c176

Table 7.4: Root-mean-square error (RMSE), normalised RMSE (nRMSE) and mean bias error (MBE) for geometric and aerodynamic parameters calculated from the benchmark data and the: ASTER, SRTM and TanDEM-X datasets. Parameters are calculated for eight directional sectors of 1 km grid-squares in the 20 km x 20 km central London area (Fig. 7.4). For each parameter, errors are calculated if both elevation models have H_{av} and $H_{max} > 2$ m and the benchmark data have: λ_p and $\lambda_f \geq 0.05$ and z_d and $z_0 > 0.1$. Parameter calculation, abbreviations and units: Fig.7.3c. $H_{av,grd}$ is the average ground height [m]. Note similarity in z_0 errors for the ASTER and SRTM is due to rounding.....178

Table 7.5: Root-mean-square error (RMSE), normalised RMSE (nRMSE) and mean bias error (MBE) of TanDEM-X parameters from the benchmark datasets in all cities using the: uncorrected TanDEM-X data, multi-city polynomial correction, and city-specific polynomial correction. No correction is attempted to the ground height ($H_{av,grd}$). For each parameter, errors are calculated if both elevation models have H_{av} and $H_{max} > 2$ m and the benchmark data have: λ_p and $\lambda_f \geq 0.05$ and z_d and $z_0 > 0.1$. For parameter calculation, abbreviations and units see Table 7.3. $H_{av,grd}$ is the average ground height [m].....183

Table 7.B1: Benchmark and global digital elevation model (GDEM) digital surface models (DSMs) compared for the 20 km x 20 km study area in central London (Fig. 7.4). Pixels in the benchmark dataset are divided into 10-m bins with the root-mean-square error (RMSE) from heights in the corresponding GDEM pixels shown. The pixel count is the number of pixels in the benchmark data height bin and the percentage of total pixels in each height bin is shown. The ‘all’ column refers to values for all pixels.....204

Table 7.B2: As for Table 7.B1, but for the digital terrain models (DTMs) extracted (Sect. 7.3.2 method) using the: **(a)** ASTER, **(b)** SRTM and **(c)** TanDEM-X models. The RMSE results for different sized windows are shown 204

Table 7.B3: As for Table 7.B1, but for the roughness-element surface models..... 205

Table 7.B4: As for Table 7.B1, but for benchmark digital surface models in four cities compared to TanDEM-X only. Note, only pixels within the ‘settlement’ layer of the global urban footprint (GUF) mask (Esch et al. 2017) are compared. (Note, benchmark DSM not available for Sao Paulo, Table 7.2)..... 205

Table 7.B5: As for Table 7.B2, but for benchmark digital terrain models in four cities compared to the TanDEM-X only. Only pixels within the ‘settlement’ layer of the global urban footprint (GUF) mask (Esch et al. 2017) are compared (Note, benchmark DTM not available for Sao Paulo, Table 7.2)..... 206

Table 7.B6: As for Table 7.B3, but for the roughness-element surface models in five cities compared to the TanDEM-X data only. In Sao Paulo, Tokyo, New York and London the pixels compared are ‘buildings’ in the benchmark data. In Auckland, the ‘settlement’ layer of the global urban footprint (GUF) mask (Esch et al. 2017) is the basis for comparison 207

Table 7.C1: Polynomial relations between parameters determined from the benchmark (y) and the TanDEM-X (x) datasets (Table 7.3a) constrained to: $y = ax^3 + bx^2 + cx$, where a , b and c are the best-fit constants (Sect. 7.3.3 method). Columns are: root-mean-square error for each parameter (original RMSE), following correction using the polynomial relation (corrected RMSE), normalised values (nRMSE), and data range of TanDEM-X derived parameters (x min, x max). No correction is attempted to ground height ($H_{av,grd}$). For each parameter, errors are calculated if both elevation models have H_{av} and $H_{max} > 2$ m and the benchmark data have: λ_p and $\lambda_f \geq 0.05$ and z_d and $z_0 > 0.1$. Fits are city-specific, except for **(f)** ‘multi-city’, which follows Sect. 7.3.3 method. Parameter calculation, abbreviations and units: Fig. 7.3c 208

Table 7.D1: Polynomial relations between geometric parameters (‘parameter’ column) determined from buildings (subscript b) in the benchmark datasets (Table 7.3b). For each pair of parameters $y = f(x)$, the fits are constrained to $y = ax^3 + bx^2 + cx$, where a , b and c are the best-

fit constants between the parameters (Sect. 7.3.3 method). Given the lack of benchmark data building footprints in Auckland, the global urban footprint mask (Esch et al. 2017) is used to retain buildings only (see main text). The root-mean-square error (RMSE) and normalised RMSE (nRMSE) correspond to the fit of the polynomial function through the data points. Data range of the fit is indicated (x min, x max). Parameter calculation, abbreviations and units: Fig. 7.3c.
..... 211

Chapter 1. Research overview

1.1 Motivation for research

The atmospheric boundary layer is the interface between humans and the atmosphere, where in a reciprocal relationship, humans (and the effects of their activities) and the atmosphere interact. These interactions frequently occur within the urban boundary layer, where over 50% of the world's population currently reside (UN 2014). With increases of urban populations expected (UN 2014), growth and rapid transformation of cities are an inevitable part of the future. It is therefore vital to improve our current understanding of urban boundary layer processes.

Over the past four decades our understanding and modelling of the urban environment across a broad spectrum of topics has improved (e.g. Roth 2000, Arnfield 2003, Stewart 2011, Tominaga and Stathopoulos 2013, Barlow 2014). This progress has benefited from increasing computational resources, which have enhanced observations in urban areas and allowed for numerical analysis of more complex geometries. However, describing the mean and turbulent characteristics of airflow above heterogeneous urban environments is still challenging due to the numerous sources and sinks of mass, momentum and heat. Physical and numerical experiments have tended to focus on idealised arrays and boundary conditions. In addition, the impracticalities of observations throughout the depth of the urban boundary layer means that few 'truth' datasets exist.

This work aims to improve the understanding and representation of the aerodynamic properties (or roughness) of urban surfaces, specifically for the purposes of wind-speed estimation. The importance of wind flow is common to all boundary layer processes, as winds are critical for the exchange of momentum and other scalars (such as pollutants). Urban wind regimes are therefore of central interest to meteorologists and engineers for: numerical weather prediction, ventilation, pollutant dispersal, wind loading, pedestrian comfort, urban heat island effects, boundary conditions for physical and numerical experiments, aviation, wind driven rain, agriculture, snow drift and urban wind energy generation. The hazards associated with wind are also of concern globally. Strong winds in the tropics mainly accompany tropical storms which leave a path of destruction, whilst mid-latitude wind storms have been shown to be the costliest natural hazards across continents (Europe) (Leckebusch et al. 2007).

An accurate model for estimating the vertical profile of wind speed in urban areas, requiring a few readily available parameters, is an appealing prospect. However, modelling the urban wind-

speed profile accurately is difficult because a patchwork of surfaces with different aerodynamic properties results in complex flows. This patchwork includes: buildings of varying height, shape, orientation and materials, in the presence of vegetation and other roughness elements, creating considerable roughness-element heterogeneity. A pre-requisite to modelling the wind-speed profile is effectively parameterising the aerodynamic properties of these complex underlying surfaces. This can be achieved using the aerodynamic roughness parameters of the zero-plane displacement (z_d) and roughness length (z_0).

The aerodynamic roughness parameters (z_d and z_0) are central to this thesis which considers their determination in urban areas, the resulting inter- and intra-method variability, improvements in their representation and implications for wind-speed estimates. With the rapidly expanding and changing form of cities, the results can inform the understanding of current processes and vulnerabilities, as well as comprehend the implications of future change.

1.2 Objectives

The overarching objective of this PhD is to improve the understanding and representation of the aerodynamic properties of urban environments using the zero-plane displacement (z_d) and aerodynamic roughness length (z_0), for the purpose of improving wind-speed estimates when the flow is free from roughness-element wakes. Specific objectives are:

- (i) To assess current methods of determining urban z_d and z_0 and the associated wind-speed estimates using observations at a European city centre site;
- (ii) To develop a method to determine z_d and z_0 accounting for buildings and vegetation form, to improve wind-speed estimates;
- (iii) To assess geometric and aerodynamic roughness parameters derived from global digital elevation models.

1.3 Thesis outline

To address the objectives, the thesis is structured in the following manner (in addition to introductory and conclusion chapters):

- (1) A site-specific evaluation of nine methods to determine z_d and z_o is conducted in Chapter 3¹, with results showing inter- and intra-method variability. The implications for modelling the spatially- and temporally-averaged wind-speed profile aloft during idealised conditions (i.e. homogeneous upwind surfaces) is assessed through comparison to wind-speed observed with Doppler lidar.
- (2) The effects of different methods to estimate the wind-speed profile from surface observations are considered in Chapter 4². Insight to the most appropriate combination of methods to use for different conditions is provided.
- (3) The impact of vegetation upon urban roughness parameters is addressed in Chapter 5³ by developing a morphometric method accounting for both buildings and vegetation. Implications for roughness parameters and wind-speed estimates are demonstrated in different neighbourhoods across the city (ranging from a city centre to an urban park).
- (4) In Chapter 6⁴, observations from two vegetated urban sites are used for assessment of the model described in Chapter 5. The variability with phenology and the implications of omitting vegetation in wind-speed estimates are considered.
- (5) In Chapter 7⁵, global digital elevation models and benchmark datasets are used to explore: urban morphology, aerodynamic roughness parameters from morphometric methods and the accuracy of wind-speed estimates using these roughness parameters.

Chapters 3 – 6 have been published and Chapter 7 is under review:

¹ Chapter 3: **Kent CW**, Grimmond CSB, Barlow J, Gatey D, Kotthaus S, Lindberg F, Halios CH (2017a) *Evaluation of Urban Local-Scale Aerodynamic Parameters: Implications for the Vertical Profile of Wind Speed and for Source Areas*. *Boundary-Layer Meteorology* 164:183-213.

² Chapter 4: **Kent CW**, Grimmond CSB, Gatey D, Barlow JF (2018a) *Assessing methods to extrapolate the vertical wind-speed profile from surface observations in a city centre during strong winds*. *Journal of Wind Engineering and Industrial Aerodynamics* 173:100-111.

³ Chapter 5: **Kent CW**, Grimmond CSB, Gatey D (2017b) *Aerodynamic roughness parameters in cities: inclusion of vegetation*. *Journal of Wind Engineering and Industrial Aerodynamics*: 169:168-176.

⁴ Chapter 6: **Kent CW**, Lee K, Ward HC, Hong JW, Hong J, Gatey D, Grimmond CSB (2017c) *Aerodynamic roughness variation with vegetation: Analysis in a suburban neighbourhood and a city park*. *Urban Ecosystems*. DOI: 10.1007/s11252-017-0710-1.

⁵ Chapter 7: **Kent CW**, Grimmond CSB, Gatey D, Hirano K (2018b) *Urban morphology parameters from global digital elevation models: implications for aerodynamic roughness and for wind-speed estimation*. Submitted to *Remote Sensing of Environment*, 4 Jan 2018.

Chapter 2. Background

2.1 The urban boundary layer (UBL)

A boundary layer is a layer in fluid flow which is directly forced by a solid surface it is in contact with (Çengel and Cimbala 2014). Boundary layer flows may be laminar (layered) or turbulent flows. In both types of flow, surface friction creates a decreasing velocity gradient towards the surface, where the velocity becomes zero (no-slip boundary condition) (Day 1990). During laminar flow, the transfer of momentum and energy is only possible through molecular diffusion. In contrast, turbulent flows are characterised by fluctuating rotating regions called ‘eddies’ which provide an additional means for the transfer of momentum, mass, heat and other scalar properties throughout the boundary layer (Schlichting and Gersten 2000). The surface roughness and thermal properties can enhance or suppress turbulent mixing (Jiménez 2004).

The urban boundary layer (UBL) is an example of a fully developed turbulent flow over a rough wall (e.g. Raupach et al. 1991, Jiménez 2004). A good working definition of the UBL is the layer of the atmosphere above urban environments, which directly responds to surface forcing on timescales of approximately a day or less and length scales of the order of the boundary layer depth or less (Oke 1976, Garratt 1994, Roth 2000, Arnfield 2003, Fernando 2010, Barlow 2014, Oke et al. 2017). The UBL height is generally between 0.1 – 3 km, with the height (and structure) varying with space and time (e.g. diurnally, through direct surface forcing or from mesoscale conditions) (Oke et al. 2017). The UBL is traditionally divided into several distinct layers (Oke 1987, Roth 2000, Fernando 2010, Barlow 2014), allowing the flow properties in each layer to be related to the underlying surface geometry (Fig. 2.1).

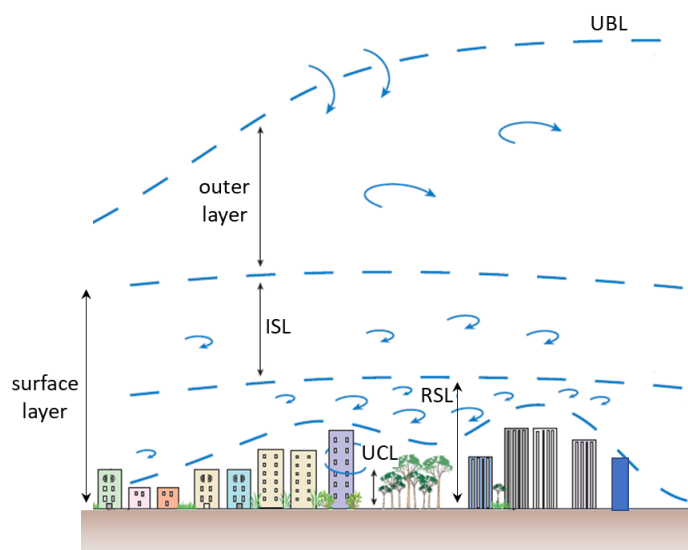


Figure 2.1: Idealised structure of the urban boundary layer (UBL), adapted from Fernando (2010). The outer layer is located above the surface layer, which is comprised of the sublayers: urban canopy layer (UCL), roughness sublayer (RSL) and inertial sublayer (ISL)

A description of the structure and expected flow in each layer is provided in Sect. 3.2.1. However, here it is important to note that the UBL structure presented in Fig. 2.1 is simplified and varies with the underlying surface, as well as mesoscale conditions (Barlow 2014). In addition, the location or even the presence of individual layers may be difficult to determine. For example, although the height of the urban canopy layer (UCL) is often accepted as the average roughness-element height, the height of the UCL and associated flow are ambiguous for roughness elements exerting height variability (Xie et al. 2008, Castro 2009), especially when the maximum heights may be several times larger than the average height. Likewise, the roughness sublayer (RSL) may encroach on the inertial sublayer (ISL), meaning an ISL may cease to exist (Cheng and Castro 2002, Cheng et al. 2007, Hagishima et al. 2009, Ho and Liu 2017). Indeed, some studies demonstrate that during particular conditions, such as when the ratio of the roughness-element height to boundary layer height is large enough, the effects of roughness elements extend throughout the boundary layer, rebutting the differentiation between and surface and outer layer (Jiménez 2004, Cheng et al. 2007, Hagishima et al. 2009, Castro 2009).

Until recently, numerical and physical experiments studying the mean and turbulent characteristics of airflow across urban-type roughness have focused upon idealised arrays. However, increasing computational resources are allowing for more complex, realistic geometries to be explored (e.g. Kastner-Klein and Rotach 2004, Kanda et al. 2013, Giometto et al. 2016, 2017). Additionally, field observations are becoming increasingly available (Barlow 2014) and remote sensing instrumentation means the impracticalities of *in-situ* observations in profile are being alleviated (e.g. Rotach et al. 2005, Barlow et al. 2011, Lane et al. 2013). In combination, the experimental and field data are consistently improving understanding of the UBL structure and associated flows, as will be demonstrated during this work.

2.2 Describing flow in the atmospheric boundary layer

2.2.1 Reynolds decomposition, stresses and the friction velocity

The flow properties of a turbulent fluid are characterised by time-dependent three-dimensional fluctuations. Through Reynolds decomposition, a property (e.g. velocity, temperature, pressure, etc.) can be stated as a summation between its mean and fluctuating part (Adrian et al. 2000). For example, in a three-dimensional Cartesian coordinate system, the instantaneous wind velocity components in the x , y and z directions, respectively, can be described by:

$$u = \bar{u} + u', v = \bar{v} + v', w = \bar{w} + w' \quad (2.1)$$

where u , v and w are the instantaneous velocity components, \bar{u} , \bar{v} , \bar{w} are the mean velocity components and u' , v' , w' are the instantaneous fluctuation from this mean (each of these has

units of m s^{-1}). The fluctuations obtained through Reynolds decomposition can be used to describe the turbulent transfer of an entity per unit time, or flux.

The entity of interest during this work is momentum. The vertical gradient of velocity in a boundary layer flow means that turbulent motion mixes air with different momentum, creating a turbulent momentum flux, or Reynolds stress. The vertical flux of horizontal momentum in the x and y directions (τ_{xz} and τ_{yz} , respectively, with units of $\text{kg m}^{-1} \text{s}^{-2}$) can be described by (Stull 2009):

$$\tau_{xz} = -\rho \overline{u'w'} \quad (2.2)$$

$$\tau_{yz} = -\rho \overline{v'w'} \quad (2.3)$$

where ρ is air density (kg m^{-3}). Note that because momentum is proportional to wind velocity, momentum increases with distance from the surface in the boundary layer, meaning that the flux is negative. The modulus of τ_{xz} and τ_{yz} provides the total vertical flux of horizontal momentum,

$$\tau = \rho \sqrt{\overline{u'w'^2} + \overline{v'w'^2}} \quad (2.4)$$

Eq. 2.4 can be stated in units of velocity to provide the relevant turbulent velocity scale for horizontal motion in the boundary layer, the friction velocity (u_* , units: m s^{-1}) (e.g. Garratt 1992):

$$u_* = \sqrt{\frac{\tau}{\rho}} = (\overline{u'w'^2} + \overline{v'w'^2})^{1/4} \quad (2.5)$$

If surface-wind coordinates are used and the frame of reference is orientated so that the x -axis is in the direction of the mean wind flow, $\overline{v} = \tau_{yz} = 0$ and

$$u_* = \sqrt{\frac{\tau_{xz}}{\rho}} \quad (2.6)$$

Note that for the turbulent boundary layer flow considered during this work, Reynolds stresses are several orders of magnitude larger than viscous stresses and the latter are therefore negligible (Stull 2009).

2.2.2 The vertical profile of wind speed in the neutral atmospheric boundary layer

Several assumptions simplify the process of deriving a spatially- and temporally-averaged wind-speed profile in the neutrally stratified atmospheric boundary layer (ABL):

- (i) a stationary atmosphere (that is, synoptic conditions are not changing with time, t) (i.e. $\partial(\overline{\quad})/\partial t = 0$, where ∂ is the partial derivative);

- (ii) a horizontally homogeneous boundary layer (i.e. $\partial(\bar{u})/\partial x = \partial(\bar{v})/\partial y = 0$), therefore the problem is relaxed to one dimension, z ;
- (iii) a barotropic atmosphere, where density is a function of pressure only and hence density can be assumed constant; and,
- (iv) there is uniform roughness with an extensive fetch and no subsidence, therefore there is no mean vertical velocity of the wind ($\bar{w} = 0$).

Based upon these assumptions, the logarithmic wind law can be derived through asymptotic similarity theory (Blackadar and Tennekes 1968, Tennekes 1973). Asymptotic similarity theory reveals a region where the non-dimensional velocity gradients determined from equations obeying the upper and lower boundary conditions of boundary layer flow are equal. The result demonstrates that in the matching region, if the flow is aligned to the mean wind direction, the mean wind speed at a height z (\bar{U}_z , units: m s^{-1}), can be described by the logarithmic law (Blackadar and Tennekes 1968, Tennekes 1973):

$$\bar{U}_z = \frac{u_*}{\kappa} \ln\left(\frac{z - z_d}{z_0}\right) \quad (2.7)$$

where the friction velocity (u_*) is the appropriate scaling velocity for both surface and outer boundary layer flow and κ is Von Karman's constant, a non-dimensional universal 'constant' determined from observations. The observed value of κ varies across experiments and in micrometeorology, a value of $\kappa = 0.4$ is generally adopted (Högström 1988, Garratt 1992, Foken 2006). Note, the upper case \bar{U} is now used to differentiate the mean wind-speed modulus (scalar) from the horizontal velocity component (\bar{u}) (vector). Detailed discussion of the aerodynamic roughness parameters, the zero-plane displacement (z_d [m]) and roughness length (z_0 [m]), is provided in Sect. 2.3. However, z_d is conceptually introduced into Eq. 2.7 as the vertical displacement of the wind-speed profile due to the presence of surface roughness elements, whilst z_0 is the height at which the wind speed would become zero in the absence of z_d (Fig. 2.2).

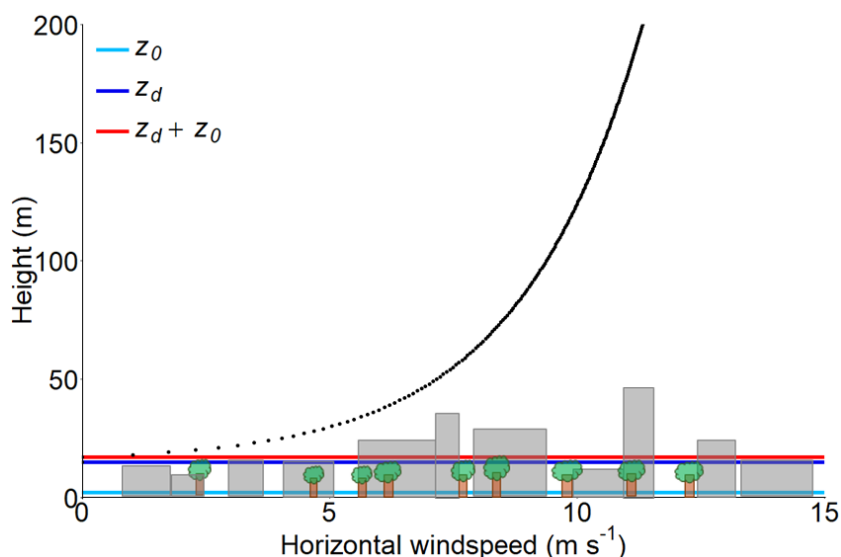


Figure 2.2: Logarithmic wind-speed profile (black dots) estimated above an urban surface showing the zero-plane displacement (z_d) and aerodynamic roughness length (z_0) (lines). Eq. 2.7 is used with: $z_d = 15$ m, $z_0 = 2$ m, $u_* = 1$ m s⁻¹ and $\kappa = 0.4$

Theoretically, the logarithmic profile is only valid in the ISL, where it is reasonable to assume constant stress with height (Blackadar and Tennekes 1968). Nevertheless, experiments indicate the logarithmic profile may provide reasonable wind-speed estimates closer to roughness elements (Cheng and Castro 2002) and at heights up to half of the boundary layer depth (Macdonald et al. 2000, Castro et al. 2006, Cheng et al. 2007). Several other models to describe the wind-speed profile exist for convenience or to extend the vertical range and/or atmospheric stability conditions over which wind-speed estimates can be made (Irwin 1979, Deaves and Harris 1978, Sedefian 1980, Wieringa 1986, Etling 2002, Wilson and Flesch 2004, Emeis et al. 2007, Gryning et al. 2007, Peña et al. 2010, Yang et al. 2016). Several are applied during this work, with the basis for selection and a more thorough description provided later (Chapter 4). However, a general principle is that as distance from the surface increases, additional length scales to z_d and z_0 become important, such as the gradient height (h), defined as the height where flow becomes free from surface friction (Deaves and Harris 1978).

The complex three-dimensional flow closer to roughness elements (within the RSL) is not of fundamental focus during this work but has been demonstrated in observations (Christen 2005, Rotach et al. 2005) and in detailed numerical and physical experiments (e.g. Kastner-Klein and Rotach 2004, Coceal et al. 2006, Giometto et al. 2016, 2017). The spatially- and temporally-averaged wind-speed profile in the RSL has been shown to be described by roughness sublayer corrections to Eq. 2.7 (e.g. Raupach 1992, Harman and Finnigan 2007, De Ridder 2010, Ho and Liu 2017). An exponential profile has been suggested within the urban canopy (e.g. Macdonald 2000, Yang et al. 2016), however this has been met with some contention (Coceal and Belcher 2004, Castro 2017).

2.2.3 Monin-Obukhov Similarity Theory

For over sixty years, Monin-Obukhov Similarity Theory (MOST) has provided a useful framework for interpreting observations in the surface layer, as well as predicting values where observations are unavailable (Monin and Obukhov 1954, Foken 2006). The principle of MOST is that for a non-rotating horizontally homogeneous surface layer flow with constant fluxes of heat and momentum (i.e. they are invariant with height), the structure of turbulence can be described by four variables:

- (i) the effective height above the surface ($z - z_d$ [m]),
- (ii) the surface kinematic heat flux ($\overline{w'T'} = Q_H/\rho c_p$) (where T is temperature [units: K], Q_H is the turbulent sensible heat flux [W m^{-2}] and c_p the specific heat capacity of air [$\text{J kg}^{-1} \text{K}^{-1}$]),
- (iii) surface drag (represented by u_*) and
- (iv) the buoyancy ratio (g/T) (where g is the acceleration due to gravity [m s^{-2}]).

As fluxes are assumed constant with height, the variables can in principle be measured anywhere in the surface layer and combined to produce the Obukhov length (L [m]) (Monin and Obukhov 1954):

$$L = -\frac{u_*^3}{\kappa \left(\frac{g}{T}\right) \left(\frac{Q_H}{\rho c_p}\right)} = \frac{T u_*^2}{\kappa g T_*} \quad (2.8)$$

where κ is introduced for convenience and $T_* = -\overline{(w'T')}/u_*$ is the temperature scale (or friction temperature), with units: K. Practically, L is a length scale characterising buoyancy in the surface layer and $|L|$ can be interpreted as the height below which atmospheric stratification is negligible (Monin and Yaglom 1973) and therefore mechanical turbulence dominates. The ratio between the effective height above the surface ($z' = z - z_d$) and L provides the non-dimensional 'Monin-Obukhov stability parameter' (Kaimal and Finnigan 1994):

$$\zeta = \frac{z - z_d}{L} \quad (2.9)$$

MOST states that the mean flow, or averaged turbulent transfer of a quantity, is a universal function of ζ only if normalised by an appropriate combination of the above scales. 'Universal' functions have been empirically determined from observations aloft surfaces that likely satisfy the assumptions of MOST (Businger et al. 1971, Dyer 1974, Panofsky et al. 1977, Panofsky and Dutton 1984, Högström 1988 and 1996, Kaimal and Finnigan 1994, Foken 2006). The original application and evaluation of MOST was for extensive flat homogeneous surfaces (e.g. Kansas Prairie, Businger et al. 1971; several Australian sites described in Garrat and Hicks 1990). In urban environments, the numerous sources and sinks of heat and momentum mean the assumptions of MOST become less suitable (Roth and Oke 1995). However, the theory has still been

demonstrated to apply particularly in the ISL, when the inherent assumptions may still be appropriate (e.g. Roth 2000, Al-Jiboori and Fei 2005, Foken 2006, Kanda et al. 2007, Vesala et al. 2008, Wood et al. 2010, Fortuniak et al. 2013, Nordbo et al. 2013, Y. Liu et al. 2017, Oke et al. 2017). The z_d was not included during the original derivation, but its larger magnitude in urban areas means it should be included here.

Two similarity relations derived from MOST are used during this work due to their potential to determine z_d from single level high frequency measurements (Rotach 1994, Toda and Sugita 2003). During unstable atmospheric stability, the normalised standard deviation of temperature (σ_T) and vertical wind velocity (σ_w) are related to the stability parameter by (e.g. Tillman 1972, Panofsky et al. 1977):

$$\frac{\sigma_T}{T_*} = -C_1 \left(C_2 - \frac{z - z_d}{L} \right)^{-\frac{1}{3}} \quad (2.10)$$

$$\frac{\sigma_w}{u_*} = C_3 \left(1 - C_4 \left[\frac{z - z_d}{L} \right] \right)^{\frac{1}{3}} \quad (2.11)$$

where C_1 to C_4 are constants derived from observations, which vary across surfaces and experiments (e.g. Sorbjan 1989, Hsieh et al. 1996, Roth 2000). The equations are revisited several times during this work where a more thorough description of their use is provided, as well as the consideration of the variability in constants C_1 to C_4 (Sect. 3.3.3 and 6.2.3).

MOST also provides a framework for wind-speed estimations during non-neutral atmospheric stability, through describing the non-dimensional wind-shear as:

$$\left(\frac{\kappa(z - z_d)}{u_*} \right) \left(\frac{d\bar{U}}{dz} \right) = \phi_m(\zeta) \quad (2.12)$$

where $\phi_m(\zeta)$ is a universal similarity function (Kaimal and Finnigan 1994, Foken 2006). Only neutral atmospheric stability is considered during this work ($\phi_m(\zeta) = 1$), allowing for ‘ideal’ conditions to be understood first, before introducing additional uncertainties associated with thermal effects (e.g. Högström 1996). However, the expected impact of atmospheric stability upon the wind-speed profile is summarised in Table 2.1.

Atmospheric stability	Expected values	Implications for wind-speed profile
Neutral	$Q_H \approx 0, L \rightarrow \infty, \zeta \rightarrow 0$	Dominated by mechanical turbulence (Reynolds stress)
Unstable	$Q_H > 0, L < 0, \zeta < 0$	Enhanced vertical mixing of momentum creates a smaller wind-speed gradient
Stable	$Q_H < 0, L > 0, \zeta > 0$	Suppressed vertical mixing of momentum creates steeper wind-speed gradient

Table 2.1: The expected effect of atmospheric stability upon the wind-speed profile. Q_H is the turbulent sensible heat flux, L is the Obukhov length (Eq. 2.8) and ζ is the Monin-Obukhov stability parameter (Eq. 2.9). (Monin-Obukhov (1954), their Fig. 1 has diagrammatic representation)

2.2.4 Source area modelling

One of the principal objectives of micrometeorology is to improve the understanding between surface-atmosphere exchanges. It is therefore important to consider the probable surrounding area contributing to observations. Source area footprint models are a tool frequently used for this purpose. Since the earliest turbulent flux source area model developments (e.g. Schuepp et al. 1990, Leclerc and Thurtell 1990), many have been proposed, ranging from one- to three-dimensional and based on different analytical, Lagrangian or large eddy simulation (LES) analysis (Leclerc and Foken 2014). Each model makes different assumptions about flow properties, based upon the principle that a measured flux is the integral of contributions from all upwind sources, with a ‘flux’ or ‘source area’ footprint describing the relative weight (or fractional contribution) given to each upwind element (Horst and Weil 1992). The turbulent flux measured at a height defined in Cartesian coordinate space, $F(0,0,z_m)$ (where z_m is measurement height), can be described by (e.g. Horst and Weil 1992, Kormann and Meixner 2001):

$$F(0,0,z_m) = \int_{-\infty}^{\infty} \int_0^{\infty} F(x,y,0)f(x,y,z_m)dx dy \quad (2.13)$$

with the x-axis in the direction of the mean wind flow. The flux-footprint, $f(x,y,z_m)$, is a weighting function describing the proportion of the flux ‘seen’ at $(0,0,z_m)$, caused by a unit point source at any surface location $(x,y,0)$. Examples of source areas modelled for a 30-min period of observations are shown in Fig. 2.3. A time series of such source areas may be aggregated to create a source area climatology, which allows characterisation of the probable upwind area influencing fluxes at a measurement site over time (e.g. Sect. 3.7).

During this work, the Kormann and Meixner (2001) analytical footprint model is used, as it is appropriate across a range of atmospheric stabilities and has been shown to have a comparatively low sensitivity to abrupt changes in surface roughness which are characteristic of urban areas (Heidbach et al. 2017). Additionally, the required model inputs can be determined from single-level high frequency observations (not requiring more sophisticated instrumentation). The Kormann and Meixner (2001) model assumes a horizontally homogenous flow and stationary conditions over the period of measurements, as well as extensive homogenous and isotropic terrain (at the height defined $z = 0$). The mathematical basis of the model includes a stationary gradient diffusion formulation, height independent cross-wind dispersion, power law profiles of mean wind velocity and eddy diffusivity and a power law solution of the two-dimensional advection-diffusion equation (Kormann and Meixner 2001). The final solution of the footprint function is calculated by fitting the power laws to Monin-Obukhov similarity profiles.

The source area varies as a function of: effective measurement height (i.e. accounting for z_d), meteorological conditions and the surface characteristics (e.g. roughness). Considering the influence of individual aspects, source area size increases with: a reduction in surface roughness, an increase in atmospheric stability and an increase in effective measurement height. Of particular interest for modelling the wind-speed profile is how the source area varies as a function of height, as this provides an indication of the upwind area of effective roughness which is 'felt' by wind speed at a given height (e.g. Fig. 4.1).

For example, if the measurement height on the modelled source area is increased by 10%, but all other conditions stay the same (cf. Fig. 2.3a and 2.3b), the increase in measurement height lengthens and broadens the source area, as more distant locations now contribute to measurements (causing a small increase in their relative contribution to the total source area, Figs. 2.3c and d). The distribution of source area weightings over a wider area causes a dampening in both the along-wind (Fig. 2.3c) and cross-wind (Fig. 2.3d) relative contributions, with the distance of maximum upwind relative contribution shifted only slightly (approximately 2%) further upwind.

In practice, such a change in the modelled source area is not expected to occur in isolation, as both meteorological conditions and the effective upwind surface roughness are also likely to vary with height. During this work, roughness parameters calculated from source areas at both single measurement heights and varying as a function of height are considered. A more detailed description of the methodology used to apply the source area is provided in Sect. 3.4.3.3. Various methods are used to estimate the wind-speed profile with these roughness parameters, with further description provided in Sect. 3.6 and Chapter 4.

The different physical or analytical basis of different source area models mean they have varying characterisation of the upwind surface area, with expected variability from observations (e.g. Leclerc et al. 2003, Göckede et al. 2005, Arriga et al. 2017, Heidbach et al. 2017). The models provide a probable location of the observation source area which is less arbitrary than assumptions of other upwind areas that are not varying with meteorological conditions or surface characteristics.

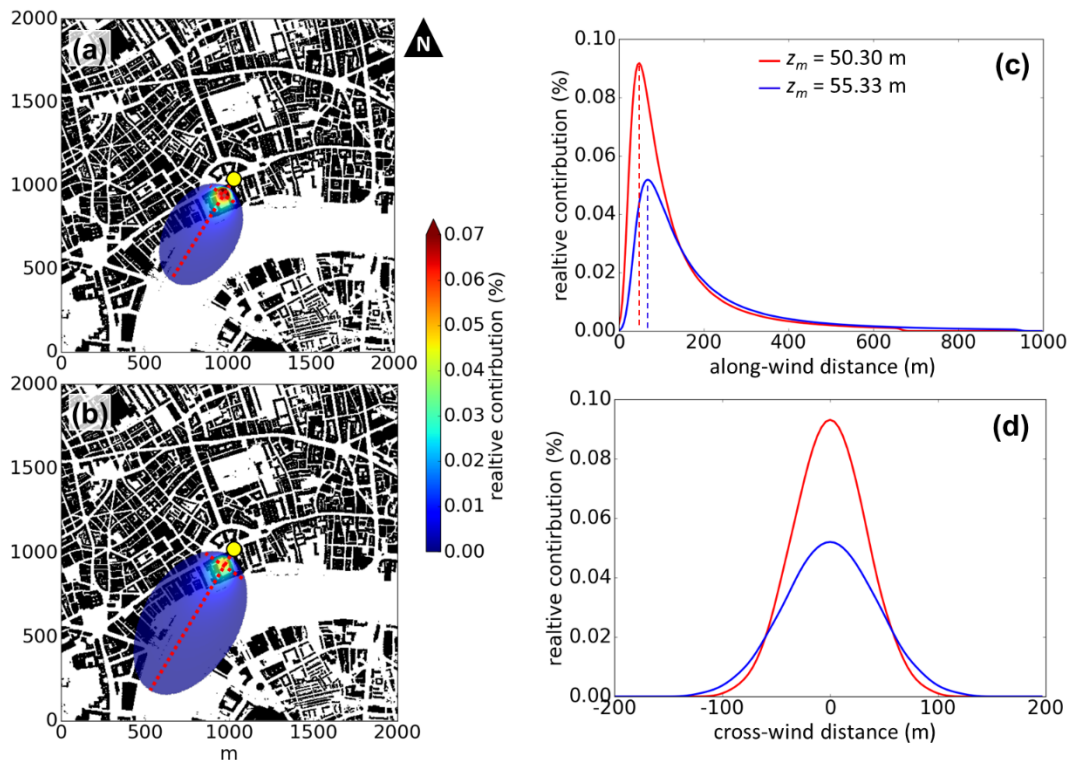


Figure 2.3: Source area for turbulent flux measurements at a central London site (yellow circle). The probable source area for the cumulative contribution to 80% of the total flux is calculated with the Kormann and Meixner (2001) model, using the median meteorological conditions of the fastest 25% of winds in 2014 (30-min averages), inputs are: standard deviation of the lateral wind velocity (σ_v) = 1.97 m s⁻¹; Obukhov length (L) = - 1513 m; friction velocity (u_*) = 0.94 m s⁻¹; wind direction 210°; zero-plane displacement (z_d) assumed = 30 m and aerodynamic roughness length (z_0) assumed = 2 m. The relative contribution of two-dimensional source area weightings are overlain upon building footprints > 2 m, assuming a measurement height (z_m) of: **(a)** 50.30 m and **(b)** 55.33 m (increase in z_m of 10%). For each source area, one-dimensional transects (red dashed lines in **(a)** and **(b)**) are shown for the: **(c)** along-wind wind direction (210°) and **(d)** cross-wind direction at the distance of maximum upwind relative contribution

2.3 Aerodynamic roughness parameters

2.3.1 The state of the art

The aerodynamic properties (or ‘roughness’) of a surface are important for characterizing the vertical fluxes of momentum and heat (as well as other scalars) close to the surface (Sect. 2.2). These aerodynamic properties can be parameterised using the aerodynamic roughness parameters, z_d and z_0 . The z_d and z_0 are critical attributes of the wind-speed profile (Sect. 2.2.2) and the focus of this work. In addition to improving wind-speed estimates, the understanding of these parameters is valuable for a range of applications, including numerical weather prediction (Varquez et al. 2015), modelling heat fluxes (W. Liu et al. 2007, Crawford et al. 2018), source area modelling (Leclerc and Foken 2014, Kljun et al. 2015, Arriga et al. 2017, Heidbach et al. 2017) and parameterisations based upon surface layer scaling (e.g. defining atmospheric stability, Eq. 2.9).

Cities are amongst the aerodynamically roughest surfaces encountered (Grimmond et al. 1998, Grimmond and Oke 1999, Wieringa et al. 2001). For a given urban site, three categories of

methods exist to determine z_d and z_o (Sect. 3.3): reference-based, anemometric and morphometric. Reference-based approaches require a comparison of a site to previously published pictures or look-up tables, anemometric methods use *in-situ* observations and morphometric methods are based upon roughness-element form. Each of these methods are applied in Chapter 3, where a more detailed explanation is provided. The limitations of using referenced-based approaches are discussed in Sect. 3.5.4 (with examples). However, it is important to note that look-up values are compiled from results of different experiments, where various methods have been applied to determine the roughness parameters (e.g. Wieringa 1993, Grimmond and Oke 1999, Wieringa et al. 2001). Therefore, the underlying data and methods used to compile a particular look-up table are important considerations when applying reference-based approaches.

Despite over half a century of research dedicated to understanding the roughness parameters for urban-type roughness, assigning appropriate values of z_d and z_o in cities remains challenging (e.g. Grimmond and Oke 1999). Nevertheless, our understanding of these rough surfaces is continuously being improved through an increasing number of field, scale and numerical studies across a range of surface types (e.g. varying roughness-element packing densities, shape, size and orientation). The impracticalities of spatially- and temporally-dense real-world measurements mean the controlled conditions achieved in physical and numerical studies provide the foundations of our current understanding of the roughness parameters over urban-like geometries. Consistent findings include:

- 1) For a group of uniform roughness elements:
 - a. The z_d increases with the packing density, until the surface becomes effectively 'closed' and z_d becomes the roughness-element height (Sect. 3.3.2.1)
 - b. The z_o increases with packing density until a peak, after which it decreases again. This can be related to the isolated, wake interference and skimming flow regimes (e.g. Grimmond and Oke 1999, Jiang et al. 2008) (Sect. 3.3.2.1).
- 2) Staggered roughness elements increase the drag and/or z_o compared to aligned arrays, with the magnitude of the increase depending upon the packing density (Hall et al. 1996, Macdonald et al. 1998, Kanda 2006, Cheng et al. 2007, Jiang et al. 2008, Cheng and Porté-Agel 2015, Yang et al. 2016, Sadique et al. 2017)
- 3) Variable orientation of roughness elements and flow direction may increase roughness parameters compared to aligned or staggered arrays (Kanda et al. 2007, Hagishima et al. 2009, Zaki et al. 2011, Claus et al. 2012, Yang and Meneveau 2016)

- 4) A consideration of roughness-element height variability appears critical, with a disproportionate influence of taller buildings increasing both z_d and z_0 compared to uniform height arrays (Cheng and Castro 2002, Kanda 2006, Jiang et al. 2008, Xie et al. 2008, Hagishima et al. 2009, Millward-Hopkins et al. 2011, Zaki et al. 2011, Kanda et al. 2013, Mohammad et al. 2015a, Yang et al. 2016)
- 5) For an array with height variability, z_d may peak at a critical packing density (Hagishima et al. 2009, Zaki et al. 2011)
- 6) Intricate details such as the presence of roofs can also influence drag and roughness parameters (Rafailidis 1997, Schultz et al. 2007, Ricci et al. 2017)

Such controlled studies have become increasingly complex over time and are undoubtedly useful during the interpretation of field observations. However, the investigated geometries still tend to be highly simplified and rarely resemble true urban environments. Therefore, a greater number of experiments of more realistic geometries or representative of real cities are required (e.g. Kastner-Klein and Rotach 2004, Feddersen 2005, Kanda et al. 2013, Giometto et al. 2016, 2017).

Furthermore, a consistent theme of the experiments is that only bluff bodies are considered (i.e. buildings). The majority of today's cities are comprised of both buildings and vegetation, and at city edges, or in urban parks, vegetation may become taller and more abundant than buildings (e.g. Fig. 2.4 and Sect. 5.3.1). Vegetation alters the aerodynamic (and indeed thermal) properties of a surface (Chapter 5) and should therefore be considered. This is the motivation for developing a morphometric method to consider both buildings and vegetation during this work.

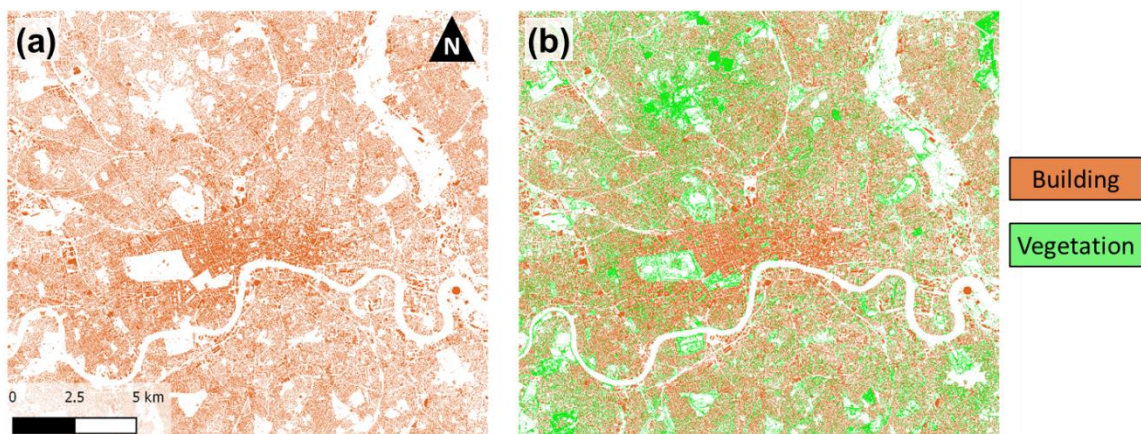


Figure 2.4: Plan area of (a) buildings > 2 m and (b) buildings and vegetation > 2 m in central London, UK. Elevation database source: Lindberg and Grimmond (2011a)

2.3.2 Morphometric methods – determining z_d and z_0 from surface geometry

Morphometric methods describe roughness parameters as a function of surface form using: theoretical arguments, experimental data, empirical values, or a combination of these. A range of methods have been developed (see Appendix 3.A), which have generally become more complex over time, incorporating both improvements in theoretical understanding and a greater number of geometric features. A selection of morphometric methods are used during this work, with the derivation of these methods described here (see Chapter 3 for selection criteria and method formula). In addition, the Macdonald et al. (1998) morphometric method is developed to include both buildings and vegetation (Chapter 5). The Macdonald et al. (1998) method is chosen as it is derived from fundamental principles and makes no assumptions about the flow effects around roughness elements, which as will be discussed vary between solid and porous elements.

Some of the earliest morphometric methods developed are empirical formulations based upon wind-speed profile measurements over arrays of roughness elements with controlled geometry (e.g. Kutzbach 1961, Lettau 1969, Counihan 1971). The limited range of geometries investigated during these experiments means their application in real urban areas is limited (see Grimmond and Oke 1999). In contrast, the improved physical and theoretical foundations of methods developed by Raupach (1992, 1994, 1995), Bottema (1995, 1997) and Macdonald et al. (1998) (from here on referred to as *Rau*, *Bot* and *Mac*, respectively) mean they may be more appropriate (Grimmond and Oke 1999). The *Rau*, *Bot* and *Mac* methods have the same physical basis, whereby the surface shear stress (i.e. drag force per unit area) is estimated and equated with the shear stress experienced in the ISL (e.g. Fig 2.5a). A formulation of the wind-speed profile is then substituted into the drag balance equation, allowing solving for z_0 . This process is demonstrated when developing the *Mac* method in Sect. 5.2.3. However, the morphometric methods make different assumptions about the form of the wind-speed profile, the mutual sheltering between roughness elements (and the variation of sheltering with density) and the calculation of z_d .

The z_d can be determined in various ways (based upon its interpretation), including: empirical fits to experimental data (e.g. *Mac*), considering roughness-element recirculation zones (e.g. *Bot*), minimising the error of fits to the logarithmic region of the wind-speed profile (e.g. Kanda et al. 2013) or calculating z_d as the centroid of the drag force profile (d_c) (e.g. *Rau*, Millward-Hopkins et al. 2011). The latter of these gives a physical definition to z_d and is based upon

Jackson's (1981) (following Thom 1971) demonstration that for rod type roughness z_d coincides with the height at which the mean drag on the surface appears to act. More recent experiments indicate z_d and d_c may differ for urban type roughness, which has been attributed to in-canopy circulation (Cheng and Castro 2002, Leonardi et al. 2003, Kanda et al. 2004, Cheng et al. 2007), but could also be due to a variable value of κ (Coceal et al. 2007, Leonardi and Castro 2010, Kanda et al. 2013, Zaki et al. 2014). However, use of either z_d or d_c has been shown to provide reasonable wind-speed estimates and no alternative physical description of z_d exists, rather than merely a fitting parameter (Leonardi and Castro 2010, Kanda et al. 2013, Zaki et al. 2014, Yang et al. 2016).

The *Rau* method is originally developed for vegetated canopies and uses dimensional analysis and drag partitioning theory for cylinder type roughness. The effective sheltering area and sheltering volume of roughness elements are estimated, producing a formulation for the bulk drag coefficient of the surface, with z_d calculated as the drag force profile centroid (i.e. d_c). The logarithmic wind law is used, with a roughness sublayer influence function accounting for the departure from the logarithmic profile closer to roughness elements (Sect. 2.2.2). Empirical constants in the method (Eqs. 3.4 – 3.6) are informed through comparison to data from wind tunnel experiments and vegetation canopies (Raupach 1992).

The *Bot* method uses the logarithmic wind law, but introduces an in-plane displacement height, which acts as a mutual sheltering parameter. The in-plane displacement height is calculated considering the volume of roughness elements and their associated frontal and leeward recirculation zones, as well as the ground area occupied by the roughness elements. The recirculation volume of roughness elements is approximated using the numerical and experimental results of Bottema (1993).

The *Mac* method also uses the logarithmic wind law with z_d as a mutual sheltering parameter. However, equations for the roughness parameters across a range of densities are developed by fitting to the wind-tunnel data of Hall et al. (1996), which produces empirical constants for square and staggered arrays (Eqs. 3.9, 3.10).

The *Rau*, *Bot* and *Mac* methods represent roughness elements by their average height and therefore do not directly consider the height variability in an array of roughness elements (see Sect. 3.3.2.2 for method formula). However, the height variability of roughness elements has been demonstrated to modify flow characteristics, impacting the magnitude of z_d and z_0 , as well as their variation with density (Sect. 2.3.1). As taller roughness elements protrude above shorter

ones, they reach heights with greater wind speeds creating the potential to exert a larger drag force (due to the proportionality between drag force and the wind-speed squared, Sect. 5.2.3). In addition, these taller roughness elements provide increased downwind sheltering compared to an array with uniform height and the tops of the taller roughness elements are less impacted by the sheltering (cf. Fig. 2.5a and b). In combination, this means taller roughness elements exert a disproportionate amount of drag upon the flow and become more influential on flow characteristics (Xie et al. 2008, Mohammad et al. 2015a). The impact varies as a function of the array geometry (e.g. roughness-element: density, height distribution, orientation, etc.) (Cheng and Castro 2002, Kanda et al. 2006, Jiang et al. 2008, Xie et al. 2008, Hagishima et al. 2009, Zaki et al. 2011, Mohammad et al. 2015a, Yang et al. 2016) and morphometric methods which directly consider roughness-element height variability (e.g. Millward-Hopkins et al. 2011 and Kanda et al. 2013) attempt to capture these effects.

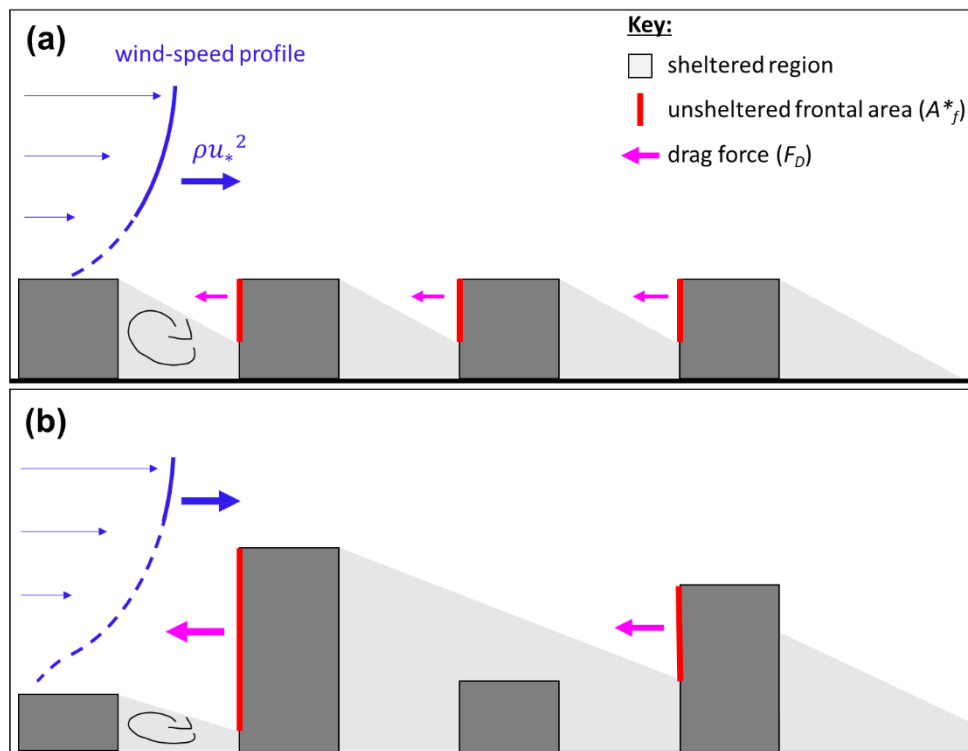


Figure 2.5: Lateral cross section of flow approaching idealised arrays of roughness elements with heights that are **(a)** homogeneous and **(b)** heterogeneous. The mutual sheltering of roughness elements is exemplified, in addition to the unsheltered frontal areas of roughness elements, which exert a drag force (F_D) upon the flow and contribute to the shear stress (ρu_*^2 , Eqs. 2.5 and 2.6) in the inertial sublayer (figure not to scale)

The Millward-Hopkins et al. (2011) method is based upon similar principles to the *Bot* and *Mac* methods, but a mutual sheltering model is developed to calculate the unsheltered frontal area of roughness elements. The logarithmic wind law is used, transitioning to an exponential profile below an inflection height. The z_d is estimated as the height of the drag force profile centroid (i.e. d_c), with the viscous drag of roughness-element rooftops and the ground considered for $\lambda_p \leq 0.19$. The canopy is divided into distinct layers and a cumulative height-normalised z_d and drag balance are calculated.

The Kanda et al. (2013) method is based upon results from large-eddy simulations using the parallelized large eddy simulation model (PALM). The LES is conducted for 107 real urban areas in Japan (with a 2 m resolution and grid dimensions of 1000 m (x) by 1000 m (y) by 600 m (z)) and 23 'simple' arrays from the literature with height variability (Cheng et al. 2007, Hagishima et al. 2009, Leonardi and Castro 2010, Zaki et al. 2011). The z_d and z_0 are determined using two parameter regression for wind-speed profiles between $H_{max} + 0.2H_{av}$ and $H_{max} + H_{av}$, a region where the profiles are demonstrated to be logarithmic.

This section has demonstrated there are various ways morphometric methods have been developed. The assumptions involved should be considered when applying the methods and interpreting the results in real urban areas. The equations for the discussed morphometric methods are included in Chapter 3, where the methods are applied in a European city Centre (London, UK).

Chapter 3. Evaluation of urban local-scale aerodynamic parameters: implications for the vertical profile of wind speed and for source areas¹

Abstract Nine methods to determine local-scale aerodynamic roughness length (z_0) and zero-plane displacement (z_d) are compared at three sites (within 60 m of each other) in London, UK. Methods include three anemometric (single-level high frequency observations), six morphometric (surface geometry) and one reference-based approach (look-up tables). A footprint model is used with the morphometric methods in an iterative procedure. The results are insensitive to the initial z_d and z_0 estimates. Across the three sites, z_d varies between 5 and 45 m depending upon the method used. Morphometric methods that incorporate roughness-element height variability agree better with anemometric methods, indicating z_d is consistently greater than the local mean building height. Depending upon method and wind direction, z_0 varies between 0.1 and 5 m, with morphometric z_0 consistently being 2 to 3 m larger than the anemometric z_0 . No morphometric method consistently resembles the anemometric methods for z_0 . Wind-speed profiles observed with Doppler lidar provide additional data with which to assess the methods. Locally determined roughness parameters are used to extrapolate wind-speed profiles to a height roughly 200 m above the canopy. Wind-speed profiles extrapolated based on morphometric methods that account for roughness-element height variability are most similar to observations. The extent of the modelled source area for measurements varies by up to a factor of three, depending upon the morphometric method used to determine z_d and z_0 .

3.1 Introduction

The urban environment is arguably the most critical interface between humans and the atmosphere. Considerable progress has been made in understanding and modelling the urban environment across a broad spectrum of topics (e.g. Roth 2000, Arnfield 2003, Stewart 2011, Tominaga and Stathopoulos 2013). Wind speed is critical to the vertical and horizontal exchange of scalars and pollutants, and is important when considering, for example, the construction and insurance of buildings (Walker et al. 2016), pedestrian comfort (Stathopoulos 2006) and renewable energy (Drew et al. 2013a). The world's urban population is expected to increase to

¹This chapter is published as: **Kent CW**, Grimmond CSB, Barlow J, Gatey D, Kotthaus S, Lindberg F, Halios CH (2017a) *Evaluation of Urban Local-Scale Aerodynamic Parameters: Implications for the Vertical Profile of Wind Speed and for Source Areas*. *Boundary-Layer Meteorology* 164:183-213.

66% by 2050 (UN 2014), and as cities grow outwards and more importantly upwards, larger populations become more exposed to urban wind regimes. Therefore, improved knowledge of urban flow effects is vital to inform the development of cities.

The prospect of an equilibrium boundary layer wind-speed profile, represented using just a few parameters, is appealing, especially above a rough urban surface with complex flow across numerous length and time scales (Britter and Hanna 2003). Several relationships to describe the spatially- and temporally- averaged vertical wind-speed profile above a surface exist, such as the power-law (Sedefian 1980), the logarithmic wind-speed profile (Tennekes 1973) and profiles described by Deaves and Harris (1978), Emeis et al. (2007), Gryning et al. (2007) and Peña et al. (2010). A precursor to the use of each method is representation of the zero-plane displacement (z_d) and the aerodynamic roughness length (z_0).

Although the magnitude of both z_d and z_0 is fundamentally related to surface morphology, assigning appropriate values remains challenging. This is particularly true in city centres, with pronounced variability in roughness-element heights and density, creating unique, complex surface morphology. Individual tall buildings often rise above mid-rise buildings, whilst in the suburbs more homogeneous roughness-element height and density are common.

The numerous methods used to determine z_d and z_0 can be grouped into three classes: (i) reference-based, (ii) anemometric and (iii) morphometric. The reference-based method is the simplest, as a neighbourhood is compared to published tables or figures (e.g. Grimmond and Oke 1999, Wieringa et al. 2001, Stewart and Oke 2012) to determine appropriate values. Anemometric and morphometric methods both directly incorporate the unique surface morphology of an area and can account for variations in meteorological conditions (e.g. wind direction, wind speed or stability).

In the present study, high-quality databases are used to compare methods to determine z_d and z_0 in urban areas. For the study area (central London, UK) the methods employed are: reference-based using aerial photography, anemometric using single- and multi- level observations and morphometric using digital elevation databases. Previous studies related to aerodynamic parameters relevant to London (Ratti et al. 2002, 2006, Padhra 2010, Drew et al. 2013a, 2013b, Kotthaus and Grimmond 2014b) have results that vary with the study area, method and gridded datasets (e.g. Evans 2009) used. Overall, the maximum z_d and z_0 from these studies are 20 m and 2 m, respectively. The objectives are a site-specific evaluation of: (i) the inter-method

variability in aerodynamic parameters, and (ii) the implications for modelling the spatially- and temporally- averaged wind-speed profile.

The methodology to determine z_d and z_0 through surface morphology is provided for use in the Urban Multi-scale Environmental Predictor (UMEP, <http://www.urban-climate.net/umep/> UMEP, Lindberg et al. 2018) for the open source geographical information software QGIS.

3.2 Background

3.2.1 The urban boundary layer and logarithmic wind law

The urban boundary layer is traditionally sub-divided into distinct layers (Fernando 2010), which are determined by urban surface characteristics and mesoscale conditions (Barlow 2014). Surface roughness elements are located within the urban canopy layer (UCL) (Roth 2000, Oke 2007), which experiences highly variable flow as a consequence of the close proximity to roughness elements. The UCL is within the roughness sublayer (RSL) (Roth 2000), of depth H_{RSL} . The depth H_{RSL} is typically 2–5 times the average roughness-element height (H_{av}) (Roth 2000, Barlow 2014), but can be considerably larger (e.g. Roth 2000, their Table 2), varying with the density (Raupach et al. 1991, Grimmond and Oke 1999, Roth 2000, Oke 2007, Barlow 2014), staggering (Cheng and Castro 2002) and height variability (Cheng and Castro 2002) of roughness elements, as well as meteorological conditions (Roth 2000). Idealised physical models (Cheng and Castro 2002, Kastner-Klein and Rotach 2004, Xie et al. 2008), large-eddy simulations (LES) (Giometto et al. 2016) and observations in a dense urban setting (Grimmond et al. 2004) suggest the minimum $H_{RSL} = 2H_{av}$.

Between a height $z = H_{RSL}$ and approximately 10% of the boundary layer depth is the inertial sublayer (ISL), though when there is considerable roughness-element height variability the RSL encroaches upon the ISL (Cheng and Castro 2002, Cheng et al. 2007, Mohammad et al. 2015a) and an ISL may cease to exist (Rotach 1999). Within the ISL, the flow becomes free of the individual wakes and channelling associated with roughness elements, and the small variation of turbulent fluxes of heat and momentum with height leads to the assumption of a constant-flux layer. In addition, if the airflow is fully adapted to upwind roughness elements (i.e. disregarding an internal boundary layer) a horizontally homogeneous flow is observed (Barlow 2014) and it is therefore possible to determine a spatially- and temporally- averaged vertical wind-speed profile.

The logarithmic wind law applies in the ISL and during thermally neutral conditions can be used to estimate wind speeds to a height of approximately 200 m (Cook 1997) using surface-based length scales (i.e. z_d and z_0) (Blackadar and Tennekes 1968, Tennekes 1973):

$$\bar{U}_z = \frac{u_*}{\kappa} \ln\left(\frac{z - z_d}{z_0}\right) \quad (3.1)$$

where \bar{U}_z is the mean horizontal wind speed at height z , u_* is the friction velocity, and $\kappa = 0.40$ is the von Karman constant (Högström 1996).

3.3 Determination of aerodynamic parameters in urban areas

3.3.1 Reference-based methods

Reference-based approaches require comparison between site photography and first-order height and/or density estimates to reference tables (e.g. Grimmond and Oke 1999, Wieringa et al. 2001). Wieringa's (1993) comprehensive review of roughness length data provides tables for homogenous surfaces, whilst Grimmond and Oke (1999) focus upon urban areas, therefore the latter is used here.

3.3.2 Morphometric methods

3.3.2.1 Relations between aerodynamic parameters and roughness-element form

Morphometrically-determined aerodynamic parameters in urban areas traditionally consider three flow regimes – isolated, wake interference and skimming (Oke 1987). These are related to the plan area index (ratio of plan built area occupied by roughness elements (A_p) to total area under consideration (A_T): $\lambda_p = A_p/A_T$) and frontal area index (ratio of the windward facing area of roughness elements (A_f) to A_T : $\lambda_f = A_f/A_T$). As surface cover (A_p) increases the magnitude of z_d scaled by H_{av} is traditionally observed to produce a convex curve asymptotically increasing from zero to 1 (Fig. 3.1a). In contrast, the relation between λ_f and z_0/H_{av} has a peak at λ_f between 0.1 and 0.4 depending on the method used to determine z_0 (Fig. 3.1b). The maximum possible λ_p is unity, however λ_f can exceed this.

Staggered and non-uniformly oriented groups of roughness elements generate a larger drag force than regular arrays, causing a more pronounced peak in z_0 , as well as larger magnitudes of z_d (Macdonald et al. 2000, Cheng et al. 2007, Hagishima et al. 2009, Zaki et al. 2011, Claus et al. 2012). Roughness-element height variability also influences flow and turbulent characteristics, as the taller roughness elements generate a disproportionate amount of drag (Xie et al. 2008, Mohammad et al. 2015a). This suggests z_d can be greater than the average roughness-element height (e.g. Jiang et al. 2008, Xie et al. 2008, Hagishima et al. 2009, Zaki et

al. 2011, Millward-Hopkins et al. 2011, Tanaka et al. 2011, Kanda et al. 2013), with a peak z_0 up to five times greater and displaced to higher λ_f (Hagishima et al. 2009, Zaki et al. 2011). Roughness-element staggering, orientation and most importantly height heterogeneity therefore need to be considered in morphometric calculations; especially in complex city centres, such as the current study site (Sect. 3.4.1).

3.3.2.2 Morphometric method application in urban areas

Numerous morphometric methods exist (Appendix 3.A) and each method has its own assumptions and intended range of applicability. Newer methods have incorporated increasingly complex geometric features or theoretical ideas pertaining to the relation between aerodynamic parameters and surface morphology.

Here, six morphometric methods (Table 3.1) are selected for assessment that meet the following criteria: (i) both z_d and z_0 are included in the formulations; (ii) the method is applicable to a wide range of urban densities and environments; (iii) geometric data required are readily obtainable in complex urban environments; (iv) given resources available, the method is computationally feasible. Hereafter, the methods assessed are referred to by their abbreviation in Table 3.1. When followed by subscript z_d or z_0 the abbreviation refers to the zero-plane displacement or aerodynamic roughness length, respectively. The geometric parameters required by each method are shown in Table 3.1.

The simplest, ‘rule of thumb’ method (RT), only requires the average roughness-element height (H_{av}) which is linearly related to RT_{z_d} and RT_{z_0} ,

$$RT_{z_d} = f_d H_{av} \quad (3.2)$$

$$RT_{z_0} = f_0 H_{av} \quad (3.3)$$

where the initial value used for f_d is 0.7 and f_0 is 0.1 (Grimmond and Oke 1999). However, the value of f_d is revisited in Sect. 3.5.1.2.

Originally derived for vegetated surfaces, The Raupach (1994) method (Rau), provides reasonable results in urban environments (e.g. Bottema and Mestayer 1998, Grimmond and Oke 1999):

$$Rau_{z_d} = \left(1 + \frac{\exp[-(C_{dl} 2\lambda_f)^{0.5}] - 1}{(C_{dl} 2\lambda_f)^{0.5}} \right) H_{av} \quad (3.4)$$

$$Rau_{z_0} = \left[\left(1 - \frac{z_d}{H_{av}} \right) \exp\left(-\kappa \frac{U_z}{u_*} + \Psi_h\right) \right] H_{av} \quad (3.5)$$

with

$$\frac{u_*}{U_z} = \min \left[(C_S + C_{Dv} \lambda_f)^{0.5}, \left(\frac{u_*}{U_z} \right)_{\max} \right] \quad (3.6)$$

Here U_z is the wind speed at roof height and empirical constants include: C_{Dv} (the drag coefficient for vegetation = 0.3), C_S (the drag coefficient for the substrate surface in the absence of roughness elements = 0.003), ψ_h (the roughness-sublayer influence function – accounting for the correction to the logarithmic wind profile in the RSL = 0.193), C_{dl} (a free parameter = 7.5) and $(u_*/U_z)_{\max} = 0.3$. These constants suggested by Raupach (1994) are used here, but they do vary depending on roughness elements (Bottema and Mestayer 1998).

The Bottema and Mestayer (1998) method (*Bot*) is a simplified version of more complex formulations (Bottema 1995, 1997) specifically designed for urban areas. In the *Bot* method, a mutual sheltering parameter is used and it is assumed the surface shear stress (τ , Sect. 2.2.1) is dominated by the drag on roughness elements (therefore: $\tau = 0.5 C_{Db} \rho U_z^2 \lambda_f$, where τ is analogous to the drag force per unit ground area, ρ is the density of air and $C_{Db} = 0.8$ is the drag coefficient for buildings):

$$Bot_{z_d} = \lambda_p^{0.6} H_{av} \quad (3.7)$$

$$Bot_{z_0} = (z - z_d) \exp \left(- \frac{\kappa}{\sqrt{0.5 \lambda_f C_{Db}}} \right) \quad (3.8)$$

The Macdonald et al. (1998) method (*Mac*) includes a fitting constant, α_M , controlling the increase of z_d/H_{av} with λ_p and a drag correction coefficient, β_M , to determine z_0 :

$$Mac_{z_d} = [1 + \alpha_M^{-\lambda_p} (\lambda_p - 1)] H_{av} \quad (3.9)$$

$$Mac_{z_0} = \left(\left(1 - \frac{z_d}{H_{av}} \right) \exp \left[- \left\{ 0.5 \beta_M \frac{C_{Db}}{\kappa^2} \left(1 - \frac{z_d}{H_{av}} \right) \lambda_f \right\}^{-0.5} \right] \right) H_{av} \quad (3.10)$$

Morphometric Methods					
Abbreviation	H_{av} (m)	λ_p	λ_f	H_{max} (m)	σ_H (m)
<i>RT</i>	✓				
<i>Rau</i>	✓		✓		
<i>Bot</i>	✓	✓	✓		
<i>Mac</i>	✓	✓	✓		
<i>Mho</i>	✓	✓	✓		✓
<i>Kan</i>	✓	✓	✓	✓	✓

Table 3.1: Morphometric methods assessed (rows) with their required geometric parameters (columns). Morphometric method abbreviations: *RT* – Rule of thumb (Grimmond and Oke 1999), *Rau* – Raupach (1994), *Bot* – Bottema and Mestayer (1998), *Mac* – Macdonald et al. (1998), *Mho* – Millward-Hopkins et al. (2011), *Kan* – Kanda et al. (2013). Geometric parameters: H_{av} – average roughness-element height, λ_p – plan area index, λ_f – frontal area index, H_{max} – maximum roughness-element height, σ_H – standard deviation of roughness-element heights

Macdonald et al. (1998) suggest $C_{Db} = 1.2$ and from wind-tunnel data (Hall et al. 1996) values of $\alpha_M = 4.43$, $\beta_M = 1.0$ for staggered arrays, and $\alpha_M = 3.59$, $\beta_M = 0.55$ for square arrays (Macdonald et al. 1998). The suitability of these experimental data as a fit to the constants has been questioned because of the short fetch used and lack of direct shear-stress measurement (Cheng et al. 2007). Ratti et al. (2002) propose a correction to the *Mac* method to account for roughness-element height variability ($z_0 = Mac_{z_0} [1+4(\sigma_H/H_{av})]$, where σ_H is the standard deviation of roughness-element heights). However, the correction is not considered here as no basis is provided and z_d is not addressed. Kastner-Klein and Rotach's (2004) empirically derived relationship using wind-tunnel results from a scaled physical model of Nantes, France, is also not considered because it does not incorporate λ_f , a parameter that is regarded as important (Millward-Hopkins et al. 2011, Mohammad et al. 2015b).

Two morphometric methods that directly incorporate roughness-element height variability are explored: the *Mho* (Millward-Hopkins et al. 2011) and *Kan* (Kanda et al. 2013) methods. Both are yet to be independently evaluated. The *Mho* method describes the viscous drag associated with the unsheltered frontal area of roughness elements (A_f^*) and their rooftops when density is below a critical threshold. The urban canopy is divided into layers and a cumulative height-normalised z_d and drag balance is calculated. This process is computationally intensive and complex to operate (Tomlin 2015 pers. comm.), therefore a relation based on the more accessible standard deviation of roughness-element heights has been developed (Millward-Hopkins et al. 2011, 2013a),

$$Mho_{z_d} = H_{av} \left[\frac{MhoU_{z_d}}{H_{av}} + \left((0.2375 \ln(\lambda_p) + 1.1738) \frac{\sigma_H}{H_{av}} \right) \right] \quad (3.11)$$

$$Mho_{z_0} = H_{av} \left[\frac{MhoU_{z_0}}{H_{av}} + (\exp(0.8867\lambda_f) - 1) \left(\frac{\sigma_H}{H_{av}} \right)^{\exp(2.3271\lambda_f)} \right] \quad (3.12)$$

where

$$MhoU_{z_0} = \left(\left(1 - \frac{z_d}{H_{av}} \right) \exp \left[- \left\{ 0.5c_{Db} \kappa^{-2} \frac{A_f^*}{A_T} \right\}^{-0.5} \right] \right) H_{av} \quad (3.13)$$

$$\frac{MhoU_{z_d}}{H_{av}} = \left(\frac{19.2\lambda_p - 1 + \exp(-19.2\lambda_p)}{19.2\lambda_p [1 - \exp(-19.2\lambda_p)]} \right) \quad (for \lambda_p \geq 0.19) \quad (3.14)$$

$$\frac{MhoU_{z_d}}{H_{av}} = \left(\frac{117\lambda_p + (187.2\lambda_p^3 - 6.1)[1 - \exp(-19.2\lambda_p)]}{(1 + 114\lambda_p + 187\lambda_p^3)[1 - \exp(-19.2\lambda_p)]} \right) \quad (for \lambda_p < 0.19) \quad (3.15)$$

The *Kan* method uses large-eddy simulations for real urban areas in Japan (107 grid squares of size 1000 m (x) by 1000 m (y) by 600 m (z) with a 2 m resolution) and 23 simple arrays from the literature (Cheng et al. 2007, Hagishima et al. 2009, Leonardi and Castro 2010, Zaki et al. 2011).

Horizontally averaged turbulent statistics, surface drag and wind-speed profiles were derived for each model grid and aerodynamic parameters determined through a least squares regression. Kanda et al. (2013) argue that the upper limit of z_d is the maximum roughness-element height (H_{max}), hence H_{max} is a more suitable scaling parameter than H_{av} ,

$$Kan_{z_d} = [c_o X^2 + (a_o \lambda_p^{b_o} - c_o) X] H_{max} \quad (3.16)$$

where a_o , b_o and c_o are taken as 1.29, 0.36 and -0.17 . X is the representative building height above the average building height ($\sigma_H + H_{av}$), relative to the maximum building height:

$$X = \frac{\sigma_H + H_{av}}{H_{max}} \quad (3.17)$$

for $0 \leq X \leq 1$. For z_0 , the Kan method is a modification to Mac_{z_0} ,

$$Kan_{z_0} = (b_1 Y^2 + c_1 Y + a_1) Mac_{z_0} \quad (3.18)$$

where a_1 , b_1 and c_1 are empirically derived coefficients (0.71, 20.21 and -0.77); and Y accounts for the impact of λ_p and σ_H on z_0 , tending to zero for homogeneous arrays (i.e. where $\sigma_H = 0$):

$$Y = \frac{\lambda_p \sigma_H}{H_{av}} \quad (3.19)$$

$0 \leq Y$.

The six morphometric methods are applied across a range of roughness-element densities with homogeneous (Fig. 3.1a, b) and heterogeneous (Fig. 3.1c, d) height. Their comparison demonstrates that aerodynamic parameters determined using the RT , Rau , Bot and Mac methods are independent of the height array used. Hereafter, these methods are collectively referred to as RE_{av} (i.e. based upon average roughness-element height). In contrast, obvious differences occur for aerodynamic parameters determined using the Mho and Kan methods because of their direct consideration of height heterogeneity. Hereafter, the Mho and Kan methods are collectively referred to as RE_{var} (i.e. they account for variable roughness-element heights).

Across the six methods, z_d increases with H_{av} and λ_p (λ_f for Rau_{z_d}). The Mho and Kan methods both resolve the more considerable drag which is exerted by groups of roughness elements with height heterogeneity, therefore Mho_{z_d} also increases with σ_H and Kan_{z_d} increases with both σ_H and H_{max} . Results for Bot_{z_d} and Mac_{z_d} vary similarly with density (λ_p). The difference between Mac_{z_d} for square or staggered arrays is negligible compared to inter-method variability (Fig. 3.1a, c). For the homogeneous array (Fig. 3.1a, b) both Kan_{z_d} and Mho_{z_d} (Mho_{z_d} at $\lambda_p < 0.8$) are larger than for the other morphometric methods. Kan_{z_d} becomes larger than H_{av} and Mho_{z_d} levels off, meaning both do not fulfil the requirement that $z_d/H_{av} = 1$ when $\lambda_p = 1$. Therefore, when $\lambda_p >$

0.50 the *Kan* and *Mho* methods may over- and under-estimate z_d of homogeneous arrays, respectively. As the methods were derived from datasets with $0.05 < \lambda_p < 0.50$ this is beyond their limits, and is uncommon for real cities (e.g. Fig. 3.1).

When roughness-element height heterogeneity is introduced (Fig. 3.1c, d), the *RE_{av}* method results are identical to the homogeneous case because H_{av} is the only height attribute used. In contrast, Kan_{z_d} and Mho_{z_d} increase by a factor of approximately two and are therefore consistently twice the values for the *RE_{av}* methods. The increase of Kan_{z_d} and Mho_{z_d} suggests z_d is larger than H_{av} for most plan area densities. This is especially true for Kan_{z_d} , which scales with H_{max} (assumed 117 m) and increases with density to become over twice H_{av} .

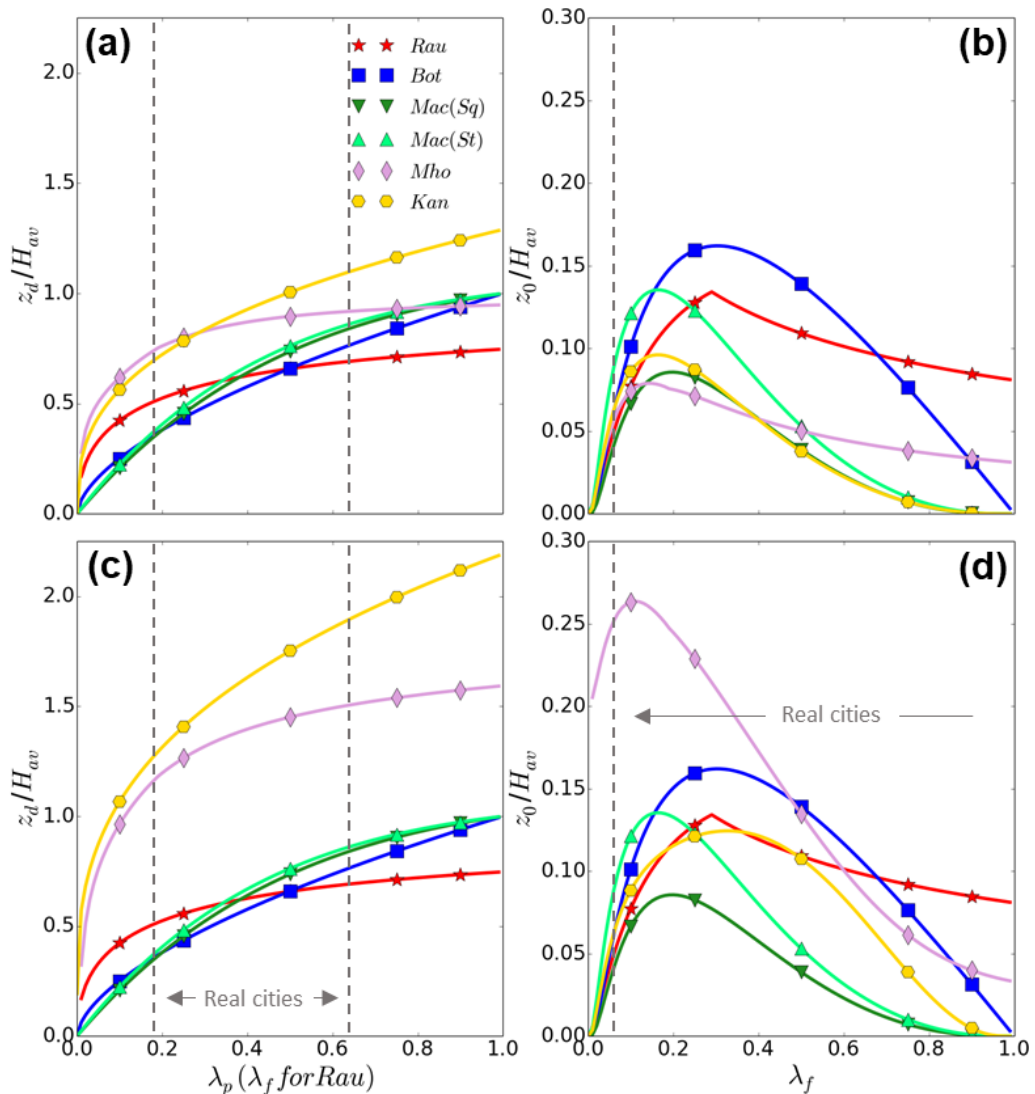


Figure 3.1: Zero-plane displacement (z_d) and aerodynamic roughness length (z_0) normalised by average roughness-element height (H_{av}) for the morphometric methods assessed (Table 3.1), assuming roughness elements with: **(a, b)** homogeneous and **(c, d)** heterogeneous heights. Geometric parameters used are informed by the built surroundings within 1000 m of the KSSW site (Table 3.3): **(a, b)**: $H_{av} = 20$ m, maximum height (H_{max}) = 20 m and standard deviation of heights (σ_H) = 0 m; **(c, d)**: $H_{av} = 20$ m, $H_{max} = 117$ m, $\sigma_H = 11$ m. In both cases, frontal area index (λ_f) and plan area index (λ_p) are varied from 0 to 1, note λ_f can become larger than 1. The *Mac* method is shown for square (*Sq*) and staggered (*St*) arrays. Real cities limits are based on Grimmond and Oke (1999). Curves shown may extend beyond the extent to which the model was originally developed

For each method, z_0 increases to a maximum ‘critical’ frontal area index (λ_{f-crit}). When roughness elements have homogeneous heights (Fig. 3.1b), λ_{f-crit} varies from a minimum of 0.11 (Mho_{z_0}) to maximum of 0.3 (Bot_{z_0}). The peak magnitude is similar for Mac_{z_0} for square arrays, Mho_{z_0} and Kan_{z_0} ($0.1H_{av}$), which is smaller than Mac_{z_0} for staggered arrays, Rau_{z_0} and Bot_{z_0} ($0.15H_{av}$). The decrease in z_0 beyond λ_{f-crit} is most obvious for Mac_{z_0} , whilst Bot_{z_0} remains larger across its wider peak. When height heterogeneity (σ_H) is introduced (Fig. 3.1d), an increase in Kan_{z_0} and especially Mho_{z_0} (up to a factor of four) is a response to the additional drag imposed by roughness elements of variable heights (Eq. 3.12 and 3.18). The Kan_{z_0} peak broadens to cover a wider range of densities.

3.3.3 Anemometric methods

Multiple anemometric methods exist (Appendix 3.A) that use slow and fast response sensors located at appropriate heights for which the logarithmic wind law is valid (Sect. 3.2.2). As single-level observations are more frequently available, two methods to determine z_d and one to determine z_0 from single level, high frequency measurements are assessed. These use the meteorological variables indicated in Table 3.2.

To determine z_d the ‘temperature variance’ (Rotach 1994, Eq. 3.20) and ‘wind variance’ (Toda and Sugita 2003, Eq. 3.21) methods are used. These methods, based upon surface layer scaling (Monin-Obukhov similarity theory, Sect. 2.2.3), use the relation between the non-dimensional temperature variance and vertical wind velocity variance and stability parameter (Wyngaard et al. 1971, Tillman 1972),

$$\phi_T = \frac{\sigma_T}{T_*} = -C_1 \left(C_2 - \frac{z - z_d}{L} \right)^{-\frac{1}{3}} \quad (3.20)$$

$$\phi_w = \frac{\sigma_w}{u_*} = C_3 \left(1 - C_4 \left[\frac{z - z_d}{L} \right] \right)^{\frac{1}{3}} \quad (3.21)$$

Anemometric Methods										
Abbreviation	z	z_d	L	u_*	\bar{U}_z	σ_w	σ_u	σ_T	T_*	Stability
(a) z_d										
TVM	✓		✓					✓	✓	Unstable
WVM	✓		✓	✓		✓				Unstable
(b) z_0										
EC	✓	✓	✓	✓	✓					Neutral

Table 3.2: Anemometric methods used to calculate the **(a)** zero-plane displacement (z_d) and **(b)** aerodynamic roughness length (z_0) with their respective meteorological variables and required stability condition. *Methods:* TVM – temperature variance method (Rotach 1994), WVM – wind variance method (Toda and Sugita 2003), EC – eddy covariance method (Grimmond et al. 1998). *Variables:* z – measurement height, z_d – zero-plane displacement, L – Obukhov length, u_* – friction velocity, \bar{U}_z – mean horizontal wind speed at height z , σ_w – standard deviation of vertical velocity component, σ_u – standard deviation of horizontal velocity component, σ_T – standard deviation of temperature, T_* – temperature scale

where σ_T and σ_w are the standard deviation of temperature and vertical velocity respectively, T_* is the temperature scale ($T_* = -(\overline{w'T'})/u_*$), L is the Obukhov length ($L = \frac{\bar{T}u_*^2}{\kappa g T_*}$, with g the acceleration due to gravity). Constants C_1 to C_4 are derived from observations, which vary across experiments and surfaces (e.g. Sorbjan 1989, Hsieh et al. 1996, Roth 2000). Using constants where z_d is assumed negligible (e.g. $C_1 = 0.99$, $C_2 = 0.06$, $C_3 = 1.25$ and $C_4 = 3$, Toda and Sugita 2003), the differences between observed (ϕ_{obs}) and estimated (ϕ_{est}) ϕ_T and ϕ_w are compared. The z_d is incrementally increased providing a new ϕ_{est} (for n iterations) and the z_d value which minimizes the root-mean-square error (RMSE) is taken as the appropriate value of z_d ,

$$RMSE = \sqrt{\left(\frac{1}{n}\right) \sum_{i=1}^n [(\phi_{est}) - (\phi_{obs})]^2} \quad (3.22)$$

With z_d determined and a direct observation of u_* the eddy-covariance (EC) method allows calculation of z_0 , through rearrangement of the logarithmic wind law,

$$z_0 = (z - z_d) \exp\left(-\frac{\bar{U}_z \kappa}{u_*}\right) \quad (3.23)$$

where \bar{U}_z and u_* are determined from observations at z . The EC method is applicable during near-neutral stability if stationarity is met (Foken and Wichura 1996). At least 20 observations are required to determine z_0 for a wind-direction sector (Beljaars 1987, Grimmond et al. 1998). In addition, low wind speeds ($\bar{U}_z < 1 \text{ m s}^{-1}$) are excluded (G. Liu et al. 2009).

3.4 Methods

3.4.1 Site description

Three London Urban Meteorological Observatory network (<http://micromet.reading.ac.uk/>) sites in the central activities zone of London (Fig. 3.2a) are used, where prior analyses have been undertaken (e.g. Kotthaus and Grimmond 2014a, b, Bjorkegren et al. 2015, Ward et al. 2015a). Instrumentation at the Strand campus of King's College London (KCL) has been mounted on towers upon the King's building (KSK), the Strand building (KSS), and to the west on the Strand building (KSSW) (Fig. 3.2c). The sites are all within 60 m, so their surroundings are similar. The local climate zone (Stewart and Oke 2012) 'compact midrise', is characterised by taller buildings amidst midrise building stock. Land cover is mostly paved and buildings constructed with stone, brick, tile, and concrete. Small gardens are located approximately 200 m east and 250 m south-west of the sites (Fig. 3.2b), with larger expanses of vegetation in parks over 1 km to the west of sites. Street canyons are located immediately north of the KSS and KSSW sites. One canyon (The Strand) extends for over 1 km in the north-east to south-west directions (orientation: 060°

– 240°), and another (Kingsway) extends approximately 500 m to the north-north-west (orientation: 330°) (Fig. 3.2b). The River Thames is located to the south between directions 092° – 223° (site dependent, Table 3.3). Although geometric parameters and land cover vary with direction and meteorological conditions (through the measurement source area, Sect. 3.7), values based on a 1-km radius are provided in Table 3.3.

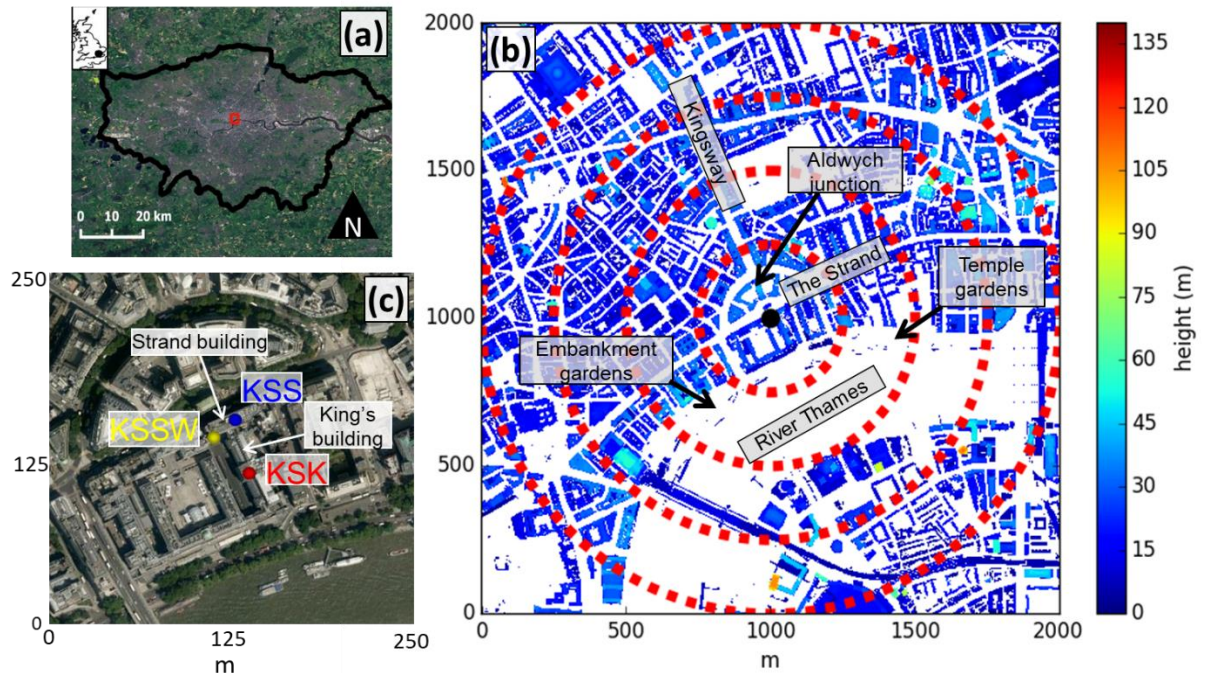


Figure 3.2: Location of measurement sites KSK, KSS and KSSW at King's College London (KCL) (see text for details) (a) within Greater London, UK (inset); (b) building heights surrounding the sites (major features labelled), red dashed lines indicate 250, 500, 750 and 1000-m radii from the KSSW site (black point); and (c) 250 m surroundings of KCL. (Photography source: Google imagery, 2014)

3.4.2 Observations

The period analysed for aerodynamic parameter determination is 2014 for the KSSW site and 2011 for the KSS and KSK sites. During independent assessment of the methods (Sect. 3.6), an additional three months in 2010 are considered at the KSS site. Identical instrumentation is used at the KSS and KSSW sites, as the equipment was moved along the Strand building (Fig. 3.2c) in 2012, preventing temporal overlap across all sites. The periods analysed allow for seasonal variability of meteorological conditions, whilst limiting surface cover changes (e.g. construction).

A sonic anemometer (CSAT3, Campbell Scientific, US) measured the 3-dimensional wind velocity and sonic temperature at a sampling frequency of 10 Hz at each site. The anemometers were supported by a single tube mast at the KSK site (Clark Masts CSQ T97/HP) and a triangular tower at the KSSW and KSS sites (Aluma T45-H). Instrument orientation was south-westerly to minimize potential mast-induced distortion for the prevailing wind directions.

The sensor heights are at $z = 1.97H_{av}$ (KSK), $2.48H_{av}$ (KSS) and $2.55H_{av}$ (KSSW) for H_{av} in the surrounding area of 1-km radius (Table 3.3). Although relative heights vary with direction and meteorological conditions (e.g. Sect. 3.7), measurements at the KSK site are closest to the top of the RSL and therefore more likely to be impacted by roughness-element wakes. In contrast the sensors at the KSS and KSSW sites are assumed to be at heights above the RSL. To evaluate this assumption, analysis of drag coefficient and turbulence intensities was undertaken around the sites to identify potential flow disturbance from nearby roughness-element wakes (e.g. Barlow et al. 2009) (Appendix 3.B). The analysis at the KSK site reveals that flow from the northern sector is disturbed by the Strand building (Fig. 3.2c, as noted by Kotthaus and Grimmond 2014b). At the KSS site, obvious flow disturbance is aligned with a nearby rooftop micro-scale anthropogenic source of moisture and heat which has previously been shown to influence turbulent fluxes (Kotthaus and Grimmond 2012). At the KSSW site, potential disturbance is aligned with a tall slender structure protruding from the Strand building roof (Fig. 3.2c). No obvious disturbances exist elsewhere, indicating the measurements at the KSS and KSSW sites are predominantly clear of roughness-element wakes and therefore above $z = H_{RSL}$.

Data are pre-processed following Kotthaus and Grimmond (2014a). Eddy-covariance planar fit coordinate transformation is performed using 'ECpack' software (van Dijk et al. 2004) and a yaw rotation provides wind speed aligned to the mean direction (Kaimal and Finnigan 1994). Humidity corrections are applied to the sonic temperature (Schotanus et al. 1983) and 30-min flux calculations are used to capture both the high and low end of the energy spectrum. An Ogive test (Moncrieff et al. 2004) ensured this was an appropriate time period.

A Halo Photonics Streamline pulsed Doppler lidar situated at the KSSW site for eight months (Table 3.3) operated in Doppler beam swinging (DBS) mode, as outlined by Lane et al. (2013). The lidar, measuring wind speed and direction, has 30-m gates with the mid-point of the first usable gate 141 m above ground level. The sampling interval of 120 s allows hourly averages to be calculated, which reduces error in the mean wind speed, whilst also ensures stationarity (Lane et al. 2013).

(a) Instrument locations								
Site	WGS84: Lat (N), Lon (E)	Instrument	Sensor height (m agl)	Host roof height (m)	Observation period analysed	Potential flow disturbance (bearing °)	River position (bearing °)	
KSSW	51° 30' 42.48" -0° 7' 0.192"	Halo Photonics Streamline pulsed Doppler LiDAR	-	35.6	1 Oct 2010 – 18 May 2011	-	097 – 212	
		CSAT3	50.3	35.6	1 Jan 2014 – 31 Dec 2014	230 – 245		
KSS	51° 30' 43.2" -0° 6' 58.8594"	Campbell Scientific 3D Sonic	48.9	35.6	1 Oct 2010 – 31 Dec 2011	045 – 090	095 – 215	
KSK	51° 30' 41.04" -0° 6' 57.9594"	Anemometer	38.8	30.2	1 Jan 2011 – 31 Dec 2011	270 – 045	092 – 223	
(b) Geometric parameters				(c) Surface Cover (%)				
H_{av} (m)	λ_p	H_{max} (m)	σ_H (m)	Built	Paved	Grass	Trees and shrubs	Water
19.74	0.41	116.72	10.83	40.7	40.3	6.8	1.0	11.2

Table 3.3: Characteristics of the measurement sites within a 1-km fetch: **(a)** sensor heights: metres above ground level, river position: bearing of the most northern point of the north bank, **(b)** geometric parameters and **(c)** surface cover

3.4.3 Determination of aerodynamic parameters

3.4.3.1 Flow diagram illustrating framework of analysis

At each of the measurement sites, local aerodynamic parameters are determined using the reference-based, morphometric and anemometric methods (Fig. 3.3) and evaluated (Sect. 3.5). Wind-speed profiles are then extrapolated using the logarithmic wind law (Eq. 3.1) and aerodynamic parameters from each method for comparison to wind speeds observed aloft using Doppler lidar (Fig. 3.3, L_1) (Sect. 3.6). An example of the impacts upon the source area for measurements is also shown (Sect. 3.7).

Application of the reference-based approach only requires aerial photography (Fig. 3.3, R_1) to provide aerodynamic parameters (Fig. 3.3, R_2). The more involved anemometric and morphometric determination of z_d and z_0 are expanded upon in Sects. 3.4.3.2 and 3.4.3.3, respectively. Decisions or available resources at each step potentially influence results; e.g. if a source area footprint model is used (Fig. 3.3, M_4).

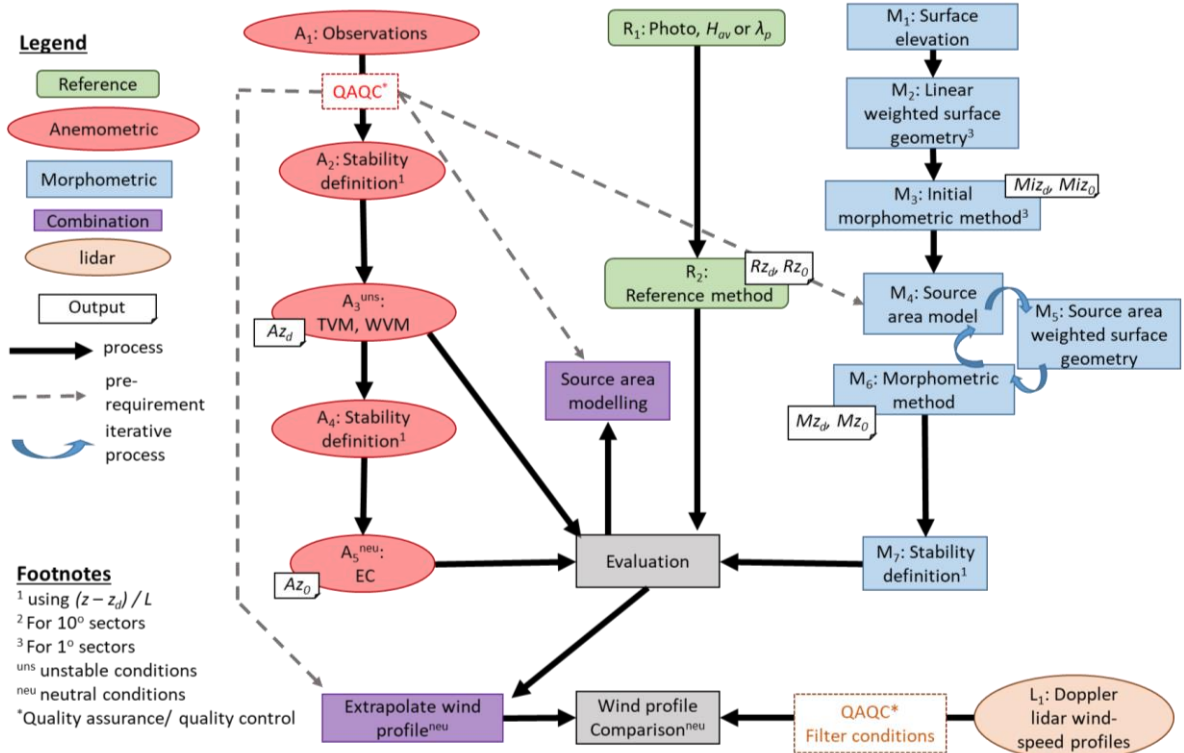


Figure 3.3: Flow diagram of the determination of aerodynamic parameters at the London sites using anemometric (A), reference (R) and morphometric (M) methods

3.4.3.2 Anemometric determination of aerodynamic parameters

To determine z_d with the temperature and wind variance methods (Fig. 3.3, A_3), 10° directional sectors are used ($000^\circ - 010^\circ$, etc) to provide sufficient observations while allowing for varying fetch. As the methods require unstable conditions ($-6.2 \leq z'/L \leq -0.05$, Roth 2000; L – Obukhov length; $z' = z - z_d$), an *a priori* assumption of z_d is required (Fig. 3.3, A_2). The methods are applied by defining stability with several values of z_d , ranging from 0 m to measurement height in 5 m increments, providing a range of solutions for each 10° sector. If the denominator in $\phi_T (T_*)$ or $\phi_w (u_*)$ (Eqs. 3.20, 3.21, respectively) approaches zero, periods are removed. The additional criteria of $u_* > 0.05 \text{ m s}^{-1}$ and $T_* < -0.05 \text{ K}$ may remove difficulties encountered using the methods in previous studies (e.g. De Bruin and Verhoef 1999, Rooney 2001). The methods are applied using rural ($C_1 - C_4$, Sect. 3.3.3) and urban (Roth 2000) constants, as well as those determined using non-linear regression (Bates and Watts 1988) of Eqs. 3.20 and 3.21 to observations at each site. However, the two latter methods require an *a priori* assumption of z_d and therefore provide a solution which is similar to the initial z_d , and not useful.

The z_d from both the temperature and wind variance methods for each 10° sector are used to determine neutral conditions $|z'/L| \leq 0.05$ (Fig. 3.3, A_4), and subsequently to calculate z_0 (Fig. 3.3, A_5) using the EC method (Eq. 3.23).

3.4.3.3 Morphometric determination of aerodynamic parameters

A 4 m resolution surface elevation dataset (Lindberg and Grimmond 2011a) is used to determine the geometric parameters required to apply the morphometric methods (Fig. 3.3, M_1). For each morphometric method an initial estimation of z_d and z_0 is made for 1° sectors and a 1-km fetch (Miz_d , Miz_0) (Fig. 3.3, M_3). During this process, four annuli are used (0-250, 250-500, 500-750 and 750-1000 m; e.g. Fig. 3.2b for the KSSW site) to weight surface geometry (50.00, 31.25, 12.50 and 6.25%, respectively), based on Kotthaus and Grimmond's (2014b) footprint climatology. The Kormann and Meixner (2001) analytical footprint model (Fig. 3.3, M_4) is then used to indicate the probable extent of the turbulent flux source area for each 30-min period of meteorological observations. The footprint model requires the measurement height and the observed σ_v (standard deviation of the lateral velocity component), L , u_* and wind direction. It also requires z_d and z_0 , hence their initial estimation (Miz_d and Miz_0) which is averaged across σ_v for each period of observations (Kotthaus and Grimmond 2014b).

The 80% cumulative source area for each measurement (30-min) is used to weight the fractional contribution of each grid square in the surface elevation database (Fig. 3.3, M_5). A weighted geometry is then determined, allowing for source area specific aerodynamic parameters (Mz_d and Mz_0) to be calculated for each morphometric method (Fig. 3.3, M_6). The Mz_d and Mz_0 values for each observation period are iteratively provided to the source area model until the mean absolute difference of the parameter between iterations is $< 5\%$ or four iterations are performed. The latter is deemed appropriate given computational requirements and the range of values across the methods (Sect. 3.5). The methodology means that Mz_d and Mz_0 vary for each 30-min time period as a consequence of the varying source area. When the source area becomes so small that it covers only the nearest few roughness elements (e.g. during very unstable conditions or large z_d) a morphometrically determined z_d or z_0 is inappropriate. Therefore, only source areas extending horizontally beyond 100 m from the measurement sensor are considered.

The initially-estimated aerodynamic parameters (Fig. 3.3, step M_3 : Miz_d and Miz_0) were found to be independent of the solution, irrespective of source area model (Kormann and Meixner 2001 and Kljun et al. 2015 models used, Appendix 3.C). Thus, it is possible to omit steps M_2 and M_3 (Fig. 3.3) and initialise the model with any reasonable roughness parameters (e.g. open country: $z_0 = 0.03$ m, $z_d = 0.2$ m). Here, steps M_2 and M_3 are retained for completeness. In addition, the Kormann and Meixner (2001) model is used, as the Kljun et al. (2015) model requires specification of the boundary layer height, which is not available for all observations.

3.5 Results

3.5.1 Zero-plane displacement (z_d)

3.5.1.1 z_d determined by anemometric methods

The stages of the application of the temperature and wind variance methods are demonstrated for the KSSW site in Fig. 3.4. The z_d determined by each method is unbiased by the initial z_d used to define stability (Sect. 3.4.3.2), which causes < 5 m variability in any wind direction (indicated by the range in each method, Fig. 3.5). In addition, the impact of varying the empirical coefficients $C_1 - C_4$ (Sect. 3.3.3) (based on Sorbjan 1989 and Hsieh et al. 1996) is < 5 m in any 10° sector, and therefore generates similar uncertainty to that of stability definition (Fig. 3.5a-c).

The similarity relations (Eqs. 3.20, 3.21) for temperature are consistently associated with a larger RMSE compared to those for vertical velocity (e.g. Fig. 3.4d, e), because the temperature data have a relatively larger spread. Across sites, RMSE for the wind variance method relation varies between 0.18 and 0.49, whilst it is 0.35 – 0.97 for the temperature variance method. The larger RMSE associated with the temperature data may be caused by the thermal inhomogeneity of the area. The RMSE for the temperature data increases with height (i.e. the largest RMSE is observed at the KSSW site), which is attributable to the larger extent of the source area and more numerous sources and sinks of heat.

Toda and Sugita (2003) suggest application of both the temperature and wind variance methods assist in the determination of z_d . This is true at both the KSSW and KSK sites where z_d determined using each method varies by approximately 5 m for each 10° sector (Fig. 3.4f and Fig. 3.5a, c). In comparison, the method solutions at the KSS site consistently vary by > 13 m (Fig. 3.5b). The large variability at the KSS site is most likely associated with the nearby rooftop micro-scale anthropogenic sources of moisture and heat (Kotthaus and Grimmond 2012) influencing turbulent fluxes.

The z_d based on the temperature variance method is consistently larger than for the wind variance method (Fig. 3.5a-c). Previous studies found z_d may be larger than H_{av} in urban areas using both the temperature (Grimmond et al. 1998, 2002, Feigenwinter et al. 1999, Kanda et al. 2002, Christen 2005, Chang and Huynh 2007, Tanaka et al. 2011) and wind (Tsuang et al. 2003) variance approaches. Results at the KCL sites support this, as z_d is up to twice H_{av} ($H_{av} = 19.74$ m, Table 3.3).

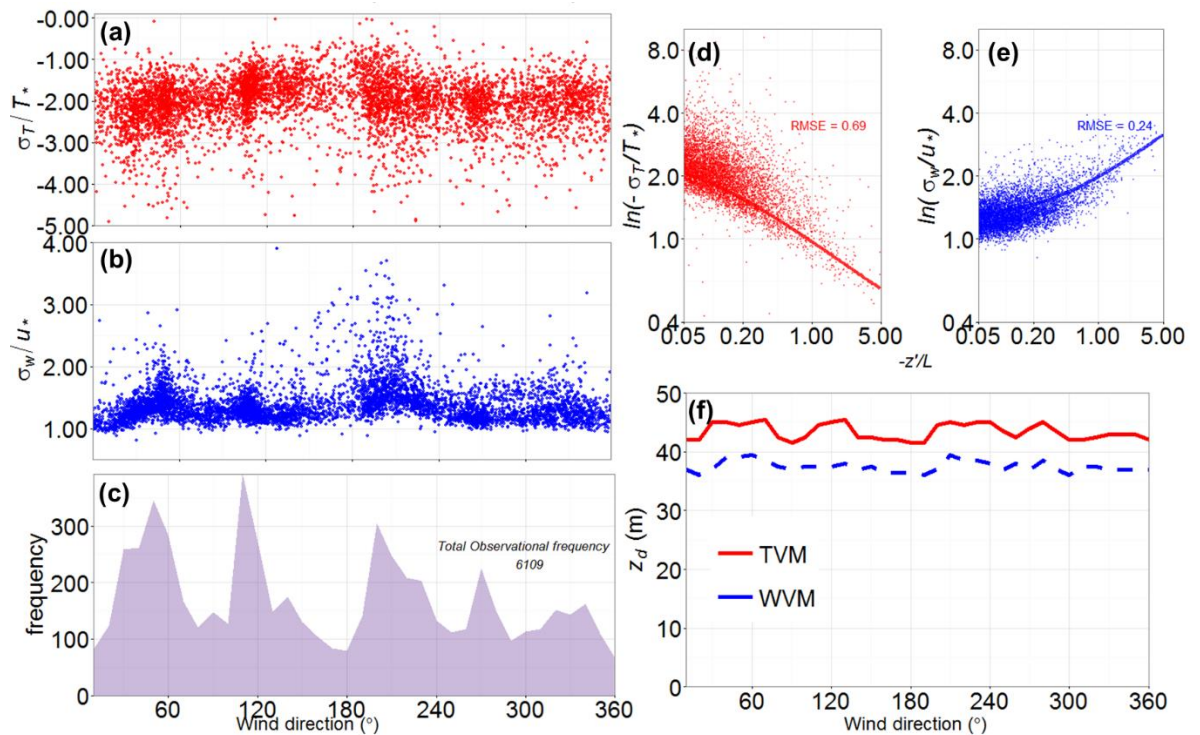


Figure 3.4: Application of the temperature variance (TVM) and wind variance (WVM) anemometric methods at the KSSW site to determine z_d during unstable conditions ($-6.2 \leq z'/L \leq -0.05$), with $z_d = 30$ m used to define stability. Results shown are 30-min observations (points) of the scaled: (a) standard deviation of temperature (σ_T/T_*) and (b) vertical wind velocity (σ_w/u_*) by wind direction; and (c) frequency of unstable conditions for 10° bins. Non-linear fit (line) to observations for (d) TVM (Eq. 3.20) and (e) WVM (Eq. 3.21), with RMSE; (f) Solution for z_d (10° sectors) for the TVM (red solid line) and WVM (blue dashed line)

No obvious association is evident between the directional variability of z_d and surface characteristics. For the temperature variance method, z_d is similar for all directions at each site (Fig. 3.5a-c), varying by less than 5 m. Whereas, the wind variance method z_d varies by up to 10 m, possibly because of occasional flow interference from roughness-element wakes. The parks (1 – 2 km upwind to the west) do not obviously influence z_d , but considering the extent of the source area for the measurements (Sect. 3.7) this is expected. The River Thames (Fig. 3.5a-c, blue shading) and small parks (Fig. 3.2b) closer to the measurement sites also do not affect the z_d values. Following Jackson (1981), z_d corresponds to the centroid of the drag profile of the roughness elements. The lack of directional variability in anemometric z_d indicates the surface drag is dominated by taller roughness elements (maximum building height is 40 – 60 m in all directions). This is consistent with the disproportionate amount of drag observed to be exerted by taller roughness elements in a heterogeneous mix (Xie et al. 2008, Mohammad et al. 2015a).

3.5.1.2 z_d determined by morphometric methods

There is less inter-site variability in z_d determined using each morphometric method, compared to the anemometric methods (Fig. 3.5a-c). However, the range of values between morphometric methods (intra-site variability) is larger than for the anemometric methods. There is an obvious separation between the methods based upon uniform (*RT*, *Bot*, *Rau*, *Mac*: RE_{av}) and

heterogeneous (*Kan* and *Mho*: RE_{var}) roughness-element heights. Across the sites, the former range between 5 and 20 m, whereas the latter are between 25 and 40 m (or almost twice the RE_{av} methods). The river, between directions $092^\circ - 223^\circ$ (site dependent, see Table 3.1) causes a reduction of average height and therefore also z_d determined by the RE_{av} methods. In comparison, the RE_{var} methods are unresponsive because σ_H becomes larger in these directions. The variability between the morphometric methods therefore becomes at least a factor of four in directions where the river is located.

When the measurement footprint has higher urban densities (non-river directions) z_d determined by the RE_{av} methods varies between 15 – 20 m across all three sites, with an approximate inter-method variability of ± 5 m. This increases to ± 10 m when the river sector is included, with z_d values as low as 5 m at the KSK site. The variability of the RE_{av} methods in the river sector (Fig. 3.5a-c) is proportional to the extent of the source area which is occupied by the river, which reduces λ_p . Between the methods, Bot_{z_d} is consistently smallest and Mac_{z_d} is the largest for more densely packed directions.

As expected from the sensitivity analysis (Fig. 3.1), Kan_{z_d} is consistently up to 5 m larger than Mho_{z_d} (Fig. 3.5a-c). Both methods indicate $z_d \geq 1.5H_{av}$ for the surrounding area – a value typically used to estimate the minimum RSL depth (Roth 2000). Such high z_d values support the contention that roughness-element height variability is important when considering the determination of H_{RSL} , in addition to, for example, H_{av} and roughness-element spacing (Cheng and Castro 2002). An effective mean building height has been suggested as a more appropriate scaling parameter for H_{RSL} that incorporates building-height variability (Millward-Hopkins et al. 2011, their Eq. 21). It may also be possible to consider the influence of height variability on the H_{RSL} through directly considering σ_H or H_{max} (e.g. $H_{RSL} = 2H_{av} + \sigma_H$). At the KSK site, the z_d determined by the RE_{var} methods is consistently of the order of the measurement height, or greater, meaning the flux footprint either cannot be calculated or is consistently smaller than 100 m in horizontal extent and therefore few values are reported here (Fig. 3.5c, f).

If the f_d constant used in the RT method is doubled (Eq. 3.2), the predicted z_d value aligns reasonably well with the z_d estimated by the RE_{var} methods (Fig. 3.5a-c, $2RT$). This suggests that if limited geometric parameters are available (i.e. only H_{av}), $2RT_{z_d}$ may provide a useful proxy for the z_d determined by the RE_{var} methods in a heterogeneous mix. Assessment of the geometric parameters for each morphometric method's respective source area indicates the magnitude of z_d for all methods is fundamentally determined by the directional variability in λ_p .

This includes Mho_{z_d} and Kan_{z_d} , which are more sensitive to variability in λ_p , despite their direct incorporation of σ_H and/or H_{max} .

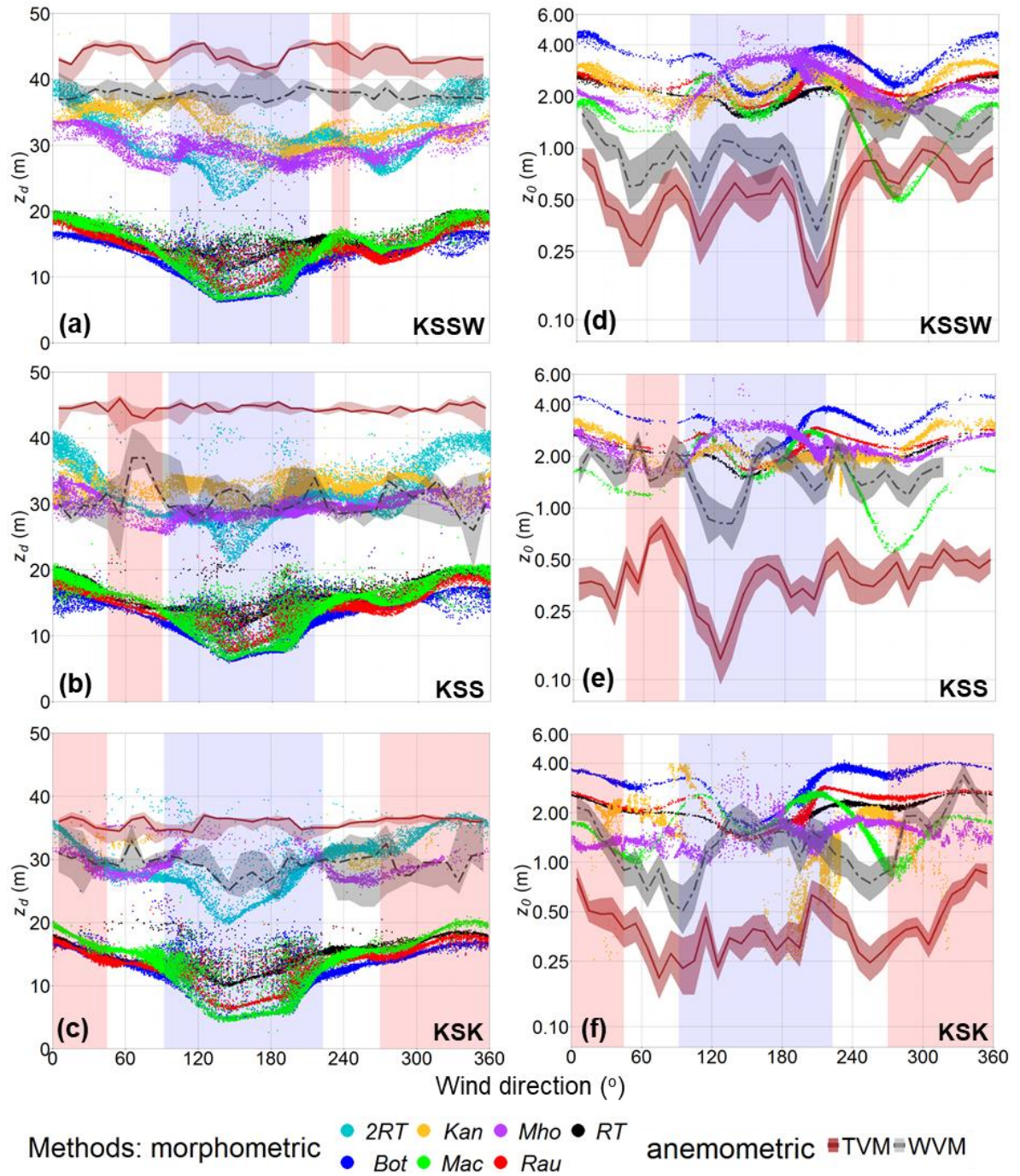


Figure 3.5: Comparison of anemometric (lines and shading) and morphometric (points) methods to determine the (a, b, c) zero-plane displacement (z_d) and (d, e, f) aerodynamic roughness length (z_0) (note ln y axis) surrounding the three assessed sites (Fig. 3.2). For anemometric methods, z_d is the median solution of the temperature variance (TVM, solid line) and wind variance (WVM, dashed line) methods, respectively, applied to 30-min observations during unstable conditions ($-6.2 \leq z'/L \leq -0.05$) for 10° sectors. The range (shading) represents all possible solutions by varying z_d used for stability definition from 0 to measurement height. z_0 is the median (lines) and upper and lower quartile (shaded) of the eddy-covariance method (Eq. 3.23) during neutral conditions ($|z'/L| \leq 0.05$) for each 10° sector using z_d from the TVM and WVM, respectively. Morphometric methods use geometry weighted by the final iterated footprint for each 30-min observation (Sect. 3.4.3.3) for the same stability conditions as anemometric methods, however, z_d in z'/L is determined by the respective morphometric method for each observation. Background shading is in directions where the River Thames is located (blue) and where turbulence data indicates disturbance (red). For method abbreviations see Tables 3.1 and 3.2

3.5.2 Aerodynamic roughness length (z_0)

3.5.2.1 z_0 determined by anemometric methods

The aerodynamic roughness length determined using the EC method is a function of both observations (i.e. \overline{U}_z and u_* for each 30-min observation) and the z_d determined using the temperature and wind variance methods. Therefore, the consistently larger z_d determined using the temperature variance method (Fig. 3.5a-c) implies that the associated z_0 is consistently lower than that of the wind variance method. For each method, the interquartile range of z_0 (Fig. 3.5d-f shading around lines) consistently falls within ± 0.25 m from the median for each 10° sector. In directions where turbulence data indicate disturbance (Sect. 3.4.2, Fig. 3.5, directions with red shading) there is an increase in z_0 because of the increased friction velocity in the same direction.

In directions without the river, the median z_0 varies between 0.25 – 3 m, tending towards the lower end of typical z_0 values reported for cities (Grimmond and Oke 1999). This is likely because the dense packing of roughness elements (λ_f and $\lambda_p \geq 0.5$) creates a flow more characteristic of skimming than chaotic (e.g. Oke 1987).

When the flow is aligned with the river (Fig. 3.5d-f, between $090^\circ - 120^\circ$, $190^\circ - 210^\circ$), z_0 values become smallest at the KSSW and KSS sites (as low as 0.1 m) because of flow along the smoother more homogeneous surface. This reduction is not obvious at the KSK site because of its lower siting and associated smaller source area (i.e. these measurements tend not to be affected by the river) (Sect. 3.7). At the KSSW site a reduction in z_0 to 0.25 m also occurs when the wind flow is aligned with the adjacent Strand street canyon (060° , Fig. 3.2), because of the reduction of drag as flow is channelled along the canyon. The effect of the channelling is not observed at the KSK site because of its lower and more southerly siting, nor at the KSS site because of the micro-scale anthropogenic heat and moisture source in the same direction (Sect. 3.4.2).

3.5.2.2 z_0 determined by morphometric methods

The morphometric methods (except for the *Mho* method) have relative peaks in z_0 at the edges of the river sector (Fig. 3.5 blue shading) similar to where anemometric z_0 becomes lowest (Sect. 3.5.2.1). This is because although the majority of a source area may lack roughness elements and be smooth, the morphometric methods are responsive to the geometry calculated within the source area, which according to the morphometric method formulations generates disrupted flow. The peaks in morphometrically-determined z_0 occur when the source area falls upon both river and buildings causing λ_f to be close to λ_{f-crit} (Fig. 3.1). When most of the source

area is river, λ_f becomes smallest ($\lambda_f = 0.2$). Here, the *Mho* method indicates the highest z_0 because the maximum Mho_{z_0} occurs at these smaller λ_f values (Fig. 3.1).

All morphometric methods indicate increased roughness to the north of the sites, in response to increased roughness-element height (H_{av} up to 30 m). The variable surface morphology means that the inter-method variability is largest in these directions, varying between 1 – 4 m. In comparison, inter-method variability is least in river sector (1.0 – 3.5 m), associated with the most consistent surface morphology. The directional variability of z_0 is primarily a function of λ_f for all methods (except the *RT* method). The λ_f value varies between 0.2 and 0.8 with wind direction, and the greater sensitivity of Bot_{z_0} and Mac_{z_0} to λ_f (Fig. 3.1), means they vary most with direction. Bot_{z_0} is consistently 2 m larger than all other morphometric methods because of its more pronounced peak of z_0 (Fig. 3.1). In comparison, Mac_{z_0} tends to be lowest, especially where there is a greater frontal area index of roughness elements (e.g. $240^\circ - 300^\circ$ where $\lambda_f \geq 0.5$) because of its comparatively steep reduction of z_0 at higher λ_f (e.g. Fig. 3.1).

The inclusion of Mac_{z_0} in Kan_{z_0} means that they vary similarly with direction. However, Kan_{z_0} tends to be 1 – 2 m larger than Mac_{z_0} in directions with higher frontal areas, as the former does not have the steep drop off found in Mac_{z_0} at higher λ_f (e.g. $240^\circ - 300^\circ$ at the KSSW and KSS sites). An increasingly smaller source area occurs as the RE_{var} method values of z_0 become similar to the measurement height at the KSK site. This explains the spread and lack of calculated Kan_{z_0} and Mho_{z_0} here (Fig. 3.5f).

3.5.3 Comparison between anemometric and morphometric aerodynamic parameters

Application of the anemometric and morphometric methods at the London sites indicates that no individual value or method is optimum for aerodynamic parameter determination. Furthermore, the variability within and between the anemometric methods suggest it is not simple to use these as a basis for assessing morphometric methods. Therefore, the morphometric and anemometric z_d are compared using the root-mean-squared error ($RMSE_{z_d}$). For comparison of z_0 the logarithmic influence (e.g. Eq. 3.1) is accounted for by using the root-mean-squared geometric error ($RMSG E_{z_0}$) (Jachner et al. 2007):

$$RMSG E_{z_0} = \exp \left[\frac{\sum_{i=1}^n \ln(A_{z_0}/M_{z_0})^2}{n} \right]^{0.5} \quad (3.24)$$

where A_{z_0} and M_{z_0} are anemometric and morphometrically determined z_0 , respectively. The $RMSE_{z_d}$ and $RMSG E_{z_0}$ values between each morphometric and anemometric method at each

site are plotted against each other in Fig. 3.6 (smaller symbols), with the larger circles representing the values for all observations.

Errors across the sites range between 2.25 and 31.40 m for zero-plane displacement and 1.25–2.70 m for roughness length (Fig. 3.6). For z_d , similarity between the anemometric methods and the RE_{var} morphometric methods (Fig. 5, 3.6), suggests $z_d > H_{av}$ in the surrounding area (20 m, Table 3.3). Use of the *Kan*, *Mho* and *2RT* methods results in the lowest $RMSE_{z_d}$ across all observations (approximately 10 m), in comparison to the RE_{av} methods which have $RMSE_{z_d} = 25$ m (Fig. 3.6, large circles). The morphometrically-determined z_0 is consistently greater than anemometric z_0 (Fig. 3.5d-f), which is more obvious for the temperature variance method ($RMSGE_{z_0}$ up to 2.70 m) than the wind variance method ($RMSGE_{z_0}$ of up to 2 m) (Fig. 3.6). No individual morphometric method calculates z_0 that is consistently similar to the anemometric methods, with $RMSGE_{z_0}$ values for all observations ranging between 1.75 and 2 m (Fig. 3.6, circles). However, *Bot* _{z_0} deviates the furthest from observations ($RMSGE_{z_0} > 2.2$ m) given its considerably larger magnitude (Fig. 3.5d-f).

Both aerodynamic parameters (z_d and z_0) are required for use in the logarithmic wind law. The difference in z_d between the RE_{var} and RE_{av} methods is not compensated for in their respective z_0 values. Therefore, $z_d + z_0$ determined by the RE_{var} methods is consistently almost twice that of the RE_{av} methods. The *2RT* method (*2RT* _{z_d} with *RT* _{z_0}) is amongst the most similar to observations for both z_d and z_0 , despite being a simple method to bring the *RT* method in line with the RE_{var} methods. In contrast, the *Bot* method is consistently furthest from observations for both aerodynamic parameters.

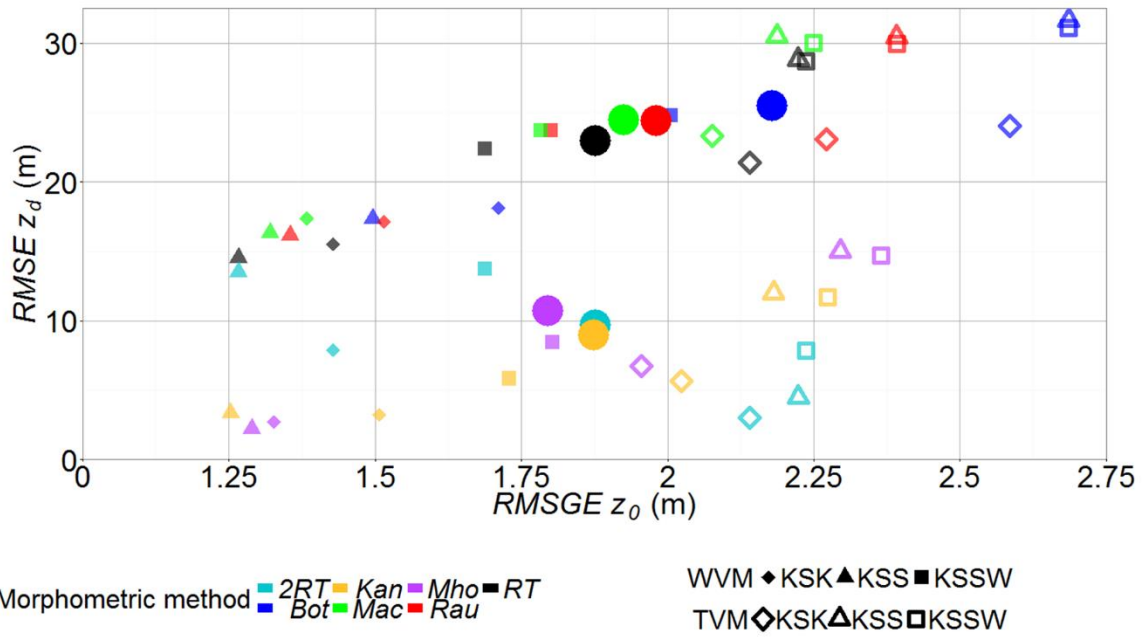


Figure 3.6: Root-mean-square error (RMSE) analysis of the aerodynamic parameters determined using the morphometric and anemometric methods for each 30-min period of observations at each site (smaller symbols) and for all observations (larger symbols). The RMSE for z_d is plotted against root-mean-square geometric error (RMSGE) for z_0 (Eq. 3.24). The z_d is for unstable conditions ($-6.2 \leq z'/L \leq -0.05$ with z_d in z'/L for each morphometric method) and z_0 is for neutral conditions ($|z'/L| \leq 0.05$, with z_d in z'/L for each morphometric method). See Tables 3.1 and 3.2 for method abbreviations

3.5.4 Reference-based approach

Aerodynamic parameters from numerous field studies using observations and morphometric methods (the RE_{av} methods only) informed Grimmond and Oke's (1999, their Table 6 and Fig. 7) synthesis, which is complemented with photography for application. Use of a reference-based approach to determine aerodynamic parameters at the KCL sites indicates only that $z_d > 7$ m and $z_0 > 0.8$ m for all directions. This demonstrates the limitations of using reference-based approaches in complex urban areas, as they offer a broad range of values. In addition, the reference-based approach does not have sufficient detail to resolve the directional variability in z_d and z_0 with local features, such as the channelling of wind flow along the river which lowered z_0 determined from observations (Sect. 3.5.2.1). The variability in both land cover and roughness-element height are only coarsely considered in reference classes. In addition, use of aerial photography remains subjective – for example 'high' and 'high-rise' categories (Grimmond and Oke 1999 their Fig. 7) both occur in the vicinity of the KCL sites, so selection may be inconsistent.

3.6 Independent method assessment – wind-speed profile extrapolation

With an observed average wind speed (\bar{U}_{ref}) at a reference height (z_{ref}) during neutral conditions, locally determined aerodynamic parameters can be used to estimate the average wind speed (\bar{U}_z) at a second height (z) using the logarithmic wind law (e.g. Wieringa 1993, Verkaik 2000):

$$\bar{U}_z = \bar{U}_{ref} \frac{\ln\left\{\frac{(z - z_d)}{z_0}\right\}}{\ln\left\{\frac{(z_{ref} - z_d)}{z_0}\right\}} \quad (3.25)$$

The different methods to determine z_d and z_0 are independently assessed through comparing wind speeds estimated using the logarithmic wind law by each method (Eq. 3.25) to wind-speed profiles observed with Doppler lidar (Fig. 3.3, L_1). For the comparison, the lidar is located at the KSSW site location (Sect. 3.4.2). Therefore, observations from the KSS site (45 m east of the KSSW site, Fig. 3.2) provide \bar{U}_{ref} ($z_{ref} = 48.9$ m) and other variables (Eq. 3.25). Hourly data are used to ensure acceptable errors in the lidar data (Lane et al. 2013). The wind speed for each method is calculated at 1 m height intervals and then averaged over 30-m ‘gates’ to correspond to the vertical resolution of the lidar.

Observations at a greater height have a larger source area. Identical fetch in any direction is rare in an urban area, therefore, it is likely that z_d and z_0 should also adjust with source area. To constrain changes in z_d and z_0 throughout the profile, as well as the likelihood of overlapping internal boundary layers from surface discontinuities (e.g. Garratt 1990), the analysis is undertaken for the most homogeneous fetch within 10 km of the KSSW site (Fig. 3.2). This is deemed to be the $000^\circ - 045^\circ$ direction based upon 500-m grid squares of average ground height and the H_{av} , H_{max} and σ_H of roughness elements from the surface elevation database (Lindberg and Grimmond 2011a).

Outside of neutral stability, corrections are required to the logarithmic wind profile (see Eq. 2.12 and Table 2.1). These are based upon empirical fits to observations aloft of idealised surfaces and can vary considerably (Högström 1996). Such corrections therefore introduce a source of uncertainty into extrapolated wind speeds and given the objective to evaluate aerodynamic parameters determined by different methods, only neutral stability is considered here. To ensure wind-speed profiles are most likely for neutral stability the highest (upper quartile) wind speeds are used (Drew et al. 2013b). Regression between the inverse of the Obukhov length ($1/L$) and wind speed measured at the KSS site for the same times confirms the tendency of the stability parameter z'/L towards zero (neutral) as wind speeds increase. Note, these strong wind-

speed conditions are later shown to correspond to neutral stability (Sect. 4.5.5). To ensure the depth of the urban boundary layer is sufficient, analysis is restricted to lower 200 m of daytime (0900 – 1700 h) profiles so the logarithmic wind law is appropriate (Cook 1997, Tieleman 2008, Li et al. 2010, Drew et al. 2013b). After filtering the lidar data, 33 profiles are available from the 000° – 045° sector with upper quartile wind speeds and where z_d and z_0 are available for all methods. Data are analysed from the lowest three gates (mid-points: 141 m, 171 m and 201 m).

The mean observed wind speeds in each 30-m gate are 10.4, 10.9 and 11.4 m s⁻¹ (lowest to highest, Fig. 3.7a). These are most similar to the greater wind speeds extrapolated using aerodynamic parameters from the *Kan*, *Mho* and temperature variance methods (Fig. 3.7a). Both z_d and z_0 are free parameters in Eq. 3.25, therefore two different pairs of values can predict the same wind speed aloft. However, the comparatively lower z_d of the RE_{av} methods and lack of compensation for this in z_0 means that their extrapolated wind speeds are less than both the RE_{var} methods and observations (Fig. 3.7).

The differences (U_{diff}) between wind speeds extrapolated using the different methods and wind speeds observed by the lidar (for each of the 33 profiles compared) are summarised in Fig. 3.7b. Over 95% of observed wind speeds are underestimated by the RE_{av} methods, with median underestimation between 1.5 and 2.9 m s⁻¹ (Fig. 3.7b). The higher extrapolated wind speeds using the RE_{var} methods have median $U_{diff} < 0.6$ m s⁻¹ for all three lidar gates, which is within 6% of the mean observed wind speed. In addition, wind speeds extrapolated using the RE_{var} methods most resemble the distribution of observed wind speeds, tending to evenly under- or over- estimate observations (approximately 50% of cases, respectively). The temperature variance method's largest z_d and smallest z_0 produce a consistent overestimate in the wind speed (75% of cases), however it still shows a median $U_{diff} < 1.1$ m s⁻¹ for all gates (Fig. 3.7b).

Results suggest that if high wind speeds are of concern, aerodynamic parameters determined using the *Mho*, *Kan* or temperature variance methods, may be the most appropriate methods to estimate the neutral vertical profile of wind speed. No relation is observed between the individual U_{diff} values and either meteorological conditions (e.g. L , \bar{U}_{ref} , u_*) or the time of day. However, there are other potential reasons why differences in wind speed occur. Although the most homogeneous direction was selected (000° – 045°), the difference in source area between the sensor used for extrapolation ($z = 48.9$ m) and lidar ($z = 126$ to 216 m) implies the flow is likely in equilibrium with different upwind surfaces. Accounting for the changes in upwind surface morphology may therefore improve wind-speed estimation, which is considered in Chapter 4. The concept of a blending height (z_b) above which the wind-speed profile is

responding to an entire heterogeneous surface (Grimmond and Oke 1999, Roth 2000, Barlow 2014) may support this hypothesis, however there is uncertainty in determination of z_b (Grimmond and Oke 1999, Grimmond et al. 2004, Barlow 2014). A further consideration is the depth of the ISL and therefore the theoretical validity of the logarithmic wind-speed profile to the heights assessed. However, the comparison was limited to daytime profiles below 216 m and the individual observed wind-speed profiles (Fig. 3.7a) indicate profiles compared are logarithmic in nature.

3.7 Source area modelling using the morphometric methods

The EC turbulent flux source area is a function of the aerodynamic parameters and meteorological conditions (Sect. 2.2.4). The surface characteristics within the source area of an EC measurement are of interest, not only for explaining the flux partitioning (Kotthaus and Grimmond 2014b) and CO₂ exchanges (Ward et al. 2015a), but also for determination of aerodynamic parameters themselves, which source areas are particularly sensitive to (Arriga et al. 2017) (which is why the iterative methodology is used, Sect. 3.4.3.3). To assess the impact of the aerodynamic parameters determined by each morphometric method on the modelled source area, a footprint climatology for each method is generated at each site. The sum of all 80% cumulative weight source areas (Sect. 3.4.3.3) for each 30-min observation is normalised by the total sum of weights. As different years are analysed (2014 at the KSSW site; 2011 at the KSS and KSK sites) direct comparison is not undertaken. However, the lower the height of the sensor, the smaller the modelled source area (i.e. KSSW, KSS to KSK site – Fig. 3.8). In addition, the source area climatology is biased towards the dominant south-westerly wind direction. The greatest wind speeds from the south-west, as well as more frequent neutral conditions, means the source areas also extend furthest upwind in this direction.

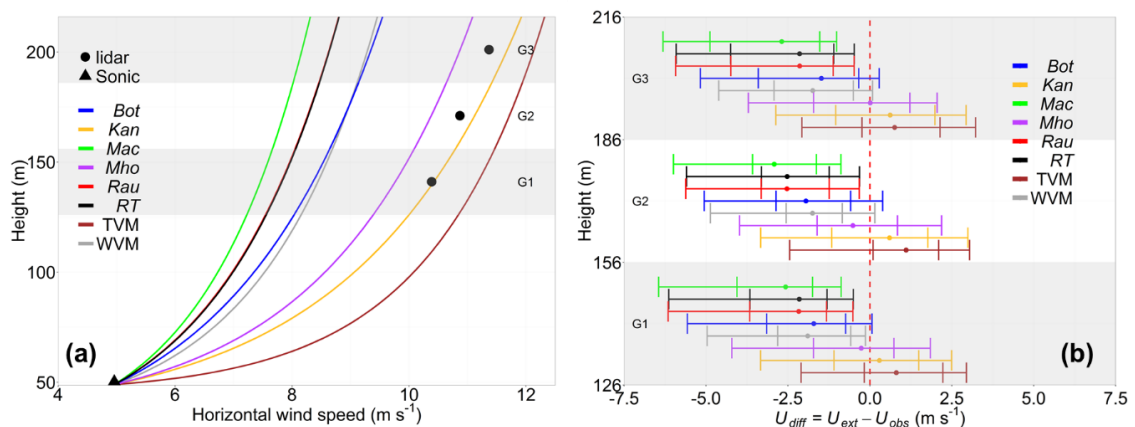


Figure 3.7: Variation of mean hourly wind speed with height (33 profiles for selection): **(a)** mean of extrapolated profiles (Eq. 3.25) with locally determined aerodynamic parameters from the KSS site (triangle) and each 30-m lidar gate (points). **(b)** Median (points) difference (U_{diff}) between observed (U_{obs}) and extrapolated (U_{ext}) wind speeds at 30-m lidar gates. Whiskers are the 5th, 25th, 75th and 95th percentiles. Lidar gates are shaded G1 – G3 (G1 = 126 – 156 m, mid-point = 141 m). See Tables 3.1 and 3.2 for method abbreviations

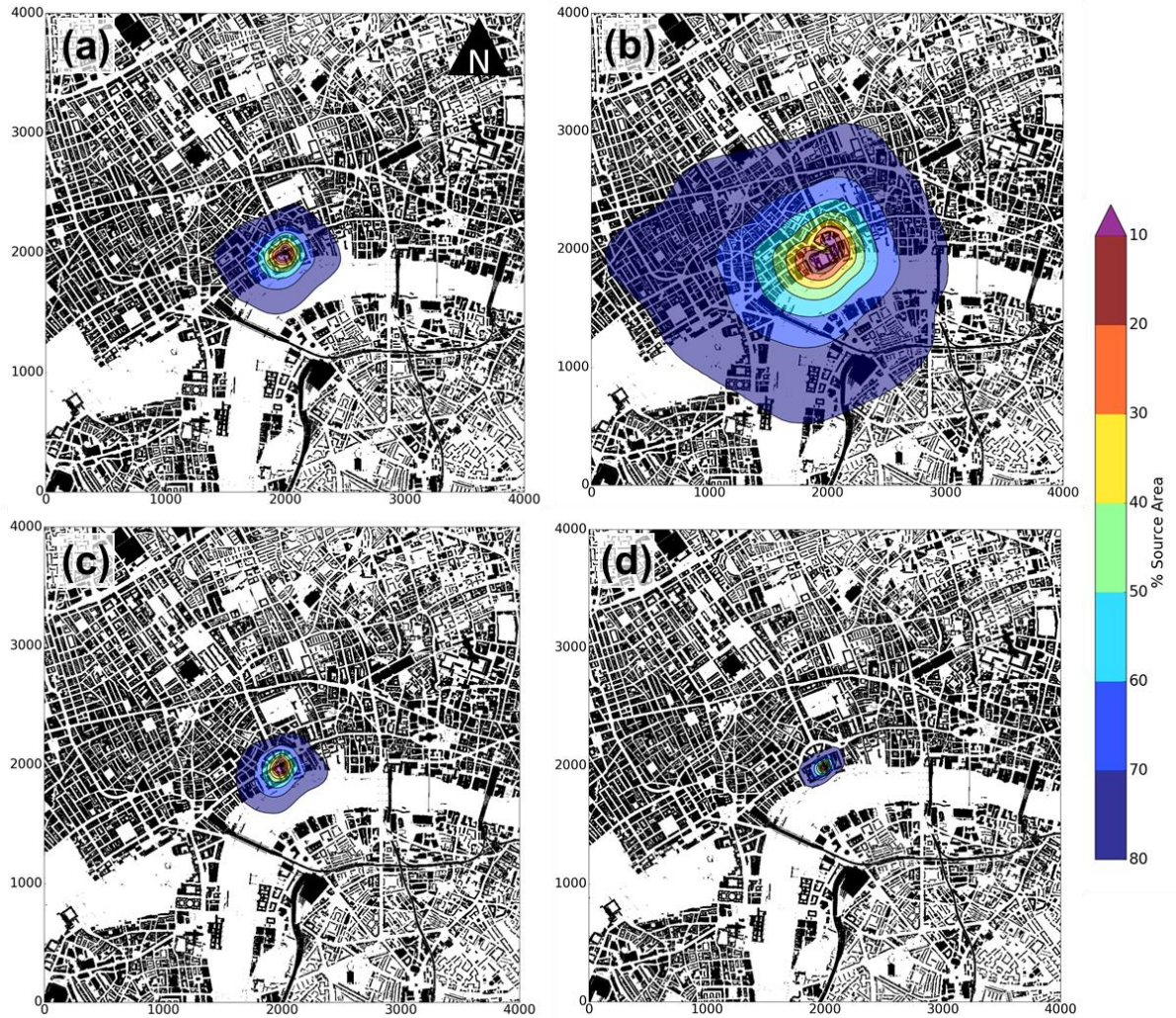


Figure 3.8: Integrated annual 80% source areas at the: (a, b) KSSW, (c) KSS and (d) KSK sites, normalised for the observation period (Table 3.3, from 30-min averaged observations, Sect. 3.3.2.2). Source areas are determined using the Kormann and Meixner (2001) analytical footprint model with aerodynamic parameters from the (a, c, d) *Mho* and (b) *Mac* morphometric methods. Cumulative source areas are shaded with 10% contours demarcated (black lines). Map units are metres

The surface characteristics weighted by the footprint climatology (Fig. 3.8, Table 3.4) are different to those of the unweighted surrounding 1-km radius (Table 3.3). The similar measurement heights at the KSSW and KSS sites implies that their footprint climatology characteristics are similar. In comparison, the lower siting of the KSK site causes a smaller source area (Fig. 3.8d), which is predominantly built and paved with only 0.7% water. A wide range of geometric parameters occur in the source areas (Table 3.4a), which modifies the ratio of the measurement height to roughness-element heights. The median H_{av} for all sites is approximately 23 m and roughness-element height varies between 9.2 m and 9.5 m (median σ_H). The smallest H_{av} recorded is 10 m, in which case measurement heights are $5H_{av}$ and likely above the RSL (Sect. 3.2.1). However, some source areas have $H_{av} = 30$ m, in which case measurements are at $z = 1.67H_{av}$ and therefore more likely influenced by roughness-element wakes.

The source areas modelled using the RE_{av} methods are larger than the RE_{var} methods because the greater zero-plane displacement of the latter leads to a smaller effective height of the measurements. For example, Mho_{z_d} is typically twice Mac_{z_d} and a comparison of the source areas modelled at the KSSW site using each respective method demonstrates this difference (Fig. 3.8a, b). The upwind distance contributing to the 80% cumulative source area is consistently over three times further in all directions for the Mac method. This influences the surface characteristics that are determined for the source area. For example, the parks to the south-west of the sites (Sect. 3.4.1) are not within the Mho method source area, but fall within the 80% of the Mac method, explaining the larger proportion of vegetated land cover (grass and trees) using the latter (Table 3.4b). Geometric parameters are also influenced, which subsequently influence morphometrically-determined aerodynamic parameters. For example, the larger source area modelled using aerodynamic parameters from the Mac method gives a relatively larger H_{max} and σ_H , but lower H_{av} , λ_p and λ_f than within the Mho method source area (Table 3.4a).

(a) Geometric parameters: median (min, max)						
Site	Morphometric method	H_{av} (m)	λ_p	λ_f	H_{max} (m)	σ_H (m)
KSSW	<i>Mho</i>	23.01 (9.80, 30.14)	0.42 (0.21, 0.90)	0.49 (0.12, 3.01)	52.11 (31.97, 184.73)	9.50 (4.71, 16.29)
	<i>Mac</i>	21.30 (9.30, 29.93)	0.40 (0.16, 0.79)	0.43 (0.04, 2.71)	77.80 (32.64, 184.73)	10.21 (4.53, 17.63)
KSS	<i>Mho</i>	23.41 (10.76, 30.74)	0.44 (0.25, 0.84)	0.48 (0.11, 2.80)	46.10 (34.42, 184.73)	9.22 (5.67, 13.96)
KSK	<i>Mho</i>	23.38 (18.38, 29.76)	0.55 (0.32, 0.99)	0.63 (0.19, 2.27)	39.51 (28.60, 184.73)	8.48 (3.66, 13.59)
(b) Surface Cover (%) for 80% source area						
Site		Built	Paved	Grass	Trees	Water
KSSW	<i>Mho</i>	42	48	3	1	6
	<i>Mac</i>	40	39	4	3	14
KSS	<i>Mho</i>	45	48	2	1	4
KSK	<i>Mho</i>	57	42	1	0	0

Table 3.4: Characteristics of the annual source area (80%) for each site (Fig. 3.8). **(a)** geometric parameters and **(b)** surface cover. See Tables 3.1 and 3.3 for measurement time periods and method/ geometry abbreviations

3.8 Conclusions

Morphometric and anemometric analysis of aerodynamic parameters for three adjacent sites in Central London give estimates of zero-plane displacement (z_d) between 5 and 45 m and aerodynamic roughness length (z_0) between 0.1 and 5 m. A source area footprint model (Kormann and Meixner 2001) is used to apply the morphometric methods in an iterative procedure. Although a first order estimate of z_d and z_0 is required, the final z_d and z_0 values are similar, independent of the initial estimation. This conclusion is true for another source area model (Kljun et al. 2015), indicating that an iterative procedure removes the need for initial site

specific values. This saves time and also ensures more appropriate values of the aerodynamic parameters and source area dimensions.

Two methods that rely on surface-layer scaling during unstable conditions, are used to determine z_d from observations (Rotach 1994, Toda and Sugita 2003). The methods, not obviously sensitive to the initial z_d used to define stability, agree that z_d is larger than the average roughness-element height (H_{av}) in the surrounding 1-km fetch. Although this conclusion is supported by the literature, previously these values have been considered unreasonably large (Grimmond et al. 1998, 2002, Feigenwinter et al. 1999, Kanda et al. 2002, Tsuang et al. 2003, Christen 2005, Chang and Huynh 2007).

Morphometric methods can be split into two types based on the attributes of roughness-element height used, i.e. the average height (RE_{av}) or the variability/ maximum height (RE_{var}). The zero-plane displacement determined by the RE_{var} methods is consistently larger than H_{av} and twice the magnitude of that from the RE_{av} methods, which is approximately $0.7H_{av}$. A simple doubling of z_d determined by a rule-of-thumb morphometric method that is based only upon average roughness-element height, brought values more in line with the z_d determined using the RE_{var} methods.

There is agreement between anemometric methods and the morphometric methods that consider height variability that z_d is larger than H_{av} . This conclusion is supported by numerical and physical experiments (e.g. Jiang et al. 2008, Hagishima et al. 2009, Zaki et al. 2011, Millward-Hopkins et al. 2011, Tanaka et al. 2011, Kanda et al. 2013) indicating the taller roughness elements in a heterogeneous mix exert a disproportionate amount of drag on the flow (Xie et al. 2008, Mohammad et al. 2015a) lifting the drag profile centroid (Jackson 1981) above $z = H_{av}$. The results verify Kanda et al.'s (2013) proposition that the maximum height (H_{max}) is a more suitable scaling parameter for z_d and the standard deviation of the roughness-element height (σ_H) (also used by Millward-Hopkins et al. 2011) is useful to parameterise roughness-element height heterogeneity. This conclusion has implications for the interpretation of output from anemometers (and potentially other meteorological sensors) in the heterogeneous urban environment. Sensors may need to be located higher above roughness elements to provide a local-scale (or neighbourhood), rather than micro-scale, measurement.

Morphometric-based z_0 are consistently larger than anemometric z_0 by 2 to 3 m. Although the two classes of morphometric methods (RE_{av} and RE_{var}) do not demonstrate an obvious difference for z_0 , root-mean-square error analysis demonstrates the RE_{var} methods are most

similar to observations. Individual RE_{av} methods consistently result in the largest (Bottema and Mestayer 1998) and smallest (Macdonald et al. 1998) z_0 values.

The ability of each method to correctly estimate wind speed with height is assessed using locally determined aerodynamic parameters and the logarithmic wind law. Wind speeds observed with Doppler lidar (up to 200 m above the canopy) are underestimated with the RE_{av} morphometric methods (median underestimation: 1.5 to 2.9 m s⁻¹ for average wind speeds: 10.4 – 11.4 m s⁻¹). Whereas, the larger z_d determined using the RE_{var} methods leads to estimates more similar to observations (median differences < 0.62 m s⁻¹), demonstrating the importance of considering roughness-element height heterogeneity when estimating the wind-speed profile.

The modelled eddy-covariance source area is typically a third (or smaller) of the size when the RE_{var} methods are used, as the effective measurement height (i.e. with z_d accounted for) tends to be half that of the RE_{av} methods. This has implications for land cover and geometric parameters determined for a source area and their subsequent uses.

The tools for morphometric determination of z_d and z_0 (including the two footprint models used) are available in the Urban Multi-Scale Environmental Predictor (UMEP, <http://www.urban-climate.net/umep/UMEP>, Lindberg et al. 2018) which is an extension to the open source geographical information software QGIS. A tutorial is available for new users (Appendix 3.D).

Appendix 3.A: Methods to calculate z_d and z_0 from the literature

(a) Morphometric method			
Reference		Background to method	
Kutzbach (1961)		Bushel baskets on frozen lake	
Lettau (1969)		Wind-tunnel and Kutzbach (1961) data	
Fang and Sill (1992)		Wind-tunnel experiments	
Kondo and Yamazawa (1986)		Two urban districts of Japan	
Counihan (1971)		Regular arrays of cubic blocks wind-tunnel data	
Theurer (1993)		Field experiments and wind-tunnel data	
*Raupach (1994) <i>Rau</i>		Wind-tunnel and rough vegetated surfaces data	
Bottema (1995, 1997)		Regular, staggered and varying density array of blocks wind-tunnel data	
*Bottema and Mestayer (1998) <i>Bot</i>		Simplification of Bottema (1995, 1997) for use in urban areas	
*Macdonald et al. (1998) <i>Mac</i>		From fundamental principles and wind-tunnel data (Hall et al. 1996)	
*Grimmond and Oke (1999) <i>RT</i>		Rule of thumb from synthesis of wind-tunnel and field results	
Kastner-Klein and Rotach (2004)		Scaled model of Nantes, France, wind-tunnel data	
Nakayama et al. (2011)		Large-eddy simulations (LES) using various building arrays	
Millward-Hopkins et al. (2011)		Quasi-empirical modelling and development of previous models	
*Millward-Hopkins et al. (2013a) <i>Mho</i>		Simplified Millward-Hopkins et al. (2011) using elevation data from Leeds, UK	
*Kanda et al. (2013) <i>Kan</i>		LES of explicitly resolved buildings in Tokyo, Japan	
(b) Anemometric method			
Method	Reference	Anemometric data required	Stability
<i>z₀</i>			
Standard deviation	Beljaars (1987)	Single level, fast or slow response	neutral
*Eddy-covariance	Grimmond et al. (1998) EC	Single level, fast response	neutral
<i>z_d</i>			
*Temperature variance	Rotach (1994) TVM	Single level, fast response	unstable
*Vertical wind variance	Toda and Sugita (2003) WVM	Single level, fast response	unstable
Spectral	Christen (2005)	Single level, fast response	neutral
<i>z₀ and z_d</i>			
Profile	Lettau (1957)	Profile, fast or slow response	neutral
Regressed profile	Schardt (1998)	Profile, fast or slow response	neutral
Least-squares	Martano (2000)	Single level, fast response	all

Table 3.A1: Methods in the literature (ordered by date) to calculate the zero-plane displacement (z_d) and aerodynamic roughness length (z_0) from **(a)** morphometric and **(b)** anemometric data with the stability conditions required. Methods used in this study are indicated (*) and have their abbreviation used in the Reference column

Appendix 3.B: Turbulence data at London sites

The directional variability of the drag coefficient (C_{DU}) and the horizontal, transverse and vertical turbulence intensities (TI_u , TI_v and TI_w , respectively) (Roth 2000) are assessed at the KCL sites (Fig. 3.B1 – 3.B3), with peaks indicating disturbance to flow (e.g. Barlow et al. 2009). The likely cause for disturbances are discussed in the main text (Sect. 3.4.2).

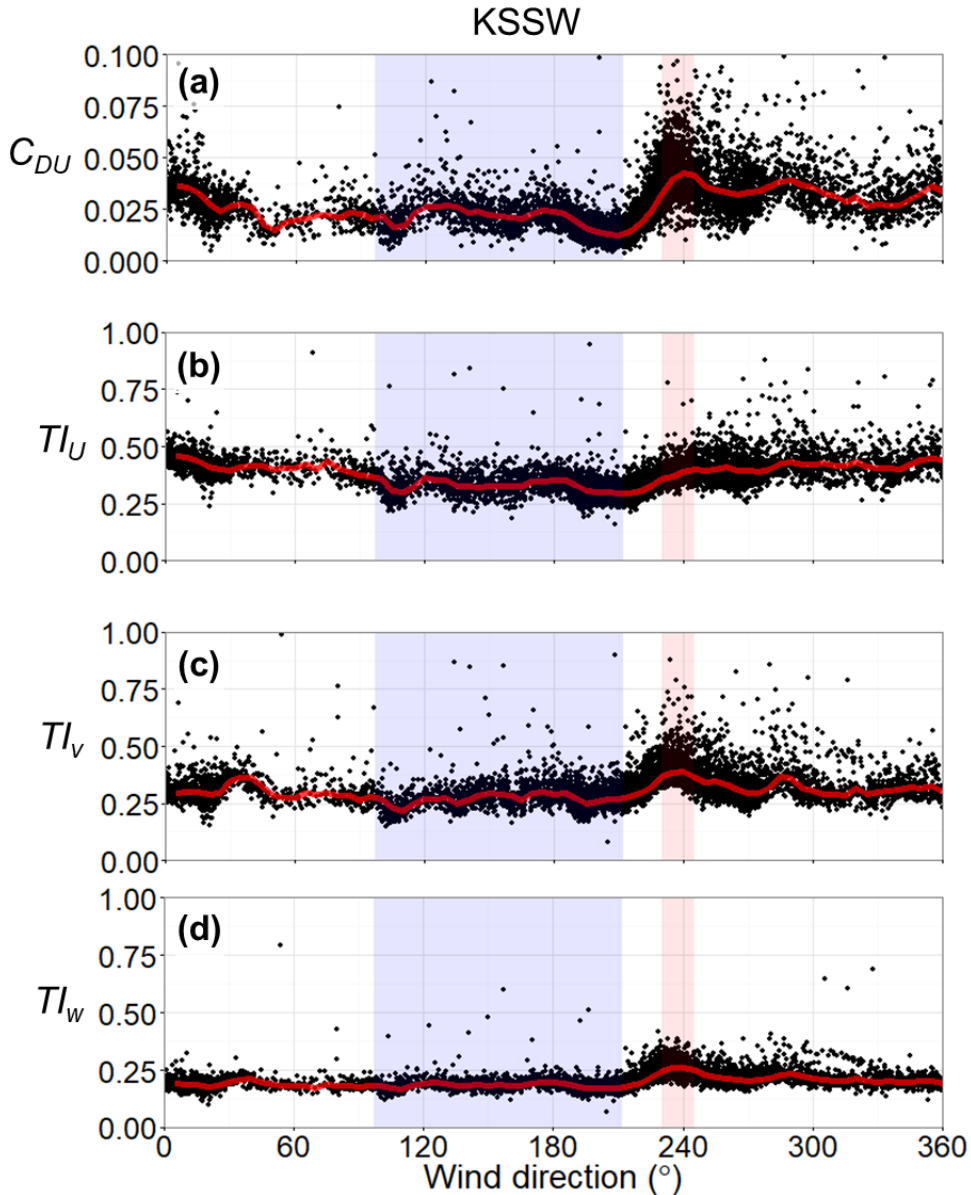


Figure 3.B1: (a) Aerodynamic drag coefficient ($C_{DU} = (u_*/\bar{U}_z)^2$), and turbulence intensities in the (b) longitudinal ($TI_u = \sigma_u/\bar{U}_z$), (c) transverse ($TI_v = \sigma_v/\bar{U}_z$) and (d) vertical ($TI_w = \sigma_w/\bar{U}_z$) wind directions, for all 30-min observations during neutral conditions (black dots) at the KSSW site. Neutral conditions are $|(z_m - z_d)/L| \leq 0.05$ (L is Obukhov length, $z_m = 50.3$ m and z_d is the average of the Millward-Hopkins (2011) and Kanda et al. (2013) morphometric methods for each time period (Fig. 3.5) (morphometric method z_d selected based upon wind-speed estimate accuracy, Fig. 3.7). The median for each 5° wind direction is shown (red line). \bar{U}_z is the average wind speed, u_* is the friction velocity and σ_u , σ_v , σ_w are the standard deviations of the longitudinal, transverse and vertical velocity components of the wind. Background shading is in directions where the River Thames is located (blue) and where turbulence data indicates disturbance (red)

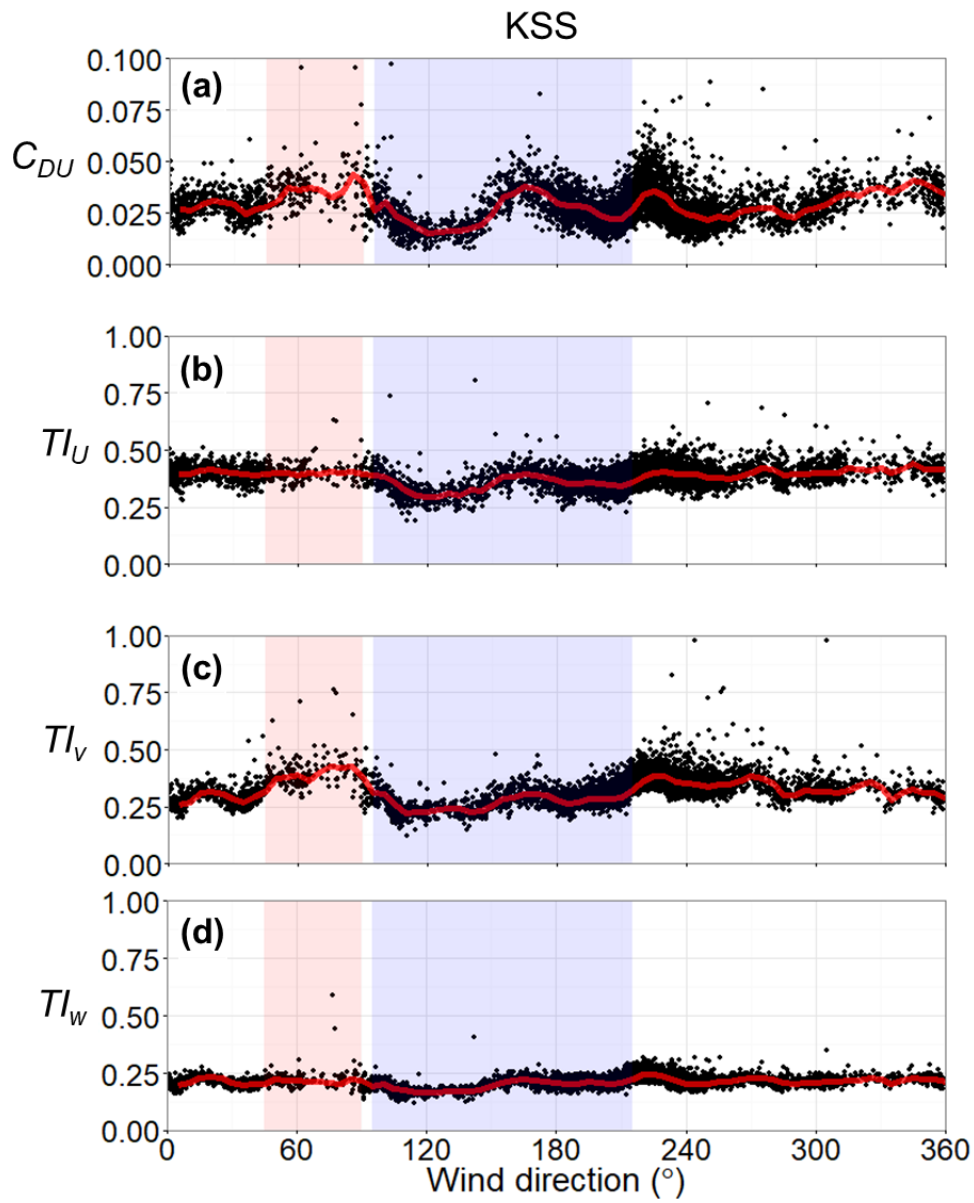


Figure 3.B2: As for Fig. 3.B1, but for the KSS site ($z_m = 48.9$ m)

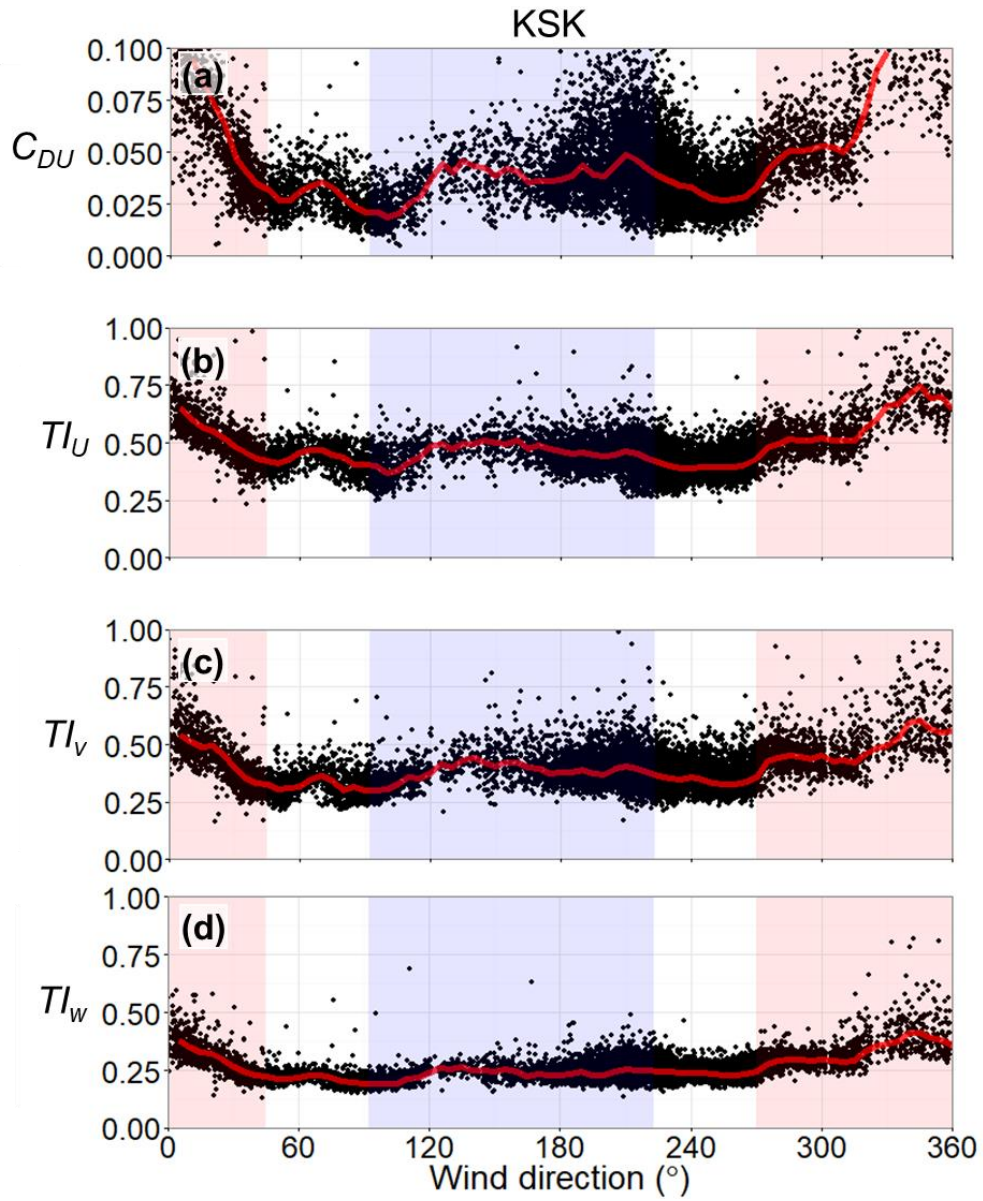


Figure 3.B3: As for Fig. 3.B1, but for the KSK site ($z_m = 38.8$ m)

Appendix 3.C: Sensitivity of source area model iterative procedure to initial estimates of z_d and z_0

The aerodynamic roughness parameters (z_d and z_0) are calculated with morphometric methods using a source-area weighted geometry (Sect. 3.4.3.3). However, initial estimates of the roughness parameters (i.e. Miz_d and Miz_0 in Fig. 3.3) are required to calculate the source area. Using the iterative procedure (Sect. 3.4.3.3) means the final z_d and z_0 results are insensitive to the initial estimates, therefore time does not need to be spent determining them (even 'open country' values can be used).

The insensitivity is demonstrated using the Kormann and Meixner (2001) source area model, with the meteorological inputs from the average of 30-min observations in 2014 at the KSSW site from the 000 – 045° wind direction: measurement height (z) = 50.3 m; standard deviation of the lateral wind velocity (σ_v) = 0.95 m s⁻¹; Obukhov length (L) = - 1075.55; friction velocity (u_*) = 0.46 m s⁻¹ and wind direction = 23.54°. The iterative procedure is initiated with a range of values for Miz_d (0.20 m to 40.20 m, in 2.00 m increments [$n = 21$]) and Miz_0 (0.03 m to 10.03 m in 0.50 m increments [$n = 21$]) (note the ranges begin from open country values), creating 441 combinations of values.

For all combinations of Miz_d and Miz_0 (Fig. 3.C1, blue dashed line) the solution for z_d and z_0 becomes similar (Fig. 3.C1, magenta line), regardless of morphometric method used. For example, after one iteration using the Kanda et al. (2013) morphometric method, the range is 11.3 m for z_d and 1.0 m for z_0 (equating to 31.9% of the mean of all iteration one solutions for z_d and 50% for z_0 , Fig. 3.C1a, b, cyan line). The range of results and percentage difference from the mean decrease as further iterations are performed. By the fourth iteration the range is 2.1 m for z_d and 0.3 m for z_0 (approximately 5% and 10% for the mean of all solutions, respectively).

The absolute range of solutions vary for each morphometric method (and therefore so do the percentage differences), but for each respective method the final solution for z_d and z_0 is always similar regardless of Miz_d and Miz_0 . For example, after four iterations using the Macdonald et al. (1998) morphometric method (Fig. 3.C1c, d) the range of z_d is 0.2 m and z_0 is 0.04 m (both are less than 3% of the mean of solutions for all Miz_d and Miz_0 combinations, respectively). For the other morphometric methods assessed (Table 3.1) the results have a range which is < 1 % of the mean of solutions for all Miz_d and Miz_0 combinations, respectively.

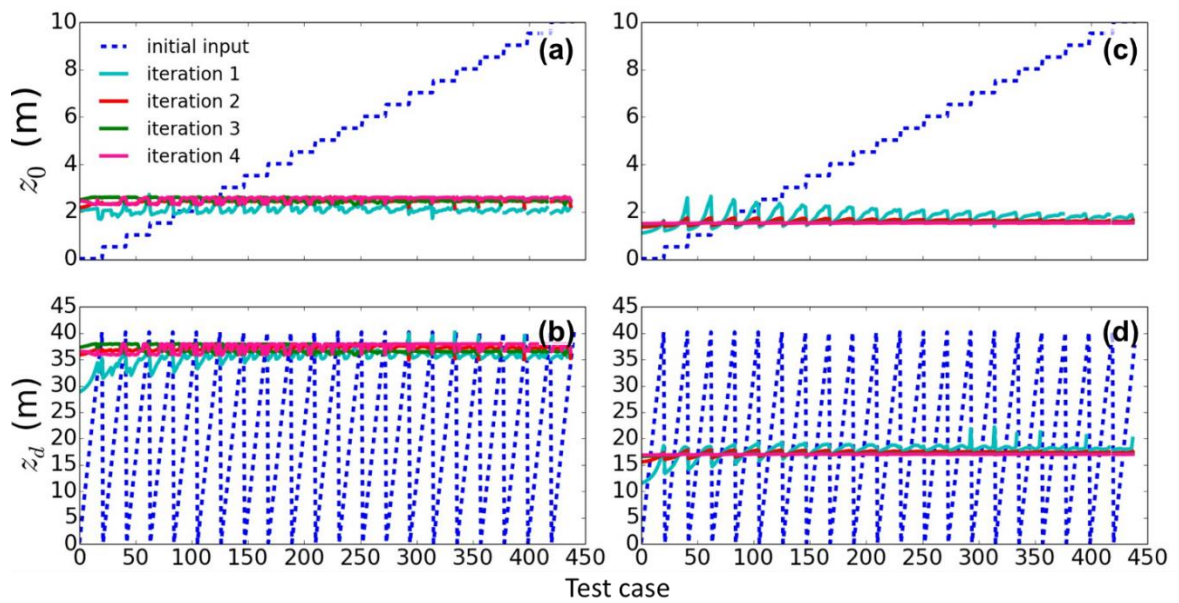


Figure 3.C1: Sensitivity to the initial zero-plane displacement (z_d) and aerodynamic roughness length (z_0) when using the iterative procedure (Sect. 3.4.3.3), with the Kormann and Mexiner (2001) source are model and **(a), (b)** Kanda et al. (2013) or **(c), (d)** Macdonald et al. (1998) morphometric methods. The initial range of z_d and z_0 'test cases' (initial input, blue dashed line: Miz_d and Miz_0 in Fig. 3.3) is shown with the z_d and z_0 result of each test case, after each iteration. See text for meteorological input and 'Test case' parameter selection

The consistency of this finding is demonstrated by applying the iterative procedure for all 30-min observations in 2014 at the KSSW site. The procedure is initiated with Miz_d and Miz_0 : (i) first-order estimates using a linear weighting procedure (Sect. 3.4.3.3) (i.e. retaining steps M_1 and M_2 in Fig. 3.3) (Fig. 3.C2, gold points); and (ii) as open country values (i.e. $z_d = 0.2$ m and $z_0 = 0.03$ and steps M_1 and M_2 in Fig. 3.3 are omitted) (Fig. 3.C2, red points). The average error between the roughness parameter solutions from using first-order estimated or open country values is 0.14 m for z_d and 0.1 m for z_0 . This is < 1% and < 5% of the average z_d and z_0 solutions across all directions, respectively, using first-order estimates for Miz_d and Miz_0 .

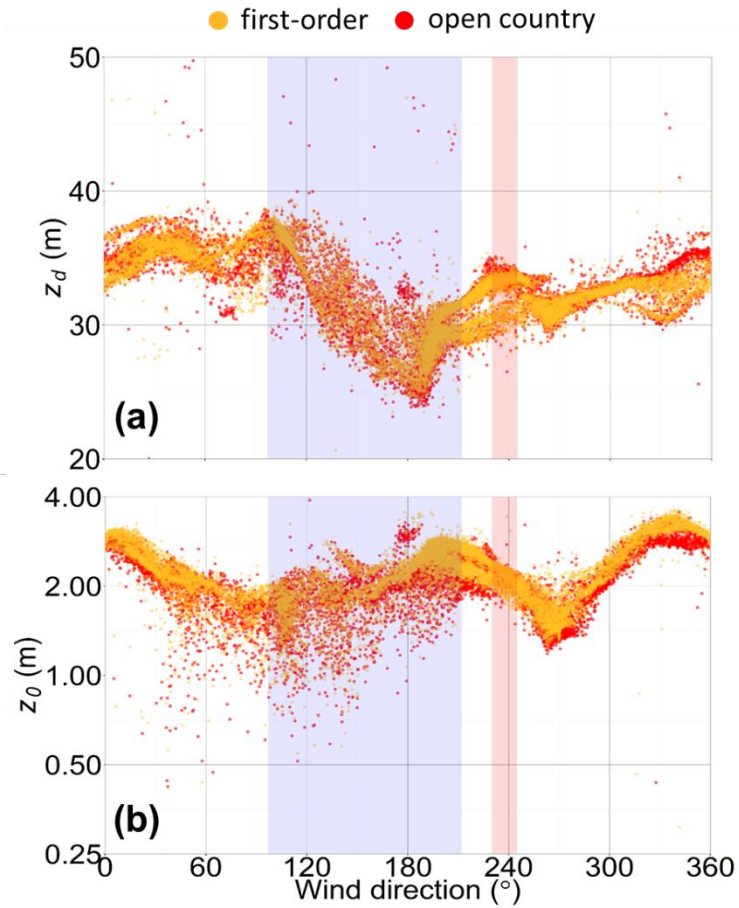


Figure 3.C2: Solution of iterative procedure (Sect. 3.4.3.3) for **(a)** zero-plane displacement (z_d) and **(b)** aerodynamic roughness length (z_0) (note ln y axis) for all 30-min observations in 2014 at the KSSW site. Roughness parameters are calculated using the Kanda et al. (2013) morphometric method and the iterative procedure is initiated with roughness parameters (i.e. Miz_d and Miz_0 in Fig. 3.3) from: (i) first-order estimates (gold points), or (ii) open country values (red points). Background shading: directions of River Thames (blue) and where turbulence data indicates disturbance (red).

Appendix 3.D: Tutorial for using the source area footprint model for roughness calculations in UMEP

UMEP (Urban Multi-scale Environmental Predictor) is a community developed open-source application (i.e. plug-in) for the geographical information software, QGIS. As an urban climatology tool designed for both researchers and service providers, UMEP's applications range from outdoor thermal comfort through to climate change mitigation (Lindberg et al. 2018). Several developments were made to UMEP as part of this PhD, including: determination of urban morphology parameters and associated z_d and z_o (using surface elevation databases) with the morphometric methods applied (Sect. 3.3.3) and option to include vegetation (see Chapters 5 and 6); implementation of the 'source area model' tool with two footprint models available (Kormann and Meixner 2001, Kljun et al. 2015) to obtain source area weighted roughness parameters (Sect. 3.4.3.3). A manual for UMEP is available online, specifically for operation of the source area model tool see: http://www.urbanclimate.net/umep/UMEP_Manual#Urban_Morphology:_Source_Area_.28Point.29UMEP. Tutorials of the different UMEP tools are available for new users, the source area model tool tutorial is provided here (available online: http://www.urban-climate.net/umep/UMEP/_Tutorials/_Footprint).

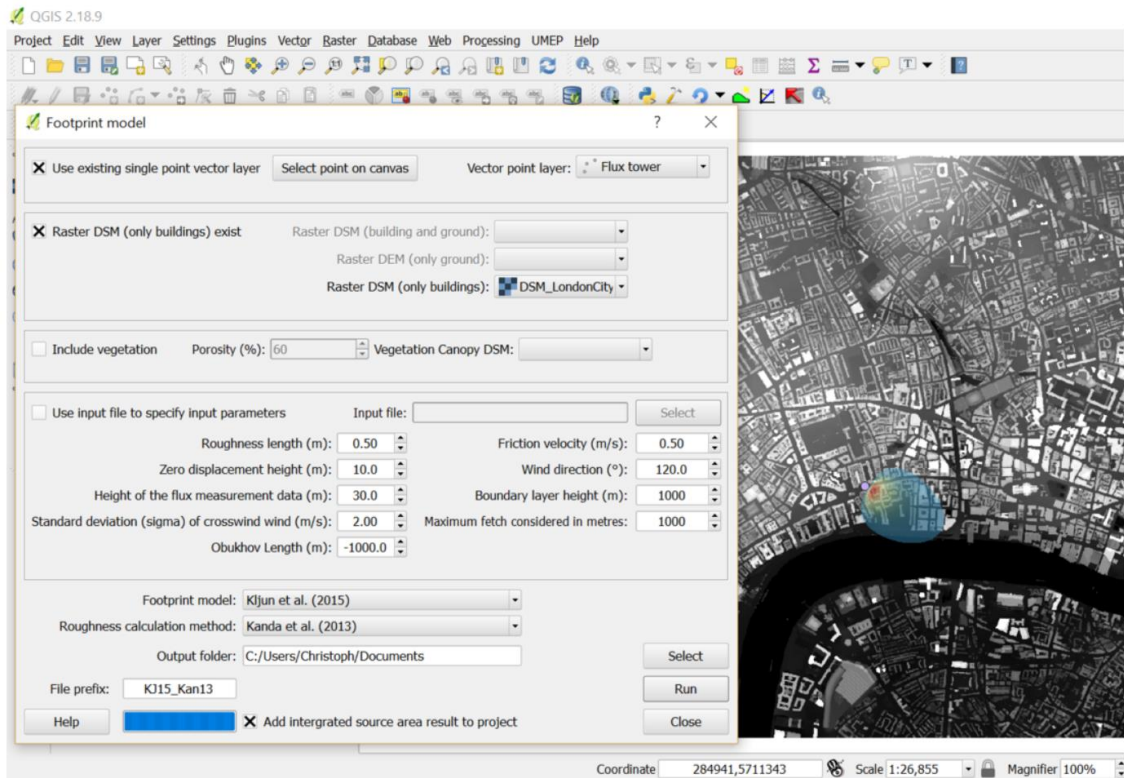
UMEP/ Tutorials/ Footprint

Contents [hide]	
1	Introduction
2	Initial Practical steps
2.1	Data for Tutorial
3	Prior to Starting
4	Source Area Modelling
5	Iterative process
5.1	Roughness parameters
6	Questions for you to explore with UMEP: Source Area
7	References
7.1	Contributors to the material covered

Introduction [edit]

Each meteorological instrument has a '*source area*' (sometimes referred to as *footprint*), the area that influences the measurement. The shape and location of that area is a function of the meteorological variable the sensor measures and the method of operation of the sensor.

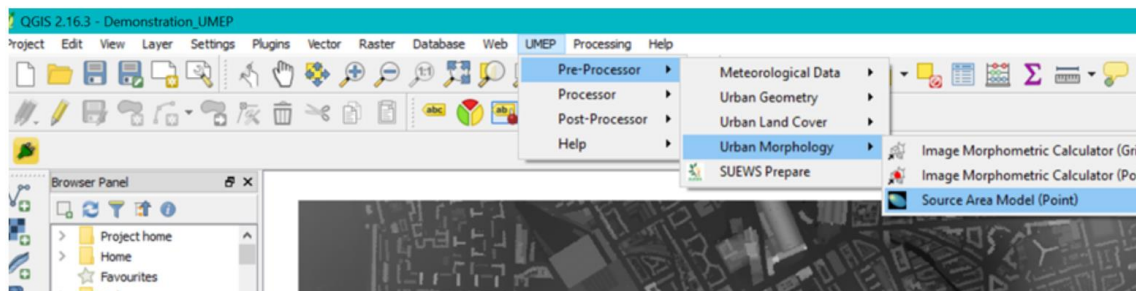
For turbulent heat fluxes measured with a sonic anemometer, extensive effort has been directed to try and model the 'probable source area location' (Leclerc and Foken 2014). Numerous models exist, but the Kormann and Meixner (2001) and Kljun et al. (2015) models are used in UMEP. Both models require input of information about the wind direction, stability, turbulence characteristics (friction velocity, variance of the lateral or crosswind wind velocity) and roughness parameters. Kljun et al. (2015) requires the boundary layer height.



Initial Practical steps

- If **QGIS** is not on your computer you will [need to install it](#)
- Then install the [UMEP plugin](#)
- Start the QGIS software
- If not visible on the desktop use the **Start** button to find the software (i.e. Find QGIS under your applications)
- Select **QGIS 2.16.3 Desktop** (or the latest version installed)

When you open it on the top toolbar you will see **UMEP**.



- If UMEP is not on your machine, download and install the [UMEP plugin](#)
- Read through the section in the [online manual](#) BEFORE using the model, so you are familiar with its operation and terminology used.

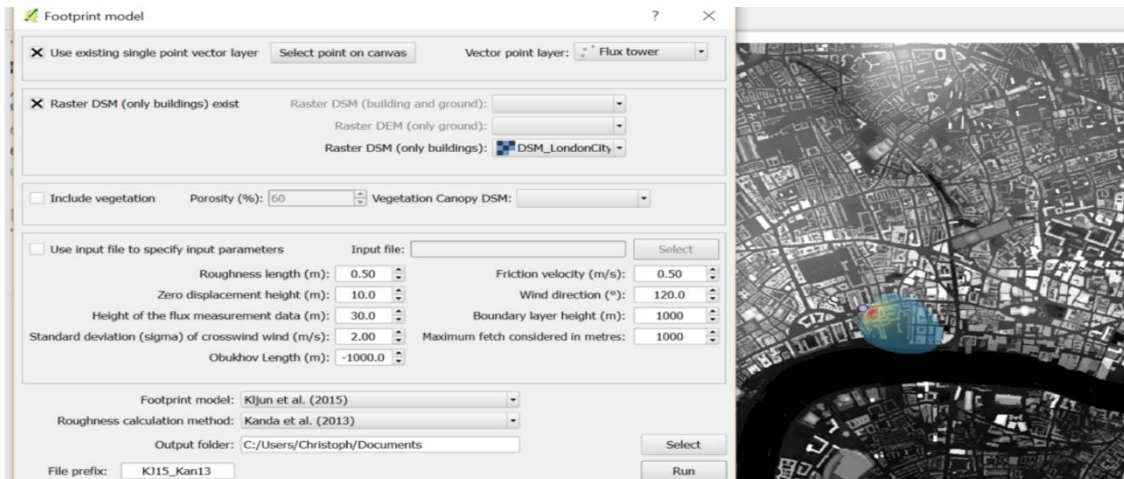
Data for Tutorial

Use the appropriate data

a) Reading -- [Download BB - week 5](#) or [here](#)

b) London - [download](#)

To get the Password if not given it already



Source Area Modelling

1. To access the Source area model or Footprint model:

- UMEP -> Pre-processor > Urban Morphology > Source Area Model (Point) [this appears like this](#)

Image	Steps
	<ol style="list-style-type: none"> 1. Click on <i>Select Point on Canvas</i> – then select a point (e.g. where an Eddy Covariance (EC) tower site is located) 2. Select the appropriate surface elevation data file names 3. Choose the model you wish to run (Kormann and Meixner 2001 or Kljun et al. 2015) 4. Some initial parameters values are given - think about what would be appropriate values for your site and period of interest. The manual has more information (e.g. definitions) of the input variables. <ul style="list-style-type: none"> • The values are dependent on the meteorological conditions and the surface surrounding the site. The former obviously vary on an hour to hour basis (or shorter time periods), whereas the others are dependent on the wind direction and the fetch characteristics. 5. Add a prefix and an output folder. 6. Tick “add the integrated source area to your project”. This will provide visual information of the location of the source area (footprint) 7. Run - If you get an error/warning message (model is unable to execute your request - as the <i>maximum fetch exceeds the extent of your grid</i> for your point of interest. measure the distance to the limit of your raster maps <ul style="list-style-type: none"> • To allow the model to work for the dataset with your point of interest you need to adjust the maximum fetch distance. • Locate the Measure tool. • Measure the distance to the point of interest to the boundary of the DSM data set. • Adjust the maximum fetch. • Click Run and wait for the calculations to finish. <p>The output is a source area grid showing the cumulative percentage of source area influencing the flux at the point of interest.</p>

The **output is a source area** grid showing the cumulative percentage of source area influencing the flux at the point of interest.

- To *display the legend*: Double-click on the source area grid and then click **OK** without doing any changes. The source area display is showing up to 98 % of the cumulative area.
- Other output: A **text file** giving both the input setting variables and the output morphometric parameters calculated based on the source area generated. More information is provided in the manual, row titled: "Output" [↗](#)

It is possible to **input a text file** to generate a source area based on morphometric parameters (e.g. an hourly dataset). However, for now you can modify the input variables set in the interface. Format of file is given in the [manual](#) [↗](#).

Iterative process

To work with a site with no value known *a priori*.

1. Use the [Image Morphometric](#) [↗](#) Parameters Calculator (Point) tool in the UMEP plugin to select a point to get the initial parameter values:
 1. UMEP-> Pre-Processor -> Urban Morphology -> Image Morphometric Calculator
 2. Open the output files
2. **Anisotropic** file – has the values in, e.g., 5 degree **sectors** – i.e. what you selected. This is appropriate if the area is very inhomogeneous.
3. **Isotropic** file - has the **average value** for the area
4. Use these values to populate the source area model window.

Roughness parameters

In the UMEP plugin the roughness length and zero plane displacement length can be calculated with a morphometric method based on the Rule of Thumb (Grimmond and Oke 1999) as the default. There are other methods available: Bottema (1995), Kanda et al. (2013), Macdonald et al. (1998), Millward-Hopkins et al. (2011) and Raupach (1994, 1995). Many of these have been developed for urban roughness elements. The Raupach method was originally intended for forested areas but has also been found to perform well for urban areas.

With wind profile and eddy covariance anemometric data and the source area model, appropriate parameters can be determined and morphometric methods assessed.

Questions for you to explore with UMEP: Source Area

1. What is the impact of the atmospheric and surface characteristics on the source area dimensions?
2. How do the source area characteristics vary for different sensor levels for the wind profile?

Potential Projects

1. How do the morphometric roughness methods compare with values obtained in the observatory? What is the influence of vegetation state?
2. Does wind direction impact the choice of the most appropriate method?
3. What is the difference in source area with models?
4. What inputs are the respective models most sensitive to?

References

- Bottema M 1995: Parameterisation of aerodynamic roughness parameters in relation to air pollutant removal efficiency of streets. Air Pollution Engineering and Management, H. Power et al., Eds., Computational Mechanics, 235–242.
- Grimmond CSB and TR Oke 1999: Aerodynamic properties of urban areas derived, from analysis of surface form. [Journal of Applied Climatology](#) 38:9, 1262-1292 [↗](#)
- Kanda M, Inagaki A, Miyamoto T, Grysckha M, Raasch S 2013: A new aerodynamic parameterization for real urban surfaces. [Boundary- Layer Meteorol](#) 148:357–377. doi:10.1007/s10546-013-9818-x [↗](#)
- Kljun N, Calanca P, Rotach MW, Schmid HP 2015: A simple two-dimensional parameterisation for Flux Footprint Prediction (FFP). [Geoscientific Model Development](#) 8(11):3695-713. [↗](#)

- Kormann R, Meixner FX 2001: An analytical footprint model for non-neutral stratification. *Bound.-Layer Meteorol.*, 99, 207–224 <http://www.sciencedirect.com/science/article/pii/S2212095513000497#b0145>
- Kotthaus S and Grimmond CSB 2014: Energy exchange in a dense urban environment – Part II: Impact of spatial heterogeneity of the surface. *Urban Climate* 10, 281–307 <http://www.sciencedirect.com/science/article/pii/S2212095513000497>
- Leclerc MY and Foken TK 2014: Footprints in Micrometeorology and Ecology. *Springer*, xix, 239 p. E-book
- Macdonald, R. W., R. F. Griffiths, and D. J. Hall, 1998: An improved method for estimation of surface roughness of obstacle arrays. *Atmos. Environ.*, 32, 1857–1864
- Millward-Hopkins JT, Tomlin AS, Ma L, Ingham D, Pourkashanian M 2011: Estimating aerodynamic parameters of urban-like surfaces with heterogeneous building heights. *Boundary-Layer Meteorol* 141:443–465. doi:10.1007/s10546-011-9640-2
- Raupach MR 1994: Simplified expressions for vegetation roughness length and zero-plane displacement as functions of canopy height and area index. *Bound.-Layer Meteor.*, 71, 211–216. doi:10.1007/BF0070922
- Raupach MR 1995: Corrigenda. *Bound.-Layer Meteor.*, 76, 303–304.

Contributors to the material covered [\[edit\]](#)

University of Reading: Christoph Kent, Simone Kotthaus, Sue Grimmond **University of Gothenburg:** Fredrik Lindberg Background work also comes from: UBC (Andreas Christen); Germany: Kormann and Meixner (2001); Japan: Kanda et al. (2013); UK: Millward-Hopkins et al. (2011), Macdonald et al. (1998); Australia: Raupach (1994, 1995); Netherlands: Bottema (1995)

Authors of this document: Kent, Grimmond (2016). Lindberg

Chapter 4. Assessing methods to extrapolate the vertical wind-speed profile from surface observations in a city centre during strong winds¹

Abstract Knowledge of the vertical wind-speed profile in cities is important for the construction and insurance industries, wind energy predictions, and simulations of pollutant and toxic gas release. Here, five methods to estimate the spatially- and temporally- averaged wind-speed profile are compared in London: the logarithmic wind law (*LOG*); the Deaves and Harris equilibrium (DH_e) and an implementation of the non-equilibrium (DH_v) model; an adaptation of the power law (*PL*) and the Gryning et al. (*GR*) profile. Using measurements at 2.5 times the average building height, a source area model is used to determine aerodynamic roughness parameters using two morphometric methods, which assume homogeneous and variable roughness-element heights, respectively. Hourly-averaged wind speeds are extrapolated to 200 m above the canopy during strong wind conditions, and compared to wind speeds observed with Doppler lidar. Wind speeds are consistently underestimated if roughness-element height variability is not considered during aerodynamic parameter determination. Considering height variability, the resulting estimations with the DH_e and *GR* profiles are marginally more similar to observations than the DH_v profile, which is more accurate than the *LOG* and *PL* methods. An exception is in directions with more homogeneous fetch and a gradual reduction in upwind roughness, where the *LOG* and *PL* profiles are more appropriate.

4.1 Introduction

Modelling the wind-speed profile in the lowest few hundred metres of the urban boundary layer (UBL) is becoming increasingly important. The rapid development of urban areas is resulting in taller buildings with unique forms and arrangements which the construction and insurance industries need to account for (Petrini and Ciampoli 2012, Tanaka et al. 2012, Taranath 2016). The threat of pollutant and hazardous material release (accidental and terror related) is increasingly being realised (Belcher 2005, Tominaga and Stathopoulos 2016), and widespread city-based renewable wind energy is being explored (Millward-Hopkins et al. 2013b, Ishugah et al. 2014, Emejeamara et al. 2015). Accurate vertical profiles of wind speed are essential boundary conditions to physical (i.e. wind tunnel) and numerical (e.g. computational fluid

¹ This chapter is published as: **Kent CW**, Grimmond CSB, Gatey D, Barlow JF (2018a) *Assessing methods to extrapolate the vertical wind-speed profile from surface observations in a city centre during strong winds*. *Journal of Wind Engineering and Industrial Aerodynamics* 173:100-111.

dynamics) models, as the final results are sensitive to these initial conditions (e.g. Schultz et al. 2005, Ricci et al. 2016). Critical questions which remain include: how well can the spatially- and temporally- averaged urban boundary layer winds be estimated, what are the minimum input requirements, and what are the associated uncertainties?

Over flat, homogeneous terrain with extensive fetch, a dynamic equilibrium between strong winds and the surface roughness is reached, which is well understood and modelled quantitatively (Harris and Deaves 1980). However, flat homogeneous fetch is rare in urban areas. There are often distinct changes in surface cover in close proximity, characterised by different land cover types and roughness elements of different form (e.g. height variability, density). The structure of the UBL is therefore highly variable because of the numerous sources and sinks of heat and momentum (Gryning et al. 2011), which means that modelling the wind-speed profile is challenging.

The UBL is traditionally divided into several distinct layers (e.g. Sect. 2.1 and Fernando 2010, his Fig. 9), the location of which is determined by surface morphology and mesoscale conditions (Barlow 2014). The urban canopy layer (UCL) is where surface roughness elements such as buildings are located (Oke 2007) and is associated with highly variable flow. The UCL is within the roughness sublayer (RSL) (Roth 2000), the depth of which is typically 2 to 5 times the average roughness-element height (H_{av}) (Roth 2000, Barlow 2014), varying with the roughness-element density (Raupach et al. 1991, Grimmond and Oke 1999, Roth 2000, Oke 2007, Barlow 2014), staggering (Cheng and Castro 2002) and height variability (Cheng and Castro 2002). Between the RSL and approximately 10% of the boundary layer depth is the inertial sublayer (ISL), where the flow becomes free of the wakes associated with individual roughness elements. If the airflow is fully adapted to upwind roughness elements in the ISL, a horizontally homogeneous flow is observed (Barlow 2014) and it is therefore possible to determine a spatially- and temporally- averaged wind-speed profile.

This Chapter assesses how well the wind-speed profile can be modelled using surface observations at a reference site in central London, United Kingdom. The aerodynamic roughness parameters of the zero-plane displacement (z_d) and aerodynamic roughness length (z_0) are determined using two morphometric methods (i.e. from surface geometry). One morphometric method assumes homogeneous roughness elements (Macdonald et al. 1998, *Mac*), the other considers their height variability (Kanda et al. 2013, *Kan*). Five different methods are then used to extrapolate the wind speed to 200 m above the canopy. These wind speeds are compared to those observed using Doppler lidar.

Specifically, the methods considered are: the logarithmic wind law (Blackadar and Tennekes 1968) (*LOG*); the Deaves and Harris equilibrium (DH_e) and non-equilibrium (DH_v) models (Deaves and Harris 1978, Harris and Deaves 1980); an adapted power law which directly considers surface roughness (Sedefian 1980) (*PL*) and a profile proposed by Gryning et al. (2007) (*GR*) (see Sect. 4.2 for the selection of methods). Analysis is undertaken for neutral conditions, to allow the accuracy of extrapolated profiles during 'ideal' conditions to be understood first, without the additional uncertainties associated with thermal effects (e.g. Högström 1996 and Table 2.1).

4.2 Describing the boundary layer wind speed using surface observations

In addition to the models named above, other methods to describe the spatially- and temporally- averaged wind-speed profile have been derived (Wieringa 1986, Etling 2002, Wilson and Flesch 2004, Emeis et al. 2007, Peña et al. 2010, Yang et al. 2016). Wieringa's (1986) two-layer model requires definition of the height above which the logarithmic wind law (*LOG*) becomes inappropriate. Given that it is both difficult to determine this height in the UBL (e.g. Roth 2000, Barlow 2014) and the performance of the *LOG* method is assessed in this study, Wieringa's (1986) method and the two-layer model of Wilson and Flesch (2004) are not considered here. Emeis et al. (2007) developed Etling's (2002) multi-layer model to incorporate the effects of atmospheric stability. As with Wieringa's (1986) model, the applicable height range of *LOG* is required. Additionally, the method requires the geostrophic wind speed (as well as surface measurements) and is therefore not considered here. For similar reasons, the Yang et al. (2016) model is not considered. Peña et al. (2010) use Gryning et al.'s (2007) mixing length model with a variety of mixing length parameterisations. However, there is no conclusive evidence that any of the assessed parameterisations provide improved accuracy for wind-speed estimation, therefore only the original formulation of Gryning et al. (2007) is used. Methods allowing roughness parameters to vary as a function of height (with associated fetch variability) in the wind-speed profile have been proposed (e.g. Millward-Hopkins et al. 2013b, 2013c). A similar procedure is applied during this work, which uses a source area footprint model to consider the probable upwind area influencing measurements throughout the profile, as well as the implications of upwind roughness change (e.g. Sect. 4.2.3.2)

For simplicity, the following assumptions are typically made when modelling the neutral wind-speed profile in the atmospheric boundary layer (e.g. Garratt 1992 and Sect. 2.2.2): (i) stationarity, (ii) horizontal homogeneity, (iii) a barotropic atmosphere, where density is a function of pressure only, and (iv) uniform roughness with an extensive fetch and no subsidence,

therefore there is no mean vertical component of the wind. These assumptions are inherent in each of the five methods assessed here, however DH_v does not assume uniform upwind roughness (assumption iv).

Observations of the vertical wind profile are becoming increasingly available in urban areas (e.g. Tamura et al. 2001, Allwine et al. 2002, Emeis 2004, Frehlich et al. 2006, Emeis et al. 2007, Drew et al. 2013b, Tan et al. 2015, J. Liu et al. 2017). Especially because remote sensing techniques, such as lidar and sodar, overcome the impracticalities associated with *in-situ* tower mounted (Al-Jiboori and Fei 2005) or tetheredsonde (Tsuang et al. 2003) observations. Lidar is often favoured to sodar in urban areas, due to the noisiness of the latter. However, both have been used to assess the structure of the UBL (Barlow et al. 2008, Barlow et al. 2011) and associated wind flow (Drew et al. 2013b, Lane et al. 2013, Wood et al. 2013, Sect. 3.6). Specifically in London, wind speeds observed with Doppler lidar have been used to assess how accurately wind speeds can be: translated from a ‘rural’ airport site to central London (Drew et al. 2013b); and, estimated using the logarithmic wind law extrapolated from observations at approximately 2.5 times the canopy height, using a range of methods to determine z_d and z_0 (Sect. 3.6). Here this work is further developed by considering wind directions with a more complex fetch, as well as different methods to extrapolate the wind-speed profile. A source area footprint model is used to estimate the upstream effective roughness.

4.2.1 The logarithmic wind law

The logarithmic wind law (*LOG*), may be derived through: (i) matching a region where the velocity gradients determined from equations obeying the upper and lower boundary conditions of ABL flow are the same (also termed asymptotic similarity theory); or (ii) eddy viscosity, or k-theory. The derivation demonstrates that for a height, z , if the flow is aligned to the wind direction, the mean wind speed \bar{U}_z during neutral atmospheric stability can be determined by (Blackadar and Tennekes 1968, Tennekes 1973):

$$\bar{U}_z = \frac{u_*}{\kappa} \ln \left(\frac{z - z_d}{z_0} \right) \quad (4.1)$$

where u_* is the friction velocity and κ is von Karman’s constant. Following full scale field observations which indicate $\kappa = 0.38 - 0.42$ and scaled experiments in wind tunnels indicating $\kappa = 0.4$ (Garratt 1992), a value of $\kappa = 0.4$ is used in this work. The zero-plane displacement (z_d) is the vertical displacement of the wind-speed profile due to surface roughness elements and has been demonstrated to correspond to the ‘drag centroid’ of the surface, or the height at which mean drag appears to act (Jackson 1981). The aerodynamic roughness length (z_0) is the height at which wind speed becomes zero in the absence of z_d . Theoretically, *LOG* applies in the ISL,

where flow is free from individual roughness-element wakes, but still scales with surface length scales only (z_d and z_0). However, it has been shown to be applicable both close to roughness elements (Cheng and Castro 2002) and for a considerable depth of the boundary layer (Macdonald et al. 2000, Castro et al. 2006, Cheng et al. 2007, Sect. 3.6)

4.2.2 Adapted power law profile

The power law provides a relation between mean wind speeds ($\bar{U}_{z_1}, \bar{U}_{z_2}$) at two different heights (z_1, z_2), with a wind shear exponent (α_{PL}) describing fetch characteristics:

$$\bar{U}_{z_1} = \bar{U}_{z_2} \left(\frac{z_1 - z_d}{z_2 - z_d} \right)^{\alpha_{PL}} \quad (4.2)$$

The exponent, α_{PL} (between 0 and 1), provides a best fit of wind speeds between the two heights and is proportional to the vertical gradient of wind speed with height. Typically, a single value of α_{PL} is used for different surfaces (e.g. Davenport 1960), which does not allow the exponent to vary with height, stability or directly consider surface roughness (Irwin 1979, Emeis 2014). Sedefian's (1980) alteration of the exponent addresses this, and is used here:

$$\alpha_{PL} = \frac{\phi_m \left(\frac{\bar{z}}{L} \right)}{\left[\ln \left(\frac{\bar{z}}{z_0} \right) - \Psi_m \left(\frac{\bar{z}}{L} \right) \right]} \quad (4.3)$$

The \bar{z} is the geometric mean of the height layer considered, $\bar{z} = [(z_1 - z_d)(z_2 - z_d)]^{0.5}$. ϕ_m and Ψ_m are empirical stability functions (which depend upon the Obukhov length, L). The formulation in Eq. 4.3 allows the exponent to increase with surface roughness (z_0), decrease with increasing height (i.e. as z_2 increases) and incorporate thermal effects upon the vertical wind-speed profile. However, Eq. 4.3 can only be used where surface layer scaling (i.e. use of z_d , z_0 and L) is appropriate. During the neutral conditions considered here, the ϕ_m and Ψ_m functions equate to 1 and 0, respectively.

The mathematical simplicity of the *PL* and limited data requirements are advantageous, given it is observed to provide reasonable estimates of wind speeds between ~30 – 300 m (Counihan 1975, Segal and Pielke 1988, Zoumakis 1993, Cook 1997, Li et al. 2010), especially during strong wind conditions (Emeis 2014). It therefore provides the basis for building codes in numerous countries (e.g. China, Japan, Canada, United States) (Ge et al. 2013).

4.2.3 The Deaves and Harris profile

By considering the modulus of mean geostrophic wind speed and its ageostrophic counterpart in the ABL, Deaves and Harris (1978) and Harris and Deaves (1980) describe an adapted similarity theory from that used to derive *LOG*. The 'equilibrium model' (DH_e) is based upon an extensive

uniform fetch (Deaves and Harris 1978). However, a ‘non-equilibrium model’ (DH_v) is developed to include upwind fetch variability (Deaves 1981). Both methods are specifically designed for strong wind conditions, defined by wind speeds greater than 10 m s^{-1} measured at 10 m.

4.2.3.1 Equilibrium model

For an extensive homogeneous fetch, DH_e is described by (Deaves and Harris 1978, Harris and Deaves 1980):

$$h = \frac{1}{\beta} \frac{u_*}{f} \quad (4.4)$$

$$\bar{U}_z = \frac{u_*}{\kappa} \left[\ln \left(\frac{z - z_d}{z_0} \right) + 5.75 \left(\frac{z - z_d}{h} \right) - 1.88 \left(\frac{z - z_d}{h} \right)^2 - 1.33 \left(\frac{z - z_d}{h} \right)^3 + 0.25 \left(\frac{z - z_d}{h} \right)^4 \right] \quad (4.5)$$

where h is the gradient height, defined as the height where atmospheric flow is free from surface stresses and becomes geostrophic, f is the Coriolis parameter ($f = 2\Omega \sin\Phi$, with Ω the Earth’s angular velocity, $7.29 \times 10^{-5} \text{ rad s}^{-1}$, and Φ the latitude) and $\beta = 6$ is an empirically determined constant from experimental profiles over sites with flat, homogeneous terrain. The values preceding the four latter terms in Eq. 4.5 are also empirical constants, selected to give a parabolic velocity defect law for a substantial portion of the ABL (i.e. the wind-speed gradient increases with increasing height) (Deaves and Harris 1978). The law provides an empirically based polynomial extension of the vertical range of *LOG* to a height where flow is free from surface stresses (i.e. at the gradient height, h). For the lowest ~ 200 m of the boundary layer, Harris and Deaves (1980) note that the last three terms of Eq. 4.5 can be neglected, compromising only 1% accuracy. However, all terms are considered during this analysis for completeness.

4.2.3.2 Non-equilibrium model

The non-equilibrium model (DH_v) is based upon ‘step-changes’ in upwind surface roughness (z_0) (Harris and Deaves 1980, Deaves 1981). An internal boundary layer (IBL) is assumed to form at each step-change and the wind-speed profile directly above the site of concern (hereafter the ‘reference’ site) can be determined through combining the effective equilibrium profiles for each IBL (according to the model in Sect 4.2.3.1) at the appropriate heights (Harris and Deaves 1980, Deaves 1981, ESDU 2002).

The details given in Harris and Deaves (1980) are complemented with recommendations for use (including calculation sheets) by the Engineering Sciences Data Unit (ESDU) 82026 (ESDU 2002). However, treating roughness in a ‘step-change’ framework presents several challenges. Firstly,

identification of discrete areas for which upwind aerodynamic roughness parameters should be determined is some-what subjective. Second, the magnitude of roughness change which is sufficient for distinct IBL formation is not well defined and therefore the fetch (i.e. distance upwind) from a reference site where a ‘step-change’ takes place is difficult to determine. For example, a clear new IBL may fail to develop if there are not sharp changes in surface characteristics (Mahrt 2000). Thirdly, if an IBL does form, there is uncertainty associated with its growth and therefore expected depth of influence at a reference site (Savelyev and Taylor 2005).

To overcome such challenges, during this study DH_v is applied using surface observations and a source area footprint model. The source area model is used to determine the probable upwind surface which would be contributing to measurements at pre-defined vertical increments (z_i) above the reference site (Fig. 4.1). Weighted roughness parameters are calculated for each source area (Sect. 3.4.3.3 methodology) and subsequently ESDU (2002) recommendations are used to estimate the wind-speed profile above the reference site considering multiple changes in upwind roughness (see Fig. 4.1). Using DH_v with the source area model means that, rather than attempting to identify surface roughness changes which may trigger IBL growth, an integrated representation of the upwind surface is considered. Definition of z_i is some-what arbitrary, but its value should provide a compromise between being large enough for computational efficiency, but small enough to consider significant changes in upwind surface characteristics. The effect of altering z_i is considered later (Sect. 4.5.2.2).

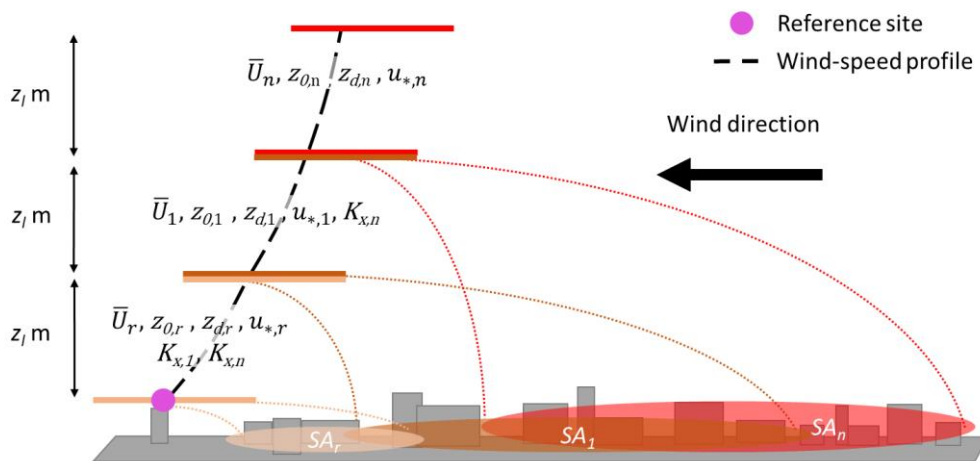


Figure 4.1: Operation of the Deaves and Harris non-equilibrium wind-speed profile method (DH_v) as applied in this work. A source area footprint model is applied at pre-defined vertical increments (height: z_i m) above the reference site. The source area for each respective height (SA_r, SA_1 and SA_n) is used to determine representative roughness parameters (z_d and z_0), which are subsequently used to calculate local friction velocities ($u_{*,r}, u_{*,1}, u_{*,n}$). The effective wind-speed profile for each ‘layer’ (depth z_i m) is then calculated (using Eq. 4.5) with the appropriate roughness transition correction ($K_{x,1}, K_{x,n}$) (ESDU 2002). Subscripts are: ‘r’ reference (i.e. from the reference site observations), ‘1’ representative of the first calculations performed z_i m above the reference site, and ‘n’ for the n^{th} calculation (performed at $n \times z_i$ m above the reference height)

4.2.4 The Gryning profile

Using observations above rural, flat and urban surfaces for 10 m wind speeds greater than 3 m s⁻¹, Gryning et al. (2007) indicate wind-speed profiles based upon surface layer scaling (i.e. the *LOG* method) are only valid up to a height of approximately 80 m. Above this, Gryning et al. (2007) argue that neutral wind speeds increase at a greater rate than the *LOG* method predicts, as a consequence of the non-linearity of the surface length scale. Therefore, in the Gryning et al. (2007) method (hereafter *GR*) three component length scales are used to represent different parts of the ABL. In addition, the friction velocity is assumed to decrease linearly with height beyond the surface layer. During neutral conditions, the surface length scale ($L_{SL,N}$) is proportional to height, the middle layer length scale ($L_{MBL,N}$) is near constant, and the upper length scale ($L_{UBL,N}$) decreases linearly to the top of the ABL ($L_{UBL,N} = h - (z - z_d)$), therefore:

$$\frac{du}{dz} = \frac{u_*}{\kappa} \left(1 - \frac{z - z_d}{h}\right) \left(\frac{1}{z - z_d} + \frac{1}{L_{MBL,N}} + \frac{1}{h - (z - z_d)}\right) \quad (4.6)$$

Integrating Eq. 4.6 between a height, z , and where the wind speed falls to zero (at height z_0):

$$\bar{U}_z = \frac{u_*}{\kappa} \left(\ln \left(\frac{z - z_d}{z_0} \right) + \frac{z - z_d}{L_{MBL,N}} - \frac{z - z_d}{h} \left(\frac{z - z_d}{2L_{MBL,N}} \right) \right) \quad (4.7)$$

Through empirical fits to observed profiles, Gryning et al. (2007) demonstrate $L_{MBL,N}$ can be determined using only surface measurements by:

$$\frac{u_*}{fL_{MBL,N}} = -2 \ln \left(\frac{u_*}{fz_0} \right) + 55 \quad (4.8)$$

To determine h , Gryning et al. (2007) recommend using Eq. 4.4 with a proportionality constant (β) of 10, 9 and 12 for rural (flat and homogeneous), residential and urban areas, respectively. The urban setting of this work means $\beta = 12$ is used here.

4.2.5 Vertical extrapolation of the surface wind speed

To extrapolate the neutral wind-speed profile from surface observations using pre-determined aerodynamic roughness parameters (z_d and z_0), the *LOG* and *PL* methods only require a reference surface wind speed (U_{ref}). The other methods require u_* and h , which without observations require an iterative procedure for their determination:

- 1) u_* is calculated using the surface wind speed (U_{ref}) and pre-determined roughness parameters (z_d and z_0) by rearranging Eq. 4.1.
- 2) h is determined using Eq. 4.4.
- 3) The wind-speed profile is extrapolated using Eq. 4.5 for the DH_e and DH_v methods or Eq. 4.7 for the *GR* method. Note when using the *GR* method $L_{MBL,N}$ must be calculated prior to this using Eq. 4.8.

- 4) A revised u_* is obtained for each respective method from rearranging Eq. 4.5 or 4.7, using U_{ref} and h .
- 5) Return to step 2) until there is convergence of u_* and h .

Convergence is rapid, typically requiring only 2-3 iterations for less than 1% variability (which is the convergence criteria used here). From step 1, the procedure is sensitive to the pre-determined z_d and z_0 .

4.3 Aerodynamic roughness parameters

A pre-requisite to determining the wind-speed profile from surface observations is accurately determining the aerodynamic roughness parameters, z_d and z_0 . Morphometric methods describe z_d and z_0 based upon surface form. The methods can be divided into two classes: (i) those assuming homogenous roughness-element heights, represented by H_{av} , and (ii) those considering roughness-element height variability. Collectively the former are termed RE_{av} and the latter RE_{var} (Sect. 3.3.2.2). For the same study site as used here, Sect. 3.6 demonstrates that wind speeds extrapolated using the RE_{var} roughness parameters are most similar to observations. These results are developed here by considering additional methods to extrapolate the wind-speed profile, as well as more complex surface cover. Aerodynamic roughness parameters are determined using the Macdonald et al. (1998) (*Mac*) and Kanda et al. (2013) (*Kan*) morphometric methods (RE_{av} and RE_{var} type, respectively). The methods are later developed to include the effects of vegetation (Chapter 5), which is shown to improve wind-speed estimation (Sect. 6.3.4). However, during this winter (i.e. leaf-off vegetation state), city centre (i.e. building dominated) analysis, vegetation is not expected to critically influence roughness parameters and the extrapolated wind speeds (e.g. Sect. 5.3.3), and is therefore not considered.

The *Mac* method zero-plane displacement (Mac_{z_d}) and aerodynamic roughness length (Mac_{z_0}) are calculated by:

$$Mac_{z_d} = [1 + \alpha_M^{-\lambda_p}(\lambda_p - 1)]H_{av} \quad (4.9)$$

$$Mac_{z_0} = \left(\left(1 - \frac{z_d}{H_{av}} \right) \exp \left[- \left\{ 0.5 \beta_M \frac{C_{Db}}{k^2} \left(1 - \frac{z_d}{H_{av}} \right) \lambda_f \right\}^{-0.5} \right] \right) H_{av} \quad (4.10)$$

where $C_{Db} = 1.2$ is the drag coefficient for buildings, $\alpha_M = 4.43$ and $\beta_M = 1.0$ are empirical constants for staggered arrays fit to the wind tunnel data of Hall et al. (1996) and λ_p and λ_f are the plan and frontal area index of roughness elements, respectively.

The *Kan* method directly considers roughness-element height variability through use of the maximum (H_{max}) and the standard deviation (σ_H) of roughness-element heights and incorporates Mac_{z_0} , such that:

$$Kan_{z_d} = [c_o X^2 + (a_o \lambda_p^{b_o} - c_o) X] H_{max}, \quad X = \frac{\sigma_H + H_{av}}{H_{max}} \quad (4.11)$$

$$Kan_{z_0} = (b_1 Y^2 + c_1 Y + a_1) Mac_{z_0}, \quad Y = \frac{\lambda_p \sigma_H}{H_{av}} \quad (4.12)$$

where $0 \leq X \leq 1$, $0 \leq Y$ and a_o , b_o , c_o , a_1 , b_1 and c_1 , are constants 1.29, 0.36, -0.17, 0.71, 20.21 and -0.77, respectively. The *Kan* method includes the effect of individual tall buildings (i.e. H_{max}) at the 1 km scale (Kanda et al. 2013), but this is expected to become less important with distance from a location. Therefore, when H_{max} is more than 1 km from the reference site, the height is weighted by the source area.

4.4 Observations

Observations using a Halo Photonics Streamline pulsed Doppler lidar for an eight-month period (October 2010 – May 2011) are analysed. The instrument was located on King's College London (KCL) Strand campus rooftop, approximately 36 m above ground level (agl) (Fig. 4.2d, KSSW position). For a detailed description of the site, see Kotthaus and Grimmond (2012, 2014a, 2014b) and Sect. 3.4.1. The lidar operated in Doppler beam swinging (DBS) mode, whereby the measured Doppler shift between transmitted and returned pulses provides horizontal wind speed and direction in 30 m vertical gates above the instrument. Beams are transmitted consecutively in three directions (first vertical, then tilted east and north by 15°), with a 21 s scan cycle and the minimum permitted interval between scans is 120 s (Lane et al. 2013). The lidar geometry means only part of the return signal is detected from the lowest three gates, which can therefore not be used. As the lower portion of boundary layer is of interest, only the next three gates are analysed (mid-points 141, 171 and 201 m). Hourly-averages are used to reduce variability in the mean wind speed whilst ensuring stationarity (Lane et al. 2013). To ensure neutral conditions, profiles which have upper quartile wind speeds in all three gates are considered. In addition, only daytime profiles are used (0900 – 1700 h), to prevent nocturnal boundary layer features (such as jets) influencing results (Mahrt 1998). The 251 hourly-averaged profiles meeting these criteria, were subdivided by upwind surface characteristics (Sect. 4.5.2) into five directional sectors (Fig. 4.2b, c). Data from a Vaisala CL31 ceilometer, located approximately 3 m south-west of the Doppler lidar, is used to determine the mixing layer height (H_{ML}) (Sect. 4.5.3).

A CSAT 3 sonic anemometer (Campbell Scientific, USA) mounted on an Aluma T45-H triangular tower measured the 3-dimensional wind velocity and sonic temperature (with a sampling frequency of 10 Hz) approximately 45 m east of the KSSW site (Fig. 4.2d, KSS site). The anemometer at the KSS site is 48.9 m agl (i.e. $2.5H_{av}$ in the surrounding 1 km) and 13.3 m above the roof hosting the tower. Minimal distortion of turbulence data indicates measurements are mostly free from local roughness-element wakes and therefore taken within the inertial sublayer (Kotthaus and Grimmond 2014b, Sect. 3.4.2). For each hourly period, observations at the KSS site are used to apply the Kormann and Meixner (2001) source area footprint model from the lidar position (KSSW) to obtain the Kan and Mac aerodynamic roughness parameters for wind profile extrapolation (Sect. 3.4.3.3). For the LOG , PL , DH_e and GR methods only roughness parameters determined from the source area calculations at 49 m height are used. For DH_v , the source area model is applied using surface observations at the specified vertical increments (z_i) to indicate the probable extent, and associated aerodynamic roughness parameters, of the upwind surface contributing to measurements at each height (e.g. Fig. 4.1).

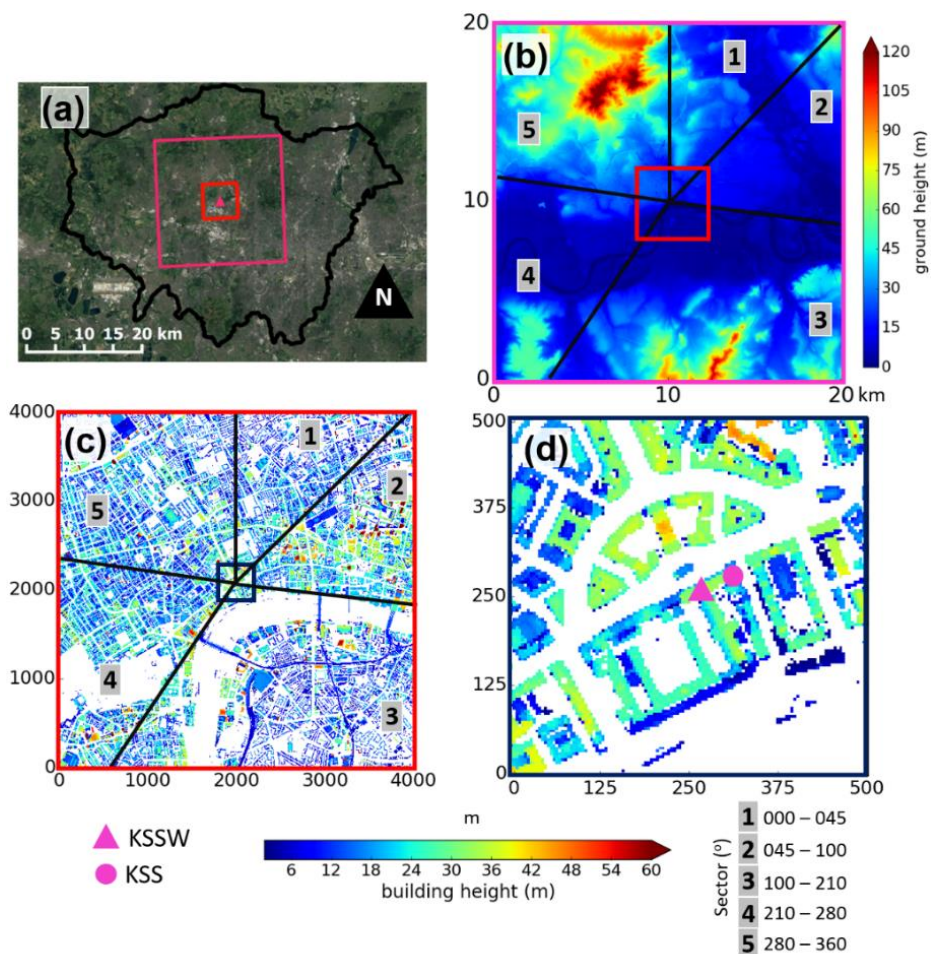


Figure 4.2: Location of the King's College London (KCL) measurement sites in (a) Greater London (black outline), United Kingdom. (b) Ground height for the 20 km x 20 km around KCL. Building heights > 2 m in the surrounding: (c) 4 km and (d) 500 m. Sector divisions 1 – 5 in (b) and (c) are manually defined based upon upwind surface characteristics (see Sect. 4.5.2). Elevation data source: Lindberg and Grimmond (2011a)

4.5 Results

4.5.1 Controlled comparison of the wind-speed profile methods

Comparison of the assessed wind-speed profile methods during similar conditions demonstrates their operation in the lower boundary layer. Assuming a neutrally stratified boundary layer, with a reference wind speed of 10 m s^{-1} (U_{ref}) measured at 50 m, the wind-speed profile is extrapolated for 200 m vertically and normalised by U_{ref} (Fig. 4.3). The aerodynamic roughness parameters (z_d and z_0) used during the extrapolation are the typical values reported by the *Mac* and *Kan* methods at the KSSW site. The most obvious difference between these is that Kan_{z_d} is twice Mac_{z_d} (for a more detailed analysis of locally determined z_d and z_0 at KCL see Sect. 3.5). For the wind profile methods which do not explicitly consider upwind changes in surface roughness (the *PL*, *LOG*, DH_e and *GR* methods), the roughness parameters used are $z_0 = 2 \text{ m}$ and $z_d = 30 \text{ m}$ (Fig. 4.3a, representative of Kan_{z_d}) or $z_d = 17.5 \text{ m}$ (Fig. 4.3b, representative of Mac_{z_d}). For the DH_v method, z_l is pre-defined as 50 m and three changes in roughness are assumed to influence the profile. The roughness parameters assumed at the bottom of the 50, 100 and 150 m layers are: $z_0 = 2, 1.5$ and 1 m , respectively, with $z_d = 30, 20$ and 10 m (Fig. 4.3a) or $z_d = 17.5, 15$ and 12.5 m (Fig. 4.3b). Note that if the surface z_d and z_0 are used at each height (representing an extensive homogenous fetch) DH_v collapses to DH_e . The Coriolis parameter (f) is determined using the latitude of KCL, $\Phi = 51.51^\circ$.

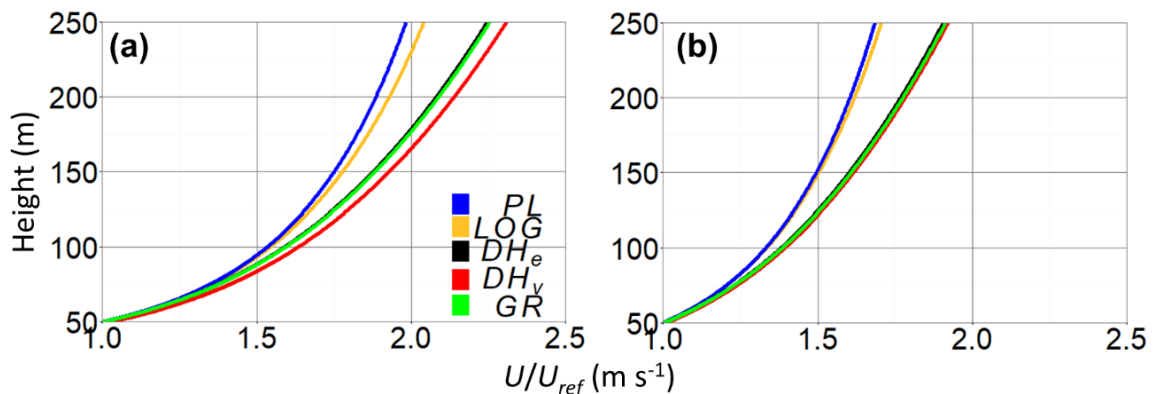


Figure 4.3: Controlled comparison of the wind-speed profile extrapolated from 50 m using the different methods assessed (Sect. 4.2), normalised by a reference wind speed (U_{ref}) of 10 m s^{-1} . The profiles are extrapolated with roughness parameters characteristic of the study site determined by the (a) Kanda et al. (2013) and (b) Macdonald et al. (1998) morphometric methods. Profile abbreviations: *PL* – power law; *LOG* – logarithmic wind law; DH_e – Deaves and Harris equilibrium model; DH_v – Deaves and Harris non-equilibrium model; *GR* – Gryning et al. (2007). See text for the values used during the extrapolation

Wind speeds extrapolated using the DH_e , DH_v and GR methods are similar to each other and all greater than the LOG and PL methods (Fig. 4.3). Close to the surface (below 100 m) the methods are dominated by surface-based length scales (i.e. z_d and z_0 , only) and therefore indicate similar wind speeds. Above this the wind speed gradients of the DH_e , DH_v and GR methods are comparatively steeper with height as they become influenced by other length scales (e.g. h). The PL method has similar wind speeds to LOG , tending towards lower wind speeds with increasing height.

Wind speeds using the GR profile are marginally greater than the DH_e method. The assumed upwind transition from a comparatively smooth to rough surface means the DH_v wind speeds are greater than both the DH_e and GR methods. However, the DH_v wind speeds are only a maximum of 2% larger than the DH_e method despite the approximate 50% decrease in upwind z_d and z_0 which affects the DH_v profile only.

All wind speeds extrapolated using the *Kan* roughness parameters (Fig. 4.3a) are greater than using the *Mac* parameters (Fig. 4.3b). For the LOG and PL methods, this is because the smaller z_d from the *Mac* method produces less shear. For the other methods the parameters calculated internally to the models (u_* and h) take effect. Following rearrangement of Eq. 4.1, a smaller z_d generates a smaller u_* , which in turn gives a smaller h (Eq. 4.4). The reduction of h ‘squeezes’ the wind-speed profile into a smaller depth of ABL and therefore acts to increase the estimated wind speed for any given height. However, this increase is countered by the reduction in u_* , which causes a larger decrease in wind speed and means the overall effect is a reduction of wind speed. In the GR method, u_* is also used to calculate the internal parameter $L_{MBL,N}$. A comparatively smaller z_d (and associated reduction in u_*) decreases $L_{MBL,N}$, which by the form of Eq. 4.7 acts to further decrease wind speed. Further attention is given to the internally calculated u_* and h later (Sect. 4.5.3).

4.5.2 Upwind surface variability

4.5.2.1 Upwind surface variability at KCL

The use of just two aerodynamic roughness parameters (z_d and z_0) to model the lower ABL wind speed, assumes these two length scales are sufficient to describe the influence of the entire underlying surface at a reference site. The extent to which this assumption is appropriate depends upon upwind surface variability (Deaves 1981) – the premise of the DH_v method is that surface characteristics further upwind may be more appropriate to describe the wind speed further from the surface (e.g. Fig. 4.1). The variability of the upwind surface from the KSSW site

is assessed by comparing the roughness parameters determined from source areas calculated at 25 m height increments (i.e. z_l is 25 m in Fig. 4.1), for each hourly period. Note that the roughness parameters will vary with the morphometric method used and therefore so will the modelled source area. For descriptive purposes the *Kan* method is discussed.

As the size of the source area increases with height, both the extent and location of the maximum influence vary. At a height of 200 m, the upwind extent of the source area reaches 5 km, which is (on average) three times larger than that calculated at 100 m (1.8 km upwind), and 30 times that calculated at 49 m (170 m upwind). The source area growth with height means a wide range of building geometries are encountered. This impacts the calculated roughness parameters, such that the variability cannot be generalised in all directions (Fig. 4.4). The obvious directional differences are used to classify observations into five directional sectors (Table 4.1, Fig. 4.2b, c).

In sector 1 ($000^\circ - 045^\circ$ from the KSSW site), as the source area becomes larger with height (e.g. Fig. 4.1), H_{av} , λ_p and λ_f all decrease gradually. However, taller buildings located approximately 600 m upwind from the KSSW site (Fig. 4.2c) cause a discontinuous increase in H_{max} and σ_H . The dependency of z_d on H_{max} (Kanda et al. 2013, Eq. 4.11) means an initial upwind increase in z_d (from 32 to 36 m) thereafter gradually decreases to 20 m (Fig. 4.4a). In comparison, z_0 gradually decreases from as large as 3 m closer to the site to between 1 and 2 m further afield (Fig. 4.4b). Sector 5 ($280^\circ - 360^\circ$) exhibits similar changes in upwind building geometry and roughness parameters to sector 1. However, the topographic variability (upwind vertical ascent of up to 135 m within approximately 6.5 km, Fig. 4.2b) means the sectors are treated separately.

Sector 2 ($045^\circ - 100^\circ$) has the greatest height heterogeneity, associated with the tallest buildings in London. High rise buildings, packed in close proximity, generate λ_p and λ_f of 0.5. In addition, H_{av} , H_{max} and σ_H all increase with distance upwind creating an increasingly chaotic surface. Sector 2 is therefore the only direction where surface roughness (both z_d and z_0) increases with distance upwind (Fig. 4.4). Unfortunately, with only six profiles available for this direction, further analysis is impossible.

Sector	1	2	3	4	5
Angle from KSSW	$000^\circ - 045^\circ$	$045^\circ - 100^\circ$	$100^\circ - 210^\circ$	$210^\circ - 280^\circ$	$280^\circ - 360^\circ$
Number of profiles	36	6	91	98	20

Table 4.1: Directional sectors used for analysis with the number of hourly profiles. Upwind surface characteristics around the KSSW site (see Fig. 4.2b, c and Fig. 4.4) are used for the classification, based on the wind direction observed in the first usable Doppler lidar gate (mid-point = 141 m)

The presence of the river in sector 3 ($100^\circ - 210^\circ$) creates a complicated fetch. Sector 3 has the lowest λ_p and λ_f (0.25) because of the river and comparatively sparse buildings on the far side of the river (Fig. 4.2c). As H_{av} tends to decrease upwind, so do z_d and z_0 , except for between $190^\circ - 210^\circ$ where taller buildings cause an initial increase in z_d and z_0 (Fig. 4.4).

In sector 4 ($210^\circ - 280^\circ$), z_d decreases from approximately 30 m close to the KSSW site to 25 m further upwind. This is caused by an abrupt reduction in H_{av} , which is also responsible for an initial decrease in z_0 . However, beyond this H_{av} is unchanged and λ_f ranges between 0.2 – 0.4, near the peak roughness range (Fig. 3.1), therefore z_0 becomes larger.

A reference-based approach to determine aerodynamic roughness parameters is recommended in ESDU (2002, their Table 13.1), based on a function of H_{av} . For cities, ESDU (2002) indicates z_d is between 15 and 25 m and z_0 is between 0.5 and 1.5 m. Such reference-based approaches are limited by the subjectivity of application and the inability to model the probable upwind surface contributing to measurements. Roughness parameters determined with the *Kan* method tend to be larger than those indicated in ESDU (2002). This is expected, as the *Kan* method directly accounts for roughness-element height variability (Eq. 4.11 and 4.12) and the considerable increase in drag exerted by taller roughness elements (Xie et al. 2008, Hagishima et al. 2009, Zaki et al. 2011, Mohammad et al. 2015a). Whereas, the *Mac* parameters are closer to the ESDU (2002) values as *Mac* incorporates H_{av} only (Eq. 4.9 and 4.10).

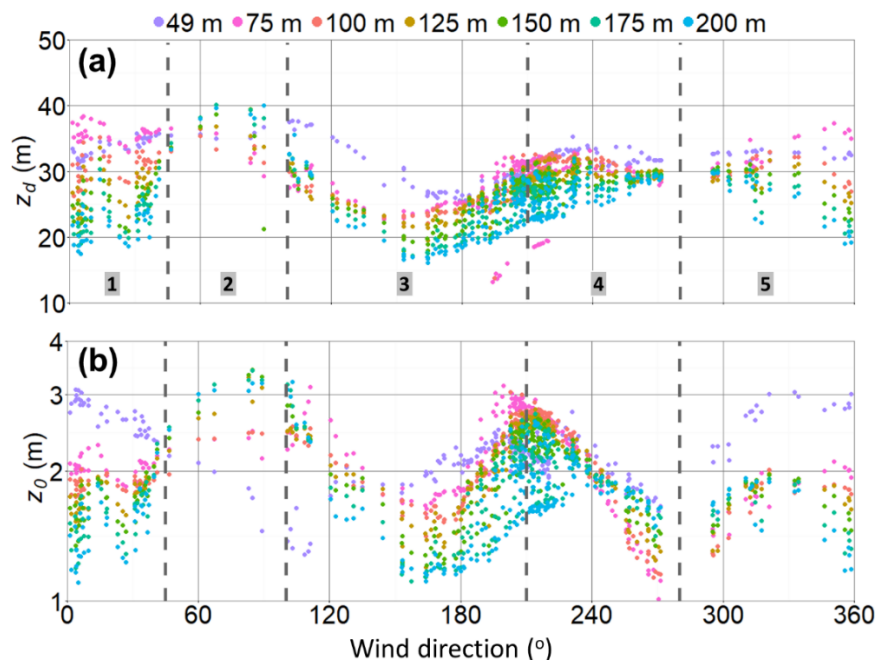


Figure 4.4: (a) Zero-plane displacement (z_d) and (b) aerodynamic roughness length (z_0) (note ln axis), determined from source areas calculated in 25 m vertical increments above the KSSW site (colour indicates different heights). For the 251 hourly periods assessed, observations from the KSS site are used with the Kormann and Meixner (2001) footprint model from the KSSW position (Fig. 4.2) at the heights indicated, with the Kanda et al. (2013) morphometric method to determine z_d and z_0 (Sect. 3.4.3.3 methodology). The five directional sectors (dashed lines, 1-5) for analysis (Table 4.1) are indicated

4.5.2.2 Influence of the upwind surface variability on the wind-speed profile

The DH_v method is a development of DH_e , allowing z_d and z_0 to vary as a function of height in the wind-speed profile. Comparison of the DH_e and DH_v profiles therefore demonstrates the implications of considering upwind roughness in this work. The mean of extrapolated wind-speed profiles in sector 1 reveals wind speeds estimated by the DH_v method are greater than the DH_e method throughout the profile, due to the reduction in upwind roughness (Fig. 4.5). The maximum wind speed difference is largest (15%), as expected, at greater heights, where roughness parameters have maximum difference from those determined at the surface (Fig. 4.4).

When using the DH_v method with pre-defined vertical increments (z_l), the recalculation of the wind-speed profile at each height increment results in a corrective shift (Fig. 4.5) which is not expected empirically. The size of each shift depends upon the change in roughness of the upwind surface, as well as the height increment (z_l) at which re-calculations are performed. For example, the magnitude of the correction is least where there is less variation in roughness parameters towards the top of the profile (Fig. 4.4). In addition, comparison between wind profiles using $z_l = 25$ m and 50 m (red and blue line in Fig. 4.5, respectively) demonstrates how less frequent re-calculation of the wind profile results in larger corrective shift, as the difference between z_d and z_0 of each upwind surface increases. Reducing z_l from 50 m to 25 m creates a maximum difference of wind speed at any given height of just 3%. Further reduction of z_l results in an even smaller difference and considering the extra computational requirements, $z_l = 25$ m is deemed sufficient.

Definition of the pertinent fetch for a reference site (i.e. upwind distance of surfaces influencing the profile aloft) is problematic and not addressed well in building codes (e.g. ESDU 2002, Abdi and Bitsuamlak 2014). Earlier work demonstrates that the fetch may be modelled through consideration of flow parameters (Elliott 1958) or upwind roughness (Miyake 1965, Wieringa 1993) and that surfaces up to 200 km upwind from a reference site will still have some influence upon the wind-speed profile (Cook 1985). However, recent work indicates only characteristics much closer to a site are of significance for a rough surface (Tamura et al. 2001, Zhang and Zhang 2001, AS/NZS (1170.2) 2002, Wang and Stathopoulos 2007). This has been associated with more rapid IBL development (Tamura et al. 2001) and contrasts with wind tunnel experiments indicating IBL growth may be slower than classical results suggest (Cheng and Castro 2002).

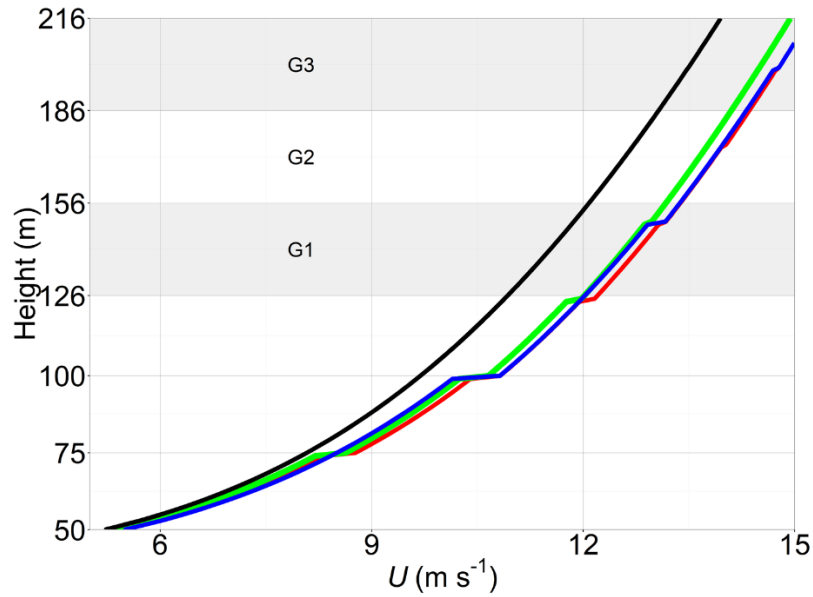


Figure 4.5: Mean of extrapolated wind-speed profiles in sector 1 ($n = 36$) using the DH_e method (black line) and DH_v method with height increment (z_i) = 50 m (blue line) and $z_i = 25$ m (red line). For the DH_v method, the extent of the upwind surface considered is dictated by the source area calculated at 200 m, which is altered to 150 m for comparison (green line). The 30 m wind gates used from lidar observations during this work are shaded G1 – G3 (G1 = 126 – 156 m, mid-point = 141 m)

The unclear definition of the pertinent fetch means that in this work, the maximum upwind extent of the surface considered is limited by the maximum height where source area calculations are performed, which is 200 m (red line, Fig. 4.5). Reducing this value to 150 m (green line, Fig. 4.5) causes a variation in wind speed above 150 m because of the disregard for upwind roughness contributing to the profile above this height. However, wind speeds below 150 m remain similar. These results exemplify that in the current application of DH_v , considering roughness contributing to the profile beyond a height of interest does not obviously influence wind speeds below that height. Given the focus of this work on the lower ABL, considering a maximum height of 200 m is therefore deemed sufficient.

4.5.3 Internal parameters used in the wind-speed profile methods

When estimating the wind-speed profile, u_* and h are calculated internally by the respective wind profile models (Sect. 4.2.5). The gradient height (h) determined by the models as the height where ABL flow becomes free from surface stresses, does not necessarily coincide with the mixing layer height (H_{ML}) determined using observations and various methods (Emeis et al. 2008). Comparison of the internally calculated parameters using the DH_e method ($u_{*,calc}$, h_{calc}) with those obtained from meteorological instrumentation at KCL ($u_{*,obs}$, H_{ML}) tests this argument. For each hourly period, $u_{*,calc}$ and h_{calc} are determined using the method outlined in Sect. 4.2.5, with the observed wind speed and roughness parameters determined from 49 m. The $u_{*,obs}$ is calculated using high frequency observations (Leclerc and Foken 2014):

$u_{*,obs} = [(\overline{u'w'})^2 + (\overline{v'w'})^2]^{1/4}$. Two independent methods are used to obtain H_{ML} using the Doppler lidar and automated lidar/ceilometer (using the methods described in Barlow et al. 2015 and Kotthaus and Grimmond 2017, respectively) and their average is used as an indication of H_{ML} .

For the 36 periods in sector 1 ($000^\circ - 045^\circ$ from KSSW), $u_{*,obs}$ varies between 0.4 and 1.0 m s^{-1} (Fig. 4.6a). These are typically expected magnitudes for an urban area (e.g. Roth 2000). Similarly, H_{ML} ranges between typically expected winter UBL heights (e.g. Seidel et al. 2010) with an average depth of 930 m (Fig. 4.6b). If the parameters are calculated internally to the wind-speed profile methods, they are sensitive to the morphometric method used and most similar to the observed values when using the *Mac* roughness parameters (Fig. 4.6, $u_{*,calc,M}$ and $h_{calc,M}$). Using the *Kan* roughness parameters, the friction velocity is on average 40% larger and h can be up to twice as large as H_{ML} .

To assess the suitability of the parameters, the mean of extrapolated wind speeds in sector 1 are compared using the DH_e method with: (i) internally calculated parameters ($u_{*,calc}$ and h_{calc}); and (ii) observed $u_{*,obs}$ and H_{ML} (Fig. 4.7). Using the internally calculated parameters, the modelled wind speeds at the extrapolation height (49 m) are equal to the observed wind speed, by definition. Above this, following Sect. 4.5.1 wind-speed estimations are larger using the *Kan* method. When $u_{*,obs}$ and H_{ML} are used, the estimated wind speeds are not constrained to a wind-speed at any height. Additionally, wind-speed estimates throughout the profile are larger

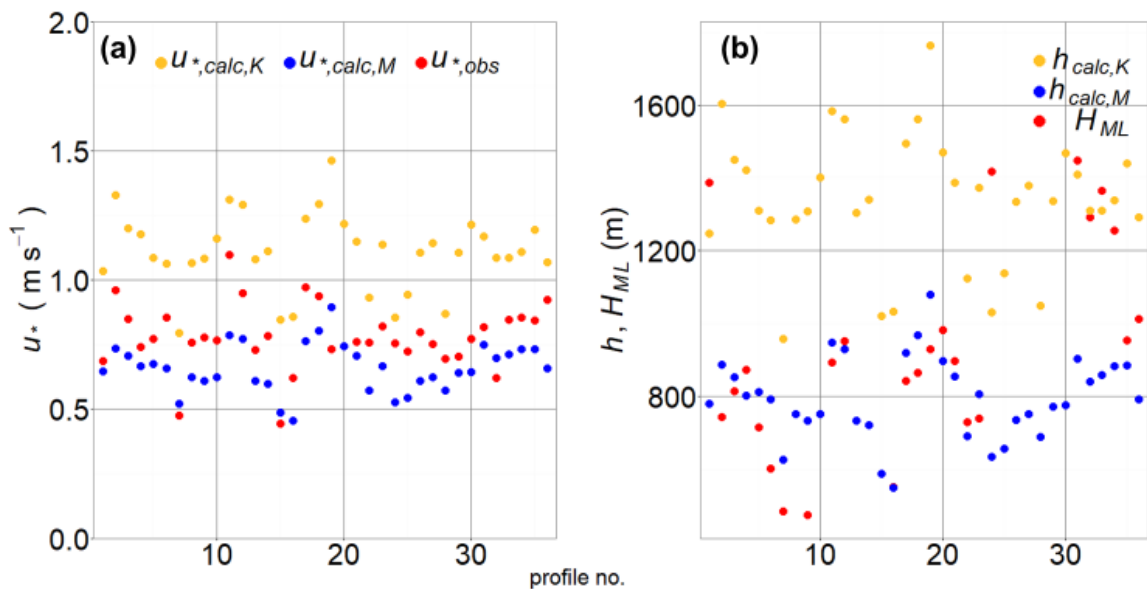


Figure 4.6: For each hourly period assessed in sector 1 ($000^\circ - 045^\circ$ wind direction from the KSSW site): **(a)** friction velocity calculated internally to the DH_e model ($u_{*,calc}$) and from observations at the KSS site and ($u_{*,obs}$), **(b)** gradient height (h) determined internally to the DH_e model and the mixing layer height determined from observations (H_{ML} , average of two observation methods, see text). Subscripts *K* and *M* refer to use of the Kanda et al. (2013) and Macdonald et al. (1998) aerodynamic roughness parameters during calculations, respectively

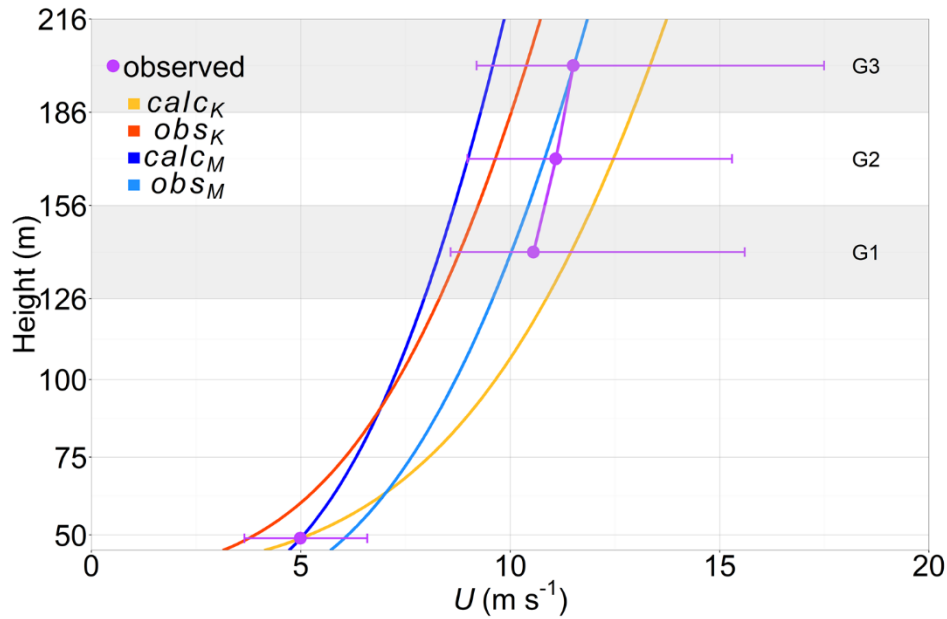


Figure 4.7: Mean wind-speed profiles extrapolated using the Deaves and Harris equilibrium model (DH_e) for all hourly periods assessed in sector 1 ($n = 36$). The profiles are extrapolated using parameters calculated internally to the model (*calc*) and from observations (*obs*). Subscripts *K* and *M* indicate use of Kanda et al. (2013) and Macdonald et al. (1998) aerodynamic roughness parameters, respectively. The mean observed wind speed at 49 m by a sonic anemometer and 30 m wind gates of the lidar are shown with whiskers to indicate the minimum and maximum observed wind speeds. The 30-m lidar gates are shaded G1 – G3, with mid-points: G1 = 141 m, G2 = 171 m and G3 = 201 m

when using the *Mac* roughness parameters because the bias from the internally calculated u_* and h no longer takes effect. The variation from observed wind speeds is largest near the surface (at 49 m) with an average difference of up to 30%. However, estimations are more similar to observations aloft, especially when using the *Mac* roughness parameters. The $u_{*,obs}$ and H_{ML} are rarely available during routine wind-speed profile estimations, therefore the internally calculated parameters are used during this work. However, the comparison indicates it is not unreasonable to use an observed u_* and H_{ML} when using the different profile methods.

4.5.4 Variability of observed wind speeds

Wind speeds observed in the UBL are, amongst other controls, a function of synoptic-scale forcing, topographical conditions, anthropogenic activity, and surface characteristics (e.g. Britter and Hanna 2003, Fernando 2010, Barlow 2014). Without additional measurements to those at KCL it is difficult to identify the impact of each upon the observed wind profile, however, comparison of wind speeds throughout the profile provides useful insight.

The lowest mean wind speeds observed throughout the profile are to the north and north-west (sectors 1 and 5), which are between 4.5 m s^{-1} and 5 m s^{-1} at the surface and 10.5 m s^{-1} and 11.5 m s^{-1} aloft (Fig. 4.8a). The highest mean wind speeds occur in southerly directions (sectors 3 and 4). The directional variability of wind speeds is predominantly dictated by synoptic-scale forcing,

with frequent frontal passage across the UK (typically from west to east) resulting in stronger winds from the south-west and less frequent, lower wind speeds from the north-east. However, it is also possible that the gradual reduction in upwind roughness to the north of the sites may be contributing to the lower observed wind speeds (e.g. Deaves 1981) (Fig. 4.4). The linear MS-micro/3 wind flow model (Walmsley et al. 1986, 1990) indicates that the surrounding topography (including the gently sloping topography to the north) does not obviously influence wind speed at the site.

The larger shear stress experienced closer to the surface is responsible for the observed wind speed at 49 m (approximately 2.5 times the canopy height) consistently being approximately half of that observed 200 m above the canopy (Fig. 4.8a). However, wind speeds do not always behave as expected throughout the profile. This is exemplified by two extreme cases (circled in Fig. 4.8b): one where a wind speed of approximately 9 m s^{-1} is observed both at 49 m (U_{49}) and the first gate of the lidar (U_{G1}); and another where U_{49} is just 3 m s^{-1} at the same time U_{G1} is 12.5 m s^{-1} . A likely source of this variability is that on occasion, the surface measurements and those aloft are responding to different flow fields as a consequence of longitudinal and transverse roughness heterogeneity upwind. Measurements closer to the surface may be responding to local obstacles, whilst flow aloft is a function of the integrated or blended surface (Grimmond and Oke 1999, Roth 2000, Grimmond et al. 2004, Barlow et al. 2008, Barlow 2014). This is supported by the better agreement of observed wind speeds aloft (between 126 – 216 m) (Fig. 4.8c), where the effects of local surface roughness variability are less pronounced. However, deviations from the idealised profiles still occur, such as the grouping of observations where wind speed decreases with height (circled in Fig. 4.8c). This demonstrates the uncertainties arising when using idealised wind profile relations to estimate the wind-speed profile.

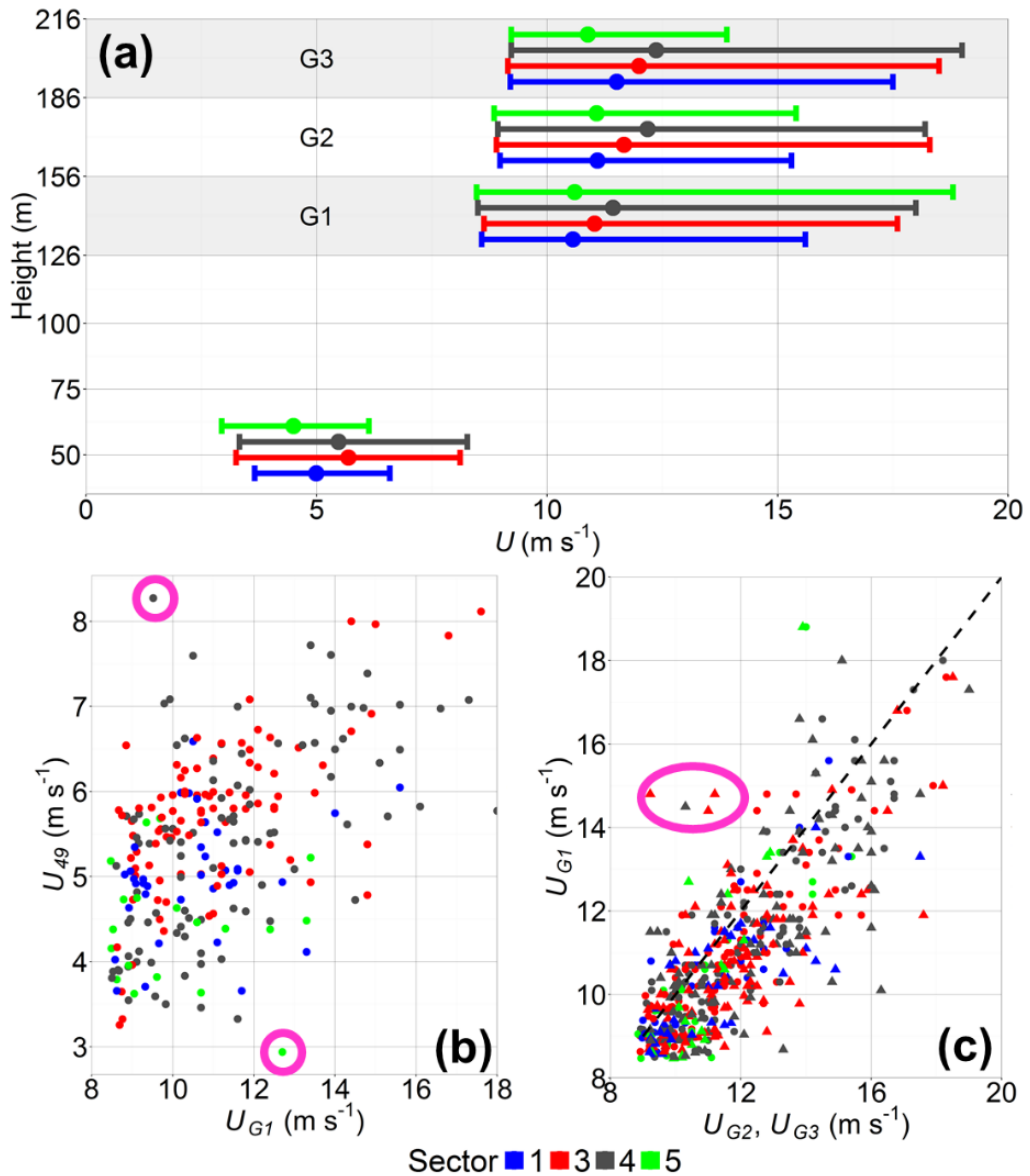


Figure 4.8: For all observations ($n = 245$): (a) average (points) and minimum/maximum (whiskers) observed wind speed at 49 m and 30 m gates of the Doppler lidar (shaded G1 – G3). Wind speed observed at: (b) 49 m (U_{49}) and the first gate of the lidar (U_{G1}), and (c) U_{G1} and the second (U_{G2} , circles) and third (U_{G3} , triangles) gates of the lidar, with a 1:1 relation (dashed line). Points circled in magenta are referred to in text. Data are selected through the filtering process outlined in Sect. 4.4 and coloured by wind direction (see Table 4.1 for sector definitions)

4.5.5 Comparison of observed and estimated wind-speed profiles

The directional variability and range of upwind surface roughness, wind speed, observational frequency and topographical variability, means that a collective analysis of wind profiles results in a bias towards more frequently observed wind directions or extremes. Hence a comparison of the observed (U_{obs}) and extrapolated wind speed by each of the wind profile methods (U_{ext}) is performed for each directional sector. For each hourly period, U_{ext} is calculated at 1 m height intervals and averaged over 30 m gates to correspond to the vertical resolution of the lidar. The difference (U_{diff}) between U_{ext} and U_{obs} for each 30 m gate is summarised in Fig. 4.9.

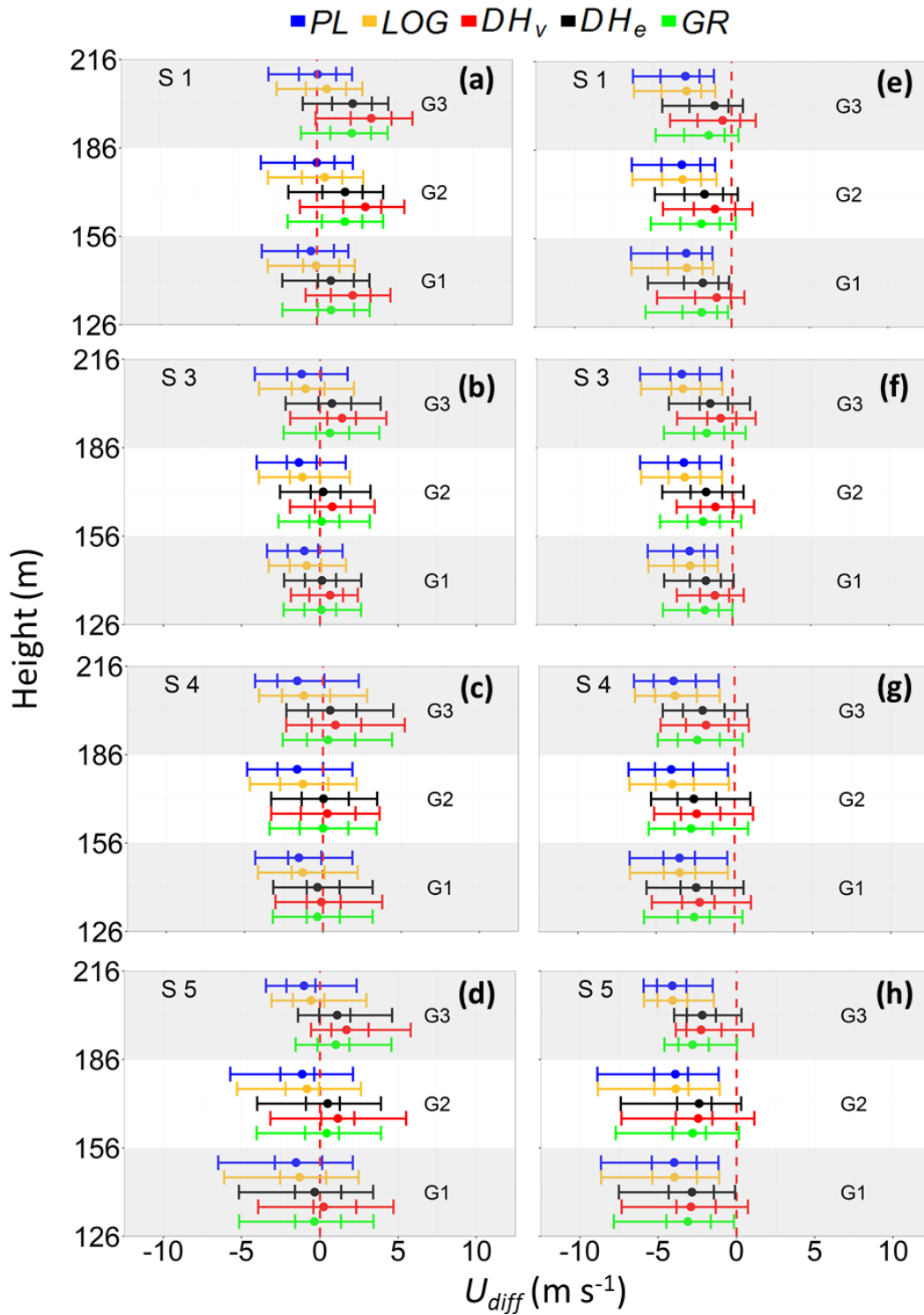


Figure 4.9: Distribution of hourly wind speed differences (U_{diff}) between observed (U_{obs}) and extrapolated (U_{ext}) wind speeds at heights corresponding to 30 m lidar gates (Gates shaded G1 – G3) ($U_{diff} = U_{ext} - U_{obs}$). Points are the median and whiskers are the 5th, 25th, 75th and 95th percentiles. The analysis is stratified into directional sectors (rows), labelled S1, S3, S4, S5 (see Table 4.1 for directions). Differences shown are using (a – d) Kanda et al. (2013) and (e – h) Macdonald et al. (1998) roughness parameters. Profile abbreviations: PL – power law; LOG – logarithmic wind law; DH_e – Deaves and Harris equilibrium model, DH_v – Deaves and Harris non-equilibrium model; GR – Gryning et al. (2007)

For all wind profile methods, the aloft wind-speed estimates are consistently most similar to U_{obs} (i.e. U_{diff} is closest to 0 m s^{-1} in Fig. 4.9) when the *Kan* method parameters are used (Fig. 4.9a – d). Whereas, using the *Mac* roughness parameters means wind speeds are underestimated (Fig. 4.9e – h). This underestimation is most obvious for the *PL* and *LOG* methods because of their least steep gradients. Both predict similar wind speeds, underestimating wind speeds in over 95% of cases with a median of between 2.5 m s^{-1} and 4.5 m s^{-1} (Fig. 4.9e – h). In more extreme cases, the underestimation can be up to 9 m s^{-1} (Fig. 4.9h), corresponding to almost 90% of the mean observed wind speed at the same height. The greater wind speeds extrapolated using the *Mac* parameters with the DH_e , DH_v and *GR* methods better resemble observations, however the wind speed is still underestimated on over 80% of occasions, with median underestimation ranging between 1 and 3 m s^{-1} . Wind speeds are most obviously underestimated in sector 5 (Fig. 4.9h), as the models have underestimated the large shear between surface and upper winds for this direction (Fig. 4.8a, b).

The greater extrapolated wind speeds with the *Kan* roughness parameters are more similar to U_{obs} , with occasional overestimation, especially further from the surface (Fig. 4.9a – d). The reduced shear of the *PL* and *LOG* profiles cause wind speeds to be underestimated approximately 75% of the time (medians between 0.5 and 2 m s^{-1}). However, as the wind shear is smallest in sector 1, the *PL* and *LOG* profiles best resemble U_{obs} , and the other methods overestimate (Fig. 4.9a). Despite the *LOG* profile being consistently reported to be appropriate only close to the surface (e.g. Roth 2000), studies have shown its applicability to up to 50% of the boundary layer depth (Macdonald et al. 2000, Castro et al. 2006, Cheng et al. 2007). Therefore, the similarity of the *LOG* method to U_{obs} at 200 m above the canopy is not unreasonable.

Using the *Kan* parameters from the remaining wind directions (sectors 3, 4 and 5), the greater wind speeds of DH_e , DH_v and *GR* best resemble observations (Fig. 4.9b – d). Of these, the DH_e and *GR* profiles are most consistently similar to U_{obs} , as the larger shear of the DH_v profile causes slight overestimation with height (i.e. especially second and third lidar gates). The DH_v overestimation is most obvious in sectors 1 and 5, where a combination of the lowest synoptically-driven winds and decreasing upwind roughness causes the smallest observed wind shear (Fig. 4.8). The increased wind shear indicated by the DH_v profile is a response to the reduction in upwind roughness (Fig. 4.4). Although uncertainties arise from calculating roughness parameters using the source area model and morphometric methods, the DH_v

method overestimation is consistent with Drew et al. (2013b), indicating DH_v may be oversensitive to reductions in upwind roughness.

Across all comparisons, $|U_{diff}|$ is largest when the range of observed wind speeds throughout the profile is greatest and most variable. This is most obvious in sector 5, where the observed wind speed variability is not well correlated throughout the profile (Fig. 4.8), producing the largest range of U_{diff} (consistently $\pm 5 \text{ m s}^{-1}$ from the median), which is up to 50% of the mean wind speed. The range of observed wind speeds increases with height in sectors 1, 3 and 4 and therefore so does the range of U_{diff} . Despite the increasing mean wind speed with height, the differences relative to the mean wind speed also slightly increase in these directions. For example, using the *Kan* method roughness parameters maximum differences range from between 24% – 45% for the lowest lidar gate, to between 35% – 53% for the upper gate.

Calculation of the Monin-Obukhov stability parameter (z'/L , where $z' = z - z_d$) indicates that the variability of estimates from observations is not likely to be associated with stability effects. Using observations from the KSS site and the z_d value from the *Kan* method (which provides the most accurate wind-speed estimations), over 97% of the hourly observations assessed have $|z'/L| \leq 0.1$, a range which corresponds to near neutral atmospheric stability (Roth 2000). The remaining values are within $|z'/L| \leq 0.2$ and eliminating these periods from the analysis does not obviously improve wind-speed estimations.

A more likely cause of the variability is that each wind-speed profile method has its own inherent assumptions and is designed or derived based upon a specific set of boundary conditions. Inherent assumptions of the *LOG*, *PL*, *GR* and DH_e methods are that there is an extensive homogeneous fetch, which is rare in urban areas. In addition, the DH_e and DH_v methods are developed for wind speeds greater than 10 m s^{-1} measured at 10 m in rural, open surface conditions (Harris and Deaves 1980) and the *GR* method is developed using wind speeds greater than 3 m s^{-1} at 10 m (Gryning et al. 2007). A 10 m measurement at the current study site would inappropriately be within the canopy (and not the constant-flux layer), therefore the more suitable height of 2.5 times the canopy height is used. In addition, the wind speeds observed during the analysis were on average only half of the minimum wind speeds used to develop the DH_e and DH_v methods (Fig. 4.8). Variability is expected when using the wind profile methods outside the conditions they were developed for, however, assessment of their performance is valuable, especially for heterogeneous urban surfaces, which have the greatest potential to breach the assumptions inherent to each method.

4.6 Conclusions

Using wind speeds observed at approximately 2.5 times the canopy height in a central business district (London, UK), wind-speed profiles were extrapolated to 200 m above the canopy using five different methods: the logarithmic wind law (Blackadar and Tennekes 1968) (*LOG*); the Deaves and Harris equilibrium (DH_e) and an adaptation of the non-equilibrium (DH_v) model (Deaves and Harris 1978, Harris and Deaves 1980); the power law (Sedefian 1980) (*PL*) and the Gryning et al. (2007) (*GR*) profile. The profiles require aerodynamic roughness parameters (z_d and z_0), which were determined using the Sect. 3.4.3.3 iterative methodology with the Kanda et al. (2013) (*Kan*) and Macdonald et al. (1998) (*Mac*) morphometric methods. The extrapolated wind speeds were compared to wind speeds observed with Doppler lidar during strong wind conditions. Based upon surface layer scaling, all of the observations have (or are very close to) neutral atmospheric stability. Directional variations in the upwind surface characteristics warranted separation into consistent sectors. The most appropriate wind-speed profile method depended upon the morphometric method used, the observed wind speed and upwind surface characteristics.

When using the DH_e , DH_v and *GR* profiles, the friction velocity and gradient height are required, which are calculated internally to the methods (using their respective equations). Use of the observed friction velocity (at approximately 2.5 times the canopy height) and mixing layer height determined from remote sensing meteorological instruments is demonstrated to also lead to reasonable wind-speed estimates. However, these observed values are typically unavailable during routine wind-speed estimation, therefore the internally calculated parameters are used during this work.

Irrespective of the wind-speed profile method used, the estimated wind speed is sensitive to the aerodynamic roughness parameters z_d and z_0 . For all of the wind-speed profile methods assessed, the greater wind speeds estimated when using the *Kan* aerodynamic roughness parameters best resembled observed wind speeds, whereas the *Mac* parameters resulted in wind-speed underestimation. Direct consideration of roughness-element height variability (as the *Kan* method does) appears to be critical to the aerodynamic roughness parameters and hence accurately estimating the wind-speed profile. Assuming the *Kan* roughness parameters are appropriate, the central London comparison indicated that for most conditions the DH_e and *GR* methods were the most suitable to extrapolate the wind speed. However, wind-speed estimations with the DH_v profile are similar and closer to observations than the *PL* and *LOG* methods, which tend to underestimate wind speeds. An exception was in directions with lower

wind speeds and gradual reduction in upwind roughness, where the resulting reduced wind shear meant that the *PL* and *LOG* profiles were more appropriate.

Selecting the most appropriate combination of morphometric and wind-speed profile methods meant wind speeds up to 200 m above could be consistently estimated with a median difference of 0 m s^{-1} from observations. However, variability of $\pm 5 \text{ m s}^{-1}$ (approximately 50% of the mean wind speed) for hourly wind estimates was unavoidable, which was attributed to using the profile methods outside of the conditions they were developed for, as well as the actual observed variability of wind speed throughout the vertical profile. The observed variability was possibly caused by the longitudinal and transverse surface heterogeneity upwind resulting in airflow throughout the profile being in equilibrium with different upwind surfaces. However, using the DH_v method which accounts for upwind roughness variability did not notably improve wind-speed estimation.

Few observations from directions with pronounced roughness-element height heterogeneity meant these conditions were not addressed. Consequently, the results pertain to a relatively homogeneous European city centre. There is a requirement for comparisons between extrapolated and observed wind speeds above other urban areas, to inform the appropriateness of both the morphometric and wind-speed profile methods assessed during this work and to inform current engineering standards.

Appendix 4.A: Implementation of DH_v for estimating the wind-speed profile

The DH_v wind-speed profile estimates follow the ESDU (2002) data item 82026 recommendations, which are an implementation of the Deaves (1981) roughness step-change model. However, an adaptation of the method is used, whereby a source area footprint model calculates upwind surface roughness parameters (z_d and z_0) at pre-defined vertical increments (z_l). For each vertical increment the wind-speed profile is determined following ESDU (2002), with locally calculated u_{*r} , roughness correction factor (K_x) and roughness parameters z_d and z_0 (Fig. 4.1). The distance of the upwind roughness change for each vertical increment is taken as the maximum upwind extent of the source area. During the analysis, the vertical increment $z_l = 25$ m is selected, achieving a balance between computational feasibility and capturing upwind roughness change. The implications of varying z_l are discussed in Sect. 4.5.2.2, as are the ‘corrective shifts’ which occur in the wind-speed profile at each height increment (Fig. 4.5).

Given the DH_v method did not lead to the most accurate wind-speed estimates (Fig. 4.9), the z_l value was not revisited. However, Fig. 4.A1 is a reproduction of Fig 4.5, including DH_v estimates with $z_l = 10$ m (Fig. 4.A1 purple line). The comparison demonstrates how as the model resolution is increased (i.e. the value of z_l is reduced), the magnitude of the corrective shifts decrease and a physically plausible model of the wind-speed profile can be achieved. For small enough z_l the shifts can be eliminated, but this is unnecessary given the computational requirements and the effect upon results. For example, the differences in wind-speed estimates at any height between DH_v profiles with $z_l = 25$ m or $z_l = 10$ m (Fig. 4.A1 red and purple lines, respectively) are $< 3\%$, but calculations for the latter require over double the computer processing time.

As with all models, the boundary conditions of development and selected application are important considerations. The DH_v method combines a source area model¹ with a roughness step-change model, but the two models may have positive and/or negative feedbacks on each other. The source area model attempts to provide an integrated representation of the upwind area contributing to surface roughness, whilst the step-change model is based upon distinct upwind surface differences (e.g. differences in z_0 of $> 85\%$) (Deaves 1981). These are factors which are likely to be contributing to the difference between the DH_v estimates and

¹ The source area model is used for the reasons discussed in Sect. 4.2.3.2, as well as the improved accuracy of wind-speed estimates using roughness parameters determined with the Sect. 3.4.3.3 methodology, compared to selecting an area which is assumed reasonable for roughness calculations without source area weighting (see Fig. 7.14 and associated discussion in Sect. 7.6).

observations (Fig. 4.9) (Cook 2018 pers. comm.). Unfortunately, observations to assess the model performance are unavailable between 49 m and 126 m, which due to the proximity to roughness elements is where the wind-speed profile may become more adapted to local geometry (e.g. Millward-Hopkins et al. 2013b) and the more frequent source area calculations (as opposed to distinct roughness changes) may improve estimates. Irrespective, further assessment of methods to consider upwind roughness variability, considering either step-changes (e.g. Deaves 1981) or up-scale/ down-scaling approaches (e.g. Millward-Hopkins et al. 2013b, 2013c) will continue to be valuable for improving wind-speed estimate accuracy.

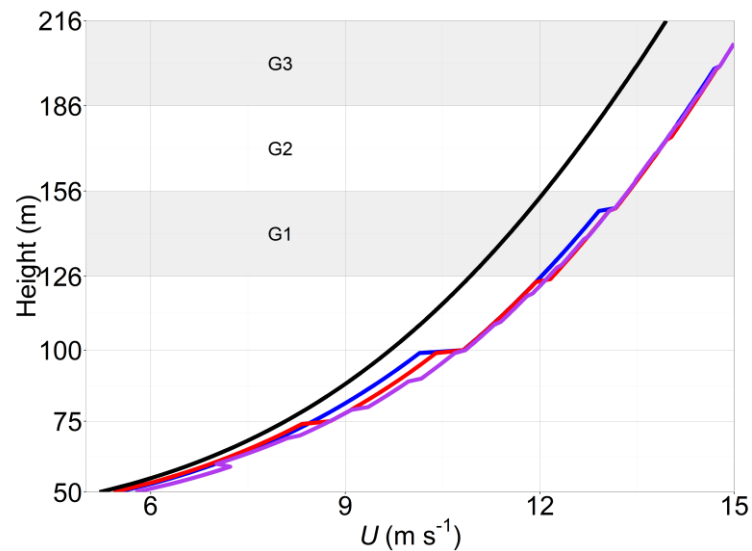


Figure 4.A1: As for Fig. 4.5, but including DH_v profiles with $z_l=10$ m and maximum source area calculation height of 200 m (purple line). For clarity, the comparative profile with $z_l=25$ m and maximum source area calculation height of 150 m (green line in Fig. 4.5) is removed.

Chapter 5. Aerodynamic roughness parameters in cities: inclusion of vegetation¹

Abstract A widely used morphometric method (Macdonald et al. 1998) to calculate the zero-plane displacement (z_d) and aerodynamic roughness length (z_0) for momentum is further developed to include vegetation. The adaptation also applies to the Kanda et al. (2013) morphometric method which considers roughness-element height variability. Roughness-element heights (mean, maximum and standard deviation) of both buildings and vegetation are combined with a porosity corrected plan area and drag formulation. The method captures the influence of vegetation (in addition to buildings), with the magnitude of the effect depending upon whether buildings or vegetation are dominant and the porosity of vegetation (e.g. leaf-on or leaf-off state). Application to five urban areas demonstrates that where vegetation is taller and has larger surface cover, its inclusion in the morphometric methods can be more important than the morphometric method used. Implications for modelling the logarithmic wind profile (to 100 m) are demonstrated. Where vegetation is taller and occupies a greater amount of space, wind speeds may be slowed by up to a factor of three.

5.1 Introduction

During neutral atmospheric stratification, the mean wind speed (\bar{U}_z) at a height z , above a surface can be estimated using the logarithmic wind law (Blackadar and Tennekes 1968, Tennekes 1973):

$$\bar{U}_z = \frac{u_*}{\kappa} \ln\left(\frac{z - z_d}{z_0}\right) \quad (5.1)$$

where u_* is the friction velocity, $\kappa \sim 0.40$ (Högström 1996) is von Karman's constant, z_0 is the aerodynamic roughness length, and z_d is the zero-plane displacement. The aerodynamic roughness parameters (z_d and z_0) can be related to surface geometry using morphometric methods (e.g. Grimmond and Oke 1999, Sect. 3.3.2).

Uncertainties in wind-speed estimations arise from using idealised wind-speed profile relations, as well as representing the surface using only two roughness parameters (z_d and z_0), which are based upon a simplification of surface geometry. Observations are therefore critical to assess the most appropriate methods to determine roughness parameters and wind-speed estimation. Results in Chapters 3 and 4 demonstrate wind-speed estimates up to 200 m above the canopy

¹ This chapter is published as: Kent CW, Grimmond CSB, Gatey D (2017b) *Aerodynamic roughness parameters in cities: inclusion of vegetation*. *Journal of Wind Engineering and Industrial Aerodynamics*: 169:168-176.

in central London (UK) can vary by up to 50% of the mean wind speed at a given height, due to the assumptions inherent to the methods used, as well as flow variability throughout the profile (e.g. Figs. 3.7 and 4.9). However, estimates best resemble observations using morphometric methods which account for roughness-element height variability (specifically, the Millward-Hopkins et al. 2011 and Kanda et al. 2013 methods).

Bluff bodies (e.g. buildings) and porous roughness elements (e.g. vegetation) have different influences upon wind flow (Taylor 1988, Finnigan 2000, Guan et al. 2000, Guan et al. 2003) which need to be accounted for. Although morphometric methods have been developed for only buildings (Sect. 3.3.2.2) or vegetated canopies (e.g. Nakai et al. 2008), existing morphometric methods do not consider both solid and porous bodies (i.e. vegetation) in combination¹.

With the intention of collectively considering buildings and vegetation to determine z_d and z_0 , this work develops the widely-used Macdonald et al. (1998, hereafter *Mac*) morphometric method to include vegetation. The development applies to the more recently proposed Kanda et al. (2013, hereafter *Kan*) development of *Mac* which considers roughness-element height variability. The implications for estimating the logarithmic wind-speed profile (Eq. 5.1) to 100 m above five different urban surfaces are discussed.

5.2 Methodology

5.2.1 Macdonald et al. and Kanda et al. morphometric methods

Morphometric methods traditionally characterise roughness elements by their average height (H_{av}), plan area index (λ_p) and frontal area index (λ_f). The λ_p is the ratio of the horizontal area occupied by roughness elements ('roof' or vegetative canopy, A_p) to total area under consideration (A_T), whereas λ_f is the area of windward vertical faces of the roughness elements (A_f) to A_T . By including the standard deviation (σ_H) and maximum (H_{max}) roughness-element heights, newer methods consider height variability (Millward-Hopkins et al. 2011, Kanda et al. 2013).

The *Mac* method is derived from fundamental principles and without assumptions about wake effects and recirculation zones of solid roughness elements (Macdonald et al. 1998), which vary

¹ Some previous simplified approaches have given attention to vegetation within building-based morphometric methods. Specifically, Bottema (1995), Grimmond and Oke (1999), Holland et al. (2008) and Millward-Hopkins et al. (2013b) include trees, accounting for their porosity by reducing geometric properties by a porosity factor (e.g. 20%). The method developed in this chapter is derived from fundamental principles and includes the combined effect of both buildings and vegetation, with a direct estimation of the drag of vegetated roughness elements (and the variability of drag with porosity).

for porous elements (Wolfe and Nickling 1993, Judd et al. 1996, Sutton and McKenna Neuman 2008; Suter-Burri et al. 2013). The formulation of z_d and z_0 is (Macdonald et al. 1998):

$$Mac_{z_d} = [1 + \alpha_M^{-\lambda_p} (\lambda_p - 1)] H_{av} \quad (5.2)$$

$$Mac_{z_0} = \left(\left(1 - \frac{z_d}{H_{av}} \right) \exp \left[- \left\{ 0.5 \beta_M \frac{C_{Db}}{k^2} \left(1 - \frac{z_d}{H_{av}} \right) \lambda_f \right\}^{-0.5} \right] \right) H_{av} \quad (5.3)$$

where the constant, α_M , is used to control the increase in z_d with λ_p , a drag correction coefficient, β_M , is used to determine z_0 and C_{Db} is the drag coefficient for buildings. Coefficients can be fitted to observations. For example, using Hall et al.'s (1996) wind tunnel data, Macdonald et al. (1998) recommend $C_{Db} = 1.2$ and $\alpha_M = 4.43$, $\beta_M = 1.0$ for staggered arrays; and $\alpha_M = 3.59$, $\beta_M = 0.55$ for square arrays. The staggered array values and $C_{Db} = 1.2$ are used here.

Using large eddy simulations for real urban districts of Japan, Kanda et al. (2013) argue that the upper limit of z_d is H_{max} and therefore:

$$Kan_{z_d} = [c_0 X^2 + (a_0 \lambda_p^{b_0} - c_0) X] H_{max}, \quad X = \frac{\sigma_H + H_{av}}{H_{max}} \quad (5.4)$$

and

$$Kan_{z_0} = (b_1 Y^2 + c_1 Y + a_1) Mac_{z_0}, \quad Y = \frac{\lambda_p \sigma_H}{H_{av}} \quad (5.5)$$

where $0 \leq X \leq 1$, $0 \leq Y$ and a_0 , b_0 , c_0 , a_1 , b_1 and c_1 are regressed parameters with values: 1.29, 0.36, -0.17, 0.71, 20.21 and -0.77, respectively.

5.2.2 Considering vegetation

Although, consideration has been given to treatment of vegetation within building-based morphometric methods (e.g. a reduction of height, Holland et al. 2008) its's flexibility, structure and porosity suggest the effects upon wind flow and aerodynamic roughness are more complex (Finnigan 2000, Nakai et al. 2008). During the method development proposed here, porosity is used, as it is the most common descriptor of the internal structure (Heisler and Dewalle 1988) and relatively easy to determine (Guan et al. 2002, Crow et al. 2007, Yang et al. 2017). Unlike other characteristics (e.g. structure or flexibility), it can be generalised across vegetation types or species with values between 0 (completely impermeable) and 1 (completely porous). Optical (P_{2D}) and volumetric/ aerodynamic (P_{3D}) porosity can be related to each other: $P_{3D} = P_{2D}^{0.40}$ (Guan et al. 2003), $P_{3D} = P_{2D}^{0.36}$ (Grant and Nickling 1998).

The drag of vegetation is also considered, which through absorbing momentum from the wind (Finnigan 2000, Guan et al. 2003, Krayenhoff et al. 2015) can significantly reduce the surface shear stress (τ) (Wolfe and Nickling 1993), as well as reduce the exchange between in-canopy

and above-canopy flow (Gromke and Ruck 2009, Vos et al. 2013). The drag generated by vegetation (Wyatt and Nickling 1997, Grant and Nickling 1998, Gillies et al. 2000, Gillies et al. 2002, Guan et al. 2003) and other porous structures (Seginer 1975, Jacobs 1985, Taylor 1988) varies from that of a solid structure with similar geometry. This variation is more complex than can be resolved by a simple reduction of the frontal area (e.g. Taylor 1988, Guan et al. 2003). Therefore, the changes in drag are directly considered using the drag coefficient.

Typically, morphometric methods use a single drag coefficient for buildings (C_{Db}), whereas here the drag coefficient of vegetation (C_{Dv}) is also used. The nature and type of vegetation (e.g. size, structure, flexibility, leaf type) affect C_{Dv} (Rudnicki et al. 2004). In addition, sheltering and the reconfiguration of shape and leaf orientation under varying flow characteristics means a single value for C_{Dv} may be inappropriate (e.g. Guan et al. 2000, Guan et al. 2003, Vollsinger et al. 2005, Pan et al. 2014). Although attempts have been made to separate the form and viscous components of vegetation drag (e.g. Shaw and Patton 2003), the components tend to be considered in combination (C_{Dv}), as is done here.

The C_{Dv} of foliage typically varies between 0.1 and 0.3 (Katul et al. 2004). From large eddy simulations, Shaw and Schumann (1992) and Su et al. (1998) propose $C_{Dv} = 0.15$. Other numerical simulations suggest $C_{Dv} = 0.25$ (da Costa et al. 2006) and $C_{Dv} = 0.2$ (Zeng and Takahashi 2000) for pine forests. Field studies in boreal canopies (pine, aspen and spruce) indicate C_{Dv} varies between 0.1 and 0.3 (Amiro 1990). A C_{Dv} of 0.2 is commonly used in numerical studies of wind flow in vegetated canopies (Van Renterghem and Botteldooren 2008). Rough- and smooth-surface cylinders (somewhat representative of a tree trunk) have $C_D = 1.2$ (Simiu and Scanlan 1996) or $C_D = 0.8$ (Guan et al. 2000), respectively.

There is evidence that that C_{Dv} varies with wind speed, with higher C_{Dv} at lower wind speeds. Results from wind tunnel studies include: for seven 5.8 – 8.5 m British forest saplings C_{Dv} varied from 0.88 to 0.15 when wind speeds were between 9 and 26 m s⁻¹ (Mayhead 1973); for 2.5 – 5 m tall conifer saplings with wind speeds between 4 and 20 m s⁻¹ C_{Dv} varied between 1.5 to 0.2 (Rudnicki et al. 2004); and, for five hardwood species C_{Dv} varied between 1.02 and 0.1 (Vollsinger et al. 2005). Conclusions are similar in the field, where Koizumi et al. (2010) report C_{Dv} for three poplar tree crowns varying from 1.1 to 0.1 with wind speeds between 1 and 15 m s⁻¹. These results indicate at high wind speeds the relative drag of an individual tree ($C_{Dv} \sim 0.1 - 0.2$) is small compared to that of buildings, but during some flow conditions C_{Dv} can approach that of a solid structure of similar shape (i.e. 1.2) and therefore exert similar drag to buildings.

The state of foliage on a tree (i.e. porosity) influences the amount of drag exerted on the flow. Koizumi et al.'s (2010) field observations at wind speeds of 10 m s^{-1} found C_{Dv} to over halve when tree crowns are defoliated (i.e. more porous). Current understanding of C_{Dv} variability with porosity is based upon artificial (i.e. two-dimensional) and natural (i.e. tree or tree model) wind break studies. Hagen and Skidmore (1971) found C_{Dv} to be similar to single tree values: $C_{Dv} \sim 0.5$ for one row deciduous windbreaks and $C_{Dv} \sim 0.6 - 1.2$ for coniferous windbreaks. Guan et al.'s (2003, their Table 4) synthesis of C_{Dv} for two-dimensional structures or naturally vegetated windbreaks of varying porosity provides a relation between C_{Dv} and porosity (P_{3D}):

$$C_{Dv} = 1.08(1 - P_{3D}^{1.8}) \quad (5.6)$$

Similarly, for an isolated model tree, Guan et al. (2000) show:

$$C_{Dv} = -1.251P_{3D}^2 + 0.489P_{3D} + 0.803 \quad (5.7)$$

Results of previous studies (summarised in Fig. 5.1) indicate that more impermeable roughness elements (i.e. $P_{3D} = 0$) tend to have the largest C_{Dv} , approaching that of a solid structure (0.8–1.2). As aerodynamic porosity increases, C_{Dv} decreases approximately as a power function to zero for an open surface (i.e. $P_{3D} = 1$). Observations by Grant and Nickling (1998) for a single conifer tree (Fig. 5.1, GN) and wind tunnel studies by Guan et al. (2000) support evidence that the relation may peak at critical porosities (Grant and Nickling 1998, Gillies et al. 2002).

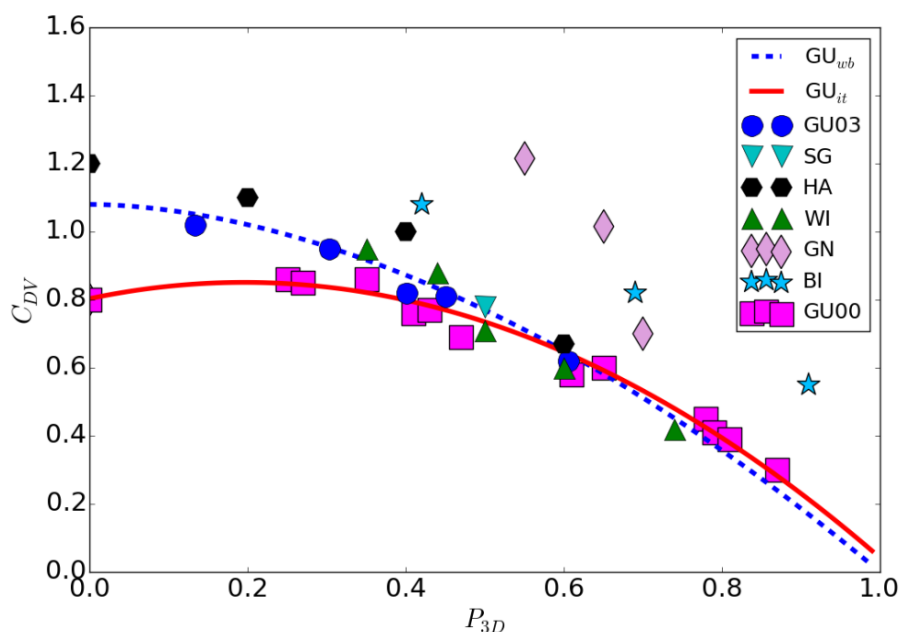


Figure 5.1: Relation between the drag coefficient of porous roughness elements (C_{Dv}) and porosity (P_{3D}), data from: Hagen and Skidmore (1971) (HA); Wilson (1985) (WI); Seginer (1975) (SG); Grant and Nickling (1998) (GN); Bitog et al. (2011) (BI), Guan et al. (2000) (GU00) and Guan et al. (2003) (GU03). Lines are relations from Guan et al. (2003) (GU_{ub} , Eq. 5.6) and Guan et al. (2000) (GU_{it} , Eq. 5.7)

5.2.3 Parameter determination and method development

In the methodology proposed here, the H_{av} , H_{max} and σ_H of all roughness elements (i.e. buildings and vegetation) are determined.

Porosity is accounted for when determining λ_p as vegetation has openings in the volume it occupies. The plan area of vegetation (A_{pv}) is reduced by a porosity factor (i.e. $1 - P_{3D}$). The λ_p of both buildings and porous vegetation becomes:

$$\lambda_p = \frac{\sum_{i=1}^n A_{pbi} + \sum_{j=1}^n (1 - P_{3D}) A_{pvj}}{A_T} \quad (5.8)$$

where A_{pb} is the plan area of buildings and i or j refers to each individual built or vegetated roughness element, respectively.

The *Mac* method (Sect. 5.2.1) considers the drag balance at the top of a group of homogeneous roughness elements (of height z) approached by a logarithmic wind profile. If the roughness elements are of variable height, z is replaced by their average height (H_{av}) (Macdonald et al. 1998). Numerical models demonstrate the relative impact of trees and buildings represented by the drag coefficient are not affected by each other and neither is the spatially-averaged flow (Krayenhoff et al. 2015). Therefore, the total surface drag (F_D) can be determined as a combination of the drag from buildings (F_{Db}) and vegetation (F_{Dv}). Using the unsheltered frontal areas of buildings (A_{fb}^*), the drag at the building tops (height H_{av}) can be written (e.g. Millward-Hopkins et al. 2011):

$$F_{Db} = 0.5\rho C_{Db} U_z^2 A_{fb}^* \quad (5.9)$$

and similarly, for still-air impermeable vegetation (A_{fv}^*) the drag on vegetation (F_{Dv}) is:

$$F_{Dv} = 0.5\rho C_{Dv} U_z^2 A_{fv}^* \quad (5.10)$$

with ρ the density of air. The total drag of both the buildings and vegetation per unit area is therefore:

$$\tau = \frac{F_{Db} + F_{Dv}}{A_T} = \rho u_*^2 = \frac{0.5\rho C_{Db} U_z^2 A_{fb}^* + 0.5\rho C_{Dv} U_z^2 A_{fv}^*}{A_T} \quad (5.11)$$

As the *Mac* method assumes the drag below the zero-plane displacement is negligible, the unsheltered frontal area exerting drag on the flow consists of only roughness-element frontal area above z_d . Therefore, Mac_{z_d} is calculated (Eq. 5.2) with the influence of vegetation incorporated through H_{av} and in the porosity parameterisation used in λ_p (Eq. 5.8). Since all roughness elements are assumed homogeneous in height, the relation between the unsheltered frontal areas of buildings and vegetation (A_{fj}^*) and their actual frontal areas (A_f) is:

$$A_f = \frac{z}{z - z_d} A_f^* \quad (5.12)$$

The unsheltered frontal areas (A_{fb}^* and A_{fv}^*) in Eq. 5.11 can be replaced by actual frontal areas (A_{fb} and A_{fv}):

$$\frac{0.5\rho C_{Db} U_z^2 \left(1 - \frac{z_d}{z}\right) A_{fb} + 0.5\rho C_{Dv} U_z^2 \left(1 - \frac{z_d}{z}\right) A_{fv}}{A_T} = \rho u_*^2 \quad (5.13)$$

Common factors are removed from the numerator on the left-hand side of Eq. 5.13. To state Eq. 5.13 in terms of C_{Db} only, the ratio of C_{Dv} and C_{Db} is used (P_v). Using the variation of C_{Dv} with porosity for a single tree, the Guan et al. (2000) relation (Eq. 5.7) gives:

$$P_v = \frac{C_{Dv}}{C_{Db}} = \frac{-1.251P_{3D}^2 + 0.489P_{3D} + 0.803}{C_{Db}} \quad (5.14)$$

Accounting for differential drag imposed by buildings and vegetation through P_v , Eq. 5.13 may then be written:

$$0.5\rho C_{Db} U_z^2 \left(1 - \frac{z_d}{z}\right) \frac{\{A_{fb} + (P_v)A_{fv}\}}{A_T} = \rho u_*^2 \quad (5.15)$$

When substituted into the logarithmic wind law (Eq. 5.1), cancellation and inclusion of the drag correction coefficient (β_M) proposed by Macdonald et al. (1998) provides z_0 :

$$\frac{z_0}{z} = \left(1 - \frac{z_d}{z}\right) \exp \left[- \left(\frac{1}{k^2} 0.5\beta_M C_{Db} \left(1 - \frac{z_d}{z}\right) \frac{\{A_{fb} + (P_v)A_{fv}\}}{A_T} \right)^{-0.5} \right] \quad (5.16)$$

Equation 5.16 is analogous to Macdonald et al.'s (1998) (Eq. 5.3). However, the frontal area of buildings and vegetation are determined separately and P_v is included within the λ_f term to describe the differential drag of buildings and vegetation of varying porosity.

It should be noted that the calculated frontal area of vegetation A_{fv} is independent of porosity. A_{fv} is determined assuming a solid structure with the same dimensions. Vegetation's influence upon z_0 is a consequence of the change in the drag coefficient for vegetation with porosity (P_v , Eq. 5.14). Additionally, β_M is observed to be unity for staggered arrays of solid cubes. Without further experimentation upon arrays consisting of porous and solid roughness elements it is inappropriate to apply the drag correction to arrays including vegetation. Therefore, if any value other than unity is used for β_M , P_v should be further reduced:

$$P_v = \frac{-1.251P_{3D}^2 + 0.489P_{3D} + 0.803}{\beta_M C_{Db}} \quad (5.17)$$

5.2.4 Demonstration of impact

Behaviour of the parameterisation is demonstrated for five study areas selected from a surface elevation database for Greater London (Lindberg and Grimmond 2011a). Study areas are

selected to characterise different urban spaces in a European city (roughness elements with heights > 2 m): city centre with low vegetation (Fig. 5.2a, CC_lv), city centre with similar building and vegetation height (Fig. 5.2b, CC_hv), suburban area with low vegetation (Fig. 5.2c, Sb_lv), suburban area with tall vegetation (Fig. 5.2d, Sb_hv) and an urban park (Fig. 5.2e, Pa).

Geometric and aerodynamic parameters for each study area are calculated iteratively (Sect. 3.4.3.3 methodology) using the Kormann and Meixner (2001) analytical source area footprint model. For each study area, the same meteorological conditions observed by a CSAT3 sonic anemometer (Campbell Scientific, USA) in central London (King's College London, Strand Campus, height 50.3 m above ground level, see Kotthaus and Grimmond 2012, 2014a, b for methods) are used. The median meteorological conditions of the fastest 25% of winds in 2014 (30-min averages) are used. Inputs to the footprint model are: measurement height (z_m) = 50.3 m; standard deviation of the lateral wind velocity (σ_v) = 1.97 m s⁻¹, Obukhov length (L) = - 1513 m; $u_* = 0.94$ m s⁻¹; wind direction 210°; z_d and z_0 . Source area calculations are initiated with open country values ($z_d = 0.2$ m, $z_0 = 0.03$ m) as the final aerodynamic parameters are insensitive to these values (Sect. 3.4.3.3). The source area analysed here is the cumulative total of 80% of the total source area.

Dynamic response of the source areas during the iterative procedure modifies the surface area considered. The initial source area is overlain upon the surface elevation databases (buildings and vegetation) for each study area and a weighted geometry is calculated, based upon the fractional contribution of each grid square in the source area. Source area specific aerodynamic parameters are determined, which are the input to the next iteration (the meteorological conditions and measurement height remain constant). Both buildings and vegetation are considered, assuming a leaf-on porosity of $P_{3D} = 0.2$, and leaf-off porosity of $P_{3D} = 0.6$ (more porous) (Heisler 1984; Heisler and DeWalle 1988, Grimmond and Oke 1999).

Variations in meteorological conditions between sites probably occur, however the objective to obtain representative study areas (Fig. 5.2a-e, Table 5.1) means the assumption of constant conditions is treated as reasonable. The resulting geometry and (Mac and Kan) aerodynamic parameters are compared for each study area (Sect. 5.3.1 and 5.3.2).

Using the logarithmic wind law (Eq. 5.1) the implications of considering vegetation during wind-speed estimation close to the surface are then assessed (Sect. 5.3.3). Using the z_d and z_0 determined for buildings only, or both buildings and vegetation, for the five study areas, wind speeds are extrapolated from $z_d + z_0$ to 100 m using Eq. 5.1. For consistency, at $z_d + z_0$ it is

assumed the wind speed is 0 m s^{-1} and throughout the profile the previously stated central London friction velocity ($u_* = 0.94 \text{ m s}^{-1}$) is assumed. Although choosing a different value of u_* will have implications for the estimated wind speeds, the relative magnitude of change for each profile is the same and therefore so are the percentage differences between profiles. The objective is to demonstrate the implications of considering (or not) vegetation for each morphometric method and study area, as opposed to providing a comparison between the study areas.

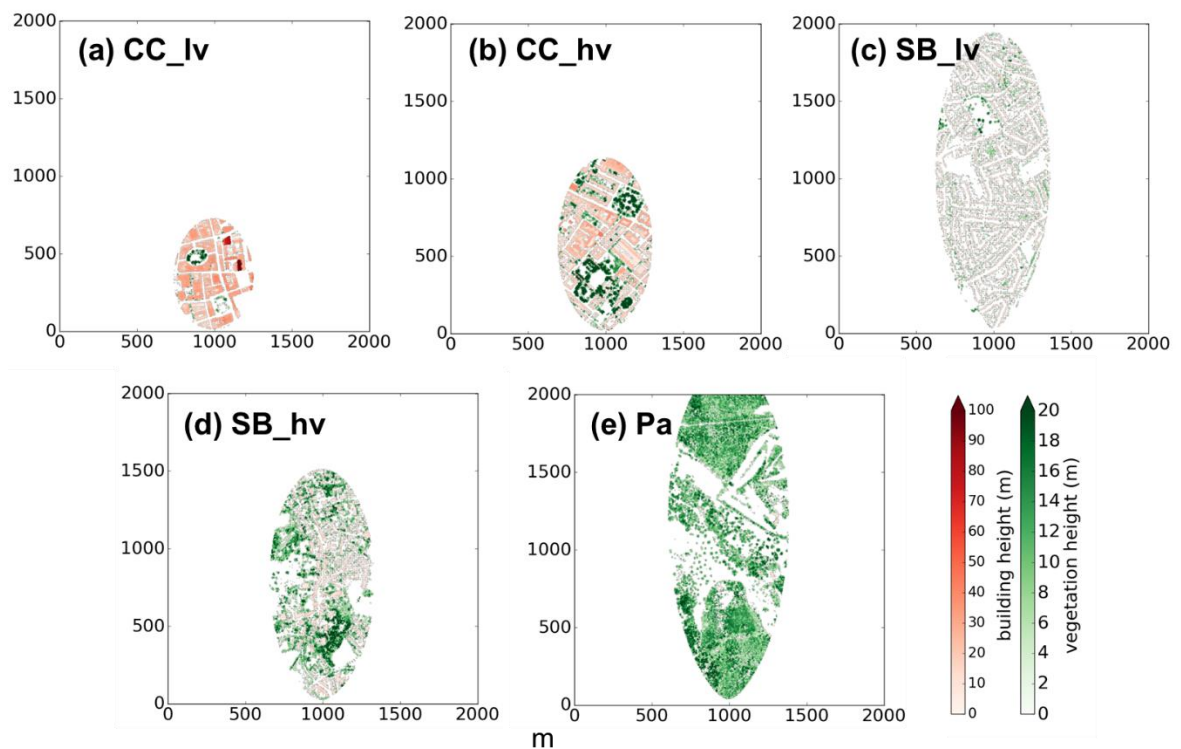


Figure 5.2: Study areas representative of: **(a)** city centre with low vegetation (CC_lv), **(b)** city centre with similar building and vegetation heights (CC_hv), **(c)** suburban with low vegetation (Sb_lv), **(d)** a suburban with taller vegetation (Sb_hv) and **(e)** an urban park (Pa). Source areas determined using the iterative methodology in Sect. 3.4.3.3, rotated into the wind direction (210°). Colour indicates roughness-element type and hue its height (see key)

5.3 Results

5.3.1 Geometric parameters

Obviously, the influence of vegetation and buildings upon geometric parameters depends upon the dominant roughness elements: when buildings dominate (CC_lv and CC_hv), height based geometric parameters for all roughness elements (both buildings and vegetation) are determined by buildings (Table 5.1); and, if vegetation is taller than buildings (SB_hv and Pa), the H_{av} , H_{max} and σ_H of all roughness elements become noticeably larger than $H_{av,b}$, $H_{max,b}$ and $\sigma_{H,b}$ (Table 5.1, subscript b denotes buildings only). In all study areas, the effect of vegetation increases both plan and frontal areas, which is expectedly more obvious for leaf-on than leaf-

off values. In CC_lv the plan and frontal area indexes of vegetation ($\lambda_{p,v}$ and $\lambda_{f,v}$) are effectively negligible. Elsewhere the taller and higher proportion of vegetation means $\lambda_{p,v}$ and $\lambda_{f,v}$ are greater than or similar to that of buildings ($\lambda_{p,b}$ and $\lambda_{f,b}$). This means plan and frontal areas calculated for all roughness elements can be double or larger than that for buildings alone (Table 5.1, SB_hv and CC_hv).

Leaf state has a greater impact upon plan than frontal area, with mean differences of 0.12 ($\lambda_{p,l-on} - \lambda_{p,l-off}$) and 0.04 ($\lambda_{f,l-on}$ and $\lambda_{f,l-off}$), respectively, across the five study areas (subscripts *l-on* and *l-off* refer to leaf-on or off vegetation state, respectively). As this difference is proportional to the amount of vegetation present, it is maximum in Pa where leaf-on plan area index is approximately double leaf-off (0.6 and 0.3, respectively).

Implications of ignoring vegetation (i.e. only considering buildings) are most obvious in Pa. Here the plan and frontal area of buildings approach 0, whilst $\lambda_{f,v}$ is 0.41 and $\lambda_{p,v}$ ranges between 0.3 and 0.59 for leaf-off and leaf-on porosity, respectively (Table 5.1). The average height of buildings is only 5.8 m with a maximum of 16.5 m. However, the average height of vegetation ($H_{av,v}$) is almost as large as the tallest building (11.4 m) and maximum tree height ($H_{max,v}$) is 29 m. Therefore, the geometry in Pa is primarily determined by the vegetation characteristics (Table 5.1).

5.3.2 Aerodynamic parameters

For aerodynamic parameter determination, the geometric parameters within the morphometric methods (e.g. Kan considers height variability) are important, in addition to the dominance of either buildings or vegetation. For a heterogeneous group of roughness elements Kan_{z_d} is typically twice as large as Mac_{z_d} at all densities. Mac_{z_0} is observed to be larger than Kan_{z_0} at λ_f below ~ 0.25 , beyond which Kan_{z_0} is larger (Fig. 3.1).

Generally, accounting for vegetation (with buildings) increases z_d because the increase in plan area acts to 'close' the canopy and therefore lift the zero-plane displacement (Table 5.2). The effect is most obvious during leaf-on and where there is a higher density of vegetation (SB_hv, Pa). This creates a greater than 40% difference between z_d calculated for buildings alone and the combined case (buildings and vegetation). CC_lv is the only area where considering vegetation reduces z_d because a small increase in λ_p is offset by a reduction in H_{av} (Table 5.2). Leaf-on z_d is always greater than leaf-off, but the difference is less obvious for the Kan method as height variability (in addition to λ_p) is accounted for.

Kan_{z_d} is consistently the order of H_{ov} (or larger) and typically over double Mac_{z_d} (Table 5.2). The range of percentage change for z_d caused by vegetation inclusion and its state (Table 5.3) are over half the inter-method variability of Kan_{z_d} and Mac_{z_d} (Table 5.4). This implies the priority of decisions for determination of z_d is firstly selection of the appropriate morphometric method, followed by the inclusion of vegetation and then its state (leaf-on or leaf-off). An exception is in Pa, where vegetation has the largest effect.

The effect of considering vegetation for z_0 depends upon: the height based geometric parameters, the increase in λ_f and λ_p ; and the associated change in z_d . The inter- and intra-method differences of Mac and Kan depend upon their response to changes in λ_f . Both methods indicate z_0 increases from zero to a maximum value at a critical λ_f (λ_{f-crit}), after which z_0 decreases again (Fig. 3.1). For Mac_{z_0} , λ_{f-crit} is between $\sim 0.15 - 0.25$ and for Kan_{z_0} this is 0.2 to 0.4. At larger λ_f , there is a steeper decline in Mac_{z_0} than Kan_{z_0} .

When an already large built frontal area is further increased due to the vegetation (CC_lv, CC_hv), leaf-on z_0 becomes smaller for both methods as there is a shift further away from λ_{f-crit} . For both CC_lv and CC_hv the percentage changes are larger for Mac_{z_0} than Kan_{z_0} given the sensitivity of the former to changes of λ_f . The reduction is greater for leaf-on because of the larger λ_f (Table 5.1).

In locations with low built frontal areas (Table 5.1, SB_hv, SB_lv) the inclusion of vegetation should increase Mac_{z_0} and Kan_{z_0} given they move towards λ_{f-crit} . This is true for Kan_{z_0} , most obviously in SB_hv (17% difference for leaf-on and 47% for leaf-off, Table 5.3), where vegetation is more dominant and H_{max} , σ_H and λ_p become obviously larger. However, for Mac_{z_0} , the λ_f increase is offset by a concurrent reduction of H_{ov} (Table 5.1) and increase in z_d (Table 5.2). Therefore Mac_{z_0} decreases for leaf-on conditions, but is similar for leaf-off. For Pa, inclusion of vegetation means $Mac_{z_0,b}$ and $Kan_{z_0,b}$ both increase from 0 m to 0.18 and 0.32 m, respectively during leaf-on, and to 0.99 and 0.92 m, respectively for leaf-off (Table 5.2). If only buildings are considered, the variability between $Kan_{z_0,b}$ and $Mac_{z_0,b}$ is less than 35% in all study areas apart from CC_lv, where $Kan_{z_0,b}$ is more than double $Mac_{z_0,b}$ because of the large $\lambda_{f,b}$ (~ 0.5).

Area	All							Vegetation					Buildings					
	H_{av}	H_{max}	σ_H	$\lambda_{p,l-on}$	$\lambda_{p,l-off}$	$\lambda_{f,l-on}^1$	$\lambda_{f,l-off}^1$	$H_{av,v}$	$H_{max,v}$	$\sigma_{H,v}$	$\lambda_{p,v,l-on}$	$\lambda_{p,v,l-off}$	$\lambda_{f,v}$	$H_{av,b}$	$H_{max,b}$	$\sigma_{H,b}$	λ_p	λ_f
CC_lv	23.50	125.00	15.00	0.54	0.52	0.52	0.51	10.90	35.00	8.78	0.03	0.01	0.04	24.50	125.00	15.00	0.51	0.49
CC_hv	14.90	46.60	7.99	0.48	0.37	0.42	0.37	15.70	34.00	7.47	0.21	0.11	0.26	14.10	46.60	8.22	0.27	0.23
SB_lv	5.34	27.80	2.64	0.29	0.25	0.18	0.17	4.82	27.80	3.46	0.08	0.04	0.08	5.58	16.60	2.00	0.21	0.13
SB_hv	10.80	33.30	5.37	0.47	0.33	0.33	0.28	11.60	33.30	5.78	0.29	0.14	0.29	9.12	28.10	3.75	0.18	0.12
Pa	11.30	29.00	4.67	0.60	0.30	0.29	0.22	11.40	29.00	4.63	0.59	0.30	0.41	5.75	16.50	2.39	0.00	0.00

¹ $\lambda_{f,l-on}$ and $\lambda_{f,l-off} = \left[\frac{(A_{fb} + (P_v)A_{fv})}{A_T} \right]$, assuming a leaf-on and leaf-off porosity, respectively

Table 5.1: Geometric parameters determined for: all roughness elements; vegetation only; and buildings only, in the five study areas (Fig. 5.2). H_{av} , H_{max} and σ_H are the average, maximum and standard deviation of roughness-element heights (in metres), respectively, λ_p is plan area index and λ_f is frontal area index. Subscripts: *v* for vegetation, *b* for buildings, *l-on* for leaf-on and *l-off* for leaf-off

Area	Mac						Kan					
	z_0			z_d			z_0			z_d		
	Buildings	All		Buildings	All		Buildings	All		Buildings	All	
	<i>l-on</i>	<i>l-off</i>		<i>l-on</i>	<i>l-off</i>		<i>l-on</i>	<i>l-off</i>		<i>l-on</i>	<i>l-off</i>	
CC_lv	1.21	1.01	1.10	18.84	18.67	18.41	2.96	2.86	2.98	44.53	44.34	43.94
CC_hv	1.48	0.78	1.30	7.19	11.11	9.57	1.62	1.44	1.78	19.92	24.65	22.72
SB_lv	0.48	0.41	0.48	2.36	2.88	2.58	0.37	0.42	0.44	6.29	7.56	7.22
SB_hv	0.89	0.49	0.98	3.42	7.91	6.28	0.68	0.80	1.10	10.16	17.25	15.29
Pa	0.00	0.18	0.99	0.05	9.44	6.24	0.00	0.32	0.92	2.07	18.33	14.58

Buildings	
All	leaf-on
	leaf-off

Table 5.2: Aerodynamic parameters determined using the Macdonald et al. (1998, *Mac*) and Kanda et al. (2013, *Kan*) morphometric methods in the five study areas (Fig. 5.2). Parameters are determined for buildings only and for all roughness elements (both buildings and vegetation), with leaf-on (*l-on*) and leaf-off (*l-off*) vegetation

(a) <i>Mac</i>	z_0			z_d		
	<i>b, l-on</i>	<i>b, l-off</i>	<i>l-on, l-off</i>	<i>b, l-on</i>	<i>b, l-off</i>	<i>l-on, l-off</i>
CC_lv	18.37	9.88	8.53	0.86	2.31	1.45
CC_hv	62.48	13.53	50.00	42.75	28.30	14.91
SB_lv	15.47	0.51	14.96	19.72	8.90	10.87
SB_hv	57.25	10.01	66.31	79.37	59.08	22.98
Pa	-	-	137.58	197.90	196.83	40.73
(b) <i>Kan</i>	z_0			z_d		
	<i>b, l-on</i>	<i>b, l-off</i>	<i>l-on, l-off</i>	<i>b, l-on</i>	<i>b, l-off</i>	<i>l-on, l-off</i>
CC_lv	3.68	0.44	4.12	0.42	1.32	0.90
CC_hv	11.67	9.47	21.08	21.22	13.12	8.16
SB_lv	12.57	18.10	5.56	18.37	13.78	4.62
SB_hv	16.70	46.76	30.66	51.74	40.36	12.01
Pa	-	-	96.76	159.38	150.23	22.80

% difference
< 10
10 < % < 25
25 < % < 50
50 < % < 100
> 100

Table 5.3: Percentage difference in aerodynamic parameters calculated using the (a) Macdonald et al. (1998, *Mac*) and (b) Kanda et al. (2013, *Kan*) morphometric methods from Table 5.2, between: buildings (x) and all roughness elements (y) assuming a leaf-on porosity (*b, l-on*); buildings (x) and all roughness elements (y) assuming a leaf-off porosity (*b, l-off*) and for all roughness elements assuming a leaf-on (x) or leaf-off porosity (y) (*l-on, l-off*). Percentage difference = $\frac{|x-y|}{(x+y)/2} \times 100$

Leaf-on z_0 is consistently smaller than leaf-off for both morphometric methods as a consequence of both λ_f and z_d increasing. The greater sensitivity of Mac_{z_0} to λ_f results in a percent difference that is twice that of Kan_{z_0} , except in Pa where both experience large increases (Table 5.3). During leaf-off, areas with λ_f similar to λ_{f-crit} (e.g. SB_lv, SB_hv) have mean inter-method variability of < ~10%. Whereas if there are already high λ_f (SB_hv, CC_hv and CC_lv), an increase in λ_f with leaf-on vegetation causes inter-method variability to increase, ranging between 48 – 95% (Table 5.4).

Therefore, if buildings dominate (e.g. CC_hv) selection of the appropriate morphometric method is more critical (causing a larger percentage difference in z_0) than if vegetation is included. The inclusion of vegetation increases inter-method variability between the two morphometric methods (e.g. CC_hv and CC_lv). Where there is more vegetation, its inclusion and state (leaf-on or off), is as or more important than the inter-method variability in z_0 . This is especially true for Pa.

Area	Buildings		All			
			<i>l-on</i>		<i>l-off</i>	
	z_0	z_d	z_0	z_d	z_0	z_d
CC_lv	83.69	81.09	95.47	81.46	92.03	81.91
CC_hv	8.44	93.88	59.54	75.76	31.22	81.49
SB_lv	26.33	90.68	1.61	89.60	7.81	94.53
SB_hv	26.65	99.31	47.88	74.19	10.81	83.52
Pa	34.07	190.60	53.76	64.09	8.10	80.10

% difference
< 10
10 < % < 25
25 < % < 50
50 < % < 100
> 100

Table 5.4: Percentage difference in aerodynamic parameters calculated using the Macdonald et al. (1998, *Mac*) (x) or Kanda et al. (2013, *Kan*) (y) morphometric methods from Table 5.2, for buildings only and all roughness elements assuming a leaf-on porosity (*l-on*) and leaf-off porosity (*l-off*). Percentage difference = $\frac{|x-y|}{(x+y)/2} \times 100$

5.3.3 Influence of considering vegetation upon wind-speed estimates

Accurately modelling the spatially- and temporally- averaged wind-speed profile above urban surfaces is critical for numerous applications, including dispersion studies and wind load determination. Various methods to estimate the wind-speed profile exist, each developed from different conditions and with different inherent assumptions (e.g. Sect. 4.2). However, the aerodynamic roughness parameters (z_d and z_0) are consistently used to represent the underlying surface. Although only two methods to determine the roughness parameters are used here (*Mac* and *Kan*), a range of methods exist which can influence wind-speed estimations (Sect. 3.6).

Using the logarithmic wind law (Eq. 5.1) without extrapolation from a reference wind speed at a reference height (i.e. Eq 3.25), wind-speeds estimated using the *Kan* method tend to be less than those using *Mac* (Fig. 5.3a-e) because of the considerably larger Kan_{z_d} . Notably, where z_d is largest in magnitude (e.g. CC_lv, Table 5.2) wind speeds at 100 m calculated using the *Kan* or *Mac* aerodynamic parameters vary between 36 and 39% of each other (depending on vegetation state). Elsewhere, extrapolated wind speeds tend to be more similar, and the least variable aerodynamic parameters in SB_lv and SB_hv mean wind speeds at 100 m vary by less than 4% and 12%, respectively.

The difference in wind speed when both buildings and vegetation are accounted for (Fig. 5.3, dashed lines), in comparison to buildings alone (Fig. 5.3, solid lines) is least where buildings dominate. For example, in CC_lv and SB_lv vegetation has little effect and regardless of its state causes a maximum wind-speed variation of < 5% for each respective morphometric method.

Consideration of vegetation in the morphometric methods has a greater influence upon predicted wind speeds where vegetation is taller and more abundant (e.g. CC_hv, SB_hv and Pa). In addition, vegetation state (i.e. leaf-on or leaf-off) is more influential upon wind speeds in these areas. Despite z_d increasing with inclusion of vegetation, there is greater inter- and intra-method variability in z_0 (Sect. 5.3.2). Therefore, because estimated wind profiles are a function of both z_d and z_0 no general comment can be made about wind-speed changes when including vegetation.

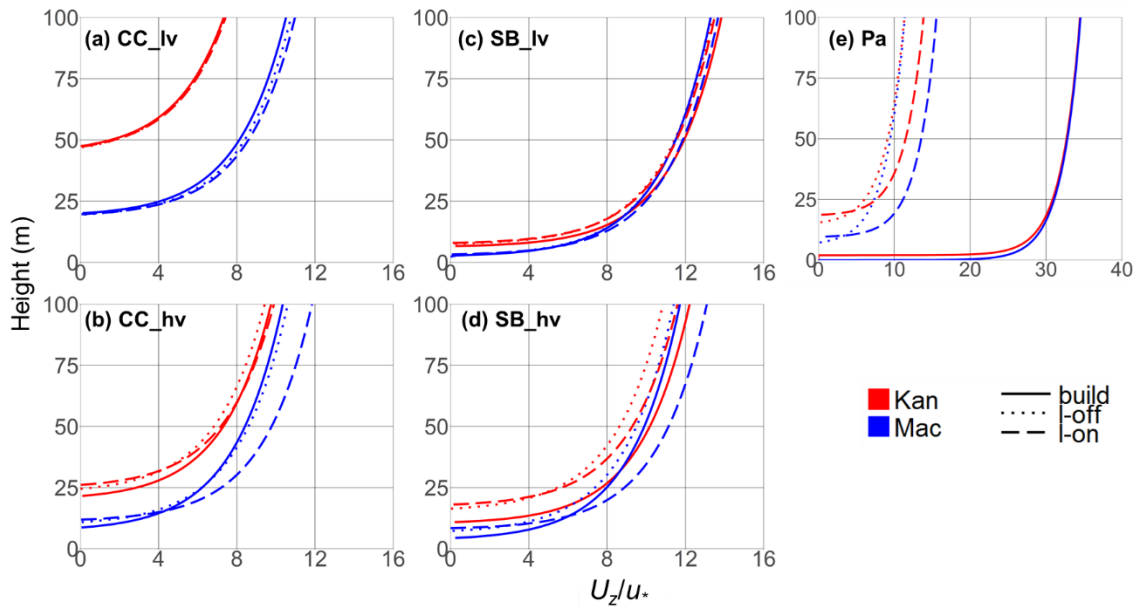


Figure 5.31: Logarithmic wind-speed profiles (using Eq. 5.1) from $z = z_d + z_0$ to $z = 100$ m, using z_d and z_0 determined for five study areas: **(a)** city centre with low vegetation (CC_lv), **(b)** city centre with similar building and vegetation heights (CC_hv), **(c)** a suburb with low vegetation (Sb_lv), **(d)** a suburb with taller vegetation (Sb_hv) and **(e)** a park (Pa). Wind speed at the bottom of the profile ($z_d + z_0$) is assumed 0 m s^{-1} and friction velocity (u_*) 0.94 m s^{-1} throughout the profile. Wind speeds are normalised by u_* (U_z/u_*). Aerodynamic parameters are determined using the Kanda et al. (2013) (*Kan*) and Macdonald et al. (1998) (*Mac*) morphometric methods (different colours) for each study area, considering buildings only (solid line), including vegetation with leaf-off porosity (short dashed line) and leaf-on porosity (long dashed line) (values in Table 5.2). Note different x scale on **(e)**

Vegetation's effect is most noticeable in Pa. High wind speeds when only buildings are considered (because of low z_d and z_0) are reduced by almost a factor of three upon consideration of vegetation (Fig. 5.3e). The reduction in wind speed is more obvious for leaf-off porosities, because of the larger associated z_0 . In CC_hv and SB_hv the effect of vegetation is less obvious, however a decrease in z_0 means wind speeds extrapolated using the *Mac* parameters increase. In contrast, wind speeds extrapolated using the *Kan* parameters tend to decrease because of the larger z_d and lesser sensitivity to changes in z_0 (Sect. 5.3.2)

In summary, when buildings dominate (CC_lv) the morphometric method chosen to determine the wind profile (i.e. *Mac* or *Kan*) is more important than whether vegetation is considered. In contrast, where vegetation is taller and accounts for a greater surface area (CC_hv, SB_hv and especially Pa) vegetation's consideration has larger implications for wind-speed estimation than the morphometric method used. In all cases, the differences between leaf-on and leaf-off wind speed are larger for the *Mac* than *Kan* method, because of the sensitivity of *Mac* to the porosity parameterisation.

¹Note this differs from Kent et al. (2017b) where \log_{10} is used. This difference in graphical presentation does not impact the results or in-text discussion as percentage differences between the profiles are referred to.

5.4 Conclusions

Vegetation should be included in morphometric determination of aerodynamic parameters, but not in the same way as solid structures. A methodology is proposed to include vegetation in Macdonald et al.'s (1998) morphometric method to determine the zero-plane displacement (z_d) and aerodynamic roughness length (z_0). This also applies to Kanda et al.'s (2013) extension, which considers roughness-element height variability.

The proposed methodology considers the average, maximum and standard deviation of heights for all roughness elements (buildings and vegetation). The plan area index and frontal area index of buildings and vegetation are determined separately (and subsequently combined for use in the morphometric methods). Aerodynamic porosity is used to determine the plan area of vegetation. Whereas, the frontal area index of vegetation is determined assuming a solid structure with the same dimensions. During determination of z_0 a parameterisation of the drag coefficient for vegetation is used, accounting for varying porosity. This follows literature that demonstrates the drag exerted by trees can be like that of a solid structure and decreases as porosity increases (Grant and Nickling 1998, Guan et al. 2000, Vollsinger et al. 2005, Koizumi et al. 2010). The relation between the drag coefficient and porosity of an individual tree (Guan et al. 2000) is used as the basis for the parameterisation, which other experimental data demonstrate is reasonable.

From analysis of five different urban areas within a European city, the effect of the inclusion of vegetation on geometric and aerodynamic parameters depends upon whether buildings or vegetation are the dominant roughness element. Where buildings are taller they control the height-based geometric parameters. The opposite is true when vegetation is taller. Inclusion of vegetation increases the plan area index (λ_p) and frontal area index (λ_f), most obviously during leaf-on periods.

The increases in λ_p and λ_f from inclusion of vegetation more obviously affect aerodynamic parameters than the change in height based geometric parameters. The higher λ_p produces a larger z_d for both morphometric methods in four study areas. In the fifth case, a reduction in average height offsets the increase in λ_p . The increase in z_d is largest for leaf-on because of the higher λ_p , as well as where vegetation is taller and more significant because of the greater increase in λ_p and H_{av} . Given the large inter-method variability in z_d , selection of the appropriate morphometric method is most critical, followed by whether vegetation is considered, then by the vegetation state (leaf-on or leaf-off).

Inclusion of the effect of vegetation on z_0 depends upon: the geometric parameters determined without vegetation and the associated λ_f that the peak z_0 occurs for each morphometric method. Therefore, a broad statement about how z_0 responds to vegetation inclusion is difficult. However, the change in z_0 is more obvious where vegetation is taller and takes up a large proportion of area. In the same areas, whether vegetation is included and its state (i.e. porosity) is as, or more important, than the inter-method variability in z_0 determined by the morphometric methods. Leaf-on z_0 is consistently smaller than leaf-off, because of the combined increase in λ_f and z_0 which create an effectively smoother surface.

Assuming a logarithmic wind profile, the influence on estimated wind speed up to 100 m is least when vegetation is lower and accounts for a smaller proportion of surface area, with wind speed varying by < 5% regardless of consideration of vegetation. In contrast, wind speeds above an urban park are demonstrated to be slowed by up to a factor of three (both methods). Therefore, if vegetation is taller and more abundant, vegetation's inclusion is as, or more, critical for wind-speed estimation than the morphometric method used.

Of course, the ultimate assessment of the parameterisation for accurate aerodynamic parameter and wind-speed estimation is comparison to observations. A later assessment of the parameterisation, demonstrates the inclusion of vegetation (in addition to buildings) captures the seasonal change in aerodynamic parameters and improves wind-speed estimates (Sect. 6). Undoubtedly, further observations and wind tunnel experiments with various arrays of solid and porous roughness elements will be valuable to assess the parameterisation.

Chapter 6. Aerodynamic roughness variation with vegetation: analysis in a suburban neighbourhood and a city park¹

Abstract Local aerodynamic roughness parameters (zero-plane displacement, z_d , and aerodynamic roughness length, z_0) are determined for an urban park and a suburban neighbourhood with a new morphometric parameterisation that includes vegetation. Inter-seasonal analysis at the urban park demonstrates z_d determined with two anemometric methods is responsive to vegetation state and is 1 – 4 m greater during leaf-on periods. The seasonal change and directional variability in the magnitude of z_d is reproduced by the morphometric methods, which also indicate z_0 can be more than halved during leaf-on periods. In the suburban neighbourhood during leaf-on, the anemometric and morphometric methods have similar directional variability for both z_d and z_0 . Wind speeds at approximately 3 times the average roughness-element height are estimated most accurately when using a morphometric method which considers roughness-element height variability. Inclusion of vegetation (in addition to buildings) in the morphometric parameterisation improves wind-speed estimation in all cases. Results indicate that the influence of both vegetation and roughness-element height variability are important for accurate determination of local aerodynamic parameters and the associated wind-speed estimates.

6.1 Introduction

The (dis)services of urban vegetation are both context and scale specific, therefore cannot be generalised (Salmond et al. 2016). However, as the socio-environmental and economic benefits of urban ‘green spaces’ are realised, they are increasingly becoming part of planning agendas to mitigate climate change, improve urban sustainability and improve human well-being (e.g. Gill et al. 2007, Landry and Chakraborty 2009, Roy et al. 2012, Andersson-Sköld et al. 2015, Kremer et al. 2015, Salmond et al. 2016, Ward and Grimmond 2017). Green spaces therefore will continue to be (a greater) part of the urban fabric. Despite this, when modelling the urban environment vegetation is often neglected to simplify the problem (e.g. references within Grimmond et al. 2010, 2011). It is imperative that the understanding of the physical implications of urban vegetation is improved across micro-, local-, and regional scales. This extends beyond

¹This chapter is published as: Chapter 6: Kent CW, Lee K, Ward HC, Hong JW, Hong J, Gatey D, Grimmond CSB (2017c) *Aerodynamic roughness variation with vegetation: Analysis in a suburban neighbourhood and a city park*. Urban Ecosystems. DOI: 10.1007/s11252-017-0710-1.

urban parks and vegetation in street canyons – as the edges of cities are approached vegetation may become the most prominent roughness elements (e.g. Giometto et al. 2017, Chapter 5).

The presence of urban vegetation has implications for the storage and fluxes of scalar properties (e.g. heat, moisture and pollutants). For example, vegetation can reduce the mean and extreme ambient and indoor temperatures (Smith et al. 2011, Schubert et al. 2012, Mavrogianni et al. 2014, Heaviside et al. 2015), whilst also reducing night-time longwave cooling (Coutts et al. 2016). Its presence tends to increase humidity (through increasing evapotranspiration) and is also responsible for precipitation interception, a reduction of run-off and increased soil water storage/ permeability (Stovin et al. 2008, Day et al. 2010, Vico et al. 2014). Vegetation contributes to pollutant absorption and deposition (Tiwary et al. 2009, Tallis et al. 2011, Salmond et al. 2016).

Vegetation influences the momentum flux by exerting drag on the mean wind flow (Finnigan 2000, Guan et al. 2003, Krayenhoff et al. 2015, Giometto et al. 2017). At critical aerodynamic porosities (P_{3D}) this drag can be as significant as solid structures of the same shape (Hagen and Skidmore 1971, Mayhead 1973, Grant and Nickling 1998, Guan et al. 2000, 2003, Rudnicki et al. 2004, Vollsinger et al. 2005, Koizumi et al. 2010, Sect. 5.2.2). Vegetation therefore influences the spatially-averaged mean and turbulent characteristics of the flow in urban areas (Krayenhoff et al. 2015), having implications for in-canopy flow (Salmond et al. 2013), as well as the exchange between in- and above-canopy air masses (Gromke and Ruck 2009, Vos et al. 2013).

The influence of a defined surface area upon fluxes of momentum can be indicated using the aerodynamic parameters of the zero-plane displacement (z_d) and aerodynamic roughness length (z_0), which are directly related to surface characteristics. Several methods exist to determine these, including reference-based approaches, methods based upon surface geometry (morphometric methods) or observations (anemometric methods) (Sect. 3.3). The presence of all roughness elements is inherently included in anemometric methods, but until recently morphometric methods did not consider both vegetation and buildings in combination. However, Sect. 5.2.3 develops the widely-used Macdonald et al. (1998) (hereafter *Mac*) morphometric method to include vegetation, which also applies to the Kanda et al. (2013) (*Kan*) extension of the *Mac* method.

The objectives of this Chapter are to use observations at two vegetated urban sites to investigate: (i) the seasonal variability in z_d and z_0 with the seasonal change of vegetation phenology, (ii) the parameterisation of vegetation in the morphometric methods presented in

Chapter 5 and (iii) the implications of considering vegetation for accurate wind-speed estimation. The interdependence of z_d and z_0 means that a single value for each parameter cannot be treated as the ‘truth’. Therefore, the analysis provides a comparison between the magnitude and directional variability of roughness parameters determined from the different methods. The wind-speed estimation application provides an independent assessment of the method performance.

6.2 Methodology

6.2.1 Site description and observations

Measurements from an urban park in Seoul, South Korea (Seoul Forest Park, hereafter SFP) and a suburban residential neighbourhood in Swindon, UK (hereafter SWD) are used. The obvious contrast of landscape with vegetation phenology means trees and other vegetation are expected to influence the aerodynamic properties of both areas, especially during leaf-on conditions when foliage is at relative maxima. Seoul Forest Park is the third largest park in Seoul (~116 ha), with a dominance of vegetation evident (Fig. 6.1a-d). The SWD site is typical of UK suburbia, with a slightly larger proportion of buildings than vegetation, but this varies with direction (e.g. Fig. 6.1e, f). Considerable research at the SWD site means anthropogenic and biogenic controls of energy, water and carbon fluxes and their temporal variability are well understood (Ward et al. 2013, 2014, 2015a, 2015b, 2015c). In addition, the site has been used during development of the Surface Urban Energy and Water Balance Scheme (SUEWS) (Ward et al. 2016). However, in-depth aerodynamic parameter analysis has not been performed at either the SFP or SWD site.

At each site, fast-response observations of temperature, wind velocity (u – horizontal, v – transverse and w – vertical components), CO_2 and H_2O are processed into 30-min averages (Table 6.1).



Figure 6.1: View from the: **(a-d)** Seoul Forest Park (SFP) and **(e-f)** Swindon (SWD) measurement locations, with approximate directions

6.2.2 Surface elevation database and differentiation between buildings and vegetation

At both sites, 1-m horizontal resolution digital surface (DSM, ground height + surface features) and digital terrain (DTM, ground height only) models are analysed (Table 6.2). The high resolution and accuracy of these data, allow intricacies of surface roughness (e.g. roof pitch) to be resolved. After subtraction of the DTM from the DSM to provide a roughness element surface model (RESM), pixels < 2 m high are removed (i.e. street furniture and temporary obstacles, such as vehicles). This retains roughness elements which are most appropriate for application of the morphometric methods. Building and vegetation pixels are differentiated by three techniques.

Site: Lat, Lon (WGS84)	Local climate zone (LCZ)*	Observation period	Measurement height. Mounting.	Instrumentation	Data processing
Seoul Forest Park (SFP) 37° 32' 40.7"N 127° 2' 16.4"E	Scattered trees (type B): predominantly mixed forest (Pine, Ginkgo, Zelkova trees), pond and turf grass. Becoming dense trees (type A) within 300 m radius.	31 May 2013 – 3 June 2015	12.2 m. 230° orientation on 3.8 m tripod atop of 8.4 m duplex building.	CSAT3 Sonic Anemometer; EC155 closed- path gas analyser (Campbell Scientific, USA)	Raw 10 Hz data processed to 30-min averages with spike detection (Papale et al. 2006; Hong et al. 2009), night-time correction (Aubinet et al. 2000) and double rotation of the wind components, aligning the wind field to the <i>u</i> direction (McMillen 1988, Kaimal and Finnigan 1994).
Swindon (SWD) 51° 35' 4.6"N 1° 47' 53.2"W	Open low-rise: well-spaced low- rise residential buildings and abundant pervious land cover	9 May 2011 – 30 April 2013	12.5 m. Pneumatic mast.	R3 Sonic Anemometer (Gill Instruments, Lymington, UK); LI-7500 open- path gas analyser (LI-COR Biosciences, Lincoln, USA)	Raw 20 Hz data processed to 30-min averages using EddyPro Advanced (v5-00, LI-COR), which includes de- spiking, double coordinate rotation, humidity correction of sonic temperature and high- and low-frequency spectral corrections (Moncrieff et al. 1997).

Table 6.1: Site observation meta-data. Heights are metres above ground level. *(Stewart and Oke 2012)

For the SFP site, initial source area calculations (using the Kormann and Meixner (2001) and Kljun et al. (2015) models) indicate the measurements are consistently influenced by an area within 300 m of the sensor. The area within this radius is classified using a manual and automated technique. The manual technique entails classification of aerial photography (Fig. 6.2a) into: building, road, impervious, water, forest, grass, bare soil and other (unclassified, but with few roughness elements) (Fig. 6.2b), with the RESM data overlain to check for inconsistencies. This manual method has some limitations, for example, although buildings (predominantly rectangular with sharp borders) are mostly captured, those within a waterworks (south of the SFP site) and in a ready mixed concrete (RMC) factory (north-west) are misclassified (Fig. 6.2b). Additionally, considerable vegetation is missed, especially at land cover interfaces (e.g. along roadsides and bare soil paths, Fig. 6.2b and c, magenta circles). After re-classification, a surface model of building (BSM) and vegetation canopy (CDSM) heights is created (Fig. 6.2c).

The automated separation of buildings and vegetation, uses the RGB colour band of aerial imagery, as vegetation tends to be darker (i.e. lower end of the saturation spectrum) for all colour bands. If higher saturation pixels are removed, a binary mask representing pixels which are likely vegetation can be retained (e.g. Fig. 6.2d) (Crawford et al. 2016). Clouds in the imagery causes some vegetation to be uncaptured by the mask (cf. Fig. 6.2a and e, magenta circle). A dark to lighter pixel transition on the edge of vegetation means the mask may be smaller than vegetation's true extent.

Site	Elevation data source	Horizontal resolution (m)	Accuracy: horizontal, vertical (m)
SFP	National Geographic Information Institute	1	0.15, 0.10
SWD	Environment agency (UK) data archive		0.40, 0.15

Table 6.2: Source and accuracy of surface elevation databases used at the Seoul Forest Park (SFP) and Swindon (SWD) measurement sites

Therefore, the binary mask and RESM are combined and a filtering algorithm flags pixels as vegetation if they are within ± 3 m of another pixel in the binary mask. Pixels not flagged are assumed to be either buildings or other urban furniture (e.g. cars, street lamps etc.). After removing pixel heights < 2 m, a final BSM and CDSM product is generated (Fig. 6.2e). Although the manual (after re-classification) and automated BSM and CDSM products are almost identical (cf. Fig. 6.2c and e), the automated method is more practical. The remainder of this work uses a combined dataset from both procedures.

At the SWD site, the abundance of vegetation and proximity of built structures makes accurate manual classification difficult. Additionally, the automated technique frequently misclassifies building pixels as vegetation because of the dark roofs and excessive shading (e.g. Fig. 6.2f). Therefore, a building footprint dataset (OS MasterMap® Topography Layer – Building Height Attribute, Ordnance Survey 2014) (Fig. 6.2g) was overlain upon the RESM to create the BSM (Fig. 6.2h, red). The remaining pixels were classed as ‘potential’ vegetation pixels, with isolated pixels removed if fewer than 6 of the 8 surrounding pixels were not ‘potential’ vegetation (Goodwin et al. 2009, Lindberg and Grimmond 2011a). The remaining pixels were stored as a CDSM (Fig. 6.2h, green).

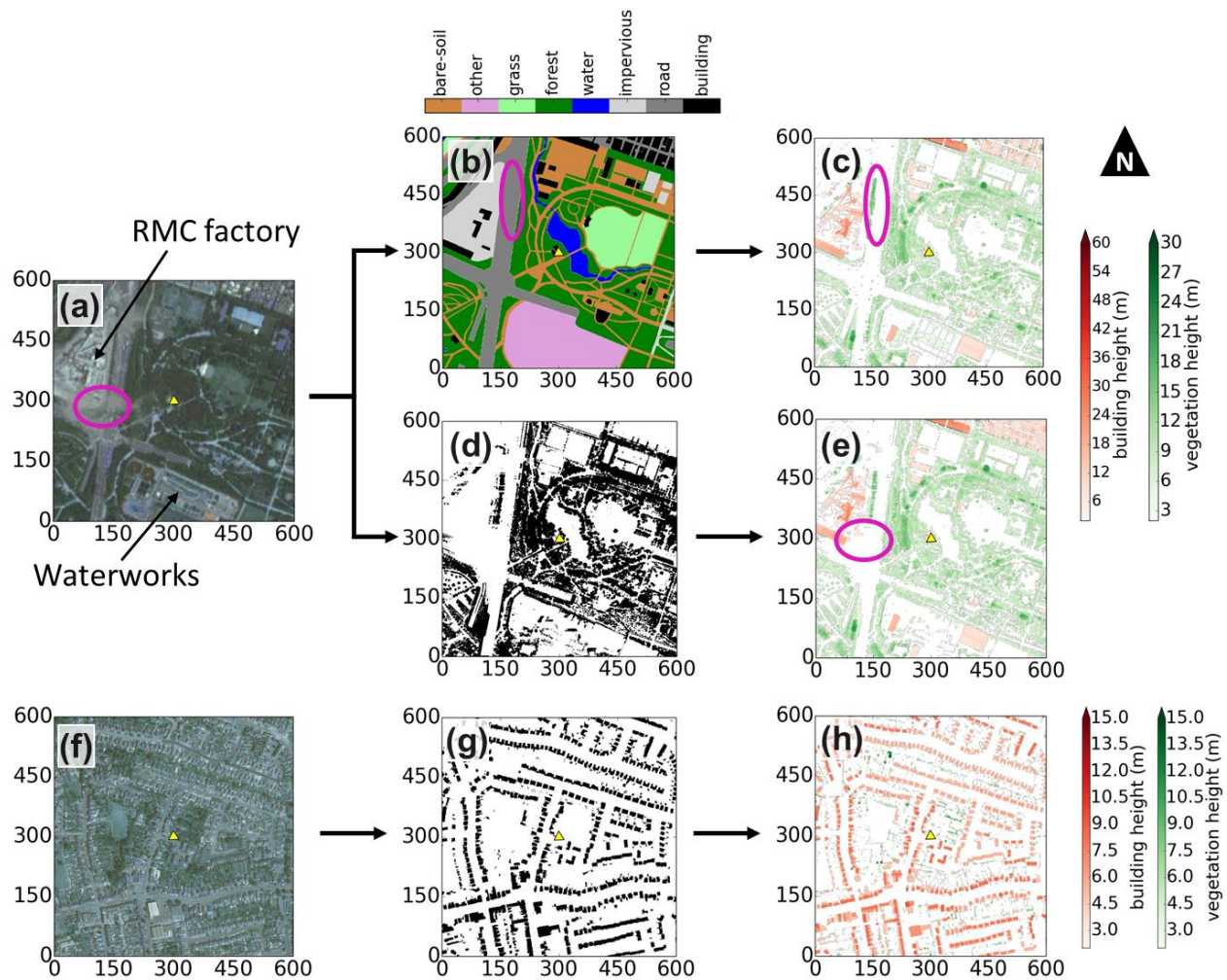


Figure 6.2: Classification of buildings and vegetation for the (a-e) Seoul Forest Park and (f-h) Swindon site (yellow triangles) surroundings: (a, f) aerial photograph; (b) manual land cover classification; (c) building digital surface model (BSM, red) and canopy digital surface model (CDSM, green) from manual technique; (d) vegetation mask from analysis of RGB colour bands in (a); (e) BSM and CDSM from automated technique; (g) building footprints and, (h) BSM and CDSM using building footprint mask. Magenta circles are referred to in text. Map units are metres. Data sources: aerial imagery – Seoul city aerial image service centre, Digimap 2017; elevation data – see Table 6.2; building footprints – Ordnance Survey 2014

6.2.3 Calculation of aerodynamic roughness parameters

Two anemometric methods are used to determine z_d : the temperature variance (TVM, Rotach 1994) and wind variance (WVM, Toda and Sugita 2003) methods. The TVM and WVM are based upon the relation between the non-dimensional standard deviation of temperature or vertical wind and stability parameter in the surface layer, during unstable conditions (Wyngaard et al. 1971, Tillman 1972):

$$\phi_T = \frac{\sigma_T}{T_*} = -C_1 \left(C_2 - \frac{z - z_d}{L} \right)^{-\frac{1}{3}} \quad (6.1)$$

$$\phi_w = \frac{\sigma_w}{u_*} = C_3 \left(1 - C_4 \left[\frac{z - z_d}{L} \right] \right)^{\frac{1}{3}} \quad (6.2)$$

where σ_T and σ_w are the standard deviation of temperature and vertical wind velocity respectively, T_* is the temperature scale, $T_* = -(\overline{w'T'})/u_*$ (with T the temperature, w the vertical wind velocity, u_* friction velocity, the overbar representing a mean value and prime indicating deviation from the mean), L is the Obukhov length, $L = \frac{\overline{T}u_*^2}{\kappa g T_*}$ (with g the gravitational acceleration and κ von Karman's constant = 0.4, Högström 1996) and $C_1 - C_4$ are constants.

The TVM and WVM are amongst the few methods that permit roughness parameters to be derived from single-level turbulence measurements. However, the methods rely on Monin-Obukhov similarity theory and that the resulting flux gradient relations used by the TVM and WVM (Eq. 6.1 and 6.2) apply in urban areas (see Roth and Oke 1995). Therefore, the applicability of the similarity relations used by the methods is assessed at both sites during this work. Although the similarity relations are expected to hold where flow is free from roughness-element wakes (i.e. within the inertial sublayer), the TVM is specifically developed to determine z_d from measurement locations which may be distorted by local roughness-element wakes (i.e. within the roughness sublayer) (Rotach 1994). Previous analysis indicates results from the WVM are appropriate in similar heterogeneous locations (Toda and Sugita 2003, Sect. 3.3.3).

The constants (C_1 to C_4) are derived from observations when z_d is assumed negligible. Although the constants vary (e.g. Sorbjan 1989, Hsieh et al. 1996, Choi et al. 2004), the z_d from the temperature and wind variance methods was found to be relatively insensitive to the range in a dense urban area (Sect. 3.5.1.1). To assess the effect of constant choice on the final solution to z_d the methods are also applied with a range of constants here (Table 6.3). Note, if constants are fit to the observations

at a site an *a priori* assumption of z_d is required and therefore the z_d retrieved is not useful (Sect. 3.4.3.2).

The right-hand sides of Eq. 6.1 and 6.2 are estimated by increasing z_d from zero to twice the measurement height (z_m) in 0.1 m increments (producing ϕ_{est}). The z_d is the value which minimises the root-mean-square error (RMSE) between ϕ_{est} and the observed value (ϕ_{obs}) of σ_T/T_* or σ_w/u_* (for the TVM and WVM, respectively). As calculations are undertaken for unstable conditions ($-6.2 \leq z'/L \leq -0.05$, Roth 2000; $z' = z_m - z_d$) an initial z_d for stability definition is required. Thus, the methods are applied to 10° wind sectors around the sites with: (i) the z_d for stability definition varied from 0 to 10 m in 2-m increments (a larger initial z_d provides insufficient data to apply the methods); and (ii) different constants (i.e. Table 6.3).

If measurements are free from roughness-element wakes (i.e. within the inertial sublayer), the ‘eddy-covariance (EC) method’ can be used to determine z_0 , which is a rearrangement of the logarithmic wind law:

$$z_0 = (z - z_d) \exp\left(-\frac{\bar{U}_z \kappa}{u_*}\right) \quad (6.3)$$

where the average wind speed (\bar{U}_z) and u_* are determined from observations at z . For each 30-min period of observations, z_d from both the temperature and wind variance methods are used, providing two z_0 solutions. The EC method, applicable under neutral conditions ($|z'/L| \leq 0.05$), requires at least 20 observations to determine z_0 for a directional sector (Beljaars 1987, Grimmond et al. 1998). Additionally, only $\bar{U}_z > 1 \text{ m s}^{-1}$ are analysed to ensure sufficient mechanical turbulence (G. Liu et al. 2009). Stability corrections may be used to apply the EC method outside of neutral conditions. However, these corrections are based upon empirical fits to observed data and vary across studies (Högström 1996). To avoid additional sources of uncertainty only neutral conditions are considered here.

Reference	TVM		WVM	
	C_1	C_2	C_3	C_4
Tillman (1972)	0.95	0.050	-	-
Panofsky et al. (1977)	-	-	1.30	3.00
De Bruin et al. (1993)*	0.95	0.035	-	-
Kustas et al. (1994)	1.1	0.085	-	-
Kaimal and Finnigan (1994)*	1.05	0.040	1.25	3.00
Toda and Sugita (2003)	0.99	0.060	1.25	3.00
Choi et al. (2004)*	1.14	0.030	1.12	2.80

Table 6.3: Constants ($C_1 - C_4$) for application of the temperature variance (TVM) and wind variance (WVM) anemometric methods (Eq. 6.1 and 6.2). For all observations, extensive flat homogeneous terrain is reported. Kaimal and Finnigan (1994) and Toda and Sugita (2003) are after synthesis of coefficients from various studies. At the SWD site, the Choi et al. (2004) constants are not applied, as they predict the scaled σ_T and σ_w to be much larger and smaller than observations, respectively, meaning z_d solutions are consistently zero. *constants obtained from $\sigma_T/T_* = C_1(1 - C_2[(z - z_d)/L])^{-\frac{1}{3}}$

As the SFP site results indicate z_d is similar to (or greater than) z_m , the EC method to determine z_0 is therefore unusable (and not applied). For both northern-hemisphere sites, leaf-off periods are selected as the (core) winter months of December, January and February; and leaf-on periods are June, July and August. With little solar radiation during winter (leaf-off periods) at the SWD site there are insufficient unstable periods to determine z_d using the temperature and wind variance methods (and hence z_0). Therefore, only leaf-on conditions are analysed at the SWD site.

The Macdonald et al. (1998, *Mac*) and Kanda et al. (2013, *Kan*) morphometric methods are used with the vegetation parameterisation presented in Chapter 5. Following Sect. 3.4.3.3, an iterative procedure is applied using the Kormann and Meixner (2001) footprint model with 30-min averaged meteorological observations. Rural z_d and z_0 values (0.2 and 0.03 m, respectively) are used to initiate the iterative procedure, as results are independent of these values (Appendix 3.C). Morphometric calculations are only applied to source areas which extend horizontally beyond 50 m from the measurement sensors, as smaller source areas become concentrated upon only a few roughness elements and the morphometric calculations are inappropriate.

For each 30-min observation, the source area weighted geometry is calculated for buildings and vegetation (using the BSM and CDSM). The average, maximum and standard deviation of *all* roughness-element heights (H_{av} , H_{max} and σ_H , respectively) are determined. The plan area index (λ_p) of roughness elements is:

$$\lambda_p = \frac{W_{p,b} + W_{p,v}(1 - P_{3D})}{W_{AT}} \quad (6.4)$$

where $W_{p,b}$ and $W_{p,v}$ are the sums of weighted pixels in the source area of buildings and vegetation, respectively, W_{AT} is the total sum of weights and P_{3D} is the aerodynamic porosity of vegetation. The weighted frontal area of buildings and vegetation is determined separately ($W_{f,b}$ and $W_{f,v}$), treating vegetation as non-porous.

Including vegetation, the *Mac* method becomes (Sect. 5.2.3):

$$Mac_{z_d} = [1 + \alpha_M^{-\lambda_p}(\lambda_p - 1)]H_{av} \quad (6.5)$$

$$Mac_{z_0} = \left(1 - \frac{z_d}{H_{av}}\right) \exp \left[- \left(\frac{1}{k^2} 0.5 \beta_M C_{Db} \left(1 - \frac{z_d}{H_{av}}\right) \frac{\{W_{f,b} + W_{f,v}(P_v)\}}{W_{AT}} \right)^{-0.5} \right] H_{av} \quad (6.6)$$

where $C_{Db} = 1.2$ is the drag coefficient for buildings and $\alpha_M = 4.43$ and $\beta_M = 1.0$ are empirical constants for staggered arrays fit to the wind tunnel data of Hall et al. (1996). P_v is the ratio between the drag coefficient for vegetation with varying P_{3D} and buildings (Sect. 5.2.3):

$$P_v = \frac{-1.251P_{3D}^2 + 0.489P_{3D} + 0.803}{C_{Db}} \quad (6.7)$$

derived from experiments with $0 \leq P_{3D} \leq 0.85$ (Guan et al. 2000). The *Kan* method is a development of the *Mac* method, incorporating roughness-element height variability (Kanda et al. 2013):

$$Kan_{z_d} = [c_0 X^2 + (a_0 \lambda_p^{b_0} - c_0) X] H_{max}, \quad X = \frac{\sigma_H + H_{av}}{H_{max}} \quad (6.8)$$

and

$$Kan_{z_0} = (b_1 Y^2 + c_1 Y + a_1) Mac_{z_0}, \quad Y = \frac{\lambda_p \sigma_H}{H_{av}} \quad (6.9)$$

where $0 \leq X \leq 1$, $0 \leq Y$, and a_0 , b_0 , c_0 , a_1 , b_1 and c_1 , are regressed constants of 1.29, 0.36, -0.17, 0.71, 20.21 and -0.77.

The methods are applicable to any combination of buildings and vegetation, with vegetation phenology and associated drag characteristics being optimisable (through P_{3D}). With this information being scarce, and the predominance of deciduous vegetation at both sites it is assumed that all vegetation has a leaf-on porosity of 20% and leaf-off porosity of 60% (i.e. $P_{3D} = 0.2$ and $P_{3D} = 0.6$, respectively, Heisler 1984; Heisler and DeWalle 1988, Grimmond and Oke 1999). During leaf-on and leaf-off transition an intermediate porosity may be used (e.g. $P_{3D} = 0.4$). However, the rapid transition at both sites (< 30 days) means there is insufficient data to investigate the transition periods here.

Determination of source-area weighted aerodynamic parameters using the morphometric methods (including vegetation) are implemented into the Urban Multi-scale Environmental Predictor (UMEP, <http://www.urban-climate.net/umep/UMEP>) climate service plugin for the open source software QGIS (Lindberg et al. 2018).

6.3 Results

6.3.1 Impact of roughness elements on observational data

To assess the disturbance to measurements from nearby roughness elements the turbulence data are inspected (Fig. 6.3). At the SFP site, the data are more variable due to the proximity to roughness elements (measurements are at $1.6H_{av}$ of all roughness elements in the 300-m radius) (Fig. 6.3a-d). In some directions z_m is similar to H_{av} (N, SW, W, NW, Table 6.4b), and H_{max} is always larger than z_m . Therefore, the measurements are probably within the roughness sublayer (RSL) and z_d is often larger than z_m . A peak in the aerodynamic drag coefficient and transverse turbulence intensity between $130^\circ - 180^\circ$ is likely caused by the rear sides of the sensor (Fig. 6.3a, c). In addition, there is a larger proportion of drag between $210^\circ - 330^\circ$ where taller roughness elements are located (Fig. 6.3a).

Although the TVM and WVM methods have been demonstrated to be appropriate in the RSL, the calculation of source areas is more uncertain (e.g. Baldocchi 1997, Rannik et al. 2000, Sogachev and Lloyd 2004, Vesala et al. 2008, Leclerc and Foken 2014). However, Fig. 6.3a-d demonstrates there is still some homogeneity to the flow and to characterise the local roughness, the Kormann and Meixner (2001) footprint model is applied at a height likely greater than the RSL ($2.5H_{av} = 20$ m).

At the SWD site, the measurement height is approximately $2.8H_{av}$ based on the measurement source area (Table 6.5). Combined with a lack of disturbance to turbulence data for most directions (Fig. 6.3e-h), this indicates measurements are predominantly taken within the inertial sublayer (ISL), where it is most appropriate to apply the anemometric methods and source area calculations. Peaks in turbulence data between 100° and 140° and at approximately 180° and 280° (Fig. 6.3e-h) are likely caused by houses with maximum heights of up to 8 m – 10 m in these directions (within 25 m of the sensor).

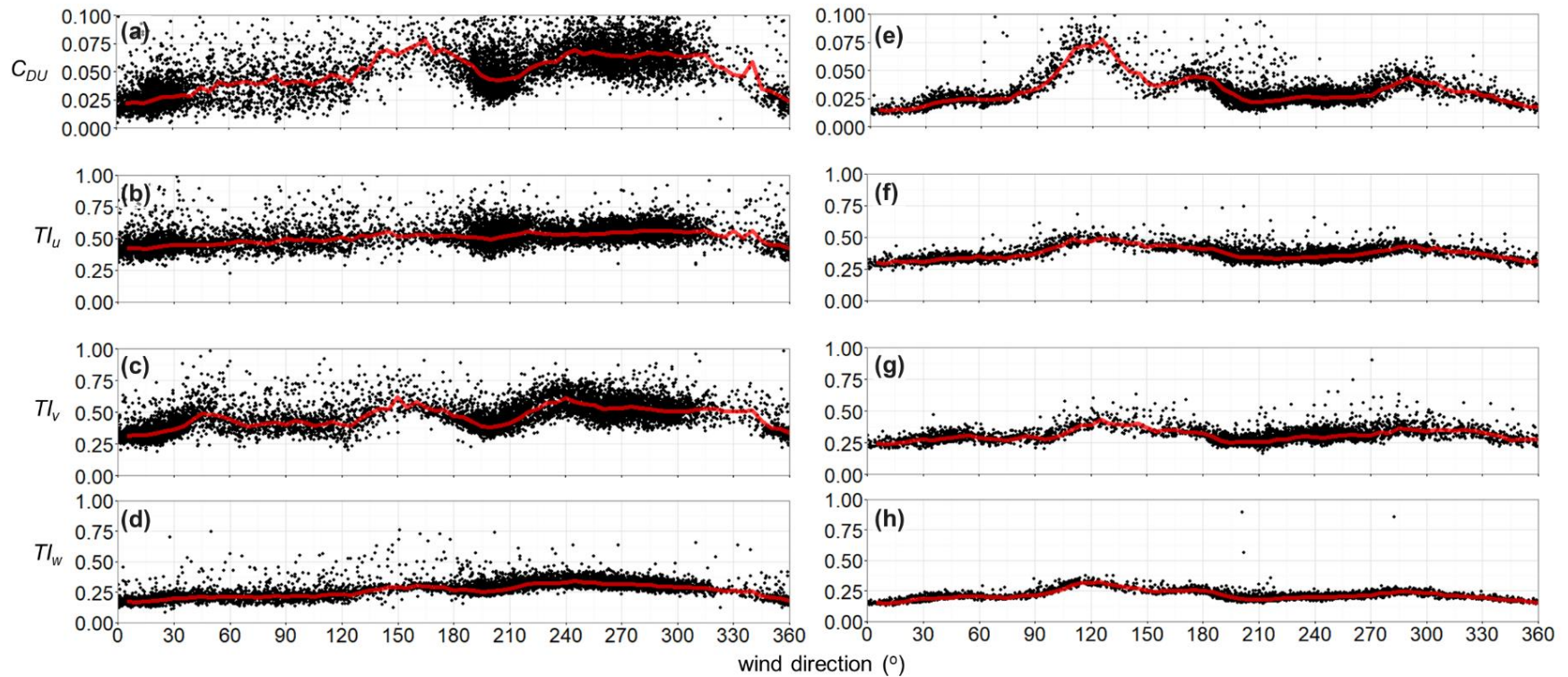


Figure 6.3: All 30-min observations during neutral conditions (black dots) at the **(a-d)** Seoul Forest Park (SFP) and **(e-h)** Swindon (SWD) sites: **(a, e)** aerodynamic drag coefficient ($C_{DU} = (u_* / \bar{U}_z)^2$), and turbulence intensities in the **(b, f)** longitudinal ($TI_u = \sigma_u / \bar{U}_z$), **(c, g)** transverse ($TI_v = \sigma_v / \bar{U}_z$) and **(d, h)** vertical ($TI_w = \sigma_w / \bar{U}_z$) wind directions. Neutral conditions are $|(z_m - z_d)/L| \leq 0.05$ (L is Obukhov length, $z_m = 12.2$ m at SFP and 12.5 m at SWD, z_d is assumed as $H_{av} = 8$ m at SFP and 4.5 m at SWD). Red line is the median for each 5° wind direction. \bar{U}_z is the average wind speed, u_* is the friction velocity and $\sigma_u, \sigma_v, \sigma_w$ are the standard deviations of the longitudinal, transverse and vertical velocity components of the wind

6.3.2 Land cover and geometry surrounding the sites

Source areas indicate the likely surface influencing turbulent fluxes measured at a point (Schmid and Oke 1990, Schmid 1997, Leclerc and Foken 2014 and Sect. 2.2.4) and can therefore be used to characterise site surroundings, with varying certainty (Heidbach et al. 2017). Source area characterisation is performed for the SWD site. However, at the SFP site, the uncertainty in the calculated source areas and the large z_d compared to z_m means 45° direction sectors are used.

Aerodynamic characteristics are expected to be dominated by the tall and abundant vegetation at the SFP site, rather than by the sparse buildings. The average vegetation height ($H_{av,v}$) ranges between 5 – 10 m and with a maximum ($H_{max,v}$) of ≥ 17.5 m in all directions it is over double H_{av} . The plan and frontal area indexes of vegetated roughness elements ($\lambda_{p,v}$ and $\lambda_{f,v}$, respectively) are consistently > 0.3 , whereas buildings have plan and frontal area indexes ($\lambda_{p,b}$ and $\lambda_{f,b}$) consistently < 0.1 (Table 6.4b). An exception is to the north and west where the built fraction increases to close to 20% due to the RMC factory (Fig. 6.2a).

(a) Land cover (%)								
direction	building	impervious (road)	impervious (non-road)	water	vegetation	grass	other	bare-soil
N	12	7	0	7	40	0	0	34
NE	18	4	5	3	49	8	0	13
E	1	0	0	4	54	33	0	8
SE	8	1	3	4	68	0	2	14
S	5	6	0	0	48	0	39	2
SW	2	25	1	0	54	0	8	10
W	16	29	20	0	33	0	0	2
NW	16	33	15	0	30	2	0	4

(b) Geometry										
direction	Buildings					Vegetation				
	H_{av}	H_{max}	σ_H	λ_p	λ_f	H_{av}	H_{max}	σ_H	λ_p	λ_f
N	12.65	33.4	8.43	0.11	0.07	7.5	28.06	3.7	0.33	0.38
NE	7.38	16.53	2.23	0.13	0.02	7.63	22.16	2.81	0.44	0.29
E	6.46	11.57	2.80	0.00	0.00	7.56	21.91	2.57	0.43	0.34
SE	6.68	12.83	1.92	0.05	0.03	6.98	19.43	2.73	0.47	0.34
S	6.16	8.82	1.06	0.05	0.01	5.76	17.51	3.17	0.41	0.31
SW	11.31	16.93	4.75	0.02	0.01	7.64	22.86	3.39	0.40	0.25
W	11.04	27.67	6.93	0.15	0.12	8.14	18.84	3.37	0.25	0.24
NW	8.29	26.45	5.32	0.08	0.09	9.47	20.74	3.62	0.20	0.20

Table 6.4: Characteristics within a 300-m radius of the Seoul Forest Park site by direction (45° sectors, $\pm 22.5^\circ$ of the stated direction): **(a)** Land cover and **(b)** Geometry of roughness elements > 2 m. ‘Other’ land cover is predominantly comprised of a water works (with few roughness elements > 2 m), which cannot be classified from aerial imagery. Geometry abbreviations: H_{av} – average height, H_{max} – maximum height, σ_H – standard deviation of heights, λ_p – plan area index, λ_f – frontal area index

Source area size varies with the model and parameters used (e.g. Leclerc and Foken 2014, Heidbach et al. 2017, Sect. 3.7), which here is demonstrated by source area climatologies calculated using aerodynamic parameters (z_d and z_0) from the *Kan* and *Mac* morphometric methods (Fig. 6.4). Independent of morphometric method, the SWD site source areas include residential housing, back gardens and impervious driveways. The source area climatology is biased towards the predominant south-westerly wind direction, where it also extends further upwind because of the greater wind speeds in this direction.

The *Mac* method source areas are larger than the *Kan* method (average upwind extents of 700 m and 400 m, respectively) due to the difference in aerodynamic parameters determined with each method. The peak flux footprint is 50 m upwind for the *Mac* method and 25 m upwind for *Kan* (Fig. 6.4). Although these differences impact the surface geometry and land cover determined within the source area, the consistent fetch at the SWD site means the parameters determined by the *Mac* and *Kan* source areas are remarkably similar (Table 6.5). The source area has 11 % built and 2 % vegetated roughness elements, with low-level vegetation (i.e. small shrubs), grass, impervious materials (e.g. roads or driveways) and soil forming the remainder. The latter have a comparatively small impact on the aerodynamic roughness parameters at the neighbourhood scale. The average height of vegetation is smaller than buildings (~3.5 m and 4.7 m, respectively), but the maximum tree height (up to 15 m) is slightly larger than buildings (up to 12 m). To the north-east (030° – 090°), trees are tallest and most abundant, whilst vegetation is least to the south-west (Fig. 6.2f, 210 – 240°).



Figure 6.4: Source area climatologies of the Swindon site (SWD) modelled using the Kormann and Meixner (2001) source area model for the months of June, July and August (Leaf-on) in 2011 and 2012. Source areas are modelled using aerodynamic parameters from the (a) Kanda et al. (2013) and (b) Macdonald et al. (1998) morphometric methods. The 80% cumulative source area weights for each 30-min average of observations are integrated and normalised by the sum of all weightings ($n = 8787$). Source areas overlain upon buildings (black) and vegetation (green) > 2 m. Map units: metres

(a) Kan												
Direction	Buildings						Vegetation					
	H_{av}	H_{max}	σ_H	λ_p	λ_f	cover (%)	H_{av}	H_{max}	σ_H	λ_p	λ_f	cover (%)
All	4.74	10.05	1.59	0.24	0.13	11	3.49	12.08	1.58	0.05	0.11	2
NE (030° – 090°)	3.92	9.80	1.31	0.15	0.06	6	3.88	13.03	1.70	0.07	0.14	4
SW (210° – 240°)	4.52	10.40	1.66	0.30	0.15	14	3.35	12.33	1.59	0.04	0.10	2
(b) Mac												
Direction	Buildings						Vegetation					
	H_{av}	H_{max}	σ_H	λ_p	λ_f	cover (%)	H_{av}	H_{max}	σ_H	λ_p	λ_f	cover (%)
All	4.67	11.96	1.65	0.24	0.12	11	3.51	14.46	1.76	0.05	0.10	2
NE (030° – 090°)	3.95	12.03	1.41	0.17	0.07	7	3.82	14.79	1.73	0.07	0.13	3
SW (210° – 240°)	4.62	12.01	1.73	0.30	0.14	13	3.39	13.76	1.61	0.04	0.09	2

Table 6.5: Roughness-element characteristics in the source areas modelled during leaf-on conditions at SWD using the **(a)** Kanda et al. (2013, *Kan*) and **(b)** Macdonald et al. (1998, *Mac*) morphometric methods (Fig. 6.4) for all observations ($n = 8787$) and in the specified north-easterly (NE) ($n = 911$) and south-westerly (SW) ($n = 2045$) directions. Geometry abbreviations: H_{av} – average height, H_{max} – maximum height, σ_H – standard deviation of heights, λ_p – plan area index, λ_f – frontal area index. Cover is the weighted percentage of pixels in the source area which are in the BSM for buildings and CDSM for vegetation

6.3.3 Aerodynamic parameters

6.3.3.1 Seoul Forest Park (SFP)

At the SFP site, the anemometrically determined z_d is relatively insensitive to both the ‘universal’ constants (Table 6.3) and initial z_d used to define stability. Both consistently cause a maximum variability of < 1 m for any 10° wind sector (Fig. 6.5a and b, shading around grey and brown lines) which corresponds to $< 10\%$ of the median z_d . Despite the proximity of measurements to roughness elements, the maximum RMSE between ϕ_{est} and ϕ_{obs} for the wind variance method is 0.4, which is similar to observations which are higher above roughness elements in other urban areas (Sect. 3.5.1.1) and provides greater confidence when using the WVM. In contrast, the RMSE for the TVM is much larger (2.0), because of the proximity to roughness elements, the thermal inhomogeneity of the area (i.e., water, grasses, trees, bare-soil, and impervious surfaces, Table 6.4) and the dissimilarity of roughness length between momentum and heat (e.g. Owen and Thomson 1963, Zilitinkevich 1995, Voogt and Grimmond 2000, Hong et al. 2012).

Both the TVM and WVM indicate z_d may be larger than z_m (12.2 m) for all wind directions (Fig. 6.5a, b). Both methods have a larger z_d during leaf-on (Fig. 6.5a) than leaf-off (Fig. 6.5b), which is approximately 1 m larger for the TVM and 2 – 4 m larger for the WVM. A seasonal increase in z_d is also observed by Giometto et al. (2017) for a suburban neighbourhood with the larger amount of leaf-on foliage exerting greater drag upon the flow, acting to raise the centroid of the drag profile (analogous to z_d , Jackson 1981).

The anemometric z_d is more variable with wind direction during leaf-on, which can be directly related to trees (and implications for z_d). For example, z_d is largest between $080^\circ - 150^\circ$, where there is maximum vegetation cover ($> 50\%$ land cover, Table 6.4a), and between $270^\circ - 010^\circ$ where $H_{av,v}$ is largest (Table 6.4b). The 6 m range in leaf-off z_d values between $270^\circ - 360^\circ$ (Fig. 6.5b) is attributed to the disturbance to airflow from the RMC factory approximately 250 m upwind (Fig. 6.2a), and a row of trees (> 20 m) just 60 m upwind. During leaf-on, this variability is not observed because the foliage on the trees dominates airflow disturbance, causing an obvious increase in z_d (Fig. 6.5a).

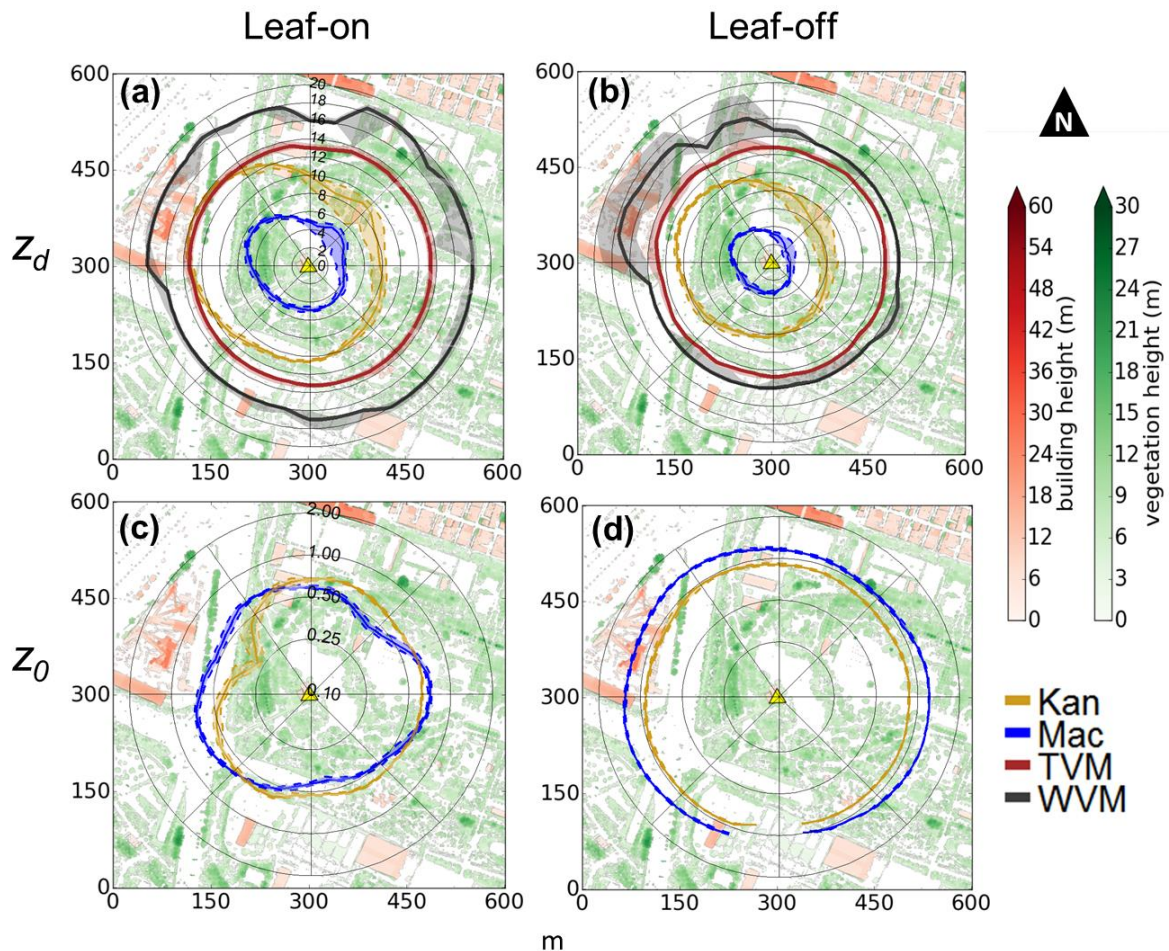


Figure 6.5: Median aerodynamic parameters determined for 10° wind sectors surrounding Seoul Forest Park site (SFP). Seasons (columns) are: leaf-on (June, July, August) and leaf-off (December, January, February). *Anemometric methods:* TVM (temperature variance, Rotach 1994); WVM (wind variance, Toda and Sugita 2003), with the range of solutions (shading) provided from varying constants used during application of the methods and initial z_d used to define stability (Sect. 6.3.2). *Morphometric methods:* Kan (Kanda et al. 2013); Mac (Macdonald et al. 1998) applied using the Kormann and Meixner (2001) footprint model for all 30-min observations, with 10th/ 90th percentile for each 10° sector shaded. z_d is for unstable conditions ($-6.2 \leq z'/L \leq -0.05$, with $z' = z_m - z_d$ and L the Obukhov length) and z_0 is for neutral conditions ($|z'/L| \leq 0.05$). For morphometric method stability definition, z_d in z'/L is determined by the respective morphometric method. Insufficient neutral conditions for southerly winds during leaf-off vegetation state means no morphometric z_0 is reported here

Similar to the anemometric methods, both morphometric methods indicate leaf-on z_d is larger than leaf-off z_d , (Fig. 6.5a, b). The effect is least obvious between 000° and 120° due to the lake and open grassed area. However, between 120° to 280° the increasing height and proportion of vegetation (Table 6.4b) increases both Mac_{z_d} and Kan_{z_d} , with leaf-on z_d 1 – 3 m larger than leaf-off (Fig. 6.5). Both morphometric methods indicate maximum z_d and seasonal signal between 270° and 330° , a similar direction to the anemometric methods. Here, Mac_{z_d} becomes as large as 7.5 m and Kan_{z_d} , with a more pronounced peak, reaches 14 m. The latter is associated with the increased vegetation plan area, H_{av} , H_{max} and σ_H (Table 6.4b). As the source area rarely extends to the RMC factory (Fig. 6.2a), the morphometric z_d is primarily a function of vegetation in these directions.

Leaf-off z_0 is typically > 0.5 m larger than leaf-on z_0 for both morphometric methods (Fig. 6.5c, d), as z_0 varies with roughness-element density. In canopies with both vegetated (Shaw and Pereira 1982, Wolfe and Nickling 1993, Raupach 1992, 1994, Nakai et al. 2008) and built (Macdonald et al. 1998, Cheng and Castro 2002, Jiang et al. 2008) roughness elements, z_0 has been demonstrated to increase with density until a peak λ_f (or leaf area index), beyond which z_0 decreases again. Therefore, the seasonal change of z_0 is expected to be canopy dependent: z_0 will increase with density for sparsely packed canopies, but will decrease with density in dense canopies. The SFP site is an example of the latter, where an already densely packed canopy during leaf-off conditions becomes denser during leaf-on. This effectively closes the canopy creating a smoother surface with a flow more characteristic of a skimming regime and reduction in z_0 . The comparatively sparsely packed neighbourhood site analysed by Giometto et al. (2017) is an example of the former, whereby leaf-on transition creates an effectively rougher surface with a flow more characteristic of a wake interference regime and resultant increase in z_0 .

At the SFP site, the seasonal change in Mac_{z_0} is more obvious than Kan_{z_0} , as the former is more sensitive to λ_f (e.g. Fig. 3.1) and Kan_{z_0} considers geometric parameters other than λ_f (H_{max} , σ_H and λ_p). Kan_{z_0} is on average 0.2 m less than Mac_{z_0} because the larger z_d determined using the Kan method means physically less frontal area of roughness elements exert drag upon the mean wind flow. For both morphometric methods, leaf-off z_0 is consistent with direction due to the relative lack of foliage (Fig. 6.5d). However, leaf-on z_0 is much more directionally variable and similarly to z_d can be related to vegetation geometry and cover. Mac_{z_0} has greater directional variability because of the aforementioned sensitivity to λ_f .

The morphometric methods were applied treating vegetation as buildings (i.e. $P_{3D} = 0$) and ignoring it (i.e. $P_{3D} = 1$), however, the dominance of vegetation in the area meant the former produced $z_0 < 0.25$ m and the latter $z_d < 5$ m. Furthermore, applying the methods without the vegetation parameterisation does not produce the seasonal change demonstrated by the observations.

6.3.3.2 Swindon (SWD)

During leaf-on, median solutions to both the temperature and wind variance methods indicate z_d varies between 4 – 10 m surrounding the SWD site (Fig. 6.6a). However, the range of z_d for any 10° sector is up to 5 m for the temperature variance methods and up to 2.5 m for the wind variance method, corresponding to as much as 50% of median z_d . This range is larger than in central London (e.g. Sect. 3.5.1.1) and at the SFP site. The z_d from the temperature variance method cannot be related to surface characteristics, providing a z_d which is consistently close to z_m and up to 5 m larger than the wind variance method. The predominantly large z_d solutions are likely because of the thermal inhomogeneity of the area, which includes buildings, vegetated, and paved land cover. Therefore, similar to the SFP site, there is considerable variability between ϕ_{est} and ϕ_{obs} for the temperature variance method (RMSE > 0.6) and less confidence in its use.

The wind variance method indicates z_d is consistently between 4 – 5 m (i.e. similar to H_{av}) (Fig. 6.6a). The directional variability of these results can be directly related to surface characteristics. Combined with the lower RMSE between ϕ_{est} and ϕ_{obs} (RMSE < 0.2), there is greater confidence in the wind variance than the temperature variance method results. Increases of z_d and z_0 of up to 7.5 m and 1 m, respectively between $130^\circ - 180^\circ$ and $240^\circ - 280^\circ$ are associated with houses within 25 m of the sensor in these directions. Elsewhere, the larger z_d from the temperature variance method means that its associated z_0 is consistently between 0.25 m to 0.5 m less than the wind variance method (Fig. 6.6b).

Relative minima of both z_d and z_0 occur when wind flow is aligned with the smoother road surface to the west of sites between $200^\circ - 210^\circ$ and $330^\circ - 360^\circ$ (Fig. 6.6a). A relative increase in z_0 for both methods (to approximately 0.25 m and 0.75 m for the temperature and wind variance methods, respectively) in the 045° direction is likely because of the taller and more abundant vegetation in the same direction. However, there is not a similar increase of z_d .

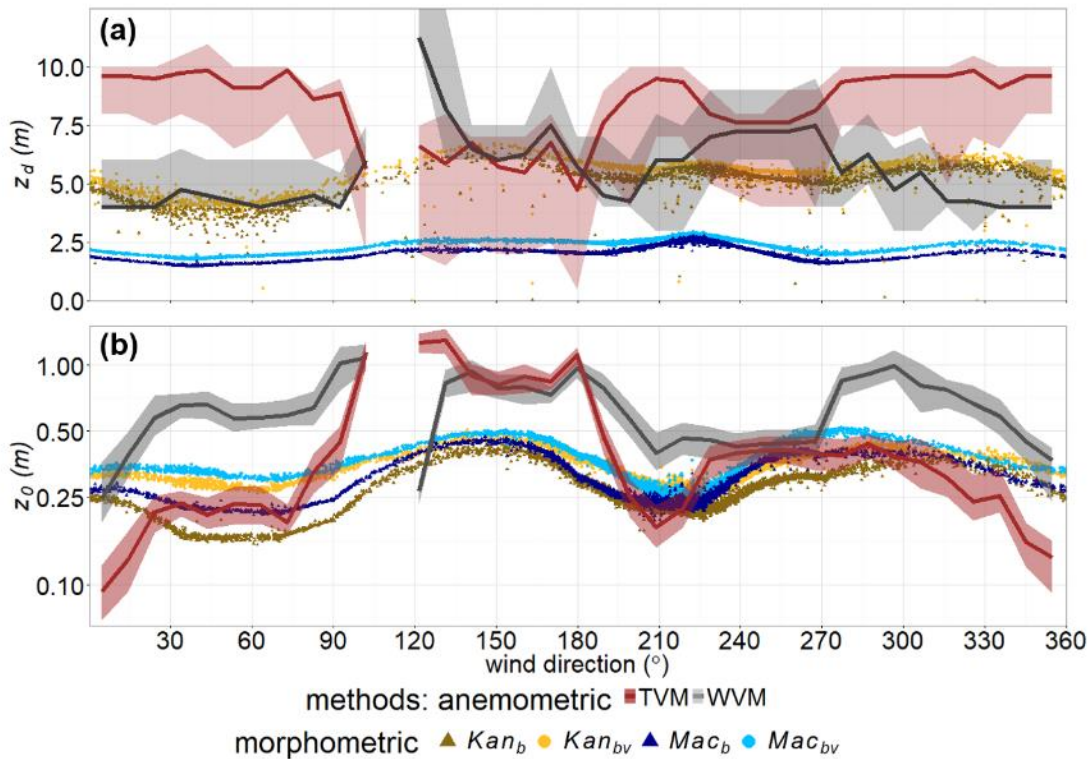


Figure 6.6: Comparison of anemometric (lines and shading) and morphometric (points) methods to determine the **(a)** zero-plane displacement (z_d) and **(b)** aerodynamic roughness length (z_0) (note in y axis) surrounding the Swindon site (Fig. 6.2f). For anemometric methods, z_d is the median solution of the temperature variance (TVM) and wind variance (WVM) methods, applied to 30-min observations during unstable conditions ($-6.2 \leq z'/L \leq -0.05$, with $z' = z_m - z_d$ and L the Obukhov length) for 10° sectors. The range (shading) represents all possible solutions by varying z_d used for stability definition and varying constants used in the methods. z_0 is the median (lines) and upper and lower quartile (shaded) of the eddy-covariance method, during neutral conditions ($|z'/L| \leq 0.05$) for each 10° sector, using z_d from the TVM and WVM, respectively. Less than 10 observations in the 110° sector means no values are reported here. The morphometric methods: Kan (Kanda et al. 2013); Mac (Macdonald et al. 1998) are for each source area during the same conditions as the anemometric methods, applied considering vegetation (subscript bv) and for buildings only (subscript b). For the morphometric method stability definition, z_d in z'/L is determined by the respective morphometric method

For both z_d and z_0 the morphometric methods have less directional variability than the anemometric methods because of the similarity in geometry surrounding the SWD site. When vegetation is considered Kan_{z_d} ranges between 2.5 m and 7 m and is therefore approximately $0.5 - 1.5H_{av}$ (Fig. 6.6a, Kan_{bv}). In comparison Mac_{z_d} is consistently half of this, ranging between $0.25 - 0.75H_{av}$ (Fig. 6.6a, Mac_{bv}). The z_d determined by the morphometric methods is more similar to the wind variance method (than the temperature variance), especially for Kan_{z_d} , which has an average difference of 0.2 m. The methods indicate relative minima and maxima of z_d in similar directions. A relative reduction between $030^\circ - 090^\circ$ occurs where fewer buildings are located (Table 6.5), whilst an increase between $130^\circ - 180^\circ$ is associated with the taller buildings close to the sensor and larger H_{av} (~ 5 m).

For the aerodynamic roughness length, incorporating vegetation in the morphometric calculations means z_0 ranges between 0.2 m and 0.5 m. The similarity of z_0 between the methods is because the frontal area index ranges between 0.15 and 0.2, a region that the methods indicate similar z_0 (Fig. 3.1). However, in directions where the roughness-element frontal area is reduced, Kan_{z_0} can be up to 0.1 m less than Mac_{z_0} . Maxima between $120^\circ - 190^\circ$ and $270^\circ - 280^\circ$ are because of the taller houses. When wind flow is aligned with the smoother surface of the road to the west ($210^\circ - 360^\circ$) values are lower. Morphometrically determined z_0 are within the anemometric range, except when increased friction velocity due to nearby roughness elements creates an anemometric z_0 that is double the morphometric results (Fig. 6.6b, $120^\circ - 180^\circ$).

When the morphometric methods are applied without considering vegetation, the average reduction of z_d is 0.3 m and z_0 is 0.1 m (Fig. 6.7b, Kan_b and Mac_b). However, these values are directionally dependent. For example, not considering the taller and more abundant vegetation between $030^\circ - 090^\circ$ means z_d and z_0 are reduced with an average of up to 20 % and 40%, respectively, for both morphometric methods. Giometto et al. (2017) also demonstrate overlooking vegetation leads to a reduction of up to 50% in both z_d and z_0 for a neighbourhood site with a larger plan area of vegetation and taller trees than the SWD site. Both results highlight the importance of considering vegetation during aerodynamic parameter determination.

6.3.3.3 Similarities in aerodynamic parameter analysis between the sites

The variability in the anemometric methods and the interdependence of z_d and z_0 (i.e. the former is used when determining the latter, Eq. 6.3) means it is difficult to use the anemometric methods as a basis for the most appropriate magnitude of z_d and z_0 . However, there are apparent similarities from the aerodynamic parameter analysis performed at both sites. There is greater uncertainty in the application of the temperature variance method to determine z_d , than the wind variance method. The RMSE between ϕ_{est} and ϕ_{obs} of the former are consistently twice the latter, which is attributed to the thermal inhomogeneity of both sites and dissimilarity of roughness length between momentum and heat. Greater uncertainty was also found in the temperature variance method in a central urban area (Sect. 3.5.1.1).

As with previous applications, z_d determined using the temperature and wind variance methods at both sites indicates z_d is larger than H_{av} (e.g. Grimmond et al. 1998, 2002, Feigenwinter et al. 1999, Kanda et al. 2002, Tsuang et al. 2003, Christen 2005, Chang and Huynh 2007, Tanaka et al. 2011,

Sect. 3.5.1.1). Additionally, morphometric z_d results are consistently smaller than anemometric results. However, the direct incorporation of height variability in Kan_{z_d} means it is more similar to the anemometric methods than Mac_{z_d} . Mac_{z_d} is less than H_{av} and may be appropriate for homogeneous groups of roughness elements. However, recent literature demonstrates that the disproportionate amount of drag imposed by taller roughness elements in a heterogeneous mix means z_d may indeed become larger than H_{av} (Jiang et al. 2008, Xie et al. 2008, Hagishima et al. 2009, Zaki et al. 2011; Millward-Hopkins et al. 2011, Tanaka et al. 2011, Kanda et al. 2013). This is particularly evident during leaf-on conditions at the SFP site (Fig. 6.5a), where z_d approaches $2H_{av}$.

The contrast in magnitude of aerodynamic parameters determined using the Kan and Mac morphometric methods (Kan_{z_d} is typically twice Mac_{z_d}) relates to the Kan method's direct consideration of roughness-element height variability. However, as the Kan method is developed from Mac , their directional variability is similar. At both sites, the morphometric methods show similar directional variability to the anemometric methods indicating sound performance of the vegetation parameterisation developed in Chapter 5.

For both morphometric methods, the range of z_d and z_0 for any direction is consistently within ± 1 m and 0.2 m of the median, respectively (Fig. 6.5 shading and Fig. 6.6 range of points for a direction). The range is attributed to the source area variability with meteorological conditions. For example, a relatively wider z_d range between $000^\circ - 120^\circ$ at the SFP site is caused by the proportion of the source area which falls upon the lake, grassed area and surrounding trees (Fig. 6.5).

6.3.4 Implications for wind-speed estimation

With pre-determined z_d and z_0 , the logarithmic wind law can be used to model the neutral vertical profile of wind speed (Blackadar and Tennekes 1968, Tennekes 1973):

$$\bar{U}_z = \frac{u_*}{\kappa} \ln\left(\frac{z - z_d}{z_0}\right) \quad (6.10)$$

which theoretically only applies in the inertial sublayer (ISL), where vertical fluxes of momentum can be assumed constant with height (e.g. Tennekes 1973). Closer to a rough surface (i.e. within the RSL) the roughness-element wakes create a highly variable flow which may deviate considerably from Eq. 6.10 (e.g. Thom et al. 1975, Simpson et al. 1998, Kastner-Klein and Rotach 2004, Christen 2005, Harman and Finnigan 2007, Barlow and Coceal 2009, Giometto et al. 2016). With

measurements at the SFP site ($1.6H_{av}$) closer to the roughness elements, there is greater confidence to use Eq. 6.10 at the SWD site (where $z_m = 2.8H_{av}$).

To assess the vegetation parameterisation within the *Kan* and *Mac* morphometric methods, the wind speeds measured at the SWD site during neutral conditions ($|z'/L| < 0.05$) are estimated using Eq. 6.10 with the observed u_* for each 30-min period and roughness parameters determined with and without vegetation (Fig. 6.6, subscript *bv* with and *b* without vegetation). The estimated wind speed (U_{est}) is regressed against the mean observed wind speed (U_{obs}) for the corresponding time period (Fig. 6.7). As the RMSE has been demonstrated to disproportionately amplify the error associated with outliers when assessing model performance (Willmott and Matsuura 2005), both the RMSE and mean absolute error (MAE) between U_{est} and U_{obs} are reported.

Wind speeds are overestimated in over 90% of cases, which is more apparent at higher U_{obs} (Fig. 6.7). Overestimation could be for several reasons, including uncertainty of the use of the logarithmic wind law closer to roughness elements or the appropriateness of z_d and z_0 values obtained from the different methods (e.g. Millward-Hopkins et al. 2012). However, irrespective of the morphometric method U_{est} most resembles U_{obs} when aerodynamic parameters determined considering vegetation and buildings are used. For example, wind speeds estimated using *Kan_{bv}* and *Mac_{bv}* have MAE from U_{obs} of 0.92 and 1.44 $m s^{-1}$, respectively, whereas ignoring vegetation (i.e. *Kan_b* and *Mac_b*) the MAE is $> 0.3 m s^{-1}$ larger for both methods (1.31 and 1.73 $m s^{-1}$, respectively). The lower errors (both RMSE and MAE) associated with the *Kan* method indicate that regardless of whether vegetation is considered, incorporating height variability improves wind-speed estimates.

Similar comparisons between U_{est} and U_{obs} are performed for wind directions with the least ($210^\circ - 240^\circ$) and greatest ($030^\circ - 090^\circ$) vegetated roughness elements (Fig. 6.8a and b, respectively). As the least vegetated directions have similar aerodynamic parameters (Fig. 6.6) their associated U_{est} are similar irrespective of whether vegetation is considered or not. However, despite the small number of trees, accounting for them still reduces the error in wind-speed estimation i.e. the lower errors of *Kan_{bv}* and *Mac_{bv}* (Fig. 6.8a). The importance of considering height variability is apparent again, as the *Kan* method reduces the errors from U_{obs} by over 0.5 $m s^{-1}$, in comparison to the *Mac* method.

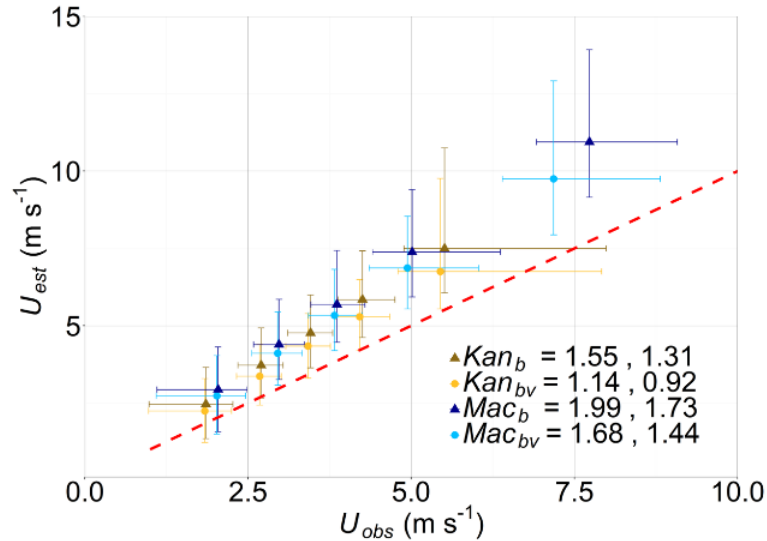


Figure 6.7: Observed (U_{obs}) and estimated (U_{est} , Eq. 6.10) wind speeds for each 30-min period (at the SWD site) using the Kanda et al. (2013, Kan) and Macdonald et al. (1998, Mac) morphometric methods, considering both buildings and vegetation (subscript bv) and only buildings (subscript b). Data are binned from lowest wind speed in groups of 1250 (30-min) data points. Median (points) and 5th and 95th percentiles shown. The root-mean-square error then mean absolute error ($m s^{-1}$) (between U_{est} and U_{obs}) are given in the legend

As expected, in directions with maximum vegetation (tree) cover ($030^{\circ} - 090^{\circ}$) the impact on estimated wind speeds is greatest. Inclusion of vegetation consistently results in an improvement of wind-speed estimation of over $0.5 m s^{-1}$ (Fig. 6.8b). The smallest differences between the errors associated with Kan_{bv} and Mac_{bv} occur in this direction ($0.2 m s^{-1}$). Combined with the errors for Kan_b being larger than Mac_b , the incorporation of vegetation appears more important for accurately estimating the wind speeds than considering height variability (in this case).

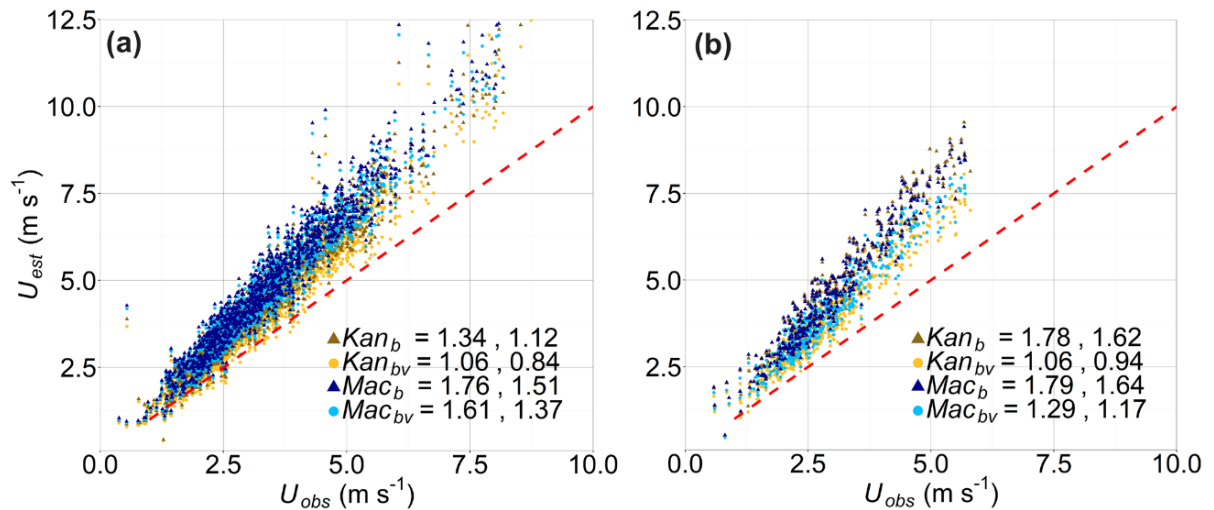


Figure 6.8: As for Fig. 6.7, but for wind directions between: **(a)** $210^{\circ} - 240^{\circ}$ and **(b)** $030^{\circ} - 090^{\circ}$. Each point represents a 30-min period of observations (data are not binned)

6.4 Conclusions

Two anemometric and two morphometric methods are used to determine the zero-plane displacement (z_d) and aerodynamic roughness length (z_0) for an urban park and a suburban neighbourhood. The anemometric methods use *in-situ* single-level high frequency observations and therefore inherently include the presence and state of vegetation. The morphometric methods have been developed for bluff bodies only, however a new parameterisation (Sect. 5.2.3) to consider both buildings and vegetation is explored.

At both sites, z_d determined using the anemometric methods is larger than the morphometric methods. There is greater uncertainty in an anemometric method based upon scaled temperature variance, as opposed to the vertical wind velocity variance, likely because of the thermal inhomogeneity of the sites. However, the Kanda et al. (2013) morphometric method, which directly considers roughness-element height variability, is consistently most similar to the anemometric methods, indicating z_d is larger than average roughness-element height at the respective sites.

Inter-seasonal analysis is performed at the urban park, which is predominantly vegetation, with few buildings. Both anemometric methods indicate z_d during leaf-on vegetation state is up to 1 – 4 m larger than leaf-off. In addition, leaf-on z_d is obviously larger in directions with taller, or a greater proportion of, vegetated roughness elements. The morphometric methods with the vegetation parameterisation have a similar magnitude and directional variability of change, indicating leaf-on z_d is 1 – 3 m larger than leaf-off, which varies with upwind roughness elements. When the anemometric z_d is similar to, or larger than, the measurement height z_0 cannot be determined from observations. However, the morphometric methods indicate leaf-on z_0 may be less than half leaf-off z_0 because the additional tree foliage in an already densely packed area creates an effectively smoother canopy.

The suburban neighbourhood has a larger proportion of buildings than trees. Morphometric analyses are undertaken during leaf-on conditions with and without vegetation. Where there is confidence in the anemometric methods, their z_d and z_0 can be directly related to surface characteristics surrounding the site. The morphometric methods have similar directional variability to the anemometric methods, but with less variability as the geometry of the site surroundings are similar. If vegetation is ignored in the morphometric calculations, z_d and z_0 decrease by up to 20 % and 40%, respectively.

Wind speeds estimated at the suburban site using the logarithmic wind law and aerodynamic parameters from the morphometric methods are compared to observed wind speed at approximately three times the average roughness-element height. Wind-speed estimations most resemble observations when vegetation, as well as the height variability of roughness elements are considered. The consideration of vegetation is more important than the roughness-element height variability in directions where vegetation cover is maximal.

The extension of the morphometric methods developed in Chapter 5 captures the presence and state of vegetation for aerodynamic parameter determination and wind-speed estimation. As green spaces become increasingly part of the urban fabric, understanding the implications of vegetation upon aerodynamic characteristics becomes more important. Further observations with different types, amounts and arrangements of vegetation will allow more thorough assessment of this parameterisation.

The methodology to determine z_d and z_0 from surface elevation databases (including vegetation) is freely available in the Urban Multi-scale Environmental Predictor (UMEP, <http://www.urban-climate.net/umep/UMEP>) for the open source software QGIS (Lindberg et al. 2018)

Chapter 7. Urban morphology parameters from global digital elevation models: implications for aerodynamic roughness and for wind-speed estimation¹

Abstract Urban morphology and aerodynamic roughness parameters are derived from three global digital elevation models (GDEM): Advanced Spaceborne Thermal Emission and Reflection Radiometer (ASTER), Shuttle Radar Topography Mission (SRTM), and TanDEM-X. Initially, each is compared to benchmark elevation datasets in central London. Ground heights are extracted from the GDEMs using a moving window, which generates a terrain model with root-mean-square accuracy of up to 3 m. Subtraction of extracted ground heights from the respective GDEMs provides roughness-element heights only, allowing for calculation of morphology parameters. The parameters are calculated for eight directional sectors of 1 km grid-squares. Apparent merging of roughness elements in all GDEMs causes height-based parameter underestimation, whilst plan and frontal areas are over- and under-estimated, respectively. Combined, these lead to an underestimation of morphometrically-derived aerodynamic roughness parameters. Parameter errors are least for the TanDEM-X data. Further comparison in five cities (Auckland, Greater London, New York, Sao Paulo, Tokyo) allows empirical corrections to TanDEM-X derived geometric parameters to be proposed. These reduce the error in parameters across the cities and for an independent location. Meteorological observations in central London provide insight to the accuracy of average wind-speed estimates using roughness parameters from the different elevation databases. The proposed corrections lead to improved wind-speed estimates, which combined with the improved spatial representation of parameters across cities demonstrates their potential for use in urban climate studies.

7.1 Introduction

Accurately resolving urban morphology is critical for modelling and understanding the urban climate (Grimmond and Souch 1994, Yan et al. 2015). The type, presence and distribution of surface roughness elements (urban morphology) influences turbulent and radiative heat fluxes, energy storage and hydrological properties (Grimmond et al. 2010, 2011, Lindberg and Grimmond 2011b,

¹This chapter is under review as: **Kent CW**, Grimmond CSB, Gatey D, Hirano K (2018b) Urban morphology parameters from global digital elevation models: implications for aerodynamic roughness and for wind-speed estimation. Submitted to Remote Sensing of Environment, 4 Jan 2018.

Garuma 2017). In addition, the morphology influences the storage and fluxes of other scalar quantities such as pollutants, which can inform ventilation pathway mapping (Gál and Unger 2009, Ng et al. 2011). Accurate representation of urban morphology is vital to accurately model fluxes of momentum. Surface roughness elements influence the spatially- and temporally-averaged properties of the air flow, as well as the turbulent characteristics. In combination, this helps define the structure of the urban boundary layer (Roth 2000, Martilli 2002, Arnfield 2003, Britter and Hanna 2003, Fernando 2010).

The influence of the surface upon momentum fluxes can be characterised using aerodynamic roughness parameters (zero-plane displacement, z_d , and roughness length, z_0). With these parameters, the spatially- and temporally-averaged wind-speed profile can be estimated if the flow is free from roughness-element wakes (e.g. Sect. 4.2). The extent of vertical displacement of the wind-speed profile is indicated by z_d , which may correspond to the 'drag centroid' or height the mean drag appears to act (Thom 1971, Jackson 1981). The z_0 is the height wind speed becomes zero in the logarithmic wind-speed profile, in the absence of z_d (Blackadar and Tennekes 1968). The morphology of roughness elements can be used to determine z_d and z_0 using morphometric methods (Grimmond and Oke 1999, Sect. 3.3.2). Therefore, elevation databases that resolve roughness-element morphology allow estimation of z_d and z_0 in cities and the associated: wind speeds (e.g. Millward-Hopkins et al. 2012, 2013a, Varquez et al. 2015, Sect.3.6, Chapter 4), surface heat fluxes (e.g. Crawford et al. 2018) and surface shear stress in meso-scale meteorological models (e.g. Weekes and Tomlin 2013).

The objective of this work is to assess global digital elevation models (GDEMs) for the determination of urban morphology. First, GDEMs from the Advanced Spaceborne Thermal Emission and Reflection Radiometer (ASTER) (Tachikawa et al. 2011), Shuttle Radar Topography Mission (SRTM) (Rabus et al. 2003, Farr et al. 2007) and TanDEM-X (Rossi et al. 2012, Wessel 2016) are compared to benchmark elevation databases in central London, derived from airborne light detection and ranging (lidar). As quantitative and qualitative analyses find the geometric and aerodynamic parameters to be more accurate with the TanDEM-X model, further comparison is undertaken in five other cities. Using these strategically, globally located cities, attempts are made to optimise geometry and aerodynamic roughness parameters derived from the TanDEM-X. To independently assess roughness parameters determined from the different elevation models with morphometric

methods, the associated wind-speed profile estimates aloft central London are compared to those observed with Doppler lidar.

7.2 Elevation databases

7.2.1 Digital elevation model terminology

Digital elevation model (DEM) is a collective term for 2-D surface elevation data (Hirt 2015), including both digital surface models (DSMs) (ground and roughness-element heights) and digital terrain models (DTMs) (ground heights only) (Fig. 7.1). Subtraction of a DTM from a DSM provides the roughness-element heights (a roughness-element surface model, RESM). Various procedures may be used (e.g. Goodwin et al. 2009, Lindberg and Grimmond 2011a, Crawford et al. 2016, Sect. 6.2.2) to identify and extract building and vegetation heights, producing a building digital surface model (BSM) and canopy digital surface model (CDSM), respectively (Fig. 7.1).

High resolution DEMs (typically obtained using airborne lidar, synthetic aperture radar (SAR) or optical techniques, e.g. Nelson et al. 2009) can accurately resolve surface features to horizontal resolutions of 1 m or less (e.g. Fig. 7.1e), but may be expensive to collect, store and process. Their collection tends to be ‘once-off’, with varying methods and/or reporting making up-to-date global elevation data unfeasible. Technological advancements (e.g. autonomous remote sensing) may improve both feasibility and accessibility in the future (e.g. Colomina and Molina 2014, Feng et al. 2015).

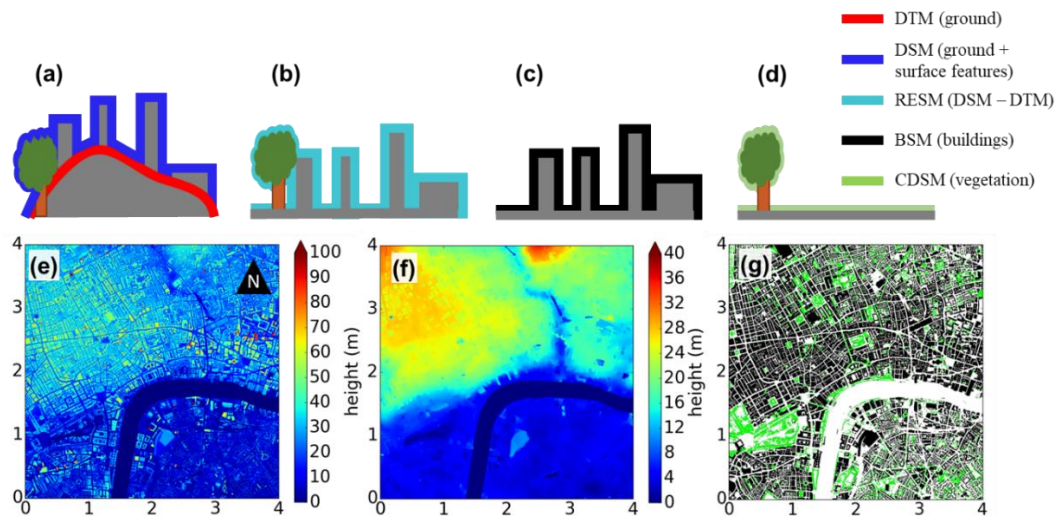


Figure 7.1: Different digital elevation models (DEMs) and terminology used: **(a)** digital surface model (DSM) and digital terrain model (DTM), **(b)** roughness-element surface model (RESM = DSM – DTM), **(c)** building digital surface model (BSM) and **(d)** canopy digital surface model (CDSM). From **(b)** to **(c)** or **(d)** requires land cover information. GIS examples are: **(e)** DSM, **(f)** DTM, **(g)** mask of pixels which are in the BSM (black) and CDSM (green) for a 4 km x 4 km area in central London, UK (map units: km). Surface elevation database details: Lindberg and Grimmond (2011a)

7.2.2 Global digital elevation models (GDEMs)

On a global scale, topographic data can be obtained from orbital SAR (e.g. SRTM and TanDEM-X) or optical stereographic images (e.g. ASTER) (Bürgmann et al. 2000, Stevens et al. 2004). Although, other GDEMs exist (e.g. Rexer and Hirt 2016), the ASTER, SRTM and TanDEM-X models are assessed here given their extensive use and accessibility (Table 7.1). Appendix 7.A summarises each model, including the meta-data supplied with TanDEM-X (e.g. water mask).

There is increasing potential for GDEM use for a wide range of applications, given the improving resolution and accuracy, development of automated processing techniques, and up-to-date, broad spatial coverage capabilities. Accuracy of each elevation model varies (e.g. Rodriguez et al. 2006, Farr et al. 2007, Tachikawa et al. 2011) depending upon spatial coverage and data preparation methodologies (Fisher and Tate 2006, Hebelier and Purves 2009). Unique artefacts such as voids (Reuter et al. 2007) or residual cloud patterns and stripe effects (Hirt et al. 2010, Tachikawa et al. 2011) may be spatially distributed across datasets, therefore GDEMs are assessed both prior to public release (e.g. Rodriguez et al. 2006, Tachikawa et al. 2011 and Wessel 2016 for the SRTM, ASTER and TanDEM-X products, respectively), and subsequently. Typically, vertical and horizontal geolocation accuracy is evaluated against ground control points (e.g. Li et al. 2013) or a higher accuracy elevation model (Hofton et al. 2006, Guth 2010, Tachikawa et al. 2011, Ioannidis et al. 2014). In this work, the latter approach is used.

DEM	Spatial extent	Temporal extent	Method of creation	Platform	Horizontal resolution ^a	Horizontal accuracy ^b	Vertical accuracy ^b	Datum: horizontal, vertical	Data source ^c	Cost	Key references
ASTER (Version 2)	83°N and S	2000 – 2010	Photogrammetry	Satellite	1 arc-second	< 6 m ^d	< 15 m (95% confidence)	WGS84 EGM96	USGS ^e	Free	ASTER GDEM Validation Team (2009), Tachikawa et al. (2011)
SRTM (1 Arc-Second Global)	60°N to 56°S	11 – 22 Feb 2000	Interferometry	Shuttle		< 12.6 m (90% confidence) ^f	< 9.0 m (90% confidence) ^f				Farr and Kobrick (2000), Farr et al. (2007)
TanDEM-X	Global	Dec 2010 – Jan 2015	Interferometry	Satellite	0.4 arc-second	< 10 m (90% confidence)		WGS84 WGS84	DLR ^g	Free for scientific grant, else €10 / km ²	Krieger et al. (2007), Rossi et al. (2012), Wessel (2016), Rizzoli et al. (2017)

^a 1 arc-second is approximately 30 m at the equator

^b As reported during internal evaluation (see key references)

^c As used during this work

^d 0.13 arc-sec. to west, 0.19 arc-sec. to north (Tachikawa et al. 2011)

^e United States Geological Survey data explorer (<https://earthexplorer.usgs.gov/>, accessed November 2016)

^f For spatial variability see Rodriguez et al. (2006)

^g Deutsches Zentrum für Luft- und Raumfahrt (German Aerospace Centre, research grant: DEM_URBAN1021, data provided: February 2017)

Table 7.1: Summary of the global digital elevation models used in this work

7.2.3 Previous assessment of GDEMs in urban areas

Although many remote sensing studies explore urban land cover change (e.g. Maktav et al. 2005, Patino and Duque 2013), few have assessed the ability of GDEMs to reproduce the 3-D structure of cities (Yang et al. 2011). Cities complex structure is problematic for remote sensing because of layover, shadowing and multipath artefacts (Farr et al. 2007, Sportouche et al. 2011, Small and Sohn 2015, Wang et al. 2018). This means individual roughness elements tend to have ‘indistinct’ boundaries (e.g. Eckert and Hollands 2010, Zeng et al. 2014, Xu et al. 2017), especially as resolution coarsens and becomes less than roughness-element dimensions and details (e.g. roof pitch, different roof heights, etc.). However, the limitations still occur using high resolution data. For example, using a combination of high-resolution (≤ 3 m) satellite-derived stereo and SAR imagery in Hong Kong, Xu et al. (2017) reveal extracted building boundaries are imperfect compared to benchmark data, with height underestimation in high-density locations and potential overestimation of lower buildings. The urban morphology parameters: building coverage, building height, frontal area index and z_0 (calculated with Macdonald et al. 1998 morphometric method, Sect. 3.3.2.2) had absolute average differences of between 22 and 30%, compared to benchmark data.

Previous analysis indicates tall buildings locations may be accurate in the SRTM model but heights are underestimated (Gamba et al. 2002, Small and Sohn 2015). Using TanDEM-X data in Berlin, Rossi and Gernhardt (2013) also found underestimation of roughness-element heights (buildings and trees) and overestimation of ground heights between them. Marconcini et al. (2014) and Geiß et al. (2015) provide methodologies to extract DTMs from the TanDEM-X model, but without quantitative assessment of the resulting roughness-element geometry. Automated analysis of the TanDEM-X data has generated a binary global urban footprint (GUF) mask, delineating ‘settlement’ or ‘non-settlement’ areas (Esch et al. 2011, 2013, 2017).

Combining ASTER, Global Multi-resolution Terrain Elevation Data 2010 (GMTED2010) and night-time light images, Darmanto et al. (2017) derive empirical relations to obtain plan area (Fig. 7.3) and average heights of buildings in three cities (Istanbul, Tokyo, Jakarta). These are used with Tokyo-based empirical relations (Kanda et al. 2013) to calculate aerodynamic roughness parameters (z_d and z_0). The parameters are not quantitatively assessed, but provide more accurate wind-speed estimates (cf. observations) than using default settings in a single-layer urban canopy model coupled with the weather research and forecasting model (SLUCM/WRF).

7.3 Methodology

7.3.1 Dataset comparison

The analysis is conducted in two stages (Fig. 7.2): Comparison 1 – ASTER, SRTM and TanDEM-X models are compared to a benchmark dataset for a 20 km x 20 km area in central London; and, Comparison 2 – TanDEM-X model is compared to benchmark datasets in five cities (Table 7.2). Note, benchmark data are not the ‘truth’ as these also have uncertainties (e.g. the precise location and height of buildings).

All comparisons are performed in the horizontal datum local to the benchmark data (Table 7.2). The ASTER and SRTM heights are already orthometric, however the TanDEM-X heights are referenced to the WGS84 ellipsoid and therefore converted to orthometric height using the National Geospatial intelligence agency’s 2.5 x 2.5-minute horizontal resolution offset between the WGS84 ellipsoid and EGM2008 Geoid (NGA 2008). Each of the assessed GDEMs are sensitive to all surface features, including vegetation (e.g. Farr et al. 2007, Tachikawa et al. 2011, Wessel 2016, Rexer and Hirt 2016). The GDEMs are therefore assumed to be DSMs and subtraction of ground heights (DTM) provides a roughness-element surface model (e.g. Fig 7.1) from which morphology parameters are calculated. The method to extract ground heights (DTMs) from the GDEMs is given in Sect. 7.3.2.

Initially, a pixel-to-pixel comparison between the GDEMs and benchmark data is undertaken. Although not central to determining the morphology parameters, the comparison informs the DTM extraction (Sect. 7.3.2) and provides insight to the GDEM’s ability to reproduce intricacies of the urban surface. For results see Appendix 7.B.

The RESM is used to calculate geometric and roughness parameters for each elevation dataset. Parameters are calculated using 1 km x 1 km grid-squares with a 500-m overlap, subdivided into eight 45° sectors or wind directions (Fig. 7.3). Directional sectors allow for the variability of urban morphology with associated upwind roughness to be included (e.g. a site’s fetch may vary with prevailing wind). The 500-m overlap ensures the entire surface area in the DEMs are considered for each direction. The upwind distance and directional sector width are based upon measurement source areas for observations during neutral atmospheric stability at approximately 2.5 times the canopy height in central London (e.g. Fig. 2.3). The scale for calculations is also consistent with the grid size used to derive z_d and z_o for the Kanda et al. (2013) morphometric method, as well as spacing

employed in commonly used urban modelling systems, e.g. within the Weather Research and Forecasting (WRF) model (Chen et al. 2011).

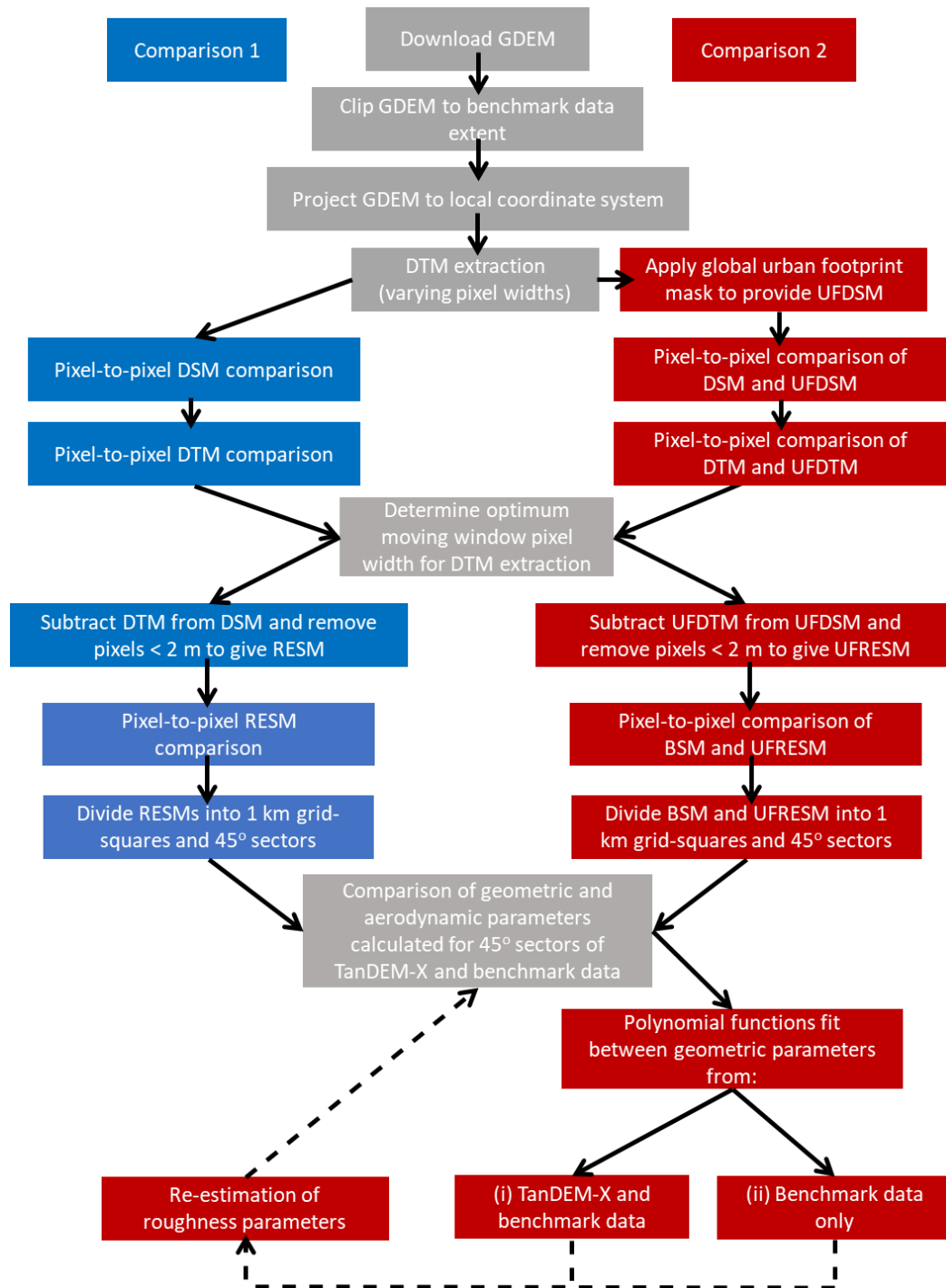


Figure 7.2: Work flow for processing the global digital elevation models (GDEMs) and for comparison to benchmark data. For abbreviations see Fig. 7.1. For comparison 2, only pixels within the global urban footprint (GUF) mask ‘settlement layer’ are retained (Esch et al. 2017), indicated with ‘UF’ prefix: UFDSM – urban footprint digital surface model = ground + surface feature heights within the GUF; UFDTM – urban footprint digital terrain model = ground heights within the GUF; UFRESM – urban footprint roughness-element surface model = roughness-element heights within the GUF

City	EPSG (WGS84 UTM zone)	Upper left co-ordinates (X _{min} , Y _{max})	x extent, y extent (km)	DSM	DTM	BSM ^a	CDSM	Resolution	Collection method	Collection date	Source
Sao Paulo	32723 (23S)	313901.002, 7411738.415	47, 57	-	-	✓ (abs)	-	Building footprint	Photogrammetry	2007, updated yearly	GeoSampa (2017), Danilo Mizuta pers. comm. (16/8/2017)
Tokyo	32654 (54N)	364005.246, 3966451.299	46, 38	-	✓	✓ (st)	-	DTM: 5 m, BSM: building footprint	DTM: lidar BSM: ground survey	2011	Geospatial Information Authority of Japan (GSI)
New York	32618 (18N)	563127.939, 4529850.727	47, 46	-	✓	✓ (abs)	-	DTM: 1 m, BSM: building footprint	DTM: Leica ALS70 lidar BSM: aerial imagery	DTM: Mar-Apr 2014 BSM: 2014	DTM: USGS CMGP (2014) BSM: NYC DoITT (2014)
London	32631 (31N)	253226.215, 5732341.367	61, 50	✓	✓	✓	✓	1 m	Optech ALTM 3033 lidar	Aug-Sept 2008	Lindberg and Grimmond (2011a)
Auckland	32760 (60S)	293156.620, 5921972.196	19, 13	✓	✓	C ^b	-	1 m	Optech ALTM 3100 lidar	July-Nov 2013	LINZ (2013)

^a Method of reporting heights above ground level: (abs) is absolute heights, (st) is storey based heights. Correction from (st) to (abs) uses the Council on Tall Buildings and Urban Habitat (CTBUH 2017) recommendations, with a storey $s = 3.5$ m, except for 'tall buildings' (> 14 stories, $H_{i,tall}$): $H_{i,tall} = 3.5s + 9.625 + 2.625(s/25)$

^b Created from the TanDEM-X global urban footprint mask 'settlement' layer (Esch et al. 2017)

Table 7.2: Source and extent of the benchmark data used in comparison 2 (Fig. 7.2). Benchmark datasets downloaded during March 2017. Symbols: ✓ = available from source, - = not available, C – created. Maps of spatial extent provided in Fig. 7.10 (New York) and Appendix 7.E

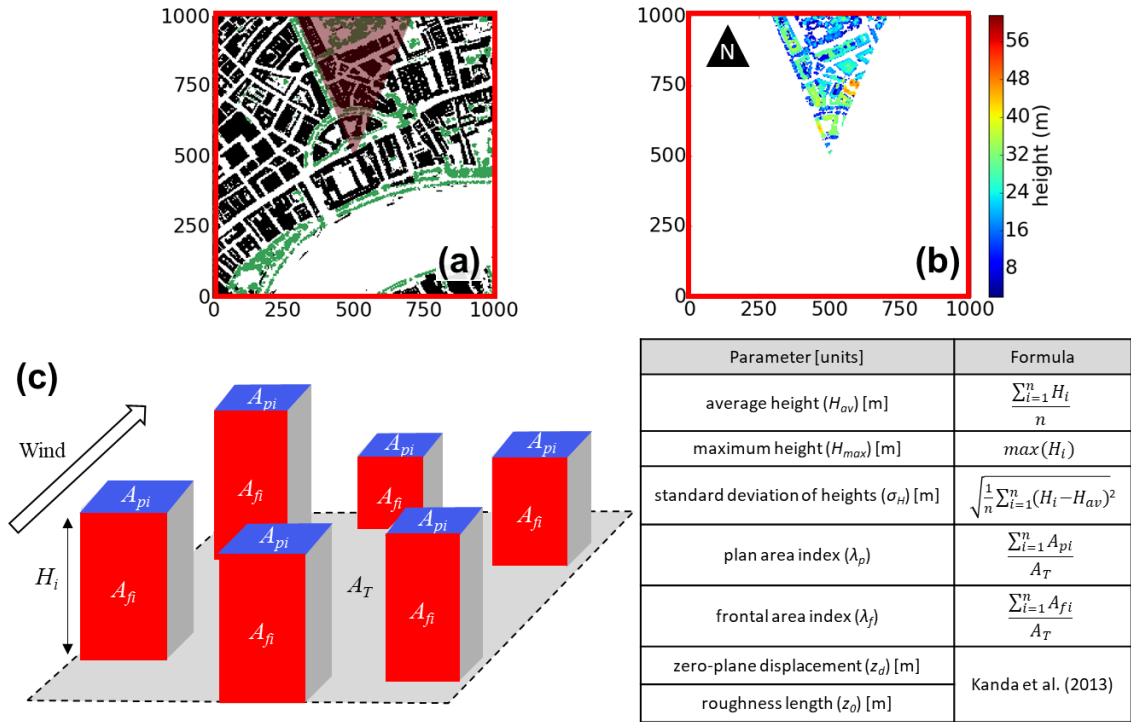


Figure 7.3: Procedure to determine morphology parameters from a directional sector of a 1 km x 1 km grid square in central London: (a) roughness-element surface model (black = buildings, green = vegetation) overlain with 45° sector representing northerly wind direction (red shading); (b) roughness-element heights within directional sector for calculation; (c) parameter calculation from idealised roughness elements

For each sector, the geometric parameters determined are the average (H_{av}), maximum (H_{max}) and standard deviation (σ_H) of roughness-element heights, the plan area index (λ_p) and the frontal area index (λ_f) (Fig. 7.3c). Only roughness elements with height > 2 m are considered, to ensure low-level street furniture (e.g. signage), vehicles, etc. are removed. The parameters are used with Kanda et al.'s (2013) morphometric method to calculate z_d and z_o , which directly incorporates roughness-elements height variability and has been found to provide more accurate wind-speed estimates than other methods (Varquez et al. 2015, Sects. 3.6, 4.5 and 6.3.4). The average ground height ($H_{av,grd}$) in each sector is recorded from the DTM.

In comparison 1, the benchmark dataset allows all roughness-element heights to be considered. However, only built roughness-elements are used in comparison 2 as some benchmark datasets only contain building heights. As with previous studies (e.g. Marconcini et al. 2014), the GUF mask is used to retain building heights from the TanDEM-X model (indicated with 'UF', i.e. UFDSM, UFDTM and UFRESM). In Auckland, the absence of benchmark building footprints data, required the GUF mask to be applied to both the benchmark and TanDEM-X data. Insight to the roughness elements captured by the GUF mask is provided in Appendix 7.A.

To permit comparison to previous analyses, the metric used to assess the results is the root-mean-square error (RMSE). For n observations, the average deviation of a predicted value (\hat{y}_i)

from the observed value (y_i) is:

$$\text{RMSE} = \left[\frac{\sum_{i=1}^n (y_i - \hat{y}_i)^2}{n} \right]^{0.5} \quad (7.1)$$

A normalised RMSE (nRMSE) is determined by dividing the RMSE by the mean value of the observations, allowing for a scale-independent comparison of errors. The mean bias error (MBE) is considered when comparing geometric and aerodynamic parameters determined from different datasets.

7.3.2 Extraction of ground heights from the GDEMs

Although sophisticated techniques are available to separate ground heights and surface features from high-resolution point-cloud data (e.g. Kraus and Pfeifer 2001, Chen et al. 2009, Schreyer et al. 2014), the comparatively coarse resolution of GDEMs require other techniques. DTMs extracted from the TanDEM-X model, assuming roughness elements are pixels above a threshold elevation (Marconcini et al. 2014), have not been quantitatively evaluated. However, threshold-differencing techniques may be inaccurate in regions where the amplitude of ground elevation range exceeds building heights, leading to higher bare-earth pixels being misidentified as buildings. Geiß et al.'s (2015) object-orientated, progressive morphological filtering techniques may overcome this limitation, but their associated RESMs are not quantitatively analysed.

Here, DTM extraction uses a square moving window. The ground height of the central pixel is assumed to correspond to the lowest elevation pixel within the window. Arbitrary moving windows have been used (e.g. 200 m x 200 m, Gamba et al. 2002). Here the pixel-width of the window is varied (3-, 5-, 7-, 11-, 21- and 31-pixels; corresponding to a 1-, 2-, 3-, 5-, 10- and 15-pixel buffer from the central pixel). The six extracted DTMs are compared to the benchmark DTM to identify the most appropriate moving window size. The DTM extraction procedure is swift and objective, eliminating the need to set subjective thresholds during threshold-differencing (e.g. Marconcini et al. 2014), and individual pixel classification during object-orientated approaches (e.g. Geiß et al. 2015). Additionally, the moving window is responsive to local elevation, alleviating a flat earth assumption.

7.3.3 Polynomial function fitting

During comparison 2, polynomial functions are fit through city-specific data on two occasions (Fig. 7.2) with the objective of investigating the relation between different geometric parameters determined with the: (i) TanDEM-X and benchmark data and (ii) benchmark data

only. Initially locally weighted scatter-plot smoother (LOWESS, Cleveland 1979) data pairs are obtained, which are used in a non-linear least squares fit (Bates and Watts 1988) constrained to the polynomial function:

$$y = ax^3 + bx^2 + cx \quad (7.2)$$

where a , b and c are best-fit coefficients for the geometric parameters x and y listed in Table 7.3. Equation 7.2 permits a variable relation across the range of data while ensuring if $y = 0$ then $x = 0$. Using the LOWESS curve data intentionally removes the sensitivity to outliers (e.g. if area has changed over time, Sect. 7.6). The Akaike (1974) information criterion indicates the selected order of polynomial (Eq. 7.2) does not lead to overfitting of the data. To ensure the fits have sufficient data, the x parameter data are binned (5 m for H_{av} and σ_H , 10 m for H_{max} , and 0.1 for λ_p and λ_f) and fits restricted to bins $n \geq 20$.

(a)		(b)	
x [TDX]	y [BM]	x [BM]	y [BM]
$H_{av,grd}$	$H_{av,grd}$	$\lambda_{p,b}$	$\lambda_{f,b}$
H_{av}	H_{av}	$H_{av,b}$	$\sigma_{H,b}$
H_{max}	H_{max}	$\sigma_{H,b}$	$H_{max,b}$
σ_H	σ_H		
λ_p	λ_p		
λ_f	λ_f		

Table 7.3: Geometric parameters x and y used during polynomial function fitting (Eq. 7.2). Polynomial fits are between geometric parameters derived from the: **(a)** TanDEM-X [TDX] and benchmark [BM] elevation data (i.e. fitting stage (i) in Fig. 7.2) and **(b)** benchmark parameters considering buildings only (represented by subscript b) (i.e. fitting stage (ii) in Fig. 7.2). Parameter calculation, abbreviations and units: Fig. 7.3c

'Multi-city' polynomial functions generated from all data points leads to bias towards cities with more data. Therefore, multi-city functions are created with the same fitting procedure as above, but through 1000 evenly sampled points along city-specific polynomials. With this number of points, a $\pm 10\%$ change (i.e. using 900 or 1100 points) does not impact the fitted coefficients in Eq. 7.2.

7.4 Results

7.4.1 Comparison 1: ASTER, SRTM and TanDEM-X in London, UK

Initial comparison of the ASTER, SRTM and TanDEM-X GDEMs for a 20 km x 20 km area in central London provides insight to their respective representations of the urban surface compared to a high-resolution (benchmark) model (Fig. 7.4). The similarity of SRTM and TanDEM-X elevations (and therefore differences from the benchmark data) are likely due to their derivation from similar interferometric methods. In contrast, elevations from the photogrammetric approach used to derive ASTER appear noisy, producing the greatest differences from the benchmark data (cf. Fig. 7.4c – h). The differences for the ASTER data can be considerable (± 20 m) across the

study area, whilst differences for the SRTM and TanDEM-X data are less, becoming largest in the city centre (due to more complex geometry).

For the pixel-to-pixel comparison (Appendix 7.B) the RMSE assessed against the benchmark data for the DSMs have values of 9.79 m (ASTER), 6.27 m (SRTM) and 6.35 m (TanDEM-X), which are all better than the accuracy given by respective agency studies (Table 7.1). The errors become larger with increases in surface height, as taller roughness elements are underestimated. Topographical variability also appears to contribute to larger errors in ASTER (Fig. 7.4f). Underestimation of roughness-element heights cannot be attributed to the DTM extraction procedure (see Appendix 7.B for discussion), for which a 5 x 5-pixel moving window extracts DTMs which best resemble the benchmark data for all GDEMs (RMSE \sim 3 m for TanDEM-X and SRTM, and 8 m for ASTER). Despite the ‘block-like’ DTM which is extracted from the GDEMs (Fig. 7.6f-h), multiple iterations of the procedure or smoothing of the extracted DTMs (e.g. Gaussian filters and interpolation techniques) were not found to improve the pixel-based accuracy of the method.

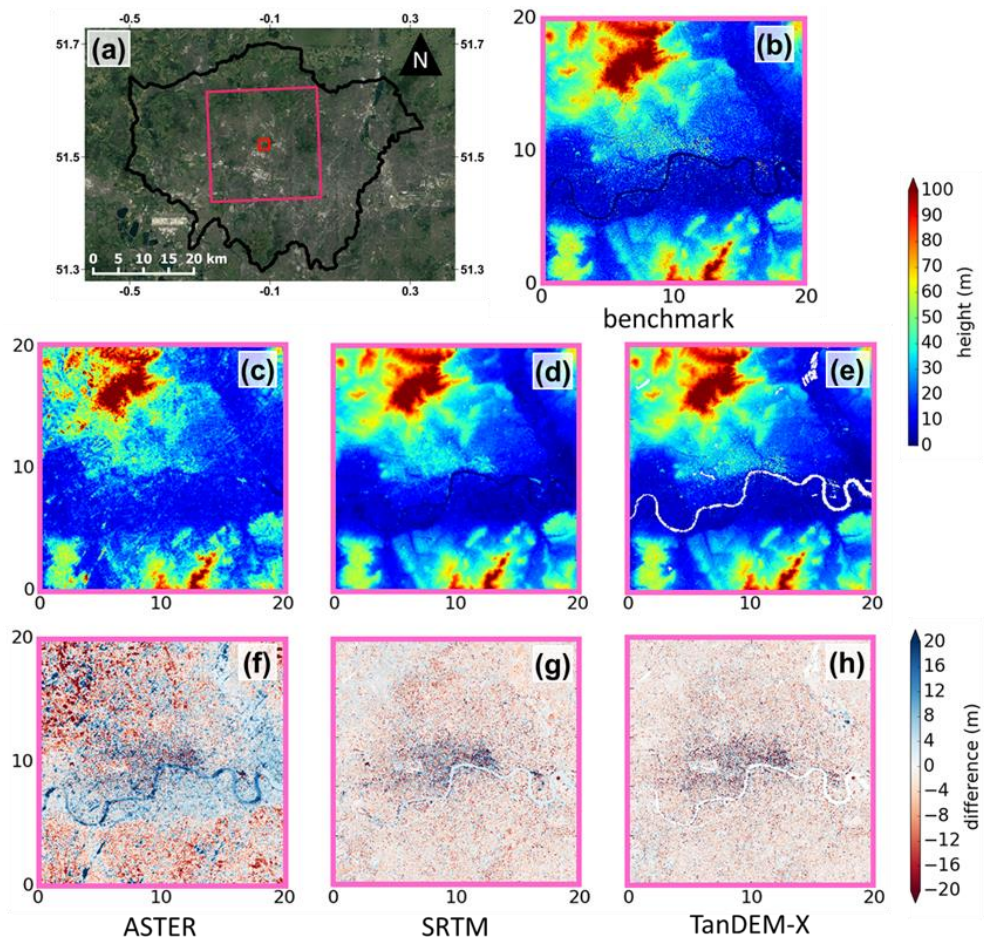


Figure 7.4: (a) Greater London (black demarcation), with the 20 km x 20 km study area (magenta) and a central area (red) with meteorological equipment (Sect. 7.5). The digital surface model (ground + roughness-element heights, DSM) of the (b) benchmark is shown, with DSMs from the (c) ASTER, (d) SRTM, and (e) TanDEM-X (with water mask applied [white]) and (f – h) their respective differences from the benchmark DSM. Map units: (a) degrees (WGS84) and (b-h) km

The 20 km x 20 km study area has 1600 overlapping 1 km grid-squares, which with the 8 directions used, gives 12800 samples for each geometric and aerodynamic parameter. The TanDEM-X data best resembles the benchmark data for all parameters (Table 7.4). However, consistent underestimation of roughness-element heights by the GDEMs causes the height based geometric parameters (H_{av} , H_{max} and σ_H) to be increasingly underestimated as roughness-element heights become taller (Fig. 7.5a-c). The underestimation is likely due to the coarse resolution of the GDEMs causing apparent merging of roughness elements (Fig. 7.6), which also results in a tendency to overestimate λ_p and underestimate λ_f (Fig. 7.5e and f). As z_d requires H_{av} , σ_H , H_{max} and λ_p (Kanda et al. 2013, their Eq. 10), the z_d results resemble the height-based parameters (Fig. 7.5d). However, the overestimation of λ_p can lead to overestimation of z_d , especially for $z_d < 10$ m. Combined these effects result in an unreasonably small z_0 (typically $\sim 10^{-3}$ m) with the largest relative error (nRMSE) from the benchmark data (Table 7.4).

Parameter	ASTER			SRTM			TanDEM-X		
	RMSE	nRMSE	MBE	RMSE	nRMSE	MBE	RMSE	nRMSE	MBE
$H_{av,grid}$	5.87	0.23	-0.27	2.22	0.09	0.00	1.43	0.06	-0.64
H_{av}	5.16	0.55	-3.33	5.75	0.61	-4.83	4.71	0.50	-4.20
H_{max}	27.64	0.77	-19.14	31.59	0.88	-26.74	21.11	0.59	-15.07
σ_H	3.95	0.80	-1.61	4.28	0.87	-3.88	2.93	0.59	-2.15
λ_p	0.26	0.65	0.19	0.22	0.55	0.07	0.23	0.57	0.19
λ_f	0.21	1.01	-0.19	0.23	1.10	-0.21	0.17	0.82	-0.16
z_d	9.33	0.63	-4.28	10.37	0.70	-8.33	6.65	0.45	-5.15
z_0	0.92	1.58	-0.59	0.92	1.58	-0.59	0.89	1.53	-0.57

Table 7.4: Root-mean-square error (RMSE), normalised RMSE (nRMSE) and mean bias error (MBE) for geometric and aerodynamic parameters calculated from the benchmark data and the: ASTER, SRTM and TanDEM-X datasets. Parameters are calculated for eight directional sectors of 1 km grid-squares in the 20 km x 20 km central London area (Fig. 7.4). For each parameter, errors are calculated if both elevation models have H_{av} and $H_{max} > 2$ m and the benchmark data have: λ_p and $\lambda_f \geq 0.05$ and z_d and $z_0 > 0.1$. Parameter calculation, abbreviations and units: Fig.7.3c. $H_{av,grid}$ is the average ground height [m]. Note similarity in z_0 errors for the ASTER and SRTM is due to rounding

The mean bias errors in Table 7.4 quantify the overall effects of the differences illustrated in Fig. 7.5, representing the overestimation of λ_p and underestimation of height-based parameters and λ_f . The MBE is consistently smaller than the RMSE, as use of squared values in the latter amplifies larger errors (e.g. Willmott and Matsuura 2005). Additionally, positive and negative bias cancel each other when using MBE, meaning it cannot be considered as a measure of error in isolation.

Results from one grid-square (Fig. 7.6) showcases the merging and underestimation of roughness-element heights by each GDEM (Fig. 7.6a-d). Merging can lead to overestimation of the ground height between roughness elements (Fig. 7.6e-h) and a lack of spaces between individual roughness elements (e.g. buildings). These effects are less pronounced for the TanDEM-X data, hence the better performance relative to benchmark data. The width and location of the river (south of grid-square) is accurately resolved by the TanDEM-X water mask

(Appendix 7.A). The SRTM data resolves the river but with a smaller width (cf. Fig. 7.6i and l), whilst the river's presence is not obvious in the ASTER model (Fig. 7.6k).

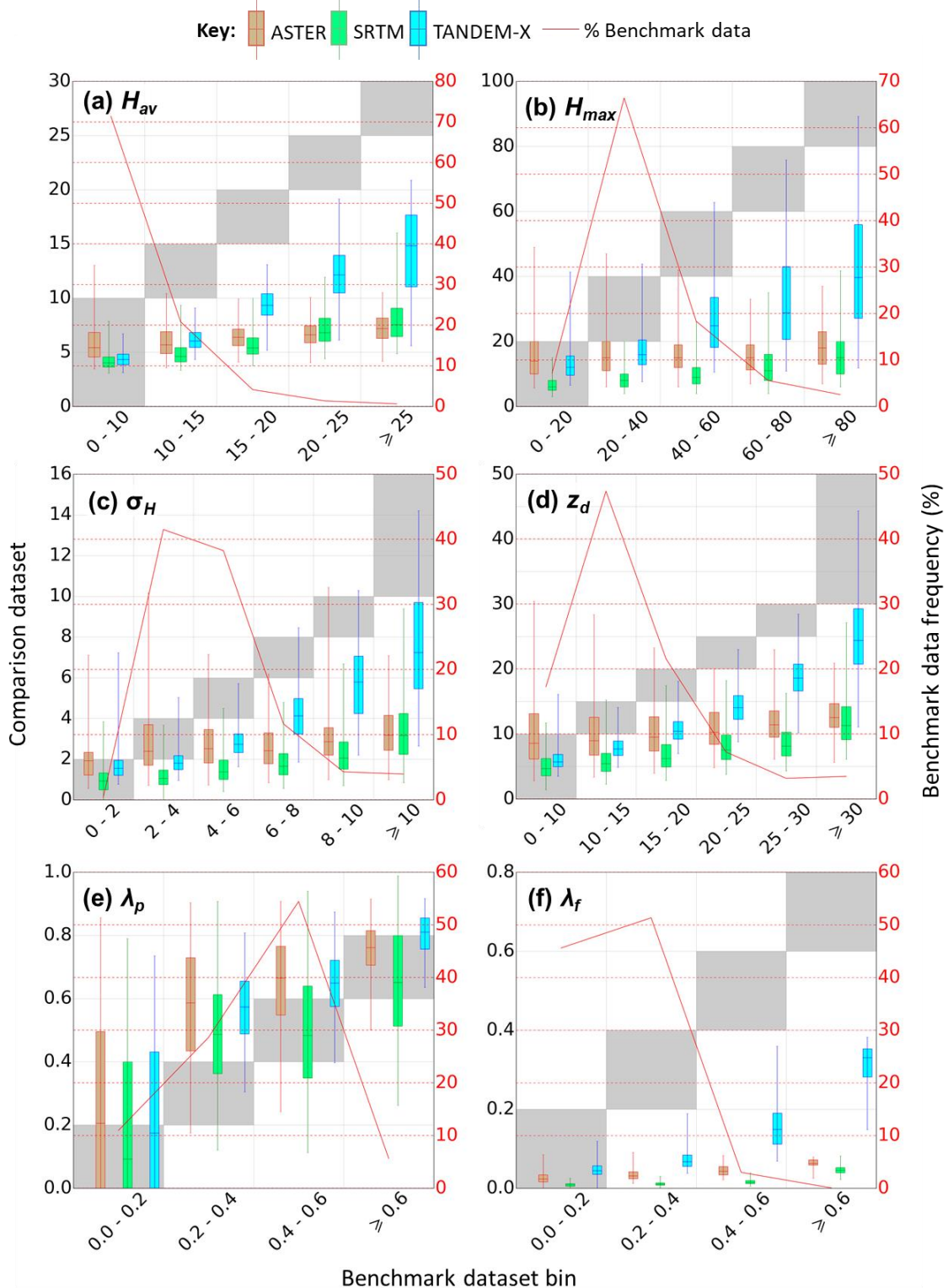


Figure 7.5: Comparison between parameters determined from the GDEMs and benchmark data for eight directional sectors of 1 km grid-squares in the 20 km x 20 km central London area (Fig. 7.4). For the comparisons, parameters in the benchmark dataset are divided into bins (x-axis, not inclusive of upper value labelled) and the distributions of parameters calculated by the GDEMs in the corresponding locations are shown for each bin (left y-axis). Whiskers are the 1st and 99th percentiles. Note, ideal distributions would be within the grey shaded areas. The percentage frequency of benchmark values within each bin are also shown (right y-axis, red line). Parameter calculation, abbreviations and units: Fig. 7.3c

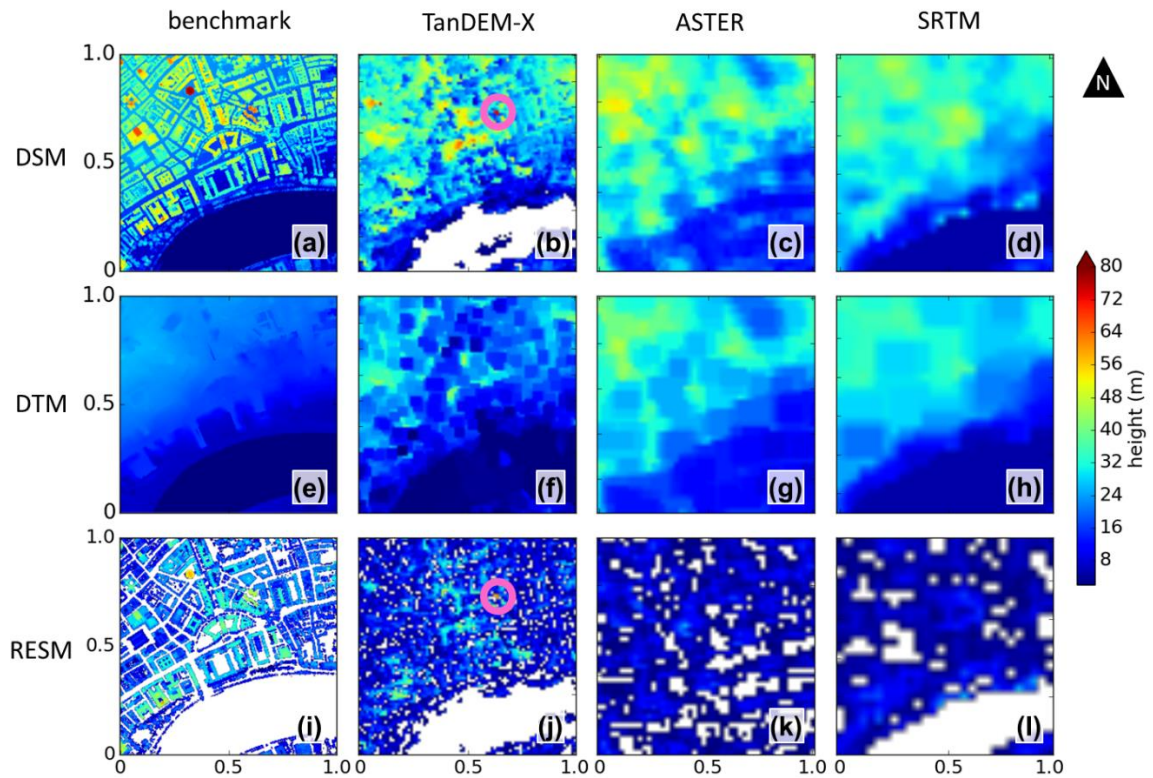


Figure 7.6: A 1 km grid-square in central London: (a-d) digital surface model (DSM), (e-h) digital terrain model extracted using the Sect. 7.3.2 methodology with a 5 x 5-pixel moving window (DTM) and (i-l) roughness-element surface model (RESM) (rows) derived from the: benchmark, TanDEM-X, ASTER and SRTM datasets (columns). Magenta circles are referred to in text (Sect. 7.5). Map units: km

7.4.2 Comparison 2: TanDEM-X in five cities

7.4.2.1 Comparison to benchmark data

The pixel-to-pixel comparison of TanDEM-X and benchmark data in five cities (Appendix 7.B) substantiates the comparison 1 findings. However, as more complex geometry is encountered errors become larger, especially in areas with densely packed, taller buildings with a smaller plan area. Errors are again associated with overestimation of ground heights between buildings (radar signal not penetrating to ground level) and underestimation of taller building heights (by up to a factor of 10). This is apparent in Manhattan, New York with the TanDEM-X elevation data clearly a merged representation of the benchmark data (Fig. 7.7). These effects are reduced in areas of less complex morphology (e.g. Auckland and London) which results in a smaller range of differences from benchmark data.

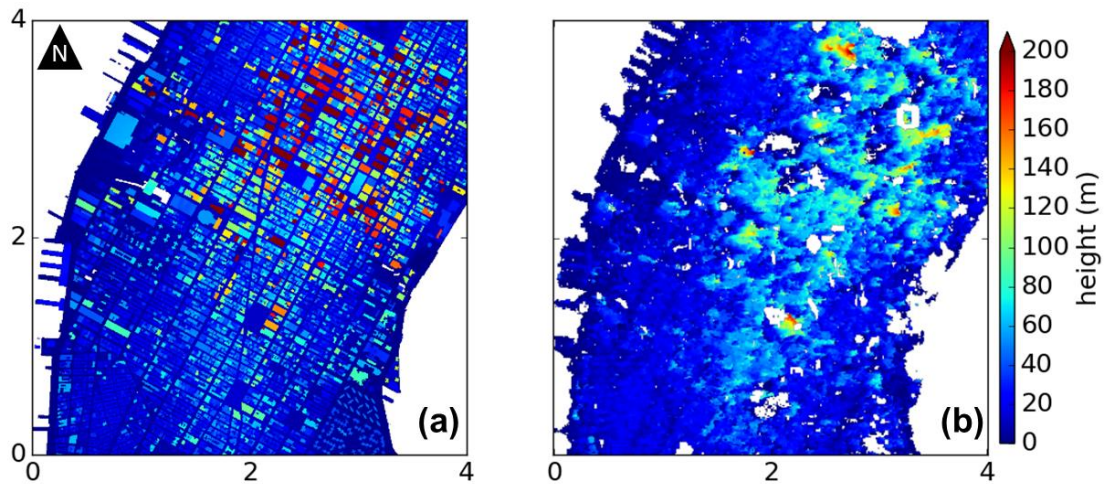


Figure 7.7: Digital surface models of downtown New York from the (a) benchmark and (b) TanDEM-X data. Only buildings and ground heights are included in the benchmark data. The global urban footprint (GUF) mask (Esch et al. 2017, see text) is applied to the TanDEM-X model. Map units: km

In all cities, except for New York, a 5 x 5-pixel moving window produces DTMs with the lowest RMSE. The larger area occupied by tall and densely packed roughness elements in New York makes true ground pixels less likely. Therefore, a 7 x 7-pixel moving window produces the best accuracy DTM. The extraction method could be optimised for specific morphologies (e.g. downtown cf. suburbia), but the focus here is cities generally. Overall, the extracted DTMs (RMSE = 2 to 4 m) may have better accuracy than more computationally and mathematically complex procedures (e.g. Geiß et al. 2015, RMSE = 4.18 m at the 90th percentile with TanDEM-X data). However, direct comparison is difficult given the different locations. Note, the error in ground height decreases as area analysed increases (Tables 7.4 and 7.5, and Fig. 7.8a).

Of the parameters calculated, the $H_{av,grd}$ is the best estimated (RMSE < 2 m; nRMSE < 0.1) (Fig. 7.8a, Table 7.5). Consistent underestimation of height-based parameters gives larger errors (Table 7.5) that increase with height (Fig. 7.8b-d). The apparent merging of roughness elements causes overestimation of λ_p (Fig. 7.8e) and underestimation of λ_f (Fig. 7.8f).

Polynomial fits (Sect. 7.3.3) between the benchmark and TanDEM-X parameters (Fig. 7.8, coloured lines) vary for each city because of inter-city morphological variability. There is also scatter around the polynomial fits due to intra-city variability (Appendix 7.C). The multi-city fits provide a starting point for the expected relation across cities globally, but are expectedly unresponsive to inter-city variability.

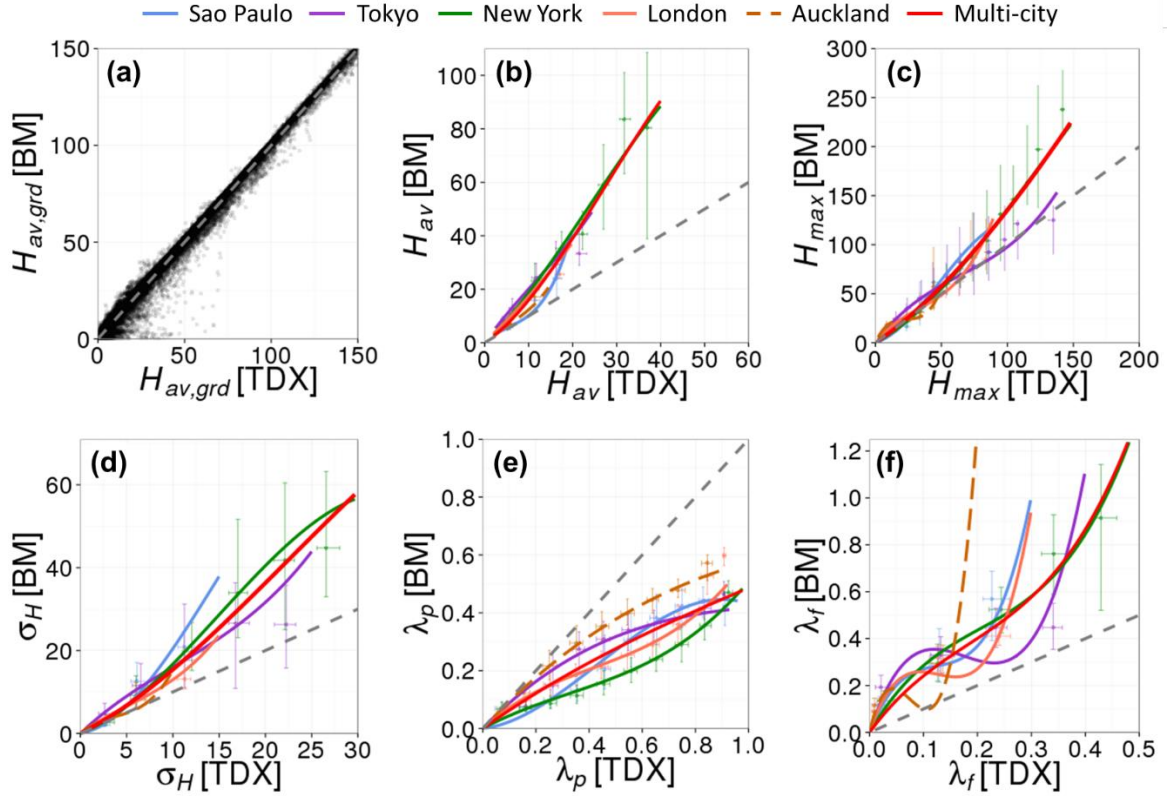


Figure 7.8: Geometric parameters determined for five cities based on 1 km grid-squares (8 directional sectors per grid, Fig. 7.3) from benchmark [BM] and TanDEM-X [TDX] datasets. All data points are shown for average ground height ($H_{av,grd}$). For the other parameters, each city's data are binned (5 m for H_{av} and σ_H ; 10 m for H_{max} ; 0.1 for λ_p and λ_f) with the median (point) and interquartile range (whiskers) per bin shown. Polynomial fits use all city-specific data for each parameter (coloured lines). See Sect. 7.3.3 for 'multi-city' fit method and text for explanation of fits in (f). For equation, error and data range of each fit see Appendix 7.C. Parameter calculation, abbreviations and units: Fig. 7.3c

7.4.2.2 Empirical correction of parameters

City-specific and multi-city polynomials are used to correct the geometric parameters derived from the TanDEM-X data. Both correction methods provide improved parameter estimates. City-specific corrections are slightly better, with the RMSE reduced for height-based parameters (H_{av} (35%), H_{max} (10%), and σ_H (15%)) and for λ_p (70%) (Table 7.5). However, the spread of λ_f data points results in city-specific fits being poor (Fig. 7.8f) and the multi-city corrections (Fig. 7.8f, red line) produce less error (Table 7.5). However, even after λ_f is corrected with the multi-city fit, considerable error may exist in smaller λ_f values. The best results are obtained when corrected λ_p is used to estimate λ_f with the multi-city fit (Appendix 7.D: Fig. 7.D1a, red line):

$$\lambda_f = 0.456\lambda_p^3 - 0.385\lambda_p^2 + 0.546\lambda_p \quad (7.3)$$

The RMSE is minimised if the additional correction (Eq. 7.3) is applied to corrected values of $\lambda_f < 0.08$.

Aerodynamic roughness parameters determined across the five cities with uncorrected geometry from the TanDEM-X data are consistent with comparison 1 results. Underestimation

of z_d increases as benchmark z_d increases (Fig. 7.9a) and z_0 values are unreasonably small (Fig. 7.9b). If the TanDEM-X geometric parameters are corrected, and then used to calculate roughness parameters, there are reductions in error of greater than 20% for z_d and 25% for z_0 (Fig. 7.9c-f, Table 7.5).

Numerous other corrections for parameters were explored (e.g. combining relations, data binned by other parameters such as H_{av} or using meta-information layers, Appendix 7.A), but hampered by compounding errors and without greater skill relative to the suggested method, which for an independent location is:

- (i) Calculate (uncorrected) morphological parameters from the UFRESM.
- (ii) Correct these using city-specific polynomial relations for the most similar city (e.g. for Beijing, Tokyo relations would be used), except for λ_f , which is corrected with the multi-city polynomial relation, but with Eq. 7.3 for $\lambda_f < 0.08$. Alternatively, the multi-city relations can be used, with the city-specific corrections offering some range of uncertainty.
- (iii) Use corrected geometry to calculate z_d and z_0 .

Parameter	Uncorrected data			Multi-city polynomial correction			City-specific polynomial correction		
	RMSE	nRMSE	MBE	RMSE	nRMSE	MBE	RMSE	nRMSE	MBE
$H_{av,grd}$	1.95	0.06	-0.49	NA	NA	NA	NA	NA	NA
H_{av}	6.29	0.74	-3.40	4.76	0.56	-1.27	4.25	0.50	-0.26
H_{max}	18.10	0.72	-5.86	17.57	0.70	-4.85	16.77	0.67	-2.89
σ_H	4.58	1.03	-1.58	4.04	0.91	-0.68	3.91	0.88	-0.47
λ_p	0.28	1.04	0.24	0.10	0.37	0.01	0.08	0.30	0.00
λ_f	0.14	0.97	-0.12	0.11 ^a	0.76 ^a	0.01 ^a	0.22	1.52	-0.03
z_d	7.57	0.72	-2.09	6.71	0.64	-1.19	6.27	0.60	-0.44
z_0	1.80	2.29	-0.59	1.34	1.71	-0.16	1.35 ^b	1.78 ^b	-0.09 ^b

^a Multi-city correction of λ_f uses Eq. 7.3 for corrected values of $\lambda_f < 0.08$ (see discussion in text)

^b Calculation of the city-specific z_0 uses λ_f corrected with the multi-city function (Fig. 7.8f, red line)

Table 7.5: Root-mean-square error (RMSE), normalised RMSE (nRMSE) and mean bias error (MBE) of TanDEM-X parameters from the benchmark datasets in all cities using the: uncorrected TanDEM-X data, multi-city polynomial correction, and city-specific polynomial correction. No correction is attempted to the ground height ($H_{av,grd}$). For each parameter, errors are calculated if both elevation models have H_{av} and $H_{max} > 2$ m and the benchmark data have: λ_p and $\lambda_f \geq 0.05$ and z_d and $z_0 > 0.1$. For parameter calculation, abbreviations and units see Table 7.3. $H_{av,grd}$ is the average ground height [m]

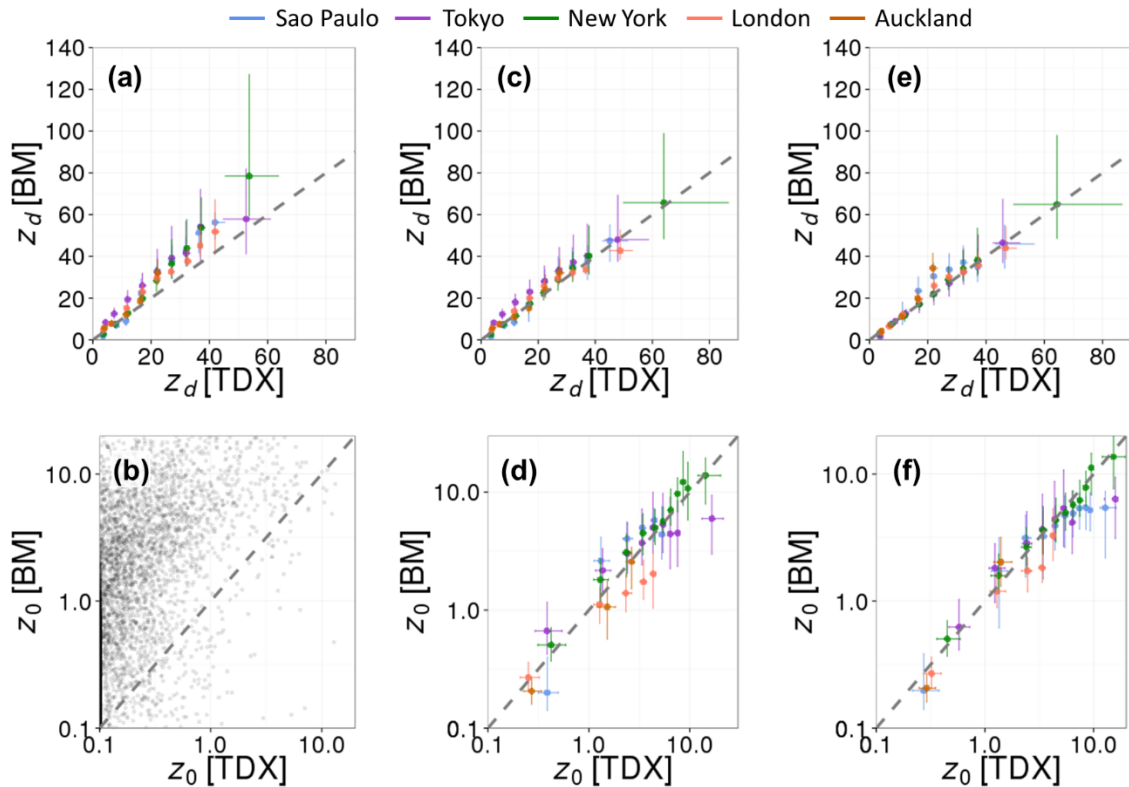


Figure 7.9: Zero-plane displacement (z_d) [m] and aerodynamic roughness length (z_0) [m] (note log axis), calculated using the Kanda et al. (2013) morphometric method for five cities based on 1 km grid-squares (8 directional sectors per grid, Fig. 7.3) from benchmark [BM] and TanDEM-X [TDX] datasets. All data points are shown in (b) and elsewhere data are binned per city (10 m for z_d ; 1 m for z_0) with the median (point) and interquartile range (whiskers) per bin shown. Parameters are calculated with TanDEM-X geometry which is: (a, b) uncorrected; (c, d) corrected with multi-city relations (Fig. 7.8, Table 7.C1); and (e, f) corrected with city-specific relations (Fig. 7.8, Table 7.C1). Note, the multi-city relation is used to correct λ_f in all cases, with Eq. 7.3 used to estimate corrected values of $\lambda_f < 0.08$ (see discussion in text). Data point errors given in Table 7.5

Using the proposed corrections in the test cities leads to improved estimates of parameters on a city-wide scale (Fig. 7.10, Appendix 7.E). Additionally, using land cover data from London and New York, the ‘settlement’ and ‘non-settlement’ TanDEM-X GUF masks were found to contain approximately 70% impervious and pervious surfaces, respectively, whilst the water mask captured up to 75% of water bodies (Appendix 7.A). In combination (e.g. Fig. 7.10 and Fig. 7.11), a wide number of parameters required within urban land surface models are available (e.g. Grimmond et al. 2010, 2011, Salamanca et al. 2011, Varquez et al. 2015). The ability of the corrections to improve wind-speed estimates is demonstrated in Sect. 7.5.

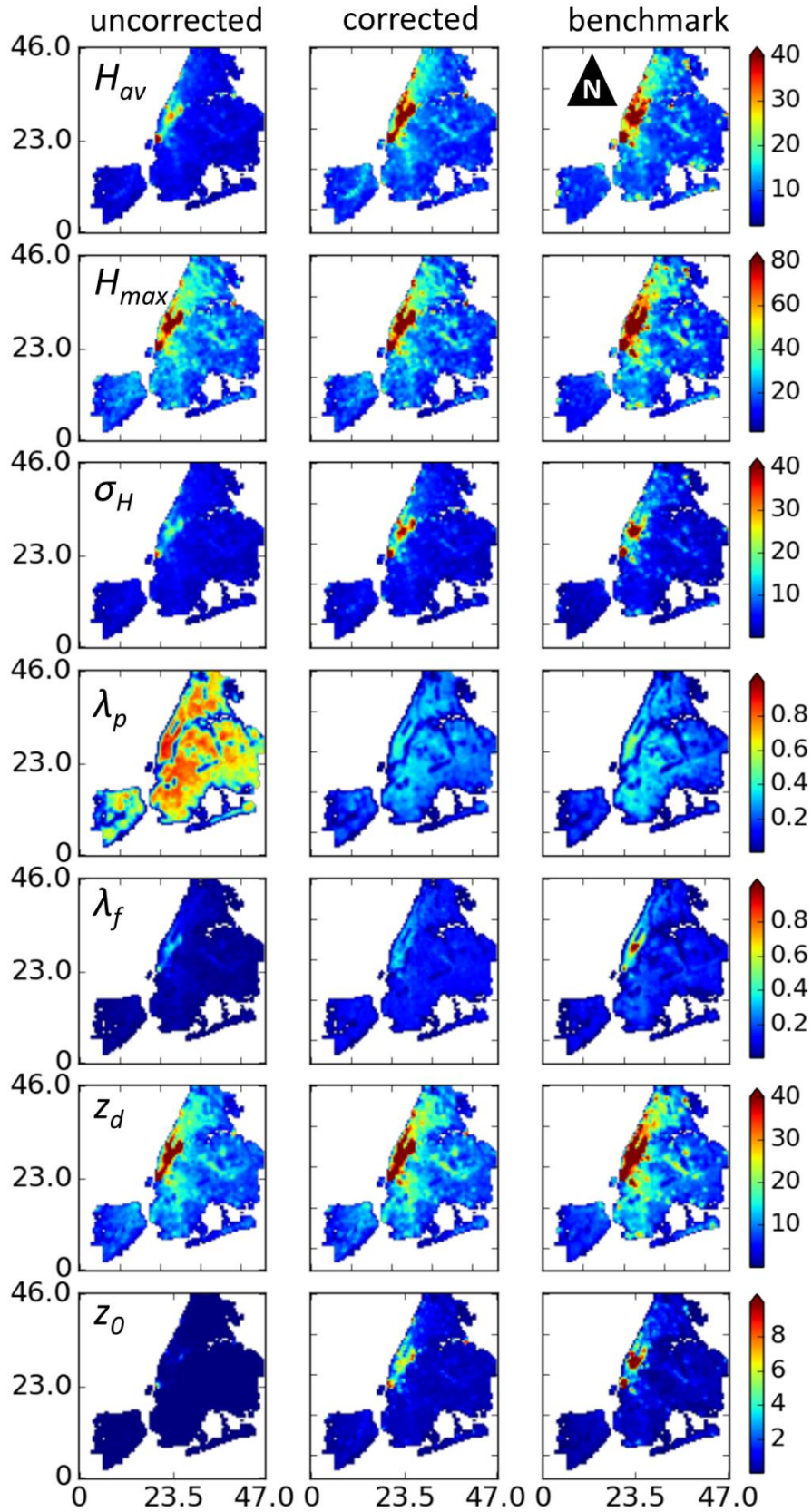


Figure 7.10: Parameters derived from the benchmark and TanDEM-X data (directly/uncorrected and corrected with suggested method, see text) for New York (mean of 1 km grid-squares from 8 sectors, Fig. 7.3). Map units: km. Parameter calculations, abbreviations and units: Fig. 7.3c. Maps for other cities are included in Appendix 7.E

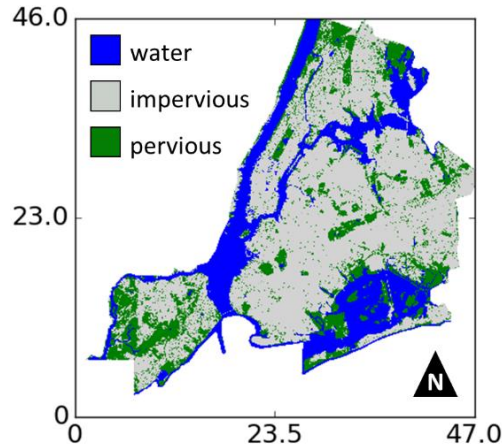


Figure 7.11: Land surface information in New York using TanDEM-X products. The water mask is used with the GUF mask (Esch et al. 2017) to indicate impervious and pervious surfaces ('settlement' and 'non-settlement' layer, respectively). For analysis of actual land cover in each mask, see Appendix 7.A. Map units: km

7.4.2.3 Assessment of empirical corrections for an independent location

A further independent assessment of the TanDEM-X derived parameters is undertaken for Slough (Fig. 7.12), an urban area west of London (Fig. 7.4a) where both data sets are available. Although, the area is not as complex as others considered in this work (cf. Fig. 7.7a and Fig. 7.12b), the area has a city centre, an industrial area with warehouses, suburbs, water bodies and areas of vegetation. A 5 x 5-pixel moving window is used for DTM extraction from the TanDEM-X model. Subsequently, uncorrected (Fig. 7.13, black points) and corrected (Fig. 7.13, blue points) parameters derived from the TanDEM-X data (Fig. 7.12c) are compared to those derived from a benchmark building footprint and height dataset (Fig. 7.12b).

Using the recommended correction procedure (London-based empirical relations and multi-city relations for λ_f) improves the characteristic underestimation of H_{av} (Fig. 7.13a) and λ_f (Fig. 7.13e), and the overestimation of λ_p (Fig. 7.13d). As H_{max} and σ_H in this area are in the range where TanDEM-X performs reasonably well (Fig. 7.8b, c), these corrections only have a small effect (~10% reduction in RMSE). Note, the outlying σ_H points in Fig. 7.13c are where two chimneys up to 100 m tall are located, which are not evident in the TanDEM-X model. In combination, the corrections improve the estimation of calculated z_d by ~10% (RMSE from 1.93 m to 1.72 m) and z_0 by ~40% (RMSE from 0.39 m to 0.22 m).

The comparison demonstrates an inherent limitation of the correction procedure. If the uncorrected TanDEM-X parameters are accurate (or unlike what the empirical fits suggest), the corrections enhance error. For example, the corrections may lead to height-based parameters (Fig. 7.13a-c) or λ_f being overestimated (Fig. 7.13e). However, as these are rare (tail) events there is an overall benefit from applying the correction. Furthermore, some evaluation differences may arise from temporal offset of datasets (Sect. 7.6).

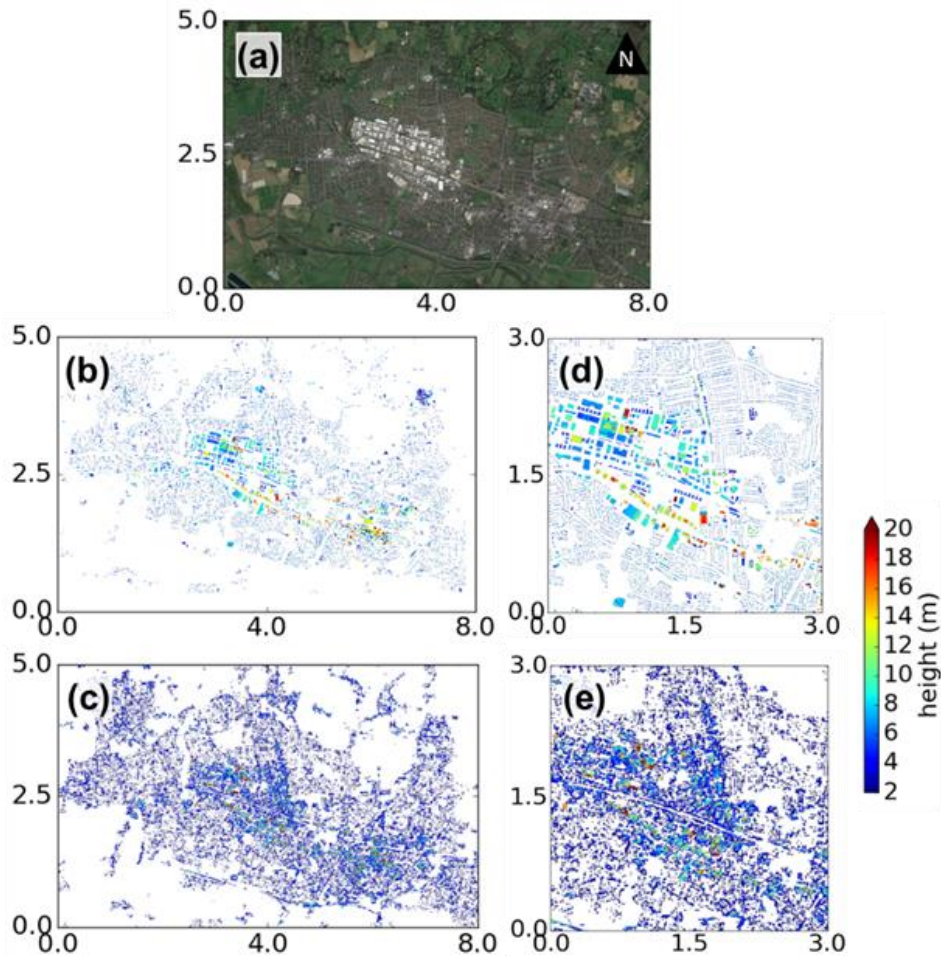


Figure 7.12: Independent assessment site of corrections to the TanDEM-X derived parameters – Slough, UK: **(a)** aerial image; **(b)** benchmark building footprints (OS MasterMap® Topography Layer – Building Height Attribute, Ordnance Survey 2014) used to mask heights derived from the 1 m resolution EA composite lidar data (UK Environment Agency 2017); and, **(c)** TanDEM-X roughness-element heights within the global urban footprint mask (UFRESM) (Esch et al. 2017) from which parameters are calculated. The central 3 km x 3 km area is shown for the **(d)** benchmark data and **(e)** TanDEM-X. Map units: km. Upper left corner coordinates (WGS84, UTM30N): $x = 661100.66$, $y = 5712952.10$

7.5 Wind-speed estimates using the DEMs

With an average wind speed (\bar{U}_{ref}) at a reference height (z_{ref}) and roughness parameters (z_d and z_0), the vertical wind-speed profile above a surface can be estimated (Sect. 4.2). To independently assess using roughness parameters derived from the different DEMs, the associated wind-speed estimates are compared to meteorological observations in central London. In the centre of the 1 km grid-square in Fig. 7.6, a sonic anemometer (CSAT3, Campbell Scientific, USA) measured wind speed (\bar{U}_{ref}) at approximately 2.5 times the canopy height (49 m above ground level, z_{ref}), with a Doppler lidar (Halo Photonics Streamline pulsed) located ~60 m to the west (Table 3.3). The latter, operating in doppler beam swinging (DBS) mode, measured the vertical wind-speed profile in 30 m gates aloft. For site, instrument and processing details see Lane et al. (2013), Kotthaus and Grimmond (2014a, b) and Sects. 3.4.1, 3.4.2 and 4.4.

During the observation campaign (Oct 2010 to May 2011), 245 hours of near neutral atmospheric stability (strong wind speeds) occur, when it is appropriate to extrapolate the 49-m wind speed to ~200 m above the canopy without stability corrections (Chapter 4). Here, the same 245 hours are analysed. The roughness parameters calculated from the benchmark and GDEM data are used with the 49-m wind speed (\bar{U}_{ref}) to extrapolate to the Doppler lidar gate level wind speed. The profile used for extrapolation varies according to wind direction. Following Sect. 4.5.5, the logarithmic wind-speed profile (Blackadar and Tennekes 1968) is used for 000° – 045° wind directions, whilst the Deaves and Harris equilibrium profile (Deaves and Harris 1978) is used elsewhere.

In previous chapters, the Kormann and Meixner (2001) source area model is used to identify the probable upwind area and weighting for roughness parameter (z_d and z_0) calculation. Here, the roughness parameters are also selected based on the sector of the mean wind direction for the hour (e.g. Fig. 7.3). This allows both the roughness parameters derived from DEMs and the impact of simplifying source area characterisation to be assessed.

Comparing the mean wind-speed profiles (Fig. 7.14a) demonstrates the smaller roughness parameters determined from the GDEMs (Sect. 7.4) leads to less shear in the wind-speed profile and wind-speed underestimation. This effect is least for the TanDEM-X data given its better ability to characterise urban morphology and larger z_d and z_0 .

Average wind-speed estimates are improved (to within ~10% of benchmark data and observations) when corrected TanDEM-X roughness parameters are used (Fig. 7.14a, TDX_{cor}). However, overestimates occur in the 000° – 045° sector (Fig. 7.14b). The TanDEM-X corrections should move wind-speed estimates towards the benchmark data (Fig. 7.14, BM), but a very tall feature in the TanDEM-X model in the 000° – 045° direction which is not present in the benchmark data (Fig. 7.6, magenta circle), leads to larger roughness parameters than the benchmark data and hence greater shear in the wind-speed profile. As perusal of historical aerial imagery did not find a large roughness element (e.g. a crane) present during the TanDEM-X data collection (2011 – 2013; tile meta-data), this is possibly an artefact of the satellite derived elevation data. Irrespective of the cause, the situation demonstrates that average corrected TanDEM-X data resembles the benchmark data well (Fig. 7.14a), but this is not always the case (Fig. 7.14b).

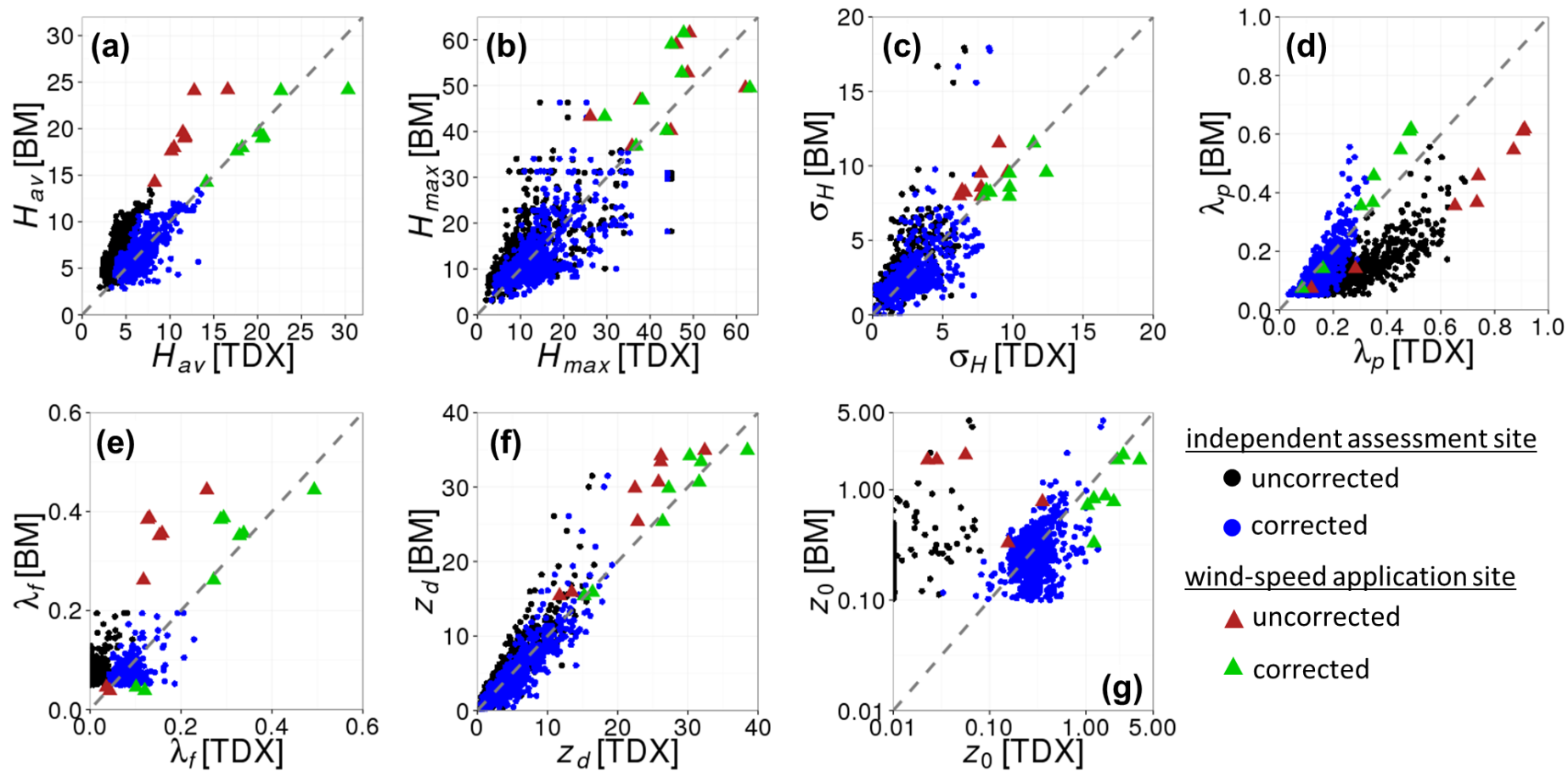


Figure 7.13: Parameters derived from benchmark [BM] and TanDEM-X [TDX] data for (i) the independent assessment site, Slough (Fig. 7.12, circles here) (Sect. 7.4.2.3) and (ii) the wind-speed application site, central London (Fig. 7.6, triangles here) (Sect. 7.5). TanDEM-X parameters are: uncorrected (black and red symbols) and corrected (using the London-fit and multi-city procedure for λ_f (see text), blue and green symbols). Each point is one of eight 45° directional sectors within a 1 km grid-square – see Fig. 7.3 for parameter calculations, abbreviations and units

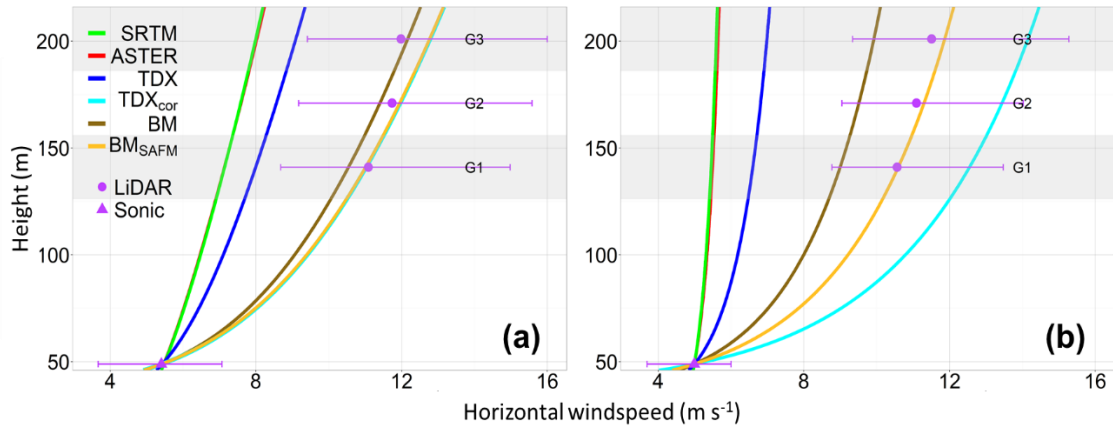


Figure 7.14: Hourly mean observed and estimated wind speed for strong wind conditions above a central London site (Fig. 7.6). Profiles when wind is from: **(a)** all directions ($n = 245$), and **(b)** $000^\circ - 045^\circ$ ($n = 36$). Observed wind speed is the average (point) and 5th and 95th percentiles (whiskers) at 49 m (sonic anemometer) and at three 30 m gates (shaded G1 – G3) by Doppler lidar. Estimated wind speed is with roughness parameters determined from different DEMs (coloured lines): SRTM, ASTER, uncorrected TanDEM-X (TDX) (Fig. 7.13, red triangles), TanDEM-X with geometry corrected (TDX_{cor}) (Fig. 7.13, green triangles), and benchmark (BM). Roughness parameters are calculated for 45° sectors with a 500-m fetch (e.g. Fig. 7.3a), except for BM_{SAFM}, which uses source area calculations. See text for more details

For all directions, roughness parameters derived from the benchmark data using sectors or source areas produce wind-speed estimates (Fig. 7.14a, BM and BM_{SAFM}, respectively) that are within 5% of each other and the observation average. This indicates the sector-based approach may provide a reasonable simplification to source-area calculations if forcing data or computer resources are limited (e.g. for city-scale). Again, upwind characteristics may influence this conclusion. For example, the sector-based results are poorer than the source area based results for the $000 - 045^\circ$ sector (Fig. 7.14b) as the latter gives a larger weighting to taller buildings close to the site in this direction (Fig. 7.6i), which the former does not.

7.6 Discussion of GDEM comparison

The differences between the benchmark data and GDEMs can be attributed to several factors. Firstly, typical urban roughness elements or their individual parts have a spatial extent which is less than the resolution of the GDEMs (especially ASTER and SRTM). Furthermore, in densely packed urban areas, layover and shadowing effects are unavoidable when using photogrammetric and interferometric techniques to retrieve surface heights. The SAR technique is also affected by foreshortening, total reflection, and multi-bounce scattering of radar in urban areas, which vary with the morphology (e.g. height and orientation) and facets of roughness elements (Gamba et al. 2003, Stilla et al. 2003, Gamba et al. 2005, Thiele et al. 2010, Auer et al. 2011, Ferro et al. 2011, Schmitt and Stilla 2014). A combination of these factors leads to positional errors (e.g. Xu et al. 2017) with the *exact* locations and well-defined edges of

roughness elements being unlikely to be resolved by the GDEMs (e.g. Mercer and Gill 1998, and Figs. 7.6 and 7.7). The pixel-to-pixel comparison (Appendix 7.B) quantifies some of these effects.

Previously, GDEMs have been demonstrated to have a density dependent signal over vegetation, with vegetation heights reported between the canopy top and bare earth surface (e.g. Hofton et al. 2006, Tachikawa et al. 2011, Li et al. 2013, Su and Guo 2014). The density dependence of the signal means the bias is expected to vary with phenology. In comparison 1, the effect of vegetation should be least for the SRTM data given it was collected during northern hemisphere winter (leaf-off, Table 7.1). In the other datasets, the relatively abundant, but not dense, vegetation in central London (e.g. Lindberg and Grimmond 2011a, b) may introduce a slight negative bias in the GDEM heights. In comparison 2, the GUF mask is used to retain buildings only for a consistent comparison to the benchmark data. As approximately 15% of the layer is vegetation > 2 m (Appendix 7.A), this is another source of bias.

Temporal differences occur between collection of raw GDEM and benchmark data (cf. Table 7.1 and 2). The GDEM data are gathered from multiple contributing passes, with uncertainty arising; for example, with variation in surface height between passes (e.g. construction or vegetation growth) or changes in atmospheric conditions for the ASTER data (which photogrammetric techniques are sensitive to). Rapidly changing urban areas make temporal variation and differences unavoidable, which ideally benchmark data for different periods could be used to quantify. However, in comparison 1 the SRTM elevations are more similar to the benchmark data than ASTER. These datasets have similar horizontal resolution, but the ASTER has less temporal difference to the benchmark data, suggesting the model error outweighs the temporal effect.

7.7 Conclusions

Critical parameters for urban meteorology are derived from three global digital elevation models (GDEM): ASTER, SRTM and TanDEM-X. The TanDEM-X data are consistently most similar to central London benchmark data (20 km x 20 km area), hence the TanDEM-X data are assessed in five other cities (Auckland, Greater London, New York, Sao Paulo and Tokyo).

A method to extract ground heights from the GDEMs is developed, which uses a moving square window to produce terrain models with RMSE < 4 m from benchmark data in the assessed cities. The optimum moving window width is found to be 5 x 5 pixels, except in New York, where the comparatively densely packed buildings led us to conclude that a 7 x 7-pixel window is best.

Pixel-to-pixel comparisons of the digital surface models (ground and roughness-element heights) in central London found both the SRTM and TanDEM-X datasets to compare best to benchmark data (RMSE < 7 m). All the GDEMs (but especially the ASTER and SRTM) are found to increasingly underestimate the height of taller surface elements, meaning taller roughness elements (> 100 m) may be estimated with medians of up to a tenth of their true value. These conclusions hold for the TanDEM-X in the five cities, with errors largest where there is the greater proportion of densely packed tall buildings within a small plan area (e.g. New York and Tokyo).

Geometric and aerodynamic parameters are calculated for 8 directional sectors (45° width) of 1 km grid-squares, and used to evaluate the GDEMs. The average ground height is the best estimated parameter, with RMSE accuracy < 2 m across the five cities using the TanDEM-X data. The average, maximum and standard deviation of roughness-element heights and the zero-plane displacement height are consistently underestimated by the GDEMs. Underestimation increases as these parameters become larger, resulting in underestimation of up to 75% using the ASTER and SRTM datasets and closer to 50% for the TanDEM-X. The apparent merging of roughness elements in the GDEMs causes the roughness-element plan and frontal areas to be over- and under-estimated, respectively. In combination, these effects produce an unreasonably small aerodynamic roughness length ($\sim 10^{-3}$ m).

To improve the parameters derived from the TanDEM-X data, city-specific and ‘multi-city’ empirical corrections are developed. For an independent location, it is recommended to use the city-specific relations of the most similar city (e.g. for Beijing, Tokyo relations would be used), but the multi-city relation should be used to correct λ_f , with Eq. 7.3 for corrected λ_f values < 0.08. Across the cities, and during evaluation at an independent location, this procedure improved estimation of all geometric parameters and reduced the error in z_d by up to 20% and z_o by up to 40%. Combined with the TanDEM-X derived water mask and GUF mask (to indicate impervious/pervious surfaces), many parameters required within urban land surface models become obtainable.

The impact of using GDEM derived roughness parameters to estimate wind speeds at up to ~ 10 times canopy height (from reference wind speeds observed at ~ 2.5 times canopy height) is assessed in central London. Results are directionally dependent, however on average, wind speeds are underestimated by up to 40% using roughness parameters from the ASTER and SRTM and 30% from the TanDEM-X. Using roughness parameters calculated with the proposed corrections to the TanDEM-X derived geometry improves estimates to within 10% of observations. Roughness parameters derived from the benchmark data with sector-based or

source area calculations led to the most accurate wind-speed estimates (within 5% of observations).

Differences between the GDEMs and benchmark data occur beyond the inherent limitations of methods used to generate DEMs in densely packed urban environments and the comparatively coarse resolution of the GDEMs. The presence of vegetation and the dynamic nature of cities causes variations when data are obtained with long time separations. The latter hinders the evaluation process but also points to the critical need for global and frequent parameter updates in cities. This will also inform the current static representation of urban morphology in future climate simulations (Garuma 2017).

Across the GDEMs assessed, the TanDEM-X data provides the most accurate representation of urban morphology and associated wind-speed estimates. The unique morphology of different cities and resulting spatial variability of the GDEM performance means these results cannot be generalised to other cities without additional uncertainty. However, the corrections to the geometric parameters derived from the TanDEM-X model provide a basis to correct data in other cities and therefore the potential to improve the representation of urban morphology for other urban climate studies, especially where data are currently unavailable.

Appendix 7.A: The assessed global digital elevation models (GDEMs)

7.A.1 Advanced Spaceborne Thermal Emission and Reflection Radiometer (ASTER)

The ASTER GDEM was derived from a multispectral imaging sensor on board NASA's Terra spacecraft since 1999 (Yamaguchi et al. 1998, Abrams et al. 2015). Nadir- (pointing directly below) and aft- (backward) looking telescopes in the near-infrared bands acquired stereo-image pairs, which were automatically processed using stereo-correlation to a DEM with 1 arc-second horizontal resolution (Fujisada et al. 2012). The 2011 release is used (ASTER version 2) with data collected between 2000 – 2010 (Table 7.1).

7.A.2 Shuttle Radar Topography Mission (SRTM)

A NASA, NIMA (National Imagery and Mapping Agency of the U.S. Department of Defence) and DLR 11-day mission (11 – 22 February 2000) mapped 99.96% of the Earth's surface between 60°N and 56°S up to four times (Farr and Kobrick 2000, Farr et al. 2007). A single-pass interferometric synthetic aperture radar (InSAR) system on-board the Endeavour space shuttle used C-band and X-band radar to produce interferograms, from which surface elevation heights were determined with 1 arc-second horizontal resolution (Farr et al. 2007).

7.A.3 TanDEM-X

The German Aerospace Centre (Deutsches Zentrum für Luft-und Raumfahrt, DLR) and AIRBUS Defence and Space TanDEM-X data were acquired from close formation flight of the TanDEM-X and TerraSAR-X satellites between December 2010 and January 2015. This provides an almost global DEM through aggregation of bistatic X-band InSAR acquisitions. Post-processing includes: single- and multi-baseline interferometric phase-unwrapping (Rossi et al. 2012), tilt and offset calibration (Gruber et al. 2012), water detection and manual quality checks (Wessel 2016). All ground areas in the GDEM were covered at least twice, allowing for a comparison between the elevation determined from multiple acquisitions. In addition to elevation, meta-information is provided for each TanDEM-X pixel (Wessel 2016):

- (i) A coverage map (COV), indicating the number of valid height values from different acquisitions (i.e. number of scenes used to produce the pixel elevation) (Fig. 7.A1a)
- (ii) A consistency mask (COM), indicating the consistency of elevation values for each pixel amongst the contributing scenes (Fig. 7.A1b)
- (iii) A height error map (HEM), indicating pixel error (Fig. 7. A1c)

- (iv) A water indication mask (WAM), initially defined using external references (e.g. MODIS satellite) and refined using amplitude threshold criteria (Fig. 7.A1d)

The 20 km x 20 km central London study area (Fig. 7.4) is used to provide insight to the usability of the COV, COM and HEM meta-information layers. Values in each layer are compared with the absolute elevation difference between the benchmark and TanDEM-X DSM in the corresponding pixels (Fig. 7.A1e-g).

The coverage of valid height pixels within the study area ranges from one to three (Fig. 7.A1a). The maximum elevation differences occur in pixels with only one coverage and as coverage increases this difference is reduced by over 10 m (Fig. 7.A1e). However, the median difference is only reduced by 0.5 m and the lower quartile of differences increases. The distribution of elevation differences between two or three coverages are similar, indicating an increase in coverage does not necessarily correspond to improved pixel accuracy.

A summary of the COM values is as follows (for more detail see Wessel 2016): a value of 8 indicates consistent heights; values of 1 and 2 have 'larger' and 'smaller' inconsistencies, respectively; values of 9 and 10 have at least one consistent height pair between coverages, with 'larger' and 'smaller' inconsistencies, respectively. Pixels with a value of 4 are those with only one coverage (and therefore analogous to pixels with COV = 1). Ranking the COM layer values by expected consistency (least to most consistent) gives: 1, 9, 2, 10, 8. Visual inspection indicates pixels with the greatest inconsistencies (i.e. COM = 1) are located where there are water bodies (e.g. river flowing west to east through the study area), or where the tallest roughness elements with the greatest height variability are located (Fig. 7.A1b, white circle). These pixels have the largest range of absolute elevation differences from the benchmark data, with a median of 10 m (Fig. 7.A1f). The next consistency classes (e.g. COM = 9, 2 or 10) occur where there are densely packed buildings with variable heights. Pixels with the most consistent heights (COM = 8) are where the least heterogeneous geometry exists, or in open spaces. The elevation differences from the benchmark data decrease with increasing consistency (i.e. 9 through 2, 10) to the value 8 layer, which with a median elevation difference of 2.5 m exhibits the least variability from the benchmark data.

Values in the HEM layer are in the form of a standard deviation and derived from interferometric coherence (Wessel 2016), hence they do not correspond to absolute elevation differences. However, as the HEM value increases so do both the range and distribution of elevation differences from the benchmark data (Fig. 7.A1g). Pixels in the HEM layer demonstrate a similar

spatial distribution to the COM layer (cf. Fig. 7.A1b and c) – with increasing surface heterogeneity resulting in a larger HEM value.

Land cover information in central London and New York (Fig. 7.A2) indicates the WAM mask accurately identifies 67% of water bodies in central London and 75% in New York, with smaller water bodies and tributaries unidentified (e.g. comparison of Fig. 7.A1d and h). This result is expected, given the WAM mask resolves bodies of water > 200 m x 100 m (Wessel 2016).

The binary global urban footprint (GUF) mask (Esch et al. 2011, 2017) is used in this work to retain building heights only, when comparing elevations between the TanDEM-X and benchmark data from five cities (comparison 2). Land cover maps for London and New York (Fig. 7.A2) allow quantitative evaluation of the actual land cover in the GUF ‘settlement’ and ‘non-settlement’ layers. Visual comparison in central London (Fig. 7.A3) demonstrates the spatial pattern of the ‘settlement’ layer resembles artificial surfaces, whilst land cover in the ‘non-settlement’ layer is more representative of vegetation, grassed areas and water bodies.

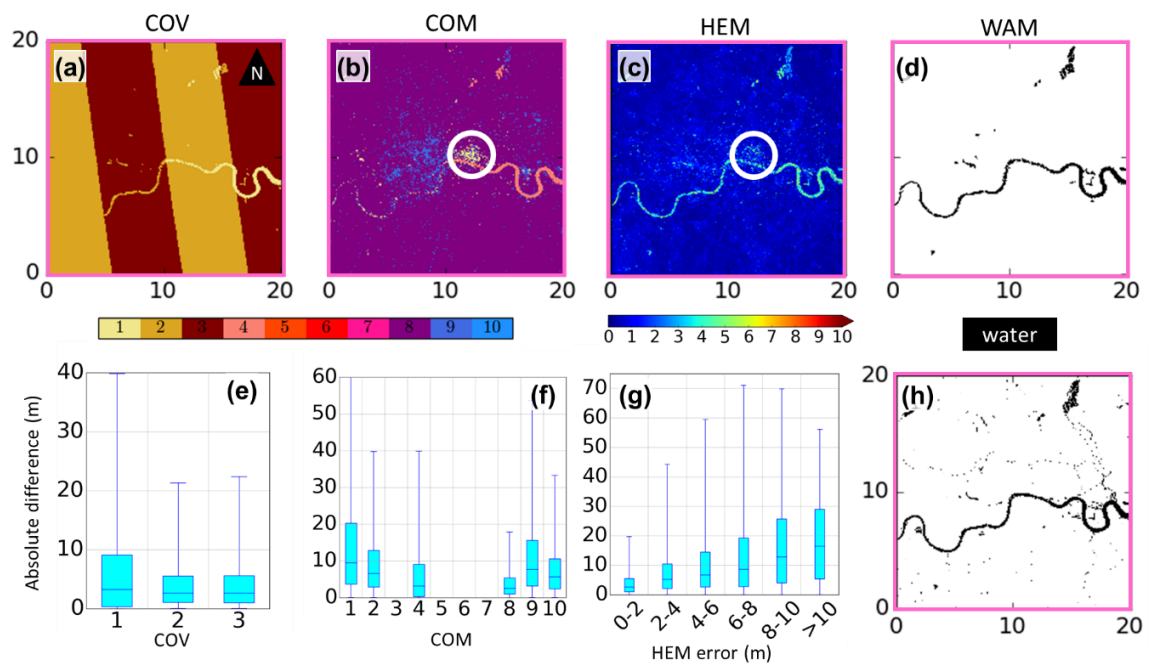


Figure 7.A1: TanDEM-X meta-information layers for the 20 km x 20 km study area in central London (Fig. 7.4): **(a)** coverage map (COV); **(b)** consistency mask (COM); **(c)** height error map (HEM); and, **(d)** water mask (WAM). **(e-g)** Distribution of absolute elevation differences between pixels in the benchmark and TanDEM-X digital surface models for the value(s) in each meta-information layer (x-axis). Whiskers are the 1st and 99th percentiles. **(h)** Water mask derived from the OS MasterMap[®] topography layer (Ordnance Survey 2010). Databases are re-sampled to 4 m pixel resolution for comparison. White circles in **(b)** and **(c)** are referred to in text. Map units: km

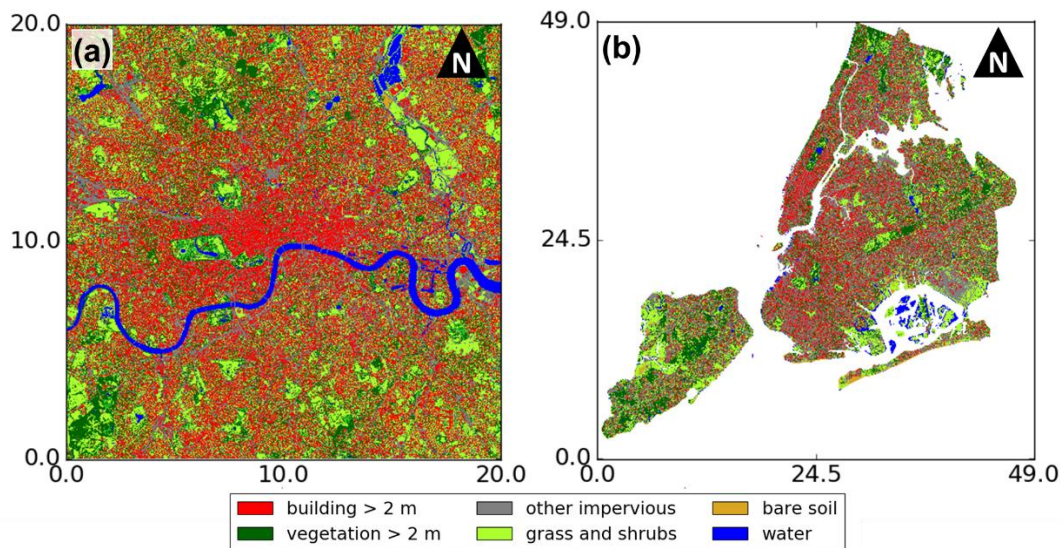


Figure 7.A2: Land cover information in (a) central London and (b) New York. For London, the OS MasterMap® topography layer (Ordnance Survey, 2010) is complimented with building and vegetation height information from the Lindberg and Grimmond (2011a) database. For New York, the New York City Landcover (2010) is used (Department of Parks and Recreation 2017), the ‘tree canopy’ layer is assumed to correspond to ‘vegetation > 2 m’ and ‘other impervious’ refers to roads, railroads and other paved surfaces. Map units: km

The GUF settlement layer is mostly buildings and other impervious surfaces, which jointly account for 65% of the layer in London and 73% in New York (Fig. 7.A4). However, up to 30% of the layer is vegetation (including grasses and/or shrubs) that is sparse but close to built structures, such as street trees or small grassed areas. Approximately 15% of this is vegetation > 2 m. Most buildings > 2 m are captured by the settlement layer, as less than 4% of the non-settlement layer contains buildings > 2 m in both cities. Less than 20% of the non-settlement layer is buildings or impervious surfaces in both cities, with 70% being grassed, vegetated and small forested areas.

In summary, results demonstrate (though not perfectly) the ability of the TanDEM-X water mask to capture most water bodies, whilst the GUF mask can assist to differentiate between impervious and pervious surfaces. The GUF mask appears to capture most buildings, but approximately 15% of the layer does comprise of vegetation > 2 m. Thus, a proportion of vegetated roughness elements may be included in geometry and roughness calculations when using the mask.

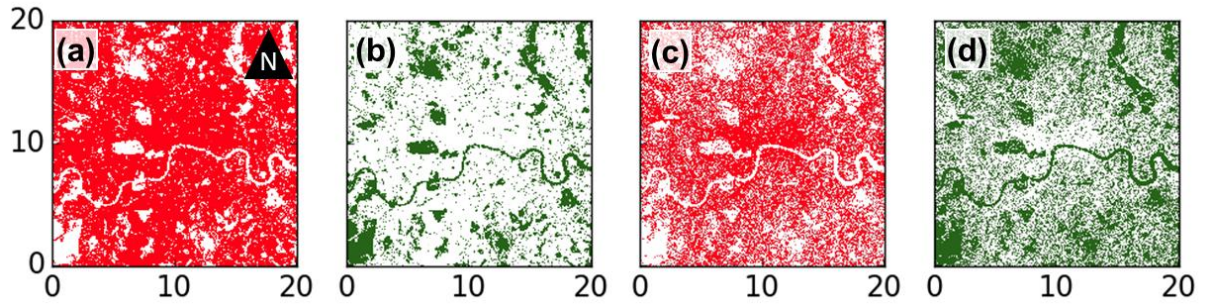


Figure 7.A3: Pixels classified as: (a) ‘settlement’ and (b) ‘non-settlement’ in the global urban footprint (GUF) mask (Esch et al. 2017) in central London. Land cover masks derived from the OS MasterMap® topography layer (Ordnance Survey 2010), comprising of: (c) built or paved surfaces and (d) tress, grasses, shrubs and water. Map units: km

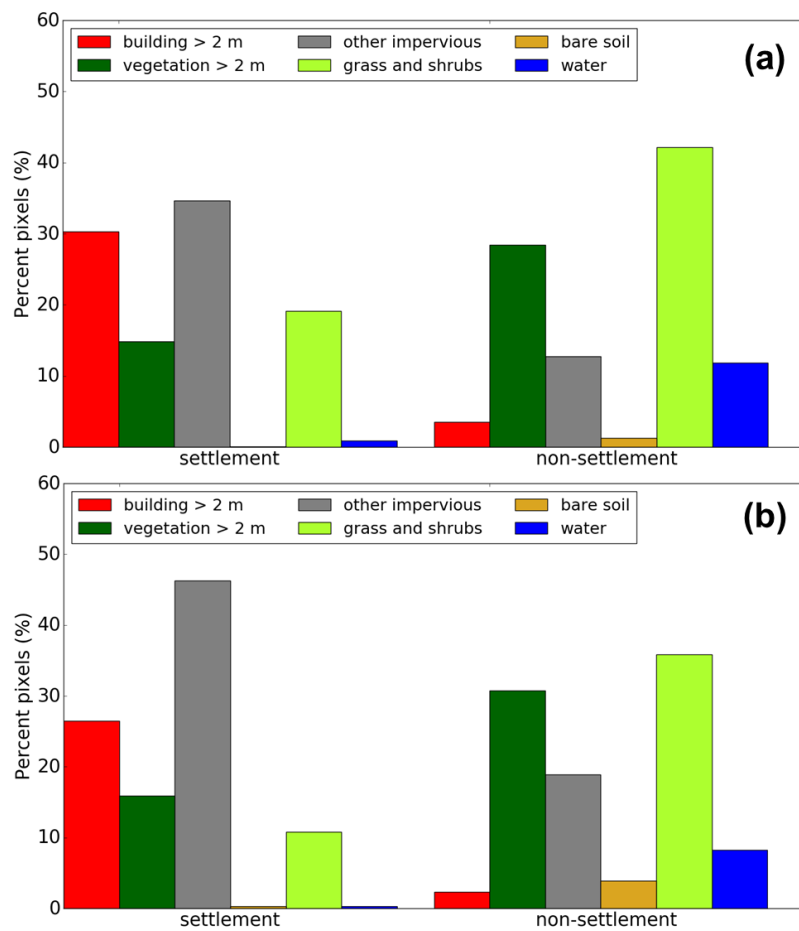


Figure 7.A4: Percentage of pixels in the ‘settlement’ and ‘non-settlement’ layers of the global urban footprint (GUF) mask (Esch et al. 2017) compared to land cover information in (a) central London study area (Fig. 7.A2a) and (b) New York (Fig. 7.A2b). For land cover source and classes see Fig. 7.A2. All databases are resampled to 4 m pixel resolution for comparison

Appendix 7.B: Pixel-to-pixel comparisons of global and benchmark DEMs

As a pixel-to-pixel comparison requires a consistent pixel size, all elevation models are resampled to 4 m resolution (except Tokyo, where the benchmark data only allowed this to be 5 m). For analysis of the pixel-to-pixel comparison, the data are binned to 10 m increments.

7.B.1 Comparison 1: ASTER, SRTM and TanDEM-X in London

Understanding the differences between the GDEMs and benchmark data requires a combined analysis of the DSM, DTM and RESM (Fig. 7.B1), as well as visual comparison (e.g. Fig. 7.4 and Fig. 7.6). All pixel-to-pixel results are given in Tables 7.B1 (DSM), 7.B2 (DTM) and 7.B3 (RESM), with information on the count, percentage and error of pixels in each height bin.

Across all pixels in the study area, the DSMs of the ASTER, TanDEM-X and SRTM have RMSEs (cf. benchmark data) of 9.79 m, 6.35 m and 6.27 m, respectively (Table 7.B1). The error increases where surface heights increase (Fig. 7.B1), which is associated with the underestimation of taller roughness elements (and not an effect of topographical variability). However, overestimation of surface heights may also occur when comparatively coarser resolution elevations reported by the GDEMs are unable to penetrate between densely packed roughness elements (e.g. Fig. 7.6b-d). These over- and under-estimation effects are most obvious for the ASTER data, resulting in the DSM (and corresponding DTM) having at least 50% of the reported heights outside the range indicated by the benchmark data for each height bin (Fig. 7.B1a, b). The distribution of differences for the TanDEM-X and SRTM datasets are remarkably similar, given the horizontal resolution of the latter is over twice as coarse as the former. Both have interquartile ranges which are consistently within the range of benchmark DSM and DTM values.

Using a 5 x 5-pixel width moving window extracts DTMs which best resemble the benchmark data for all GDEMs. The RMSE (cf. benchmark data) is approximately 3 m for the TanDEM-X and SRTM data and 8 m for ASTER (Table 7.B2). Figure 7.B2 shows the impact of using different sized moving windows. A smaller moving window results in consistent ground height overestimation because numerous neighbouring non-ground pixels may occur within the window. Whereas, using a large window, the lowest height becomes too distant from the point of interest and is consistently lower than the 'true' ground height.

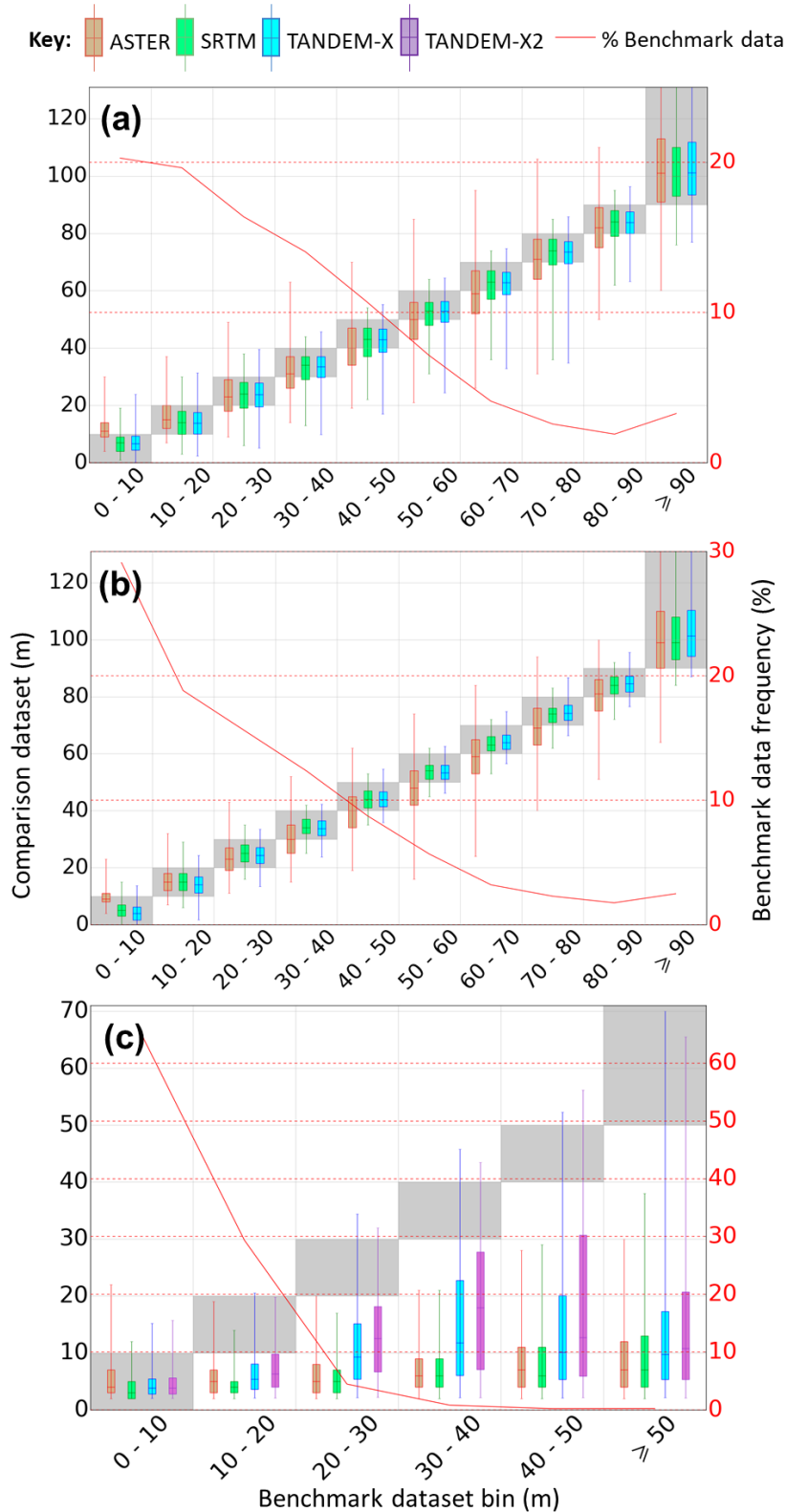


Figure 7.B1: Comparison between pixels in the benchmark and assessed global digital elevation models for the: **(a)** digital surface model (DSM), **(b)** digital terrain model (DTM) extracted with a 5 x 5-pixel moving window and **(c)** roughness-element surface model (RESM). In **(c)** the additional RESM assessed (TanDEM-X2) is from subtracting the benchmark DTM from the TanDEM-X DSM. For the comparisons, pixels in the benchmark dataset are divided into 10 m bins (x-axis, not inclusive of upper value labelled) and the distribution of heights in the corresponding GDEM pixels are shown for each bin (left y-axis). Whiskers are the 1st and 99th percentiles. Note, ideal distributions would be within the grey shaded areas. The percentage frequency of benchmark pixels within each bin are also shown (right y-axis, red line). For count/ percentage of pixels in each height bin and root-mean-square errors from the benchmark data, see Tables 7.B1, 7.B2 and 7.B3 for the DSM, DTM and RESM, respectively

Median heights of roughness-elements calculated from the GDEMs range between 5 – 12 m irrespective of height bin (Fig. 7.B1c). Most roughness-element heights in the study area are less than 20 m (95%), where the GDEMs are more accurate. This means the RMSE across all pixels is 8 m for the TanDEM-X data and 1 m larger for the other GDEMs (Table 7.B3). However, for the tallest roughness elements (> 50 m), median roughness-element heights may appear up to one tenth of their true value by the GDEMs.

To determine if the underestimation of roughness-element heights by the GDEMs is an artefact of the DTM extraction procedure (Sect. 7.3.2), the ‘true’ ground heights (i.e. the benchmark DTM) are subtracted from the GDEM surface models. The resulting RESMs are also compared to the benchmark data. An example with the TanDEM-X data is shown in Fig. 7.B1c (labelled TanDEM-X2). The procedure demonstrates how the distribution of differences from the benchmark RESM are only slightly improved (i.e. closer to the grey boxes) when the benchmark DTM is used. The resulting RMSE across all pixels is reduced by 0.6 m, which is 7.5% of the RMSE using the extracted DTM (Table 7.B3). The underestimation of roughness-element heights therefore appears inherent in the GDEMs and cannot be attributed to the DTM extraction procedure.

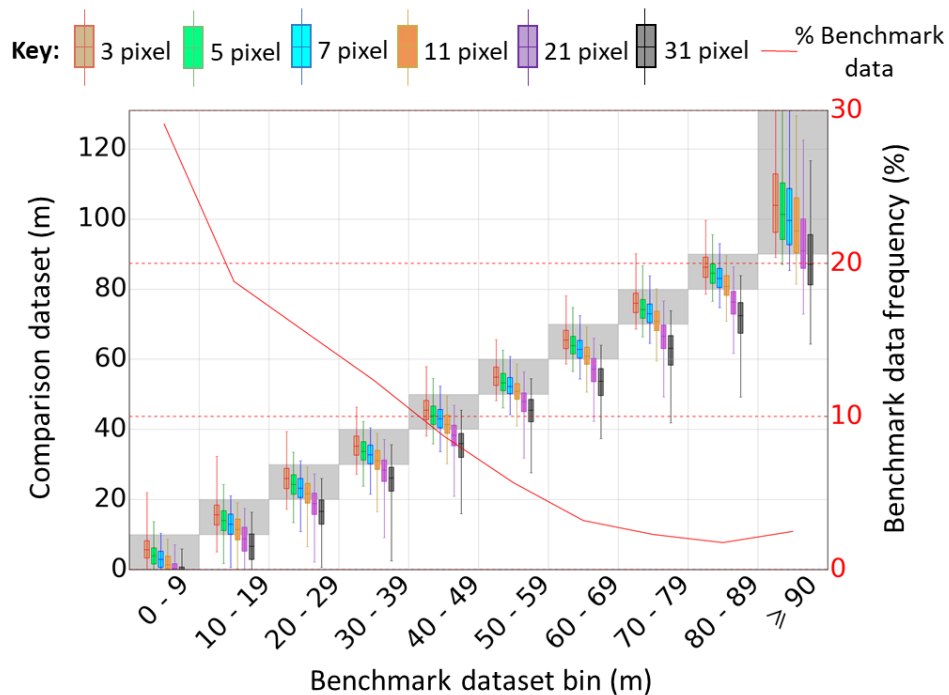


Figure 7.B2: As for Fig. 7.B1b, but for a comparison between pixels in the benchmark dataset and pixels of the digital terrain models (DTMs) extracted from the TanDEM-X dataset. The DTMs are extracted as outlined in Sect. 7.3.2 varying the width of the moving window by the indicated pixels (colours). Counts and error results are provided in Table 7.B2c

7.B.2 Comparison 2: TanDEM-X in five cities

A pixel-to-pixel comparison of the TanDEM-X and benchmark data in five cities (Table 7.2) substantiates the findings in comparison 1. However, as more complex geometry is encountered, errors from the benchmark data become larger. The comparable morphology of London and Auckland means their respective distributions of differences from the benchmark data are similar (Fig. 7.B3). The same is true for New York and Tokyo.

For the DSMs, the inter-quartile range of the TanDEM-X data consistently falls within the range indicated by the benchmark data, except for New York, where there is a tendency towards height underestimation (Fig. 7.B3). Like comparison 1, the underestimation is due to buildings and not topography. Tokyo, and especially New York, have the largest height differences from the benchmark DSM (RMSE across all pixels of 7.8 m and 11.5 m, respectively, Table 7.B4) because buildings are tall, densely packed and have small plan areas. This means the heights of surface elevations can be: (i) overestimated by greater than 20 m, due to the radar signal's inability to penetrate to ground level; and, (ii) underestimated by up to a factor of 10 where the heights of taller buildings are not resolved (see Fig. 7.7 and description in main text). These effects, also demonstrated in Small and Sohn (2015), are less pronounced for the less complex morphology in Auckland and London, creating a smaller range of differences from the benchmark data (Fig. 7.B3a) with resulting RMSE accuracies of between 4 and 5 m across all DSM pixels.

During the DTM extraction procedure, a 5 x 5-pixel moving window results in the lowest RMSE (c.f. benchmark data) for all cities except New York, where a 7 x 7-pixel window is optimum (see main text for explanation). The inter-quartile range of the resulting DTMs are within the range indicated by the benchmark data, producing RMSE across all pixels of between 2 and 4 m (Fig. 7.B3b, Table 7.B5).

In each city, more than half of all roughness-element heights are between 2 – 10 m (Fig. 7.B3c). The heights of these shorter roughness elements are resolved well by the TanDEM-X data, with over 90% of elevations within the range of the benchmark values. However, roughness-element heights are increasingly underestimated as they become taller. For heights beyond 10 m, less than 25% of TanDEM-X elevations tend to be within the range of the benchmark data. Beyond 50 m only a few are close to the benchmark values, with a median underestimation of up to a factor of 10. Figure 7.7 demonstrates the cause, which is an apparent merging of roughness elements in the TanDEM-X elevations, meaning both the height and location of the taller roughness elements are less likely to be resolved.

Key: Sao Paulo Tokyo New York London Auckland % Benchmark data

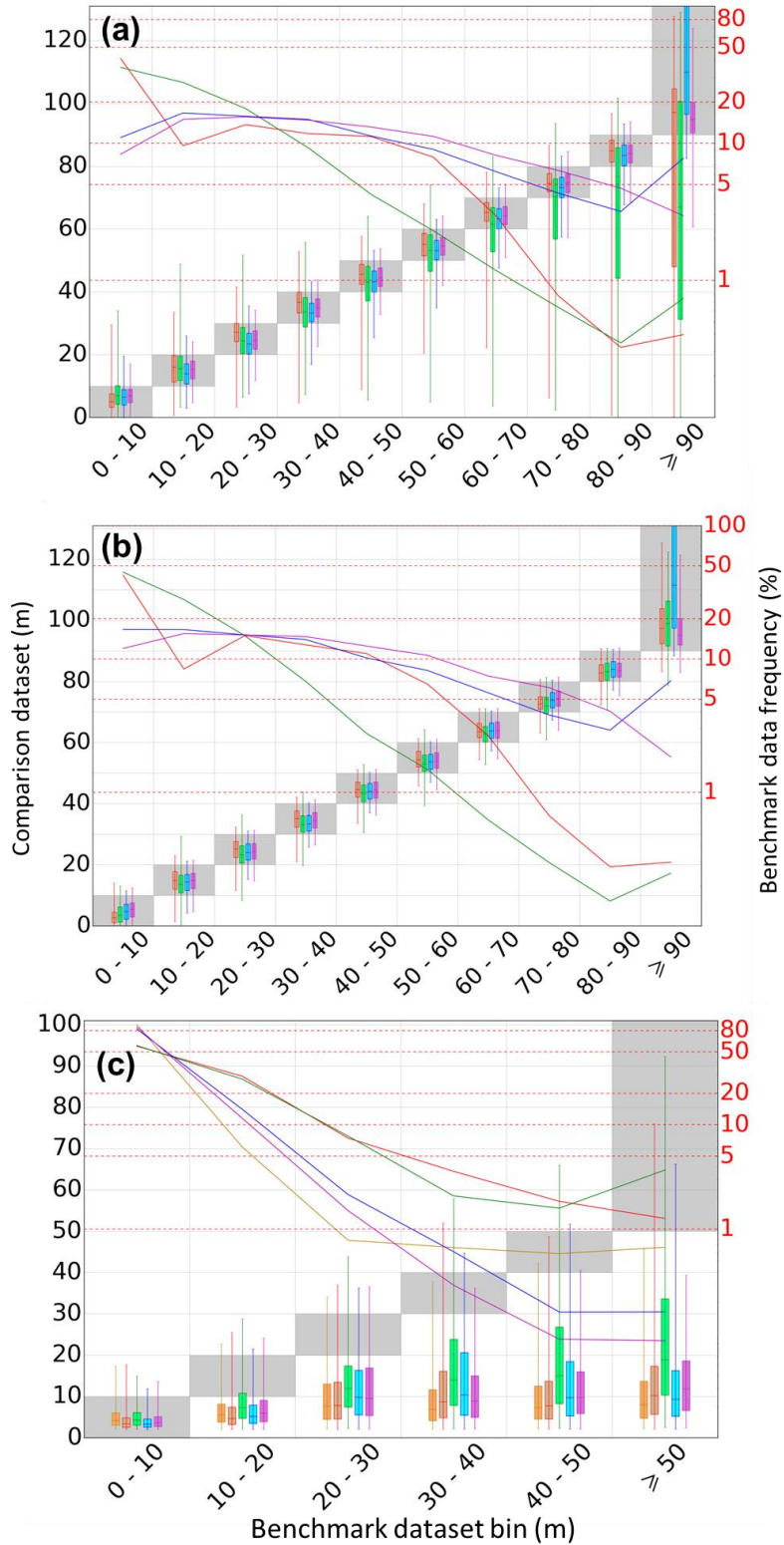


Figure 7.B3: As for Fig. 7.B1, but for benchmark data in five cities compared to the TANDEM-X model with the global urban footprint mask (Esch et al. 2017) applied: **(a)** urban footprint digital surface model (UFDSM), **(b)** urban footprint digital terrain model (UFDTM) and **(c)** urban footprint roughness-element surface model (UFRESM). UFDTMs are extracted using Sect. 7.3.2 method with a 5 x 5-pixel moving window, except for New York (7 x 7-pixel). For count/percentage of pixels in each height bin and root-mean-square errors from the benchmark data see Tables 7.B4, 7.B5 and 7.B6 for the UFDSM, UFDTM and UFRESM, respectively

Digital surface model											
Height bin	0 – < 10	10 – < 20	20 – < 30	30 – < 40	40 – < 50	50 – < 60	60 – < 70	70 – < 80	80 – < 90	≥ 90	all
Pixel count	5119465	4956038	4132715	3543767	2697738	1803043	1033659	649840	480344	826751	25243360
% data	20.29	19.63	16.37	14.04	10.69	7.14	4.09	2.57	1.90	3.28	100.00
ASTER	9.12	6.59	8.31	9.98	11.15	12.54	13.14	13.29	11.69	13.95	9.79
SRTM	4.20	5.35	6.35	6.24	6.96	7.07	7.52	8.13	7.18	11.37	6.27
TanDEM-X	4.58	5.50	6.35	6.32	7.05	7.17	7.35	7.84	7.07	10.74	6.35

Table 7.B1: Benchmark and global digital elevation model (GDEM) digital surface models (DSMs) compared for the 20 km x 20 km study area in central London (Fig. 7.4). Pixels in the benchmark dataset are divided into 10-m bins with the root-mean-square error (RMSE) from heights in the corresponding GDEM pixels shown. The pixel count is the number of pixels in the benchmark data height bin and the percentage of total pixels in each height bin is shown. The ‘all’ column refers to values for all pixels

Digital terrain model											
Height bin	0 – < 10	10 – < 20	20 – < 30	30 – < 40	40 – < 50	50 – < 60	60 – < 70	70 – < 80	80 – < 90	≥ 90	all
Pixel count	7345642	4749633	3934730	3121852	2203549	1431317	807597	576930	442702	627475	25241427
% data	29.09	18.82	15.59	12.37	8.73	5.67	3.20	2.29	1.75	2.49	100.00
(a) ASTER											
3 pixel	8.25	6.67	7.93	8.63	9.76	11.33	11.61	10.49	9.34	8.94	8.56
5 pixel	6.33	5.09	6.88	8.54	10.14	12.27	12.55	11.35	10.02	9.16	7.90
7 pixel	5.21	4.45	6.85	9.28	11.34	13.80	14.43	13.20	11.89	10.76	8.22
11 pixel	4.05	4.37	7.80	11.21	14.07	16.92	18.54	17.38	16.25	15.04	9.75
21 pixel	3.06	5.26	10.21	15.00	19.33	22.69	26.63	27.08	26.24	25.29	13.46
31 pixel	2.73	6.00	11.78	17.49	22.86	26.69	31.85	34.41	34.40	33.92	16.22
(b) SRTM											
3 pixel	3.67	4.17	4.04	2.67	2.77	2.71	2.98	3.10	3.13	3.98	3.58
5 pixel	2.75	3.30	3.30	2.52	2.74	2.68	3.34	3.65	3.51	3.82	3.01
7 pixel	2.61	3.22	3.50	3.44	3.94	3.89	5.17	5.91	5.93	6.30	3.58
11 pixel	2.87	3.81	4.72	5.55	6.73	6.75	8.78	10.37	11.21	12.03	5.45
21 pixel	3.67	5.80	7.67	9.71	12.16	12.81	15.35	18.28	21.32	24.06	9.53
31 pixel	4.22	7.35	9.97	12.75	16.04	17.51	20.03	23.50	28.08	33.76	12.58
(c) TanDEM-X											
3 pixel	4.28	4.04	3.80	2.94	2.96	3.00	3.05	3.50	3.68	5.52	3.82
5 pixel	3.04	3.19	3.05	2.78	2.56	2.48	2.47	2.76	2.68	4.01	2.97
7 pixel	3.02	3.68	3.57	3.46	3.09	2.92	3.00	3.20	3.04	3.81	3.32
11 pixel	3.48	4.98	5.00	4.98	4.55	4.35	4.75	5.08	4.92	5.27	4.52
21 pixel	4.33	7.34	7.94	8.26	8.11	7.72	9.04	10.06	10.09	10.72	7.25
31 pixel	4.80	8.89	10.22	10.91	11.22	10.60	12.51	14.25	14.94	15.75	9.47

Table 7.B2: As for Table 7.B1, but for the digital terrain models (DTMs) extracted (Sect. 7.3.2 method) using the: **(a)** ASTER, **(b)** SRTM and **(c)** TanDEM-X models. The RMSE results for different sized windows are shown

Roughness-element surface model							
Height bin	0 – < 10	10 – < 20	20 – < 30	30 – < 40	40 – < 50	≥ 50	all
Pixel count	6930176	3136365	475974	86526	23055	24520	10676616
% data	64.90	29.38	4.46	0.81	0.22	0.23	100.00
ASTER	4.87	9.14	17.83	26.95	36.16	71.29	8.87
SRTM	3.81	9.98	18.53	27.16	36.76	70.06	9.02
TanDEM-X	3.84	8.43	14.38	21.63	32.18	63.36	7.79
TanDEM-X2	3.89	7.66	12.66	19.45	29.88	60.24	7.17

Table 7.B3: As for Table 7.B1, but for the roughness-element surface models

Digital surface model											
Height bin	0 – < 10	10 – < 20	20 – < 30	30 – < 40	40 – < 50	50 – < 60	60 – < 70	70 – < 80	80 – < 90	≥ 90	all
(a) Tokyo											
Pixel count	16323211	3773193	5379406	4625697	4412577	3114824	1167430	302940	127553	158040	39384871
% data	41.46	9.58	13.66	11.74	11.20	7.91	2.96	0.77	0.32	0.40	100.0
RMSE	6.43	6.00	5.82	7.07	6.86	7.24	9.62	16.61	24.17	59.05	7.83
(b) New York											
Pixel count	12485082	9698127	6250419	3234932	1485451	803604	413137	221877	122193	257828	34972650
% data	35.70	27.73	17.87	9.25	4.25	2.30	1.18	0.63	0.35	0.74	100.00
TanDEM-X	7.35	8.11	8.03	8.51	10.87	14.09	19.76	24.16	33.24	87.57	11.54
(c) London											
Pixel count	7246096	10832625	10261395	9720685	7359524	5869764	4045496	2813479	2068047	5057480	65274591
% data	11.10	16.60	15.72	14.89	11.27	8.99	6.20	4.31	3.17	7.75	100.00
TanDEM-X	3.83	4.38	4.93	4.85	5.35	5.29	5.38	5.62	5.41	6.12	4.98
(d) Auckland											
Pixel count	586681	1052977	1099178	1040001	926596	791514	576990	446253	331347	208863	7060400
% data	8.32	14.91	15.57	14.73	13.12	11.21	8.17	6.32	4.69	2.96	100.00
TanDEM-X	3.02	3.27	3.58	3.64	3.56	3.83	4.24	4.78	4.96	9.18	4.02

Table 7.B4: As for Table 7.B1, but for benchmark digital surface models in four cities compared to TanDEM-X only. Note, only pixels within the ‘settlement’ layer of the global urban footprint (GUF) mask (Esch et al. 2017) are compared. (Note, benchmark DSM not available for Sao Paulo, Table 7.2)

Digital Terrain Model											
Height bin	0 – < 10	10 – < 20	20 – < 30	30 – < 40	40 – < 50	50 – < 60	60 – < 70	70 – < 80	80 – < 90	≥ 90	all
(a) Tokyo											
Pixel count	15837951	3128953	5584790	4754432	4095289	2414506	990750	248643	102949	111643	37269906
% data	42.50	8.40	14.98	12.76	10.99	6.48	2.65	0.66	0.28	0.30	100.00
3 pixel	4.90	3.83	3.45	3.92	2.71	2.46	2.66	2.50	2.51	2.50	4.08
5 pixel	3.20	3.13	3.11	3.37	2.45	2.01	2.30	2.67	3.15	3.44	3.04
7 pixel	2.75	3.78	4.02	4.16	3.20	2.63	3.06	3.99	4.87	5.53	3.34
11 pixel	2.82	5.33	6.02	6.13	4.94	4.22	4.90	6.76	8.31	9.70	4.61
21 pixel	3.31	8.08	9.83	10.07	8.54	7.62	8.85	12.41	14.69	18.30	7.35
31 pixel	3.59	9.84	12.49	12.93	11.23	10.28	11.96	16.63	19.34	24.02	9.35
(b) New York											
Pixel count	15398270	9608949	5151666	2340063	951712	511258	213386	102398	52728	85342	34415772
% data	44.74	27.92	14.97	6.80	2.76	1.49	0.62	0.30	0.15	0.25	100.00
3 pixel	5.83	7.92	6.96	5.31	5.01	5.22	4.45	4.03	3.27	4.73	6.57
5 pixel	3.67	5.51	4.94	3.68	3.34	3.91	3.09	3.40	2.65	3.28	4.44
7 pixel	3.04	4.67	4.42	3.67	3.50	4.26	3.46	4.19	3.47	3.88	3.85
11 pixel	3.20	4.93	5.21	5.11	5.35	6.33	5.51	6.62	5.55	6.36	4.36
21 pixel	4.16	7.20	8.39	9.04	10.29	12.18	11.38	12.89	11.42	13.62	6.74
31 pixel	4.73	8.91	10.91	12.34	14.67	17.71	17.06	19.47	17.37	22.07	8.69
(c) London											
Pixel count	10817628	10802596	9868707	9105862	6626193	5338087	3628152	2476706	1903998	4471379	65039308
% data	16.63	16.61	15.17	14.00	10.19	8.21	5.58	3.81	2.93	6.87	100.00
3 pixel	2.87	2.73	2.57	1.83	1.69	1.70	1.77	1.72	1.82	1.92	2.29
5 pixel	2.16	2.30	2.34	1.92	1.75	1.69	1.69	1.67	1.68	1.92	2.04
7 pixel	2.46	2.81	2.90	2.60	2.42	2.36	2.40	2.44	2.47	2.87	2.62
11 pixel	3.15	3.92	4.16	3.90	3.78	3.75	3.99	4.11	4.24	5.06	3.92
21 pixel	4.18	5.95	6.68	6.60	6.72	6.80	7.61	7.89	8.32	10.52	6.73
31 pixel	4.76	7.41	8.63	8.77	9.21	9.39	10.64	11.07	11.82	15.44	9.07
(d) Auckland											
Pixel count	845505	1093274	1067701	1038192	880845	751710	525199	430462	286070	129796	7048754
% data	12.00	15.51	15.15	14.73	12.50	10.66	7.45	6.11	4.06	1.83	100.00
3 pixel	2.88	2.47	2.48	2.49	2.26	2.45	2.40	2.53	2.51	2.62	2.50
5 pixel	2.22	2.29	2.29	2.10	2.01	2.30	2.30	2.35	2.34	2.61	2.23
7 pixel	2.65	3.13	3.26	3.02	3.05	3.34	3.38	3.37	3.43	4.11	3.16
11 pixel	3.61	4.99	5.56	5.41	5.60	5.85	5.92	5.84	5.93	7.56	5.40
21 pixel	4.92	8.20	10.36	10.88	11.48	11.69	11.96	11.63	11.70	15.19	10.33
31 pixel	5.53	10.12	13.50	15.15	16.47	16.69	17.10	16.69	17.09	21.44	14.27

Table 7.B5: As for Table 7.B2, but for benchmark digital terrain models in four cities compared to the TanDEM-X only. Only pixels within the ‘settlement’ layer of the global urban footprint (GUF) mask (Esch et al. 2017) are compared (Note, benchmark DTM not available for Sao Paulo, Table 7.2)

Roughness-element surface model							
Height bin	0 – < 10	10 – < 20	20 – < 30	30 – < 40	40 – < 50	≥ 50	all
(a) Sao Paulo							
Pixel count	17782457	1191816	152573	129783	113353	130725	19500707
% data	91.19	6.11	0.78	0.67	0.58	0.67	100.00
RMSE	3.66	7.65	16.94	27.24	35.68	54.52	7.75
(b) Tokyo							
Pixel count	3620592	1862005	476135	228282	117809	80664	6385487
% data	56.70	29.16	7.46	3.58	1.84	1.26	100.00
RMSE	4.20	8.34	16.09	24.71	36.58	91.51	15.34
(c) New York							
Pixel count	5597081	2661281	758595	202203	154448	357963	9731571
% data	57.50	27.35	7.80	2.08	1.59	3.68	100.00
RMSE	4.16	7.81	13.08	21.68	29.56	80.65	17.72
(d) London							
Pixel count	14111170	2392415	364963	103325	27316	27403	17026592
% data	82.88	14.05	2.14	0.61	0.16	0.16	100.00
RMSE	3.60	8.10	14.48	22.59	32.58	62.21	6.69
(e) Auckland							
Pixel count	3584789	477304	62302	11999	3643	3526	4143563
% data	86.51	11.52	1.50	0.29	0.09	0.09	100.00
RMSE	2.96	7.44	14.76	24.58	33.93	61.44	4.99

Table 7.B6: As for Table 7.B3, but for the roughness-element surface models in five cities compared to the TanDEM-X data only. In Sao Paulo, Tokyo, New York and London the pixels compared are ‘buildings’ in the benchmark data. In Auckland, the ‘settlement’ layer of the global urban footprint (GUF) mask (Esch et al. 2017) is the basis for comparison

Appendix 7.C: Polynomials between benchmark and TanDEM-X model parameters

Parameter	a	b	c	Original RMSE	Original nRMSE	Corrected RMSE	Corrected nRMSE	x min	x max
(a) Sao Paulo									
$H_{av,grd}$	-	-	-	-	-	-	-	-	-
H_{av}	0.008	-0.142	1.594	2.68	0.43	2.55	0.41	2.04	19.85
H_{max}	-1.83E-04	0.026	0.415	17.96	0.74	18.14	0.74	2.04	89.73
σ_H	-0.005	0.220	0.342	3.41	0.89	3.08	0.80	0.04	14.99
λ_p	-1.091	1.417	0.104	0.32	0.93	0.11	0.32	0.00	0.96
λ_f	118.780	-44.233	5.937	0.12	0.89	0.07	0.52	0.00	0.30
(b) Tokyo									
$H_{av,grd}$	-	-	-	1.80	0.09	-	-	-	-
H_{av}	0.001	-0.040	2.295	9.61	0.77	6.21	0.50	2.44	24.32
H_{max}	8.56E-05	-0.017	1.790	27.76	0.69	24.65	0.61	2.72	137.64
σ_H	0.002	-0.075	2.104	8.02	1.01	6.62	0.83	0.54	25.00
λ_p	0.196	-0.728	0.950	0.25	0.79	0.09	0.28	0.01	0.93
λ_f	85.820	-45.179	7.139	0.19	0.89	0.11	0.52	0.00	0.40
(c) New York									
$H_{av,grd}$	-	-	-	2.69	0.18	-	-	-	-
H_{av}	-5.40E-04	0.038	1.542	10.47	0.82	6.74	0.53	2.14	39.94
H_{max}	-2.30E-05	0.009	0.727	21.19	0.76	19.25	0.69	2.20	147.80
σ_H	-0.002	0.107	0.843	6.40	1.08	5.18	0.88	0.08	29.66
λ_p	0.576	-0.561	0.493	0.40	1.63	0.07	0.29	0.01	0.98
λ_f	21.199	-13.038	3.938	0.15	0.88	0.10	0.59	0.00	0.50
(d) London									
$H_{av,grd}$	-	-	-	1.63	0.03	-	-	-	-
H_{av}	1.70E-04	0.009	1.626	3.36	0.50	1.91	0.28	2.00	19.72
H_{max}	2.85E-04	-0.028	1.673	11.19	0.59	9.79	0.52	2.00	89.23
σ_H	0.006	-0.089	1.601	1.93	0.65	1.64	0.55	0.01	14.96
λ_p	0.920	-1.156	0.826	0.21	1.04	0.07	0.35	0.00	0.92
λ_f	151.523	-57.645	6.825	0.10	0.95	0.06	0.57	0.00	0.30
(e) Auckland									
$H_{av,grd}$	-	-	-	2.38	0.07	-	-	-	-
H_{av}	0.005	-0.078	1.530	1.84	0.32	1.22	0.21	2.02	14.51
H_{max}	0.002	-0.120	2.918	12.76	0.57	10.28	0.46	2.02	48.30
σ_H	0.031	-0.349	1.956	1.57	0.52	1.34	0.45	0.03	9.76
λ_p	0.088	-0.489	0.978	0.13	0.41	0.07	0.22	0.04	0.90
λ_f	725.997	-162.175	9.960	0.11	0.91	0.07	0.58	0.00	0.20
(f) Multi-city									
$H_{av,grd}$	-	-	-	1.95	0.06	-	-	-	-
H_{av}	-6.87E-04	0.057	1.099	6.29	0.74	4.76	0.56	2.00	39.94
H_{max}	-5.77E-06	4.91E-03	0.919	18.10	0.72	17.57	0.70	2.00	147.80
σ_H	-7.26E-04	0.049	1.120	4.58	1.03	4.04	0.91	0.01	29.66
λ_p	0.070	-0.236	0.652	0.28	1.04	0.10	0.37	0.00	0.98
λ_f	16.155	-8.884	3.135	0.14	0.97	0.13	0.90	0.00	0.50

Table 7.C1: Polynomial relations between parameters determined from the benchmark (y) and the TanDEM-X (x) datasets (Table 7.3a) constrained to: $y = ax^3 + bx^2 + cx$, where a , b and c are the best-fit constants (Sect. 7.3.3 method). Columns are: root-mean-square error for each parameter (original RMSE), following correction using the polynomial relation (corrected RMSE), normalised values (nRMSE), and data range of TanDEM-X derived parameters (x min, x max). No correction is attempted to ground height ($H_{av,grd}$). For each parameter, errors are calculated if both elevation models have H_{av} and $H_{max} > 2$ m and the benchmark data have: λ_p and $\lambda_f \geq 0.05$ and z_d and $z_o > 0.1$. Fits are city-specific, except for (f) 'multi-city', which follows Sect. 7.3.3 method. Parameter calculation, abbreviations and units: Fig. 7.3c

Appendix 7.D: Empirical relations between geometric parameters

Empirical relations between different geometric parameters are useful when there is incomplete or unreliable information about an area's morphology. The global use of these empirical relations relies upon all urban morphology behaving identically, which is often not the case. However, deriving relations for areas with varying geometry provides a basis for their application in areas exhibiting similar characteristics. Therefore, polynomial fitting is used to provide empirical relations between the best correlated parameters in each benchmark dataset used during this work (Fig. 7.D1). More appropriate fits could be obtained through initially classifying areas based upon their morphology (e.g. data binned by H_{av} , Fig. 7.D1), however applying the resulting fits to an independent location requires *a priori* knowledge of the location's morphology.

Kanda et al. (2013) describe three empirical relations between the geometric parameters of buildings within 1 km grid-squares for a 622 km² area in Tokyo (where the additional subscript b refers to buildings only):

$$\lambda_{f,b} = 1.42\lambda_{p,b}^2 + 0.4\lambda_{p,b} \quad (0.05 < \lambda_{p,b} < 0.45) \quad (7.D1)$$

$$\sigma_{H,b} = 1.05H_{av,b} - 3.7 \quad (7.D2)$$

$$H_{max,b} = 12.51\sigma_{H,b}^{0.77} \quad (7.D3)$$

Based on data from Ratti et al. (2002), Kanda et al. (2013) demonstrate the relations may be appropriate for the cities of Toulouse (France), Berlin (Germany), Salt Lake City and Los Angeles (USA), but not necessarily for London. Similar to Kanda et al. (2013), the geometric parameters with the best relation across the benchmark datasets used in this work are found to be: $\lambda_{f,b}$ and $\lambda_{p,b}$; $\sigma_{H,b}$ and $H_{av,b}$; and $H_{max,b}$ and $\sigma_{H,b}$, all of which have positive correlations (Fig. 7.D1). The RMSE of polynomial fits between these parameters (Fig. 7.D1, coloured lines) are less than 0.1, 4.0 m and 13.5 m, respectively. The relation between $H_{max,b}$ and $\sigma_{H,b}$ is consistently most accurate with the lowest nRMSE (between 0.3 – 0.4). The equation, error and data range for each polynomial fit is provided in Table 7.D1.

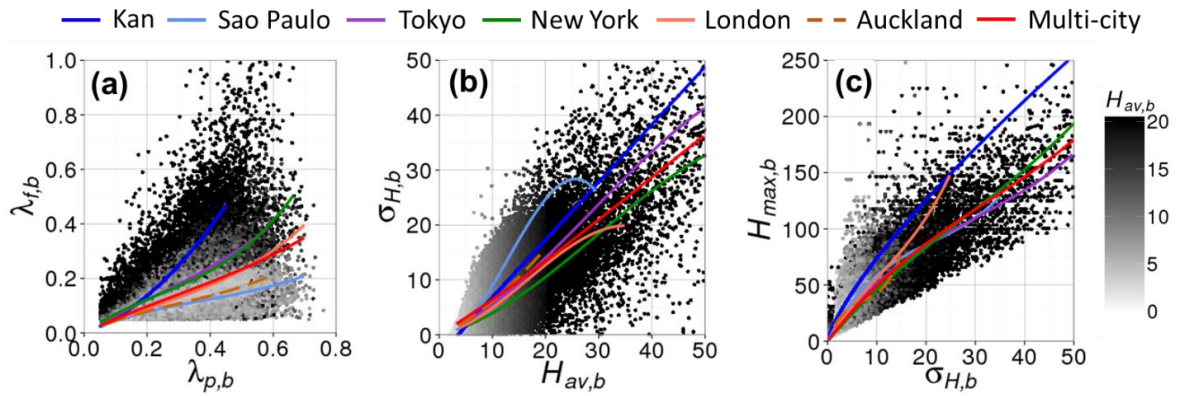


Figure 7.D1: Polynomial relations between geometric parameters determined from the benchmark data (buildings only, represented by subscript b). Polynomial fits use all city-specific data for each parameter (coloured lines) and the ‘multi-city’ polynomial is by Sect. 7.3.3 method. Auckland is dashed, as a lack of benchmark data building footprints mean the global urban footprint mask (Esch et al. 2017) is used to retain buildings only (see main text). Kanda et al. (2013) relations (Eqs. 7.D1 – 7.D3) are also shown (Kan). Each point is one of eight 45° directional sectors within a 1 km grid-square and is coloured by the average building height ($H_{av,b}$) in that 1 km grid-square. Table 7.D1 has the equation, error and data range of fits. Parameter calculation, abbreviations and units: Fig. 7.3c

There is considerable scatter from the polynomial fits due to the inter- and intra-city morphological variability. For example, densely-packed favela type morphology in Sao Paulo means that an increase in $\lambda_{p,b}$ does not result in as larger an increase of $\lambda_{f,b}$ which is found in other cities which have taller buildings (Fig. 7.D1a). Both Fig. 7.D1 and Kanda et al. (2013, their Fig. 2) demonstrate that as $\lambda_{f,b}$, $\sigma_{H,b}$ and $H_{max,b}$ increase, there is increasing variability about the fitted relations. An increase in these parameters indicates more heterogeneous building morphology, suggesting use of the empirical relations becomes less certain with heterogeneity. This is supported by the largest errors from the relations being in Tokyo and New York (Table 7.D1), the cities with the most heterogeneous morphology. Interestingly, although Eqs. 7.D1 – 7.D3 were derived for an area in Tokyo, they deviate from the larger area of Tokyo considered here (Fig. 7.D1, blue and purple lines, respectively). This demonstrates the sensitivity of empirical relations to the selected input data and exemplifies the caution which should be taken during their ‘global’ application. Fitting multi-city relations to the parameters (Fig. 7.D1, red line) does not resolve the inter-city variability and therefore tends to have larger errors than city-specific fits (Table 7.D1).

Parameter	a	b	c	RMSE	nRMSE	x min	x max
(a) Sao Paulo							
$\lambda_{f,b} = f(\lambda_{p,b})$	0.677	-0.779	0.513	0.07	0.52	0.05	0.70
$\sigma_{H,b} = f(H_{av,b})$	-0.004	0.143	-0.171	2.07	0.47	3.22	29.50
$H_{max,b} = f(\sigma_{H,b})$	0.005	-0.292	8.302	10.77	0.37	0.01	34.98
(b) Tokyo							
$\lambda_{f,b} = f(\lambda_{p,b})$	0.839	-0.520	0.677	0.07	0.33	0.05	0.58
$\sigma_{H,b} = f(H_{av,b})$	-2.46E-04	0.021	0.372	3.49	0.43	3.85	64.52
$H_{max,b} = f(\sigma_{H,b})$	0.001	-0.128	6.236	13.37	0.31	0.33	64.99
(c) New York							
$\lambda_{f,b} = f(\lambda_{p,b})$	2.020	-1.432	0.820	0.11	0.64	0.05	0.66
$\sigma_{H,b} = f(H_{av,b})$	-2.24E-04	0.020	0.217	2.93	0.49	5.34	59.91
$H_{max,b} = f(\sigma_{H,b})$	7.73E-04	-0.064	5.145	11.28	0.37	0.08	64.58
(d) London							
$\lambda_{f,b} = f(\lambda_{p,b})$	0.967	-0.631	0.535	0.03	0.29	0.05	0.73
$\sigma_{H,b} = f(H_{av,b})$	-7.64E-04	0.038	0.192	1.20	0.36	3.78	80.00
$H_{max,b} = f(\sigma_{H,b})$	0.007	-0.227	7.164	7.13	0.33	1.27	67.98
(e) Auckland							
$\lambda_{f,b} = f(\lambda_{p,b})$	0.908	-0.827	0.525	0.03	0.25	0.07	0.69
$\sigma_{H,b} = f(H_{av,b})$	-1.94E-04	0.024	0.388	0.64	0.21	3.57	26.67
$H_{max,b} = f(\sigma_{H,b})$	0.058	-1.265	11.121	6.77	0.28	1.32	25.48
(f) Multi-city							
$\lambda_{f,b} = f(\lambda_{p,b})$	0.456	-0.385	0.546	0.06	0.56	0.05	0.70
$\sigma_{H,b} = f(H_{av,b})$	-3.63E-05	4.35E-03	0.601	4.19	0.96	3.22	64.52
$H_{max,b} = f(\sigma_{H,b})$	8.70E-04	-0.086	5.700	10.78	0.44	0.01	64.99

Table 7.D1: Polynomial relations between different geometric parameters ('parameter' column) determined from buildings (subscript b) in the benchmark datasets (Table 7.3b). For each pair of parameters $y = f(x)$, the fits are constrained to $y = ax^3 + bx^2 + cx$, where a , b and c are the best-fit constants between the parameters (Sect. 7.3.3 method). Given the lack of benchmark data building footprints in Auckland, the global urban footprint mask (Esch et al. 2017) is used to retain buildings only (see main text). The root-mean-square error (RMSE) and normalised RMSE (nRMSE) correspond to the fit of the polynomial function through the data points. Data range of the fit is indicated (x min, x max). Parameter calculation, abbreviations and units: Fig. 7.3c.

Appendix 7.E: Urban morphology parameters for five global cities

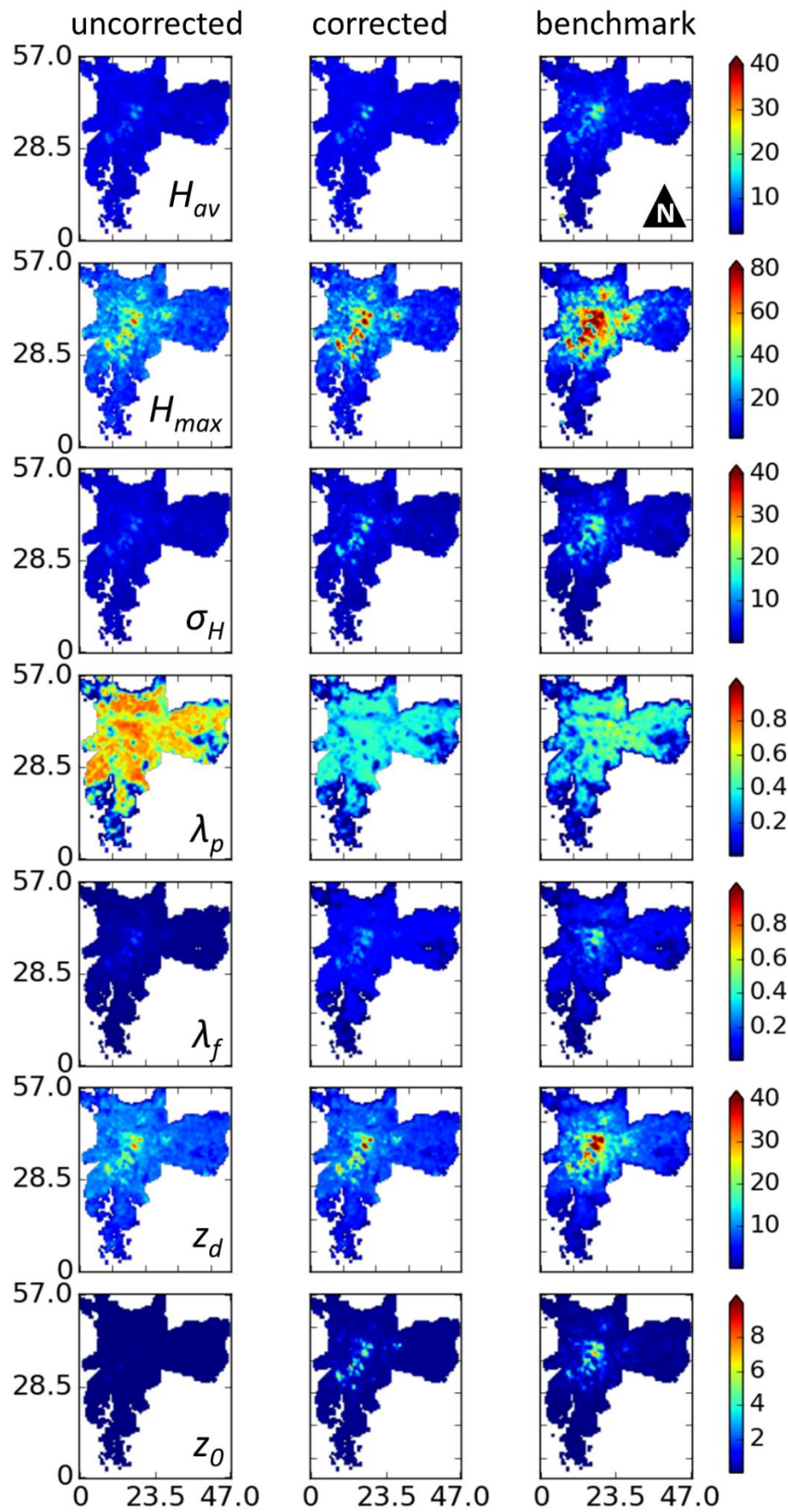


Figure 7.E1: As for Fig. 7.10, but for Sao Paulo

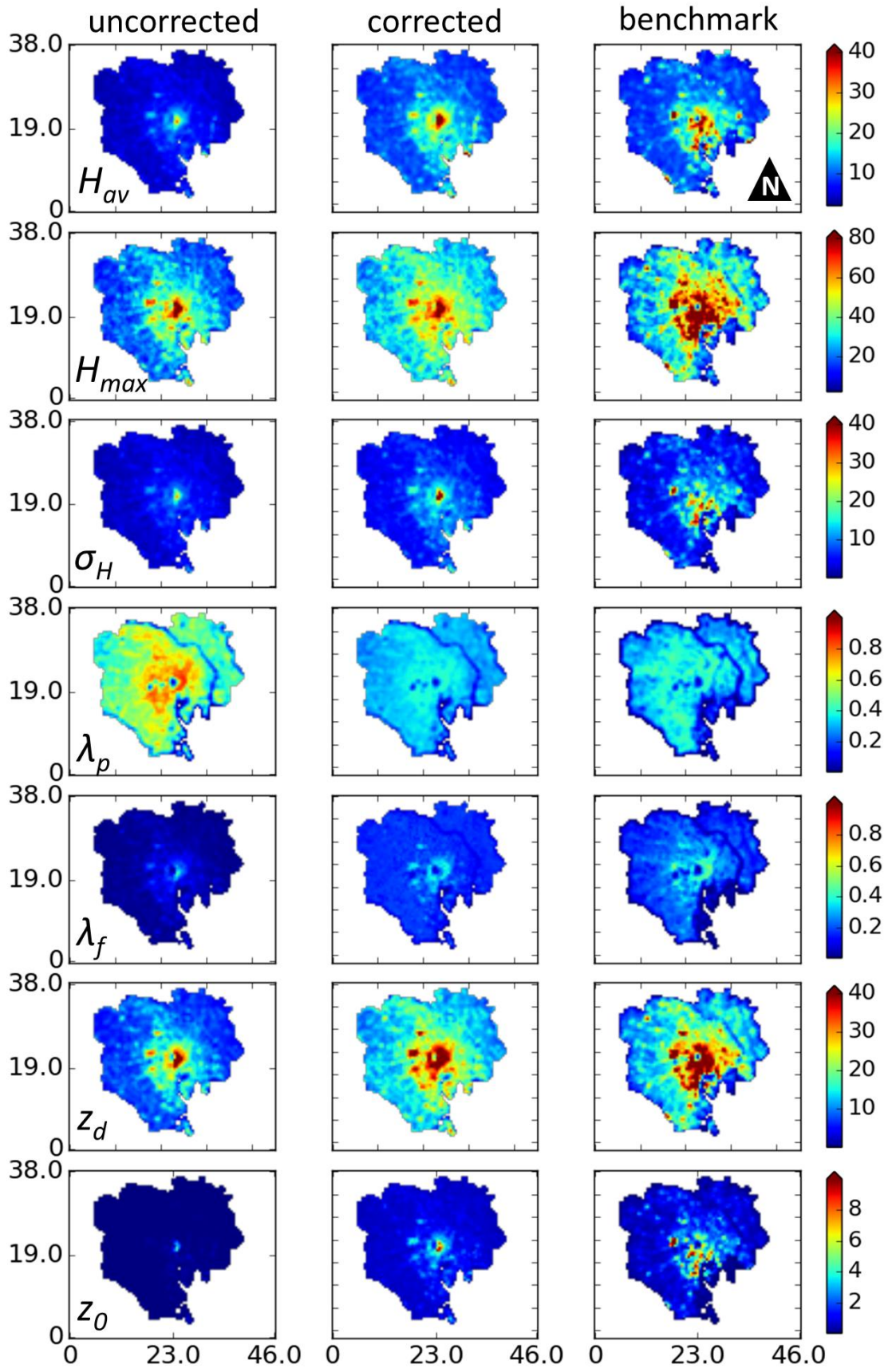


Figure 7.E2: As for Fig. 7.10, but for Tokyo

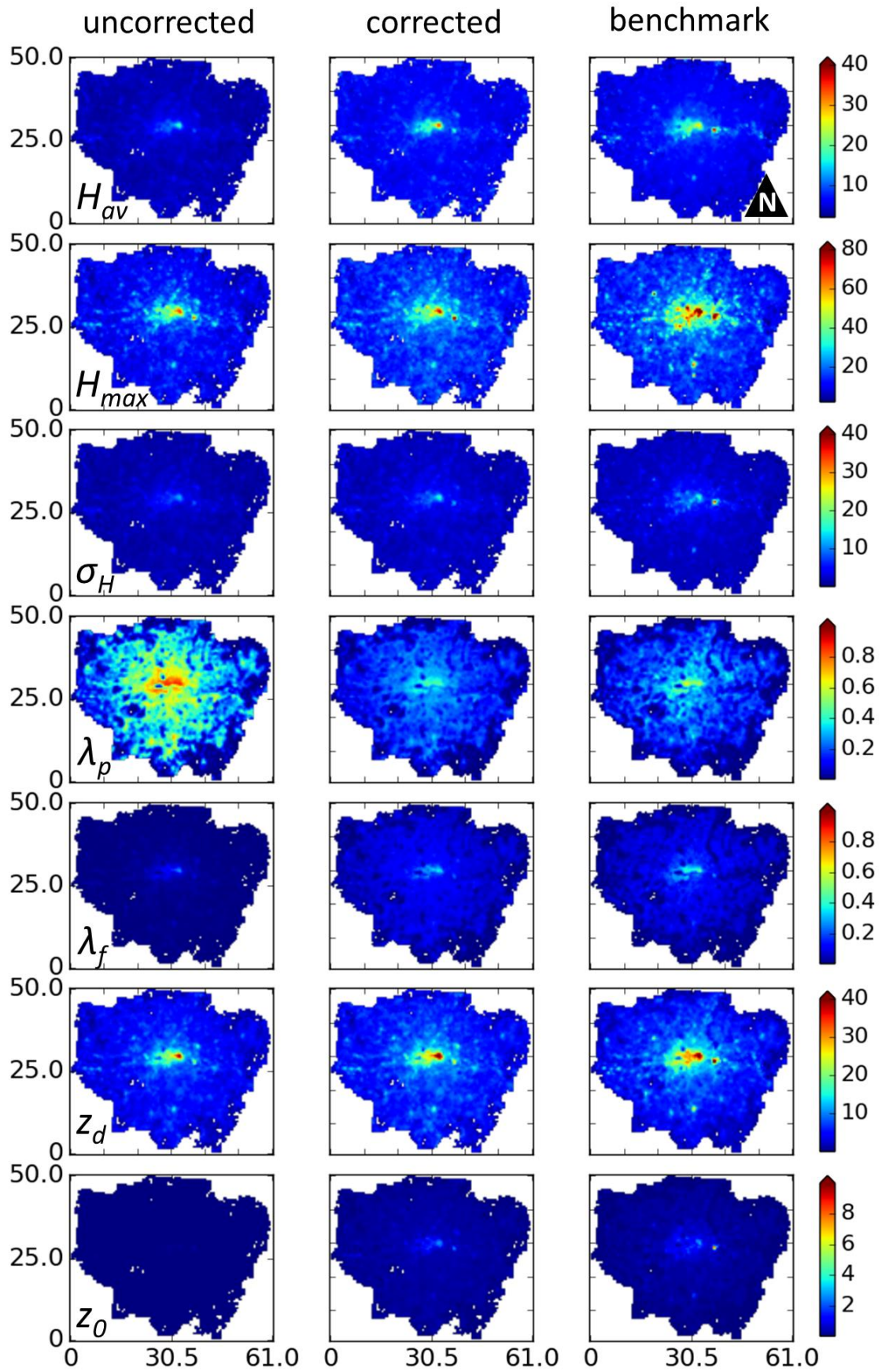


Figure 7.E3: As for Fig. 7.10, but for Greater London

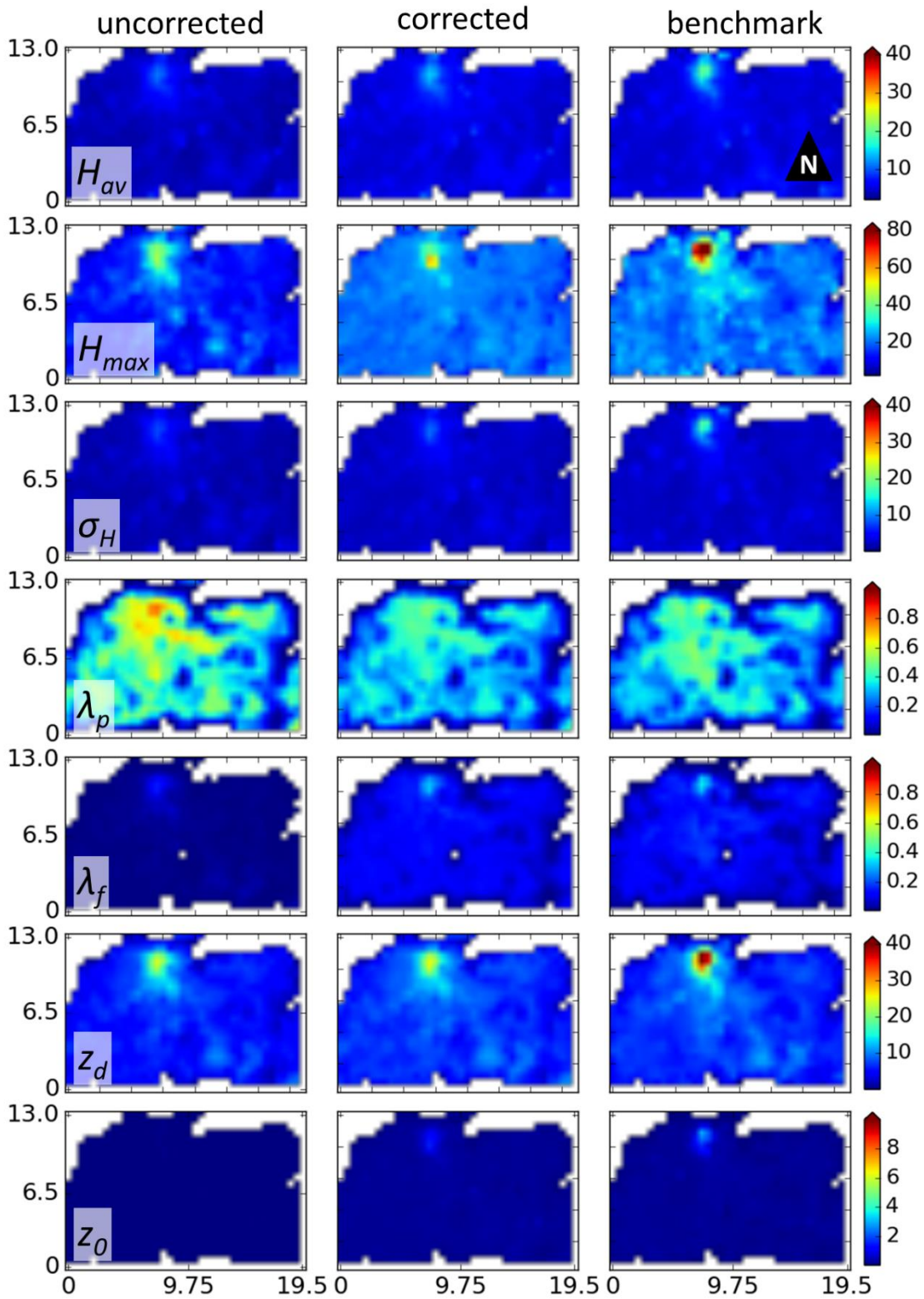


Figure 7.E4: As for Fig. 7.10, but for Auckland

Chapter 8. Conclusions

8.1 Research summary

The aerodynamic roughness parameters, zero-plane displacement (z_d) and roughness length (z_0), can be used to estimate the wind-speed profile in the atmospheric boundary layer. As urban surfaces are rough, with numerous sources and sinks of momentum, the determination of z_d and z_0 and is challenging, impacting the associated wind-speed estimates. The objective of this PhD was to improve the understanding and representation of the aerodynamic properties (or roughness) of urban surfaces, notably for wind-speed estimates where the flow is free from roughness-element wakes. The key scientific contributions are summarised as:

- (i) *Indication of the most appropriate combination of methods to determine both aerodynamic roughness parameters and estimate wind speeds from surface observations in a European city (London, UK).* Existing methods to determine z_d and z_0 were compared and the spatially- and temporally-averaged wind-speed profile was extrapolated using five wind-speed profile methods. Estimates were compared to wind speeds observed at up to 200 m above the canopy.
- (ii) *Consideration of the combined presence of buildings and vegetation in roughness parameter values (and therefore wind-speed estimates) through development and assessment of a novel morphometric method.* The developed method is demonstrated to be responsive to surface changes caused by phenology and land cover variations, as well as provide more accurate wind-speed estimates compared to considering buildings alone.
- (iii) *Recommendation of how to determine the morphology and roughness parameters for cities globally.* Global digital elevation models are assessed. The TanDEM-X data are identified as the most useful (currently). Empirical corrections are proposed, which are demonstrated to improve the accuracy of parameter values and wind-speed estimates.

8.2 Major conclusions

Urban aerodynamic roughness parameters (z_d and z_0) can be determined using numerous methods within three general types: reference-based, anemometric (observations) or morphometric (surface form). Through application of nine different methods at a European city centre site (London, UK) it was concluded that:

- Inter-method variability can lead to wide range of values: the z_d was between 5 and 45 m (~ 0.25 to 2.25 the local H_{av} (mean building height) and z_0 was between 0.1 and 5 m (0.005 to $0.250H_{av}$).

- Results vary with fetch (e.g. directional variability of methods in Fig. 3.5). The variability is less obvious for z_d determined with the anemometric methods and morphometric methods which directly incorporate height variability, which is attributed to the influence of the tallest roughness elements. The variability of the anemometric z_0 can be directly related to surface characteristics, including reductions in z_0 when wind directions are aligned to a river and along a street canyon.
- Results are sensitive to application technique. For example: (i) varying the empirical constants in anemometric methods produced a range of up to 50% from median z_d (Sect. 6.3.3.2); (ii) morphometric method roughness parameters and associated wind-speed estimates vary depending upon whether a source area model or simplified sector-based technique is used (Sect. 7.5).
- Comparison between roughness parameters determined with different methods is useful for prognostic/ diagnostic purposes but cannot necessarily identify the most appropriate method, especially for wind-speed estimates. This is because the z_d and z_0 are interdependent and a larger/smaller value of one parameter may be accounted for in the other. Therefore, two different pairs of values can lead to similar wind-speed estimates for a given height and wind-speed observations provide an independent method to assess appropriateness.

Although the anemometric z_d (from the temperature and wind variance methods, Eqs. 3.20 and 3.21) and z_0 (from the EC method, Eq. 3.23) are observationally-based, they should not be treated as 'truth', because:

- (i) The EC method to determine z_0 is sensitive to z_d (e.g. Fig. 3.5) and given the uncertainty in z_d values (presented throughout this work) the resulting z_0 cannot be interpreted in isolation.
- (ii) The TVM and WVM z_d values are calculated using surface layer similarity relations, derived from observations with an extensive, flat and homogeneous fetch (Sect. 2.2.3, Rotach 1994, Toda and Sugita 2003). Although field studies indicate the relations may be appropriate aloft heterogeneous urban environments, the numerous sources and sinks of heat and momentum may mean the methods are stretched to their theoretical limits, hence there is potential for observations to deviate from the similarity relations (e.g. Fig. 3.4 and Roth and Oke 1995, Roth 2000, Wood et al. 2010, Fortuniak et al. 2013, Nordbo et al. 2013, Liu et al. 2017).

- (iii) Use of roughness parameters derived from the anemometric methods did not produce the most accurate wind-speed estimates above a European city centre (London, UK) compared to other methods (Fig. 3.7).

The confidence in the TVM and WVM results is quantified by assessing the error of the similarity relations from observations. The root-mean-square error for the TVM relation is consistently double that of the WVM at three independent sites. This is attributed to the thermal inhomogeneity of the sites, with the largest error at an urban park which is likely to cause the greatest thermal inhomogeneity (a combination of water, grasses, trees, bare-soil, and impervious surfaces). The smaller error of the WVM relation is possibly due to the dissimilarity between the roughness length for momentum and for heat (e.g. Roth and Oke 1995, Kanda et al. 2007) and suggests there is greater confidence using the WVM in urban environments. However, varying the empirical constants used in the methods led to a range of z_d results of up to 50% of the median z_d for the TVM and 25% for the WVM. Combined with the impracticalities of spatially- and temporally-dense urban observations, morphometric methods are an attractive alternative to determine roughness parameters, especially given the increasing availability of surface elevation data.

Morphometric methods were classified as: RE_{av} methods, which assume homogeneous roughness-element heights (based upon H_{av}); and, RE_{var} methods which directly incorporate height variability (through the σ_H and/or H_{max}). The RE_{var} method z_d was consistently twice the RE_{av} value, with the former more similar to anemometric results and implying the z_d is larger than H_{av} . Traditionally, z_d is treated as a fraction of H_{av} and therefore results from the anemometric methods have been deemed unreasonable (Grimmond et al. 1998, 2002, Feigenwinter et al. 1999, Kanda et al. 2002, Tsuang et al. 2003, Christen 2005, Chang and Huynh 2007). However, the results are consistent with recent experiments and quasi-empirical models which indicate the disproportionate drag exerted by taller roughness elements in a heterogeneous mix can raise the z_d above H_{av} (Sect. 2.3.1). The literature also demonstrates the effect of height heterogeneity upon z_0 , but such an obvious contrast as for z_d is not found in this work.

Wind speeds estimated up to 200 m above a European city-centre ($\sim 10H_{av}$ or $1.7H_{max}$ of surrounding 1-km fetch, Table 3.3) were compared to hourly-averaged observations from Doppler lidar during strong winds (i.e. upper quartile of wind speeds). In the most homogeneous upwind direction, estimates with the logarithmic wind law and roughness parameters from two morphometric methods which directly incorporate roughness-element height variability (RE_{var}

class) (Millward-Hopkins et al. 2011, Kanda et al. 2013) were most accurate (median within ~5% of the mean wind speed) (Sect. 3.6). Not considering height variability (RE_{av} class) led to consistent wind-speed underestimation (median of 15 to 30% of the mean wind speed). Five different wind-speed profile laws were used for estimates and it was concluded that for more heterogeneous upwind directions the Deaves and Harris (1978) equilibrium (DH_e) or Gryning et al. (2007) (GR) profiles were consistently most accurate.

The most appropriate combination of methods to determine aerodynamic parameters and wind-speed profile laws allowed wind speeds to be estimated with an almost negligible median difference from observations (Sect. 4.5.5). However, a range of up to $\pm 5 \text{ m s}^{-1}$ is attributed to the upwind variability in transverse and longitudinal roughness, as well as applying the methods with different conditions from where they were developed. An implementation of the Deaves and Harris non-equilibrium profile (DH_v) (Harris and Deaves 1980) used pre-defined vertical increments and a source area footprint model to incorporate changes in upwind roughness. The procedure did not lead to notably improved wind speed estimates. However, this conclusion is not expected to hold where there are more abrupt changes in upwind roughness. The importance of fetch variability should not be overlooked.

A combination of both buildings and vegetation should be considered when determining roughness parameters. Morphometric methods have been developed to determine z_d and z_0 from vegetation (Nakai et al. 2008) or buildings (Sect. 3.3.2) only, but vegetation is typically ignored in urban studies to reduce complexity (e.g. assumed negligible or lack of method for its inclusion). Some previous attention has been given to the treatment of vegetation within building-based morphometric methods, by for example using porosity corrected geometry (e.g. Bottema 1995, Grimmond and Oke 1999, Holland et al. 2008, Millward-Hopkins et al. 2013b). However, at lower aerodynamic porosities the drag exerted by a porous roughness element (e.g. a tree) may be as large as a bluff body of the same shape (e.g. Sect. 5.2.2). Therefore, a morphometric method was developed from fundamental principles to account for the combined effects of both buildings and vegetation, with a direct estimation of the drag exerted by porous roughness elements, which is informed by the literature (Chapter 5). Expectedly, the effect of vegetation upon roughness parameters and the associated wind-speed estimates is greatest with larger vegetation cover and where vegetation is as tall as/ taller than buildings (Table 5.3, Fig. 5.3). The method development allowed for the seasonal aspects of the influence of vegetation to be explored.

Observations from a park (Seoul, South Korea) and a suburban neighbourhood (Swindon, UK) demonstrated the response of roughness parameters to vegetation (Chapter 6). Inter-seasonal analysis at the urban park indicated leaf-on z_d was 1 – 4 m larger than leaf-off and leaf-on z_0 was consistently over 0.5 m smaller than leaf-off. The z_0 results highlight a possible misconception – considering vegetation in addition to buildings (or indeed an increase in any roughness-element cover) does not necessarily lead to a larger z_0 , because the expected change is dependent upon canopy density (see Sect. 6.3.3).

For the suburban neighbourhood (which has less vegetation than the park) including vegetation in the morphometric methods (in addition to buildings) led to an average increase of 20% for z_d and 40% for z_0 . This compares to increases of up to 50% in more densely vegetated locations (Giometto et al. 2017). Wind-speed estimates with roughness parameters calculated considering both buildings and vegetation were at least 25% more accurate, compared to omitting vegetation (Sect. 6.3.4). Consistent to the London comparison, estimates were more accurate when using roughness parameters from a RE_{var} method compared to RE_{av} . However, where there was abundant vegetation, considering vegetation was more important for accurate wind-speed estimates than considering height variability.

Global digital elevation models (GDEMs) can be used to retrieve urban morphology parameters globally, which are critical for calculating aerodynamic roughness parameters (using morphometric methods) and wind-speed estimates. However, (currently) available GDEMs tend to have coarse resolution and the methods used to retrieve surface elevations have limitations in urban environments (such as layover effects of buildings in close proximity or multi-scattering of radar). Here, GDEMs from ASTER (Advanced Spaceborne Thermal Emission and Reflection Radiometer), SRTM (Shuttle Radar Topography Mission) and TanDEM-X were compared to benchmark elevation data (Chapter 7). As GDEMs have surface heights only (a DSM), a method was developed to extract ground heights (a DTM) from the GDEMs (Sect. 7.3.2), producing DTMs with ≤ 4 m RMSE from benchmark data.

Subtracting the DTM from the DSM creates a roughness-element surface model (RESM = DSM-DTM) allowing for calculation of geometric and aerodynamic roughness parameters. Apparent merging of roughness elements in the GDEMs leads to underestimation of height-based geometric parameters (H_{av} , H_{max} and σ_H), with plan- (λ_p) and frontal- (λ_f) area indexes over- and under-estimated, respectively. In combination, this results in consistent underestimation of z_d and z_0 . The errors associated with the TanDEM-X model were least for a 20 km x 20 km study

area in central London. TanDEM-X analysis was undertaken in five other cities: Auckland, Greater London, New York, Sao Paulo and Tokyo.

Empirical corrections to the TanDEM-X derived parameters were developed, which reduced errors for parameters on a city-wide scale (e.g. Table 7.5, Fig. 7.10) and for an independent city (where the corrections were not derived from). If these results are combined with the TANDEM-X derived water mask, and global urban footprint mask (GUF) (Esch et al. 2017) (to delineate pervious/ impervious surfaces), a wide number of parameters required within urban land surface models are obtainable.

The accuracy of wind-speed estimates up to approximately 10 times the canopy height (200 m) using roughness parameters determined from different elevation databases (ASTER, SRTM, TanDEM-X and benchmark data) in central London was assessed (i.e. for the same conditions as the previous London site comparison). Wind speeds were underestimated using roughness parameters determined directly from the GDEMs due to their small z_d and z_0 . This was especially apparent for the ASTER and SRTM models which had up to 40% underestimation. Results may vary with fetch but for all directions using the proposed corrections to the TanDEM-X derived parameters improved average wind-speed estimates to within 10% of observations. Roughness parameters derived from the benchmark data led to the most accurate wind-speed estimates, especially using a source area footprint model with the proposed iterative procedure (Sect. 3.4.3.3). However, if the forcing conditions for source area calculations are not available, simplified sector-based calculations may provide similar results. The most appropriate sector size will vary as a function of the source area for measurements (e.g. with measurement height, meteorological conditions and upwind surface) and local source area calculations informed the 500-m fetch and 45° width sectors (for different wind directions) used during this work.

Much of the research within this PhD is reproducible through the Urban Multi-scale Environmental Predictor (UMEP) climate service plugin for the open source geographical information system software QGIS (Lindberg et al. 2018, <http://www.urban-climate.net/umep/UMEP>). The morphometric methods applied during the work (including vegetation) and two source area footprint models (Kormann and Meixner 2001 and Kljun et al. 2015) are included, facilitating similar studies elsewhere, as well as applications beyond the current research objectives, including: interpretation of observations, new instrument siting, or, evaluation of flux models. A tutorial is available for new users (Appendix 3.D).

8.3 Limitations of analysis and possibilities for future work

This thesis contributes to the growing literature concerned with the appropriate determination of aerodynamic roughness parameters in cities and the impact upon wind-speed estimations. Specific attention has been given to wind-speed estimations in the inertial sublayer, during neutral atmospheric stability, with results having both direct and indirect implications for numerous fields of study. For example, estimating the average wind-speed profile is critical for the insurance and construction industries to understand the wind loading on buildings (e.g. Taranath 2016) and provides a basis to predict the magnitude of stronger gusts (e.g. Verkaik 2000). Pollutant concentrations and thermal comfort are of growing concern in urban environments and the flow field above a city impacts the dispersion of pollutants (e.g. Britter and Hanna 2003) and advection of heat (e.g. Stewart 2011). Wind speeds in the inertial sublayer provide the reference for wind-speed estimations closer to roughness elements (i.e. in the RSL), where additional corrections (e.g. Sect. 2.2.2) can inform wind energy predictions, building ventilation and pedestrian comfort.

Although observations from the three sites used in this work provide consistent findings, the generalisation of conclusions to other locations has additional uncertainty, especially if the urban surfaces are notably different. For example, London results can be treated as representative of other European cities but in locations with different surface characteristics (e.g. Ratti et al. 2002, their Table 1) the conclusions drawn may not hold. Locations with isolated or clusters of taller buildings may result in poorly represented area-averaged geometric parameters (Kanda et al. 2013). Furthermore, as roughness-element heights become larger compared to the UBL height, their effects may extend throughout the depth of the UBL (Sect. 2.1). Therefore, similar analysis as conducted in this work is required for a range of urban forms.

Wind-speed observations are critical to provide an independent assessment of method appropriateness. Remote sensing techniques (e.g. Doppler lidar) with profile capabilities are especially useful, given they permit UBL structure and flow characteristics to be explored in real conditions (e.g. Sect. 2.1). The focus of this work was where the flow is free from roughness-element wakes (i.e. the ISL), which was evaluated using turbulence data from high frequency observations. However, a lack of such observations means the UBL structure and expected validity of different wind-speed profile forms are typically related to H_{av} (e.g. the logarithmic profile becomes theoretically valid at the bottom of the ISL, the lower limit of which is typically assumed $2H_{av}$) (Sect. 2.2.2). The literature (e.g. Millward-Hopkins et al. 2011, Yang et al. 2016) and results from this work suggest other length scales (e.g. H_{max} and σ_H) may influence UCL, RSL

and ISL extents. Future systematic studies investigating the relation between these parameters and the UBL structure will therefore be valuable.

Physical (e.g. wind-tunnel) and numerical (e.g. CFD) experiments allow a wide variety of city forms to be investigated without limitations (e.g. siting) of real world observations. Systematic studies of simplified arrays have results which vary from more realistic heterogeneous geometries (e.g. Sect. 2.3), with the latter providing results with greater potential for interpretation of field experiments (as found throughout this work). Analysis of realistic geometries, with quantification of the effects of geometric simplifications (e.g. Bou-Zeid et al. 2009, Ricci et al. 2017) would be useful.

Progress towards considering geometric complexity was made in this work through developing a morphometric method to incorporate both buildings and vegetation. The method was assessed at two sites (urban park and suburban neighbourhood) and further assessment of the method will be valuable. Two optimisable parameters are required by the method, the vegetation aerodynamic porosity (P_{3D}) and drag coefficient (C_{DV}). The literature for these parameters is scarce (Sect. 5.2.2) and experiments are required to improve their understanding. Additionally, there is a lack of systematic studies that investigate the combined effect of built and porous roughness elements.

Comparisons between estimated and observed wind speeds were intentionally restricted to periods of neutral atmospheric stability in this work. In central London, strong wind-speed conditions corresponded to neutral atmospheric stability defined by surface layer scaling (Sect. 4.5.5). However, the extent to which this is true in other cities should be tested. Additionally, the analysis can be extended beyond neutral conditions, by comparing observations to wind-speed estimations which include stability corrections. The accuracy of wind-speed estimates using the Gryning et al. (2007) profile (Chapter 4) are promising for such comparisons, due to the profiles ability to consider the effects of atmospheric stability. Although estimates with the Deaves and Harris profile were similarly accurate, the profile is developed for strong winds only.

Errors in the assessed GDEMs demonstrate there is still scope for improving GDEM accuracy in urban environments. Therefore, there is potential for the development of alternative techniques for extracting urban morphology from GDEMs, such as progressive morphological filters (e.g. Geiß et al. 2015) or using combinations of different datasets (e.g. Sportouche et al. 2011, Darmanto et al. 2017, Xu et al. 2017, Wang et al. 2018). Errors also have the potential to be reduced through using DEMs with higher horizontal resolution, which are become

increasingly available. For example, TanDEM-X has the instrumental capacity to improve its operational horizontal resolution by a factor of two (from approximately 12 m to 6 m) (Wessel 2016). Additionally, the use of very high resolution (VHR) satellites and associated methodologies (e.g. tri-stereo imagery) have been demonstrated to perform well in urban areas (e.g. Perko et al. 2015, Panagiotakis et al. 2018). Unmanned aircraft remains a possible source of high resolution elevation data in the future (e.g. Colomina and Molina 2014, Feng et al. 2015).

Despite these numerous possibilities for improving urban DEM accuracy, a GDEM is currently unavailable from these sources. Additionally, more sophisticated methodologies for roughness-element extraction, using combinations of datasets, and high-resolution data, are all associated with larger computational cost (storage and processing). Therefore, the empirical corrections proposed to the TanDEM-X in this work provide a resource to swiftly estimate urban surface characteristics across large areas and are particularly useful in locations where no pre-existing information is available. The unique morphology of different cities and associated spatial variability of the TanDEM-X performance (e.g. Fig. 7.8) means that results cannot be generalised to other cities without additional uncertainty. Therefore, where benchmark data are available in other cities, the proposed corrections to TanDEM-X derived geometric parameters can be assessed and further insight to the land cover within the GUF and water mask provided. In combination, results will continue to inform parameters required for use in urban land surface models.

References

- Abdi D, Bitsuamlak GT (2014) Numerical evaluation of the effect of multiple roughness changes. *Wind and Structures* 19:585-601.
- Abrams M, Tsu H, Hulley G, Iwao K, Pieri D, Cudahy T, Kargel J (2015) The advanced spaceborne thermal emission and reflection radiometer (ASTER) after fifteen years: review of global products. *International Journal of Applied Earth Observation and Geoinformation* 38:292-301.
- Adrian RJ, Christensen KT, Liu ZC (2000) Analysis and interpretation of instantaneous turbulent velocity fields. *Experiments in Fluids* 29: 275-290.
- Akaike H (1974) A new look at the statistical model identification. *IEEE transactions on automatic control* 19:716-723.
- Al-Jiboori MH, Fei H (2005) Surface roughness around a 325-m meteorological tower and its effect on urban turbulence. *Advances in Atmospheric Sciences* 22:595-605.
- Allwine KJ, Shinn JH, Streit GE, Clawson KL, Brown M (2002) Overview of URBAN 2000: A multiscale field study of dispersion through an urban environment. *Bulletin of the American Meteorological Society* 83:521-536.
- Amiro B (1990) Drag coefficients and turbulence spectra within three boreal forest canopies. *Boundary-Layer Meteorology* 52:227-246.
- Andersson-Sköld Y, Thorsson S, Rayner D, Lindberg F, Janhäll S, Jonsson A, Moback U, Bergman R, Granberg M (2015) An integrated method for assessing climate-related risks and adaptation alternatives in urban areas. *Climate Risk Management* 7:31-50.
- Arnfield AJ (2003) Two decades of urban climate research: a review of turbulence, exchanges of energy and water, and the urban heat island. *International Journal of Climatology* 23:1-26.
- Arriga N, Rannik Ü, Aubinet M, Carrara A, Vesala T, Papale D (2017). Experimental validation of footprint models for eddy covariance CO₂ flux measurements above grassland by means of natural and artificial tracers. *Agricultural and Forest Meteorology* 242:75-84.
- AS/NZS (2002) Joint Technical Committee Australian/New Zealand Standard, Structural design actions, Part 2: wind actions. Standards Australia International Ltd, Sydney and Standards New Zealand, Wellington.

- ASTER GDEM Validation Team (2009) ASTER Global DEM Validation—Summary Report. METI & NASA 28 pp.
- Aubinet M, Grelle A, Ibrom A, Rannik U, Moncrieff J, Foken T, Kowalski AS, Martin PH, Berbigier P, Bernhofer C, Clement R (2000) Estimates of the annual net carbon and water exchange of forests: The EUROFLUX Methodology-X. *Advances in Ecological Research* 30:113-175.
- Auer S, Gernhardt S, Bamler R (2011) Ghost persistent scatterers related to multiple signal reflections. *IEEE Geoscience and Remote Sensing Letters*. 8:919-23.
- Baldocchi D (1997) Flux footprints within and over forest canopies. *Boundary-Layer Meteorology* 85:273-292.
- Barlow JF (2014) Progress in observing and modelling the urban boundary layer. *Urban Climate* 10:216-240.
- Barlow JF, Coceal O (2009) A review of urban roughness sublayer turbulence. UK Met Office Technical Report no. 527, 68 pp.
- Barlow JF, Dobre A, Smalley R, Arnold S, Tomlin A, Belcher SE (2009) Referencing of street-level flows measured during the DAPPLE 2004 campaign. *Atmospheric Environment* 43:5536-5544.
- Barlow JF, Dunbar T, Nemitz E, Wood CR, Gallagher M, Davies F, O'Connor E, Harrison R (2011) Boundary layer dynamics over London, UK, as observed using Doppler lidar during REPARTEE-II. *Atmospheric Chemistry and Physics* 11:2111-2125.
- Barlow JF, Halios CH, Lane S, Wood CR (2015) Observations of urban boundary layer structure during a strong urban heat island event. *Environmental Fluid Mechanics* 15:373-398.
- Barlow JF, Rooney G, von Hünenbein S, Bradley S (2008) Relating urban surface-layer structure to upwind terrain for the Salford Experiment (Salfex). *Boundary-Layer Meteorology* 127:173-191.
- Bates DM, Watts DG (1988) Nonlinear regression: iterative estimation and linear approximations. In: Bates DM, Watts DG (eds) *Nonlinear Regression Analysis and Its Applications*. Wiley, Hoboken, 365 pp.
- Belcher SE (2005) Mixing and transport in urban areas. *Philosophical Transactions of the Royal Society: Mathematical, Physical and Engineering Sciences* 363:2947-2968.

- Beljaars AC (1987) The measurement of gustiness at routine wind stations: a review. Royal Netherlands Meteorological Institute Special Report WR-87-11 (WMO Instruments and Methods of Observation Report. 31), 50 pp.
- Bitog J, Lee I, Hwang H, Shin M, Hong S, Seo I, Mostafa E, Pang Z (2011) A wind tunnel study on aerodynamic porosity and windbreak drag. *Forest Science and Technology* 7:8-16.
- Björkegren A, Grimmond CSB, Kotthaus S, Malamud B (2015) CO₂ emission estimation in the urban environment: Measurement of the CO₂ storage term. *Atmospheric Environment* 122:775-790.
- Blackadar AK, Tennekes H (1968) Asymptotic similarity in neutral barotropic planetary boundary layers. *Journal of the Atmospheric Sciences* 25:1015-1020.
- Bottema M (1993) Wind climate and urban geometry. PhD. thesis, Eindhoven University of Technology, The Netherlands.
- Bottema M (1995) Aerodynamic roughness parameters for homogenous building groups - Part 2: Results. Ecole Centrale de Nantes, France Document SUB-MESO #23, 80 pp.
- Bottema M (1997) Urban roughness modelling in relation to pollutant dispersion. *Atmospheric Environment* 31:3059-3075.
- Bottema M, Mestayer PG (1998) Urban roughness mapping-validation techniques and some first results. *Journal of Wind Engineering and Industrial Aerodynamics* 74:163-173.
- Bou-Zeid E, Overney J, Rogers BD, Parlange MB (2009) The effects of building representation and clustering in large-eddy simulations of flows in urban canopies. *Boundary-layer Meteorology* Sep 132:415-436.
- R, Hanna S (2003) Flow and dispersion in urban areas. *Annual Review of Fluid Mechanics* 35:469-496.
- Bürgmann R, Rosen PA, Fielding EJ (2000) Synthetic aperture radar interferometry to measure Earth's surface topography and its deformation. *Annual Review of Earth and Planetary Sciences* 28:169-209.
- Businger JA, Wyngaard JC, Izumi Y, Bradley EF (1971) Flux-profile relationships in the atmospheric surface layer. *Journal of the Atmospheric Sciences* 28:181-189.
- Castro IP (2009) Turbulent flow over rough walls. In: Eckhardt B (eds) *Advances in Turbulence XII*. Springer Proceedings in Physics, vol 132. Springer, Berlin, Heidelberg, pp. 381-388.

- Castro IP (2017) Are Urban-Canopy Velocity Profiles Exponential? *Boundary-Layer Meteorology* 164: 337–351.
- Castro IP, Cheng H, Reynolds R (2006) Turbulence over urban-type roughness: deductions from wind-tunnel measurements. *Boundary-Layer Meteorology* 118:109-131.
- Çengel YA, Cimbala JM (2014) *Fluid mechanics fundamentals and applications* (3rd ed.). McGraw-Hill, New York, 983 pp.
- Chang S, Huynh G (2007) A comparison of roughness parameters for Oklahoma City from different evaluation methods. *AMS 7th Symposium on the Urban Environment* 9.2. Available:
https://ams.confex.com/ams/7Coastal7Urban/techprogram/paper_126674.htm
- Chen F, Kusaka H, Bornstein R, Ching J, Grimmond CSB, Grossman-Clarke S, Loridan T, Manning KW, Martilli A, Miao S, Sailor D (2011) The integrated WRF/urban modelling system: development, evaluation, and applications to urban environmental problems. *International Journal of Climatology* 31:273-288.
- Chen Y, Su W, Li J, Sun Z (2009) Hierarchical object oriented classification using very high resolution imagery and LIDAR data over urban areas. *Advances in Space Research* 43:1101-1110.
- Cheng H, Castro IP (2002) Near wall flow over urban-like roughness. *Boundary-Layer Meteorology* 104:229-259.
- Cheng H, Hayden P, Robins A, Castro I (2007) Flow over cube arrays of different packing densities. *Journal of Wind Engineering and Industrial Aerodynamics* 95:715-740.
- Cheng WC, Porté-Agel F (2015) Adjustment of turbulent boundary-layer flow to idealized urban surfaces: a large-eddy simulation study. *Boundary-Layer Meteorology* 155:249-270.
- Choi T, Hong J, Kim J, Lee H, Asanuma J, Ishikawa H, Tsukamoto O, Zhiqiu G, Ma Y, Ueno K, Wang J (2004) Turbulent exchange of heat, water vapour, and momentum over a Tibetan prairie by eddy covariance and flux variance measurements. *Journal of Geophysical Research: Atmospheres* 109(D21).
- Christen A (2005) Atmospheric turbulence and surface energy exchange in urban environments: results from the Basel Urban Boundary Layer Experiment (BUBBLE). Atmospheric turbulence and surface energy exchange in urban environments: results from the Basel Urban Boundary Layer Experiment (BUBBLE). PhD. thesis, Department of Science, University of Basel, Switzerland.

- Claus J, Coceal O, Thomas TG, Branford S, Belcher S, Castro IP (2012) Wind-direction effects on urban-type flows. *Boundary-Layer Meteorology* 142:265-287.
- Cleveland WS (1979) Robust locally weighted regression and smoothing scatterplots. *Journal of the American statistical association* 74:829-836.
- Coceal O, Belcher SE (2004) A canopy model of mean winds through urban areas. *Quarterly Journal of the Royal Meteorological Society* 130:1349-1372.
- Coceal O, Dobre A, Thomas TG, Belcher SE (2007) Structure of turbulent flow over regular arrays of cubical roughness. *Journal of Fluid Mechanics* 589:375-409.
- Coceal O, Thomas TG, Castro IP, Belcher SE (2006) Mean flow and turbulence statistics over groups of urban-like cubical obstacles. *Boundary-Layer Meteorology* 121:491-519.
- Colomina I, Molina P (2014) Unmanned aerial systems for photogrammetry and remote sensing: A review. *ISPRS Journal of Photogrammetry and Remote Sensing* 92:79-97.
- Cook NJ (1985) The designer's guide to wind loading of building structures, Part I: Background, damage survey, wind data and structure classification, Building Research Establishment Report, Butterworths, London, 371 pp.
- Cook NJ (1997) The Deaves and Harris ABL model applied to heterogeneous terrain. *Journal of Wind Engineering and Industrial Aerodynamics* 66:197-214.
- Counihan J (1971) Wind tunnel determination of the roughness length as a function of the fetch and the roughness density of three-dimensional roughness elements. *Atmospheric Environment* (1967) 5:637-642.
- Counihan J (1975) Adiabatic atmospheric boundary layers: a review and analysis of data from the period 1880–1972. *Atmospheric Environment* (1967) 9:871-905.
- Coutts AM, White EC, Tapper NJ, Beringer J, Livesley SJ (2016) Temperature and human thermal comfort effects of street trees across three contrasting street canyon environments. *Theoretical and Applied Climatology* 124:55-68.
- Crawford B, Grimmond CSB, Gabey A, Marconcini M, Ward HC, Kent CW (2018) Variability of urban surface temperatures and implications for aerodynamic energy exchange in cities. In Review.
- Crawford B, Krayenhoff ES, Cordy P (2016) The urban energy balance of a lightweight low-rise neighborhood in Andacollo, Chile. *Theoretical and Applied Climatology* Oct:1-14.

- Crow P, Benham S, Devereux B, Amable G (2007) Woodland vegetation and its implications for archaeological survey using LiDAR. *Forestry* 80:241-252.
- CTBUH (2017) Council on Tall Buildings and Urban Habitat. Height calculator. Available: <http://www.ctbuh.org/TallBuildings/HeightStatistics/HeightCalculator/tabid/1007/language/en-GB/Default.aspx>, accessed: March 2017.
- da Costa JL, Castro F, Palma J, Stuart P (2006) Computer simulation of atmospheric flows over real forests for wind energy resource evaluation. *Journal of Wind Engineering and Industrial Aerodynamics* 94:603-620.
- Darmanto NS, Varquez AC, Kanda M (2017) Urban roughness parameters estimation from globally available datasets for mesoscale modeling in megacities. *Urban Climate* 21:243-261.
- Davenport A (1960) Wind loads on structures. Technical paper No. 88, Division of Building Research, National Research Council of Canada, Ottawa, Canada.
- Day MA (1990) The no-slip condition of fluid dynamics. *Erkenntnis* 33:285-296.
- Day SD, Wiseman EP, Dickinson SB, Harris RJ (2010) Tree root ecology in the urban environment and implications for a sustainable rhizosphere. *Arboriculture & Urban Forestry* 36:193-204.
- De Bruin HAR, Verhoef A (1999) Reply to the Comments on 'a new Method to Determine the Zero-Plane Displacement', by Zhang and Park. *Boundary-Layer Meteorology* 91:141-143.
- De Bruin HAR, Kohsiek W, Van Den Hurk BJM (1993) A verification of some methods to determine the fluxes of momentum, sensible heat, and water vapour using standard deviation and structure parameter of scalar meteorological quantities. *Boundary-Layer Meteorology* 63:231-257.
- De Ridder K (2010) Bulk transfer relations for the roughness sublayer. *Boundary-Layer Meteorology* 134:257-267.
- Deaves D (1981) Computations of wind flow over changes in surface roughness. *Journal of Wind Engineering and Industrial Aerodynamics* 7:65-94.
- Deaves D, Harris R (1978) A mathematical model of the structure of strong winds. Construction Industry Research and Information Association Report number 76, London, England.
- Drew D, Barlow J, Cockerill T (2013a) Estimating the potential yield of small wind turbines in urban areas: A case study for Greater London, UK. *Journal of Wind Engineering and Industrial Aerodynamics* 115:104-111.

- Drew DR, Barlow JF, Lane SE (2013b) Observations of wind speed profiles over Greater London, UK, using a Doppler lidar. *Journal of Wind Engineering and Industrial Aerodynamics* 121:98-105.
- Dyer AJ (1974) A review of flux-profile relationships. *Boundary-Layer Meteorology* 7:363-372.
- Eckert S, Hollands T (2010) Comparison of automatic DSM generation modules byprocessing IKONOS stereo data of an urban area. *IEEE Journal of Selected Topics in Applied Earth Observations and Remote Sensing* 3:162–167.
- Elliott WP (1958) The growth of the atmospheric internal boundary layer. *Eos, Transactions American Geophysical Union* 39:1048-1054.
- Emeis S (2004) Vertical wind profiles over an urban area. *Meteorologische Zeitschrift* 13:353-359.
- Emeis S (2014) Current issues in wind energy meteorology. *Meteorological Applications* 21:803-819.
- Emeis S, Baumann-Stanzer K, Piringer M, Kallistratova M, Kouznetsov R, Yushkov V (2007) Wind and turbulence in the urban boundary layer—analysis from acoustic remote sensing data and fit to analytical relations. *Meteorologische Zeitschrift* 16:393-406.
- Emeis S, Schäfer K, Münkel C (2008) Surface-based remote sensing of the mixing-layer height—a review. *Meteorologische Zeitschrift* 17:621-630.
- Emejamara F, Tomlin A, Millward-Hopkins J (2015) Urban wind: Characterisation of useful gust and energy capture. *Renewable Energy* 81:162-172.
- Esch T, Heldens W, Hirner A, Keil M, Marconcini M, Roth A, Zeidler J, Dech S, Strano E (2017) Breaking new ground in mapping human settlements from space – The Global Urban Footprint. *ISPRS Journal of Photogrammetry and Remote Sensing* 134:30-42
- Esch T, Marconcini M, Felbier A, Roth A, Heldens W, Huber M, Schwinger M, Taubenböck H, Müller A, Dech S (2013) Urban footprint processor—Fully automated processing chain generating settlement masks from global data of the TanDEM-X mission. *IEEE Geoscience and Remote Sensing Letters* 10:1617-1621.
- Esch T, Schenk A, Ullmann T, Thiel M, Roth A, Dech S (2011) Characterization of Land Cover Types in TerraSAR-X Images by Combined Analysis of Speckle Statistics and Intensity Information. *IEEE Transactions on Geoscience and Remote Sensing* 49:1911-1925

- ESDU (Engineering Sciences Data Unit) (2002) Data Item 82026: Strong winds in the atmospheric boundary layer, Part 1: hourly-mean wind speeds, 55 pp.
- Etling D (2002) *Theoretische Meteorologie Eine Einführung*. Springer-Verlag, Berlin, Heidelberg, New York, 354 pp.
- Evans S (2009) *3D Cities and Numerical Weather Prediction Models: an Overview of the Methods Used in the LUCID Project*. UCL Centre for Advanced Spatial Analysis, London.
- Fang C, Sill B (1992) Aerodynamic roughness length: Correlation with roughness elements. *Journal of Wind Engineering and Industrial Aerodynamics* 41:449-460.
- Farr TG, Kobrick M (2000) Shuttle Radar Topography Mission produces a wealth of data. *Eos, Transactions American Geophysical Union* 81:583-585.
- Farr TG, Rosen PA, Caro E, Crippen R, Duren R, Hensley S, Kobrick M, Paller M, Rodriguez E, Roth L (2007) The shuttle radar topography mission. *Reviews of Geophysics* 45:2005RG000183.
- Feddersen B (2005) *Wind tunnel modelling of turbulence and dispersion above tall and highly dense urban roughness* PhD. thesis, Swiss Federal Institute of Technology, Zurich, Switzerland.
- Feigenwinter C, Vogt R, Parlow E (1999) Vertical structure of selected turbulence characteristics above an urban canopy. *Theoretical and Applied Climatology* 62:51-63.
- Feng Q, Liu J, Gong J (2015) UAV remote sensing for urban vegetation mapping using random forest and texture analysis. *Remote Sensing* 7:1074-1094.
- Fernando H (2010) Fluid dynamics of urban atmospheres in complex terrain. *Annual Review of Fluid Mechanics* 42:365-389.
- Ferro A, Brunner D, Bruzzone L, Lemoine G (2011) On the relationship between double bounce and the orientation of buildings in VHR SAR images. *IEEE Geoscience and Remote Sensing Letters*. 8:612-616.
- Finnigan J (2000) Turbulence in plant canopies. *Annual Review of Fluid Mechanics* 32:519-571.
- Fisher PF, Tate NJ (2006) Causes and consequences of error in digital elevation models. *Progress in Physical Geography* 30:467-489.
- Foken T (2006) 50 years of the Monin–Obukhov similarity theory. *Boundary-Layer Meteorology* 119:431-447.

- Foken T, Wichura B (1996) Tools for quality assessment of surface-based flux measurements. *Agricultural and Forest Meteorology* 78:83-105.
- Fortuniak K, Pawlak W, Siedlecki M (2013) Integral turbulence statistics over a central European city centre. *Boundary-Layer Meteorology* 146:257-276.
- Frehlich R, Meillier Y, Jensen ML, Balsley B, Sharman R (2006) Measurements of boundary layer profiles in an urban environment. *Journal of Applied Meteorology and Climatology* 45:821-837.
- Fujisada H, Urai M, Iwasaki A (2012) Technical methodology for ASTER global DEM. *IEEE Transactions on Geoscience and Remote Sensing* 50:3725-3736.
- Gál T, Unger J (2009) Detection of ventilation paths using high-resolution roughness parameter mapping in a large urban area. *Building and Environment* 44:198-206.
- Gamba P, Dell'Acqua F, Houshmand B (2002) SRTM data characterization in urban areas. *International Archives of Photogrammetry Remote Sensing and Spatial Information Sciences* 34:55-58.
- Gamba P, Dell'Acqua F, Dasarathy BV (2005) Urban remote sensing using multiple data sets: Past, present, and future. *Information Fusion* 6:319-26.
- Gamba P, Dell'Acqua F, Houshmand B (2003) Comparison and fusion of LIDAR and InSAR digital elevation models over urban areas. *International Journal of Remote Sensing* 24:4289-4300.
- Garratt JR (1990) The internal boundary layer—a review. *Boundary-Layer Meteorology* 50:171-203.
- Garratt JR (1992) *The atmospheric boundary layer*. Cambridge atmospheric and space science series. Cambridge University Press, Cambridge, 444 pp.
- Garratt JR (1994) The atmospheric boundary layer. *Earth-Science Reviews* 37:89-134.
- Garratt JR, Hicks BB (1990) Micrometeorological and PBL experiments in Australia. *Boundary-Layer Meteorology* 50:11-29.
- Garuma GF (2017) Review of urban surface parameterizations for numerical climate models. *Urban Climate*, DOI: <https://doi.org/10.1016/j.uclim.2017.10.006>
- Ge Y, Cao S, Jin X (2013) Comparison and harmonization of building wind loading codes among the Asia-Pacific Economies. *Frontiers of Structural and Civil Engineering* 7:402-410.

- Geiß C, Wurm M, Breunig M, Felbier A, Taubenböck H (2015) Normalization of TanDEM-X DSM data in urban environments with morphological filters. *IEEE Transactions on Geoscience and Remote Sensing* 53:4348-4362.
- Geosampa (2017) Mapa Digital da Cidade de São Paulo – Digital Map of São Paulo City. Available: http://geosampa.prefeitura.sp.gov.br/PaginasPublicas/_SBC.aspx, accessed March 2017.
- Gill SE, Handley JF, Ennos AR, Pauleit S (2007) Adapting cities for climate change: the role of the green infrastructure. *Built Environment* 33:115-133.
- Gillies J, Lancaster N, Nickling W, Crawley D (2000) Field determination of drag forces and shear stress partitioning effects for a desert shrub (*Sarcobatus vermiculatus*, greasewood). *Journal of Geophysical Research: Atmospheres* 105:24871-24880.
- Gillies J, Nickling W, King J (2002) Drag coefficient and plant form response to wind speed in three plant species: Burning Bush (*Euonymus alatus*), Colorado Blue Spruce (*Picea pungens glauca.*), and Fountain Grass (*Pennisetum setaceum*). *Journal of Geophysical Research: Atmospheres* 107:4760.
- Giometto M, Christen A, Meneveau C, Fang J, Krafczyk M, Parlange M (2016) Spatial characteristics of roughness sublayer mean flow and turbulence over a realistic urban surface. *Boundary-Layer Meteorology* 160:425-452.
- Giometto MG, Christen A, Egli PE, Schmid MF, Tooke RT, Coops NC, Parlange MB (2017) Effects of trees on mean wind, turbulence and momentum exchange within and above a real urban environment. *Advances in Water Resources* 106:154-168.
- Göckede M, Markkanen T, Mauder M, Arnold K, Leps JP, Foken T (2005) Validation of footprint models using natural tracer measurements from a field experiment. *Agricultural and forest meteorology* 135:314-325.
- Goodwin NR, Coops NC, Tooke TR, Christen A, Voogt JA (2009) Characterizing urban surface cover and structure with airborne lidar technology. *Canadian Journal of Remote Sensing* 35:297-309.
- Grant P, Nickling W (1998) Direct field measurement of wind drag on vegetation for application to windbreak design and modelling. *Land Degradation and Development* 9:57-66.
- Grimmond C, Souch C (1994) Surface description for urban climate studies: a GIS based methodology. *Geocarto International* 9:47-59.

- Grimmond CSB, Blackett M, Best M, Barlow J, Baik J, Belcher S, Bohnenstengel S, Calmet I, Chen F, Dandou A, Fortuniak K, Gouvea ML, Hamdi R, Hendry M, Kawai T, Kawamoto Y, Kondo H, Krayenhoff ES, Lee SH, Loridan T, Martilli A, Masson V, Miao S, Oleson K, Pigeon G, Porson A, Ryu YH, Salamanca F, Shashua-Bar L, Steeneveld GJ, Tombrou M, Voogt JA, Young DT, Zhang N (2010) The international urban energy balance models comparison project: first results from phase 1. *Journal of Applied Meteorology and Climatology* 49:1268-1292.
- Grimmond CSB, Blackett M, Best MJ, Baik JJ, Belcher SE, Beringer J, Bohnenstengel SI, Calmet I, Chen F, Coutts A, Dandou A, Fortuniak K, Gouvea ML, Hamdi R, Hendry M, Kanda M, Kawai T, Kawamoto Y, Kondo H, Krayenhoff ES, Lee SH, Loridan T, Martilli A, Masson V, Miao S, Oleson K, Ooka R, Pigeon G, Porson A, Ryu YH, Salamanca F, Shashua-Bar L, Steeneveld GJ, Tombrou M, Voogt JA, Young DT, Zhang N (2011) Initial results from Phase 2 of the international urban energy balance model comparison. *International Journal of Climatology* 31:244-72.
- Grimmond CSB, King TS, Roth M, Oke TR (1998) Aerodynamic roughness of urban areas derived from wind observations. *Boundary-Layer Meteorology* 89:1-24.
- Grimmond CSB, Oke TR (1999) Aerodynamic properties of urban areas derived from analysis of surface form. *Journal of Applied Meteorology and Climatology* 38:1262-1292.
- Grimmond CSB, Salmond J, Offerle BD, Oke TR (2002) Local-scale surface flux measurements at a downtown site in Marseille during the ESCOMPTE field campaign, in *Proceedings, 4th Conference on Urban Environment, Norfolk, U.S.A., 20–24 May 2002*, American Meteorological Society, Boston, MA, pp. 21–22.
- Grimmond CSB, Salmond J, Oke TR, Offerle B, Lemonsu A (2004) Flux and turbulence measurements at a densely built-up site in Marseille: Heat, mass (water and carbon dioxide), and momentum. *Journal of Geophysical Research: Atmospheres* 109:D24101.
- Gromke C, Ruck B (2009) On the impact of trees on dispersion processes of traffic emissions in street canyons. *Boundary-Layer Meteorology* 131:19-34.
- Gruber A, Wessel B, Huber M, Roth A (2012) Operational TanDEM-X DEM calibration and first validation results. *ISPRS journal of photogrammetry and remote sensing* 73:39-49.
- Gryning S, Batchvarova E, Brümmner B, Jørgensen H, Larsen S (2007) On the extension of the wind profile over homogeneous terrain beyond the surface boundary layer. *Boundary-Layer Meteorology* 124:251-268.

- Gryning S, Batchvarova E, Quante M, Matthias V (2011) Evaluation of vertical profiles in mesoscale meteorological models based on observations for the COST728 study of winter 2003 PM episodes in Europe. In: Steyn DG, Castelli ST (eds) *Air Pollution Modeling and its Application XXI*. Springer, Dordrecht, pp. 499-503.
- Guan D, Ting-Yao Z, Shi-Jie H (2000) Wind tunnel experiment of drag of isolated tree models in surface boundary layer. *Journal of Forestry Research* 11:156-160
- Guan D, Zhang Y, Zhu T (2003) A wind-tunnel study of windbreak drag. *Agricultural and Forest Meteorology* 118:75-84.
- Guan D, Zhu T, Han S (2000) Wind tunnel experiment of drag of isolated tree models in surface boundary layer. *Journal of Forestry Research* 11:156-160
- Guan W, Li C, Li S, Fan Z, Xie C (2002) Improvement and application of digitized measure on shelterbelt porosity. *Journal of Applied Ecology* 13: 651-657.
- Guth P. (2010) Geomorphometric comparison of ASTER GDEM and SRTM. Joint Symposium of ISPRS Technical Commission IV, Orlando, FL, USA, 10 pp.
- Hagen L, Skidmore E (1971) Windbreak drag as influenced by porosity. *Transactions of the American Society of Agricultural Engineers* 14:464-465.
- Hagishima A, Tanimoto J, Nagayama K, Meno S (2009) Aerodynamic parameters of regular arrays of rectangular blocks with various geometries. *Boundary-Layer Meteorology* 132:315-337.
- Hall D, Macdonald JR, Walker S, Spanton AM (1996) Measurements of dispersion within simulated urban arrays—a small scale wind tunnel study, BRE Client Report, CR178/96.
- Harman I, Finnigan J (2007) A simple unified theory for flow in the canopy and roughness sublayer. *Boundary-Layer Meteorology* 123:339-363.
- Harris RI, Deaves DM (1980) The structure of strong winds, paper no. 4. In: *Proceedings of the CIRIA Conference, London, 12–13 November 1980, Construction Industry Research and Information Association, 6 Storey's Gate, London SW1P 3AU*.
- Heaviside C, Cai X, Vardoulakis S (2015) The effects of horizontal advection on the urban heat island in Birmingham and the West Midlands, United Kingdom during a heatwave. *Quarterly Journal of the Royal Meteorological Society* 141:1429-1441.
- Hebeler F, Purves RS (2009) The influence of elevation uncertainty on derivation of topographic indices. *Geomorphology* 111:4-16.

- Heidbach K, Schmid HP, Mauder M (2017) Experimental evaluation of flux footprint models. *Agricultural and Forest Meteorology* 246:142-153.
- Heisler GM (1984) Measurements of solar radiation in the shade of individual trees. In: Hutchinson BA, Hicks BB (eds) *The Forest-Atmosphere interaction*. Springer, Netherlands, pp 319 - 355.
- Heisler GM, Dewalle DR (1988) Effects of windbreak structure on wind flow. *Agriculture, Ecosystems & Environment* 22:41-69.
- Hirt C (2015) Digital terrain models. *Encyclopedia of Geodesy*. Springer, Switzerland, 6 pp.
- Hirt C, Filmer M, Featherstone W (2010) Comparison and validation of the recent freely available ASTER-GDEM ver1, SRTM ver4. 1 and GEODATA DEM-9S ver3 digital elevation models over Australia. *Australian Journal of Earth Sciences* 57:337-347.
- Ho YK, Liu CH (2017) A wind tunnel study of flows over idealised urban surfaces with roughness sublayer corrections. *Theoretical and Applied Climatology* 130:305-320.
- Hofton M, Dubayah R, Blair JB, Rabine D (2006) Validation of SRTM elevations over vegetated and non-vegetated terrain using medium footprint lidar. *Photogrammetric Engineering & Remote Sensing* 72:279-285.
- Högström U (1988) Non-dimensional wind and temperature profiles in the atmospheric surface layer: A re-evaluation. *Boundary-Layer Meteorology* 42:55-78.
- Högström U (1996) Review of some basic characteristics of the atmospheric surface layer. *Boundary-Layer Meteorology* 78:215–246
- Holland DE, Berglund JA, Spruce JP, McKellip RD (2008) Derivation of effective aerodynamic surface roughness in urban areas from airborne lidar terrain data. *Journal of Applied Meteorology and Climatology* 47:2614-2626.
- Hong J, Kim J, Byun Y (2012) Uncertainty in carbon exchange modelling in a forest canopy due to kB^{-1} parameterizations. *Quarterly Journal of the Royal Meteorological Society* 138:699-706.
- Hong J, Kwon H, Lim J, Byun Y, Lee J, Kim J (2009) Standardization of KoFlux eddy-covariance data processing. *Korean Journal of Agricultural and Forest Meteorology* 11:19-26.
- Hsieh C, Katul GG, Schieldge J, Sigmon J, Knoerr KR (1996) Estimation of Momentum and Heat Fluxes Using Dissipation and Flux-Variance Methods in the Unstable Surface Layer. *Water Resources Research* 32:2453-2462.

- Ioannidis C, Xinogalas E, Soile S (2014) Assessment of the global digital elevation models ASTER and SRTM in Greece. *Survey Review* 46:342-354.
- Irwin JS (1979) A theoretical variation of the wind profile power-law exponent as a function of surface roughness and stability. *Atmospheric Environment* 13:191-194.
- Ishugah T, Li Y, Wang R, Kiplagat J (2014) Advances in wind energy resource exploitation in urban environment: A review. *Renewable and Sustainable Energy Reviews* 37:613-626.
- Jachner S, Van den Boogaart G, Petzoldt T (2007) Statistical methods for the qualitative assessment of dynamic models with time delay (R Package qualV). *Journal of Statistical Software*, 22: 1-30.
- Jackson P (1981) On the displacement height in the logarithmic velocity profile. *Journal of Fluid Mechanics* 111:15-25.
- Jacobs AF (1985) The normal-force coefficient of a thin closed fence. *Boundary-Layer Meteorology* 32:329-335.
- Jiang D, Jiang W, Liu H, Sun J (2008) Systematic influence of different building spacing, height and layout on mean wind and turbulent characteristics within and over urban building arrays. *Wind and Structures* 11:275-289.
- Jiménez J (2004) Turbulent flows over rough walls. *Annual Review of Fluid Mechanics* 36:173-196.
- Judd M, Raupach M, Finnigan J (1996) A wind tunnel study of turbulent flow around single and multiple windbreaks, part I: velocity fields. *Boundary-Layer Meteorology* 80:127-165.
- Kaimal JC, Finnigan JJ (1994) *Atmospheric boundary layer flows: their structure and measurement*. Oxford University Press, Oxford, 289 pp.
- Kanda M (2006) Large-eddy simulations on the effects of surface geometry of building arrays on turbulent organized structures. *Boundary-Layer Meteorology* 118:151-168.
- Kanda M, Inagaki A, Miyamoto T, Gryschka M, Raasch S (2013) A new aerodynamic parametrization for real urban surfaces. *Boundary-Layer Meteorology* 148:357-377.
- Kanda M, Kanega M, Kawai T, Moriwaki R, Sugawara H (2007) Roughness lengths for momentum and heat derived from outdoor urban scale models. *Journal of Applied Meteorology and Climatology* 46:1067-1079.

- Kanda M, Moriwaki R, Kasamatsu F (2004) Large-eddy simulation of turbulent organized structures within and above explicitly resolved cube arrays. *Boundary-Layer Meteorology* 112:343-368.
- Kanda M, Moriwaki R, Roth M, Oke TR (2002) Area-averaged sensible heat flux and a new method to determine zero-plane displacement length over an urban surface using scintillometry. *Boundary-Layer Meteorology* 105:177-193.
- Kastner-Klein P, Rotach MW (2004) Mean flow and turbulence characteristics in an urban roughness sublayer. *Boundary-Layer Meteorology* 111:55-84.
- Katul GG, Mahrt L, Poggi D, Sanz C (2004) One-and two-equation models for canopy turbulence. *Boundary-Layer Meteorology* 113:81-109.
- Kent CW, Grimmond CSB, Barlow J, Gatey D, Kotthaus S, Lindberg F, Halios CH (2017a) Evaluation of Urban Local-Scale Aerodynamic Parameters: Implications for the Vertical Profile of Wind Speed and for Source Areas. *Boundary-Layer Meteorology* 164:183-213.
- Kent CW, Grimmond CSB, Gatey D (2017b) Aerodynamic roughness parameters in cities: Inclusion of vegetation. *Journal of Wind Engineering and Industrial Aerodynamics* 169:168-176.
- Kent CW, Grimmond CSB, Gatey D, Barlow JF (2018a) Assessing methods to extrapolate the vertical wind-speed profile from surface observations in a city centre during strong winds. *Journal of Wind Engineering & Industrial Aerodynamics* 173:100-111.
- Kent CW, Lee K, Ward HC, Hong JW, Hong J, Gatey D, Grimmond CSB (2017c) Aerodynamic roughness variation with vegetation: Analysis in a suburban neighbourhood and a city park. *Urban Ecosystems*, DOI: <https://doi.org/10.1007/s11252-017-0710-1>
- Kent CW, Grimmond CSB, Gatey D, Hirano K (2018b) Urban morphology parameters from global digital elevation models: implications for aerodynamic roughness and for wind-speed estimation. Submitted to *Remote Sensing of Environment*, 4 Jan 2018.
- Kljun N, Calanca P, Rotach M, Schmid H (2015) A simple two-dimensional parameterisation for Flux Footprint Prediction (FFP). *Geoscientific Model Development* 8:3695-3713.
- Koizumi A, Motoyama J, Sawata K, Sasaki Y, Hirai T (2010) Evaluation of drag coefficients of poplar-tree crowns by a field test method. *Journal of Wood Science* 56:189-193.
- Kondo J, Yamazawa H (1986) Aerodynamic roughness over an inhomogeneous ground surface. *Boundary-Layer Meteorology* 35:331-348.

- Kormann R, Meixner FX (2001) An analytical footprint model for non-neutral stratification. *Boundary-Layer Meteorology* 99:207-224.
- Kotthaus S, Grimmond CSB (2012) Identification of micro-scale anthropogenic CO₂, heat and moisture sources—processing eddy covariance fluxes for a dense urban environment. *Atmospheric Environment* 57:301-316.
- Kotthaus S, Grimmond CSB (2014a) Energy exchange in a dense urban environment—Part I: Temporal variability of long-term observations in central London. *Urban Climate* 10:261-280.
- Kotthaus S, Grimmond CSB (2014b) Energy exchange in a dense urban environment—Part II: Impact of spatial heterogeneity of the surface. *Urban Climate* 10:281-307.
- Kotthaus S, Grimmond CSB (2017) Characterising London's urban boundary layer based on Ceilometer observations, In preparation.
- Kraus K, Pfeifer N (2001) Advanced DTM generation from LIDAR data. *International Archives Of Photogrammetry Remote Sensing And Spatial Information Sciences* 34:23-30.
- Krayenhoff E, Santiago J, Martilli A, Christen A, Oke T (2015) Parametrization of drag and turbulence for urban neighbourhoods with trees. *Boundary-Layer Meteorology* 156:157-189.
- Kremer P, Andersson E, McPhearson T, Elmqvist T (2015) Advancing the frontier of urban ecosystem services research. *Ecosystem Services* 12:149-151.
- Krieger G, Moreira A, Fiedler H, Hajnsek I, Werner M, Younis M, Zink M (2007) TanDEM-X: A satellite formation for high-resolution SAR interferometry. *IEEE Transactions on Geoscience and Remote Sensing* 45:3317-3341.
- Kustas WP, Blanford JH, Stannard DI, Daughtry CS, Nichols WD, Weltz MA (1994) Local energy flux estimates for unstable conditions using variance data in semiarid rangelands. *Water Resources Research* 30:1351-1361.
- Kutzbach JE (1961) Investigations of the modification of wind profiles by artificially controlled surface roughness. Msc. Thesis, Department of Meteorology, University of Wisconsin-Madison, USA.
- Landry SM, Chakraborty J (2009) Street trees and equity: evaluating the spatial distribution of an urban amenity. *Environment and Planning A* 41:2651-2670.

- Lane S, Barlow JF, Wood CR (2013) An assessment of a three-beam Doppler lidar wind profiling method for use in urban areas. *Journal of Wind Engineering and Industrial Aerodynamics* 119:53-59.
- Leckebusch GC, Ulbrich U, Fröhlich L, Pinto JG (2007) Property loss potentials for European midlatitude storms in a changing climate. *Geophysical Research Letters* 34: L05703
- Leclerc MY, Foken T (2014) *Footprints in micrometeorology and ecology*. Springer, Berlin, 239 pp.
- Leclerc MY, Meskhidze N, Finn D (2003) Comparison between measured tracer fluxes and footprint model predictions over a homogeneous canopy of intermediate roughness. *Agricultural and Forest Meteorology* 117:145-158.
- Leclerc MY, Thurtell GW (1990) Footprint prediction of scalar fluxes using a Markovian analysis. *Boundary-Layer Meteorology* 52:247-258.
- Leonardi S, Castro IP (2010) Channel flow over large cube roughness: a direct numerical simulation study. *Journal of Fluid Mechanics* 651:519-539.
- Leonardi S, Orlandi P, Smalley RJ, Djenidi L, Antonia RA (2003) Direct numerical simulations of turbulent channel flow with transverse square bars on one wall. *Journal of Fluid Mechanics* 491:229-38.
- Lettau H (1957) Compilation of Richardson Numbers, Classification of Profiles and Determination of Roughness Parameters. In: Lettau HH, Davidson B (eds) *Exploring the Atmosphere's 1st Mile*, Pergamon Press, London, 376 pp.
- Lettau H (1969) Note on aerodynamic roughness-parameter estimation on the basis of roughness-element description. *Journal of Applied Meteorology and Climatology* 8:828-832.
- Li P, Shi C, Li Z, Muller J, Drummond J, Li X, Li T, Li Y, Liu J (2013) Evaluation of ASTER GDEM using GPS benchmarks and SRTM in China. *International Journal of Remote Sensing* 34:1744-1771.
- Li Q, Zhi L, Hu F (2010) Boundary layer wind structure from observations on a 325m tower. *Journal of Wind Engineering and Industrial Aerodynamics* 98:818-832.
- Lindberg F, Grimmond C (2011b) The influence of vegetation and building morphology on shadow patterns and mean radiant temperatures in urban areas: model development and evaluation. *Theoretical and applied climatology* 105:311-323.

- Lindberg F, Grimmond CSB (2011a) Nature of vegetation and building morphology characteristics across a city: influence on shadow patterns and mean radiant temperatures in London. *Urban Ecosystems* 14:617-634.
- Lindberg F, Grimmond CSB, Gabey A, Huang B, Kent CW, Sun T, Theeuwes NE, Järvi L, Ward HC, Capel-Timms I, Chang YY, Jonsson P, Krave N, Liu DW, Meyer D, Olofson KFG, Tan JG, Wästberg D, Xue L, Zhang Z (2018) Urban Multi-scale Environmental Predictor (UMEP): An integrated tool for city-based climate services. *Environmental Modelling & Software* 99:70-87.
- LINZ (2013) Land and information New Zealand. Available: <https://data.linz.govt.nz/>, accessed March 2017.
- Liu G, Sun J, Jiang W (2009) Observational verification of urban surface roughness parameters derived from morphological models. *Meteorological Applications* 16:205-213.
- Liu J, Gao Z, Wang L, Li Y, Gao CY (2017) The impact of urbanization on wind speed and surface aerodynamic characteristics in Beijing during 1991–2011. *Meteorology and Atmospheric Physics*. DOI: <https://doi.org/10.1007/s00703-017-0519-8>.
- Liu W, Ji C, Zhong J, Jiang X, Zheng Z (2007) Temporal characteristics of the Beijing urban heat island. *Theoretical and Applied Climatology* 87:213-221.
- Liu Y, Liu H, Wang L (2017) The vertical distribution characteristics of integral turbulence statistics in the atmospheric boundary layer over an urban area in Beijing. *Science China Earth Sciences* 60:1533-1545.
- Macdonald R (2000) Modelling the mean velocity profile in the urban canopy layer. *Boundary-Layer Meteorology* 97:25-45.
- Macdonald R, Griffiths R, Hall D (1998) An improved method for the estimation of surface roughness of obstacle arrays. *Atmospheric Environment* 32:1857-1864.
- Macdonald RW, Carter S, Slawson PR (2000) Measurements of mean velocity and turbulence statistics in simple obstacle arrays at 1:200 scale. Department of Mechanical Engineering, University of Waterloo, Thermal Fluids Report 2000-1.
- Mahrt L (1998) Nocturnal boundary-layer regimes. *Boundary-Layer Meteorology* 88:255-278.
- Mahrt L (2000) Surface heterogeneity and vertical structure of the boundary layer. *Boundary-Layer Meteorology* 96:33-62.

- Maktav D, Erbek F, Jürgens C (2005) Remote sensing of urban areas. *International Journal of Remote Sensing* 26:655-659.
- Marconcini M, Marmanis D, Esch T, Felbier A. (2014) A novel method for building height estimation using TanDEM-X data. *Proceedings of the 2014 IEEE International Geoscience and Remote Sensing Symposium (IGARSS)*, Quebec City, QC, Canada, pp. 4804-4807.
- Martano P (2000) Estimation of surface roughness length and displacement height from single-level sonic anemometer data. *Journal of Applied Meteorology and Climatology* 39: 708-715.
- Martilli A (2002) Numerical study of urban impact on boundary layer structure: Sensitivity to wind speed, urban morphology, and rural soil moisture. *Journal of Applied Meteorology* 41:1247-1266.
- Mavrogianni A, Davies M, Taylor J, Chalabi Z, Biddulph P, Oikonomou E, Das P, Jones B (2014) The impact of occupancy patterns, occupant-controlled ventilation and shading on indoor overheating risk in domestic environments. *Building and Environment* 78:183-198.
- Mayhead G (1973) Some drag coefficients for British forest trees derived from wind tunnel studies. *Agricultural Meteorology* 12:123-130.
- McMillen RT (1988) An eddy correlation technique with extended applicability to non-simple terrain. *Boundary-Layer Meteorology* 43:231-245.
- Mercer JB, Gill M (1998) Radar-Derived DEMs for Urban Areas. *International Archives of Photogrammetry and Remote Sensing* 32:382–388.
- Millward-Hopkins JT, Tomlin A, Ma L, Ingham D, Pourkashanian M (2013a) Aerodynamic parameters of a UK city derived from morphological data. *Boundary-Layer Meteorology* 146:447-468.
- Millward-Hopkins JT, Tomlin A, Ma L, Ingham D, Pourkashanian M (2013b) Assessing the potential of urban wind energy in a major UK city using an analytical model. *Renewable Energy* 60:701-710.
- Millward-Hopkins J, Tomlin A, Ma L, Ingham D, Pourkashanian M (2013c) Mapping the wind resource over UK cities. *Renewable Energy* 55:202-211.
- Millward-Hopkins J, Tomlin A, Ma L, Ingham D, Pourkashanian M (2012) The predictability of above roof wind resource in the urban roughness sublayer. *Wind Energy* 15:225-243.

- Millward-Hopkins J, Tomlin A, Ma L, Ingham D, Pourkashanian M (2011) Estimating aerodynamic parameters of urban-like surfaces with heterogeneous building heights. *Boundary-Layer Meteorology* 141:443-465.
- Miyake M (1965) Transformation of the Atmospheric Boundary Layer Over Inhomogeneous Surfaces. Scientific report, University of Washington, Seattle, 63 pp.
- Mohammad A, Zaki S, Hagishima A, Ali M (2015b) Determination of aerodynamic parameters of urban surfaces: methods and results revisited. *Theoretical and Applied Climatology* 3: 635-649.
- Mohammad AF, Zaki, SA, Ali MSM, Aya H, Razak AA, Shirakashi M, Arai N (2015a) Large Eddy Simulation of wind pressure distribution on heterogeneous buildings in idealised urban models. *Energy Procedia* 78:3055-3060.
- Moncrieff JB, Clement R, Finnigan J, Meyers T (2004) Averaging, detrending, and filtering of eddy covariance time series. In: Lee X, Massman W, Law B (eds) *Handbook of micrometeorology*. Springer, Netherlands, 250 pp.
- Moncrieff JB, Massheder JM, De Bruin H, Elbers J, Friborg T, Heusinkveld B, Kabat P, Scott S, Soegaard H, Verhoef A (1997) A system to measure surface fluxes of momentum, sensible heat, water vapour and carbon dioxide. *Journal of Hydrology* 188:589-611.
- Monin AS, Obukhov AM (1954) Osnovnye zakonomernosti turbulentnogo peremeshivaniya v prizemnom sloe atmosfery (Basic Laws of Turbulent Mixing in the Atmosphere Near the Ground). *Trudy Geofizicheskogo Instituta, Akademiya Nauk SSSR* 24:163–187.
- Monin AS, Yaglom AM (1973) *Statistical Fluid Mechanics: Mechanics of Turbulence, Vol. 1*, MIT Press, Cambridge, London, 769 pp.
- Nakai T, Sumida A, Daikoku KI, Matsumoto K, van der Molen MK, Kodama Y, Kononov AV, Maximov TC, Dolman AJ, Yabuki H, Hara T (2008) Parameterisation of aerodynamic roughness over boreal, cool-and warm-temperate forests. *Agricultural and Forest Meteorology* 148:1916-1925.
- Nakayama H, Takemi T, Nagai H (2011) LES analysis of the aerodynamic surface properties for turbulent flows over building arrays with various geometries. *Journal of Applied Meteorology and Climatology* 50:1692-1712.
- Nelson A, Reuter HI, Gessler P (2009) DEM production methods and sources. *Developments in soil science* 33:65-85.

- Ng E, Yuan C, Chen L, Ren C, Fung JC (2011) Improving the wind environment in high-density cities by understanding urban morphology and surface roughness: a study in Hong Kong. *Landscape and Urban Planning* 101:59-74.
- NGA (2008) National Geospatial Agency Earth Gravitational Model 2.5 minute Geoid heights. Available: http://earth-info.nga.mil/GandG/wgs84/gravitymod/egm2008/egm08_wgs84.html, accessed March 2017.
- Nordbo A, Järvi L, Haapanala S, Moilanen J, Vesala T (2013) Intra-city variation in urban morphology and turbulence structure in Helsinki, Finland. *Boundary-Layer Meteorology* 146: 469-496.
- NYC DoITT (2014) New York City Department of Information Technology and Telecommunications. Available: <https://www1.nyc.gov/site/doitt/residents/gis-mapping.page>, accessed March 2017.
- Oke TR (1976) The distinction between canopy and boundary-layer urban heat islands. *Atmosphere* 14:268-277.
- Oke TR (1987) *Boundary Layer Climates* (2nd edn). Routledge/John Wiley & Sons, London/New York, 435 pp.
- Oke TR (2007) Siting and exposure of meteorological instruments at urban sites. In: Borrego C, Norman AL (eds) *Air Pollution Modelling and Its Application XVII*. Springer, USA, 744 pp.
- Oke TR, Mills G, Christen A, Voogt JA (2017) *Urban climates*. Cambridge University Press, Cambridge, pp. 519.
- Ordnance Survey (2010) MasterMap® Topography Layer, Crown Database Right 2010. An Ordnance Survey/EDINA supplied service.
- Ordnance Survey (2014) MasterMap® Topography Layer building height attribute, Crown Database Right 2014. An Ordnance Survey/EDINA supplied service.
- Owen PR, Thomson WR (1963) Heat transfer across rough surfaces. *Journal of Fluid Mechanics* 15: 321-334.
- Padhra A (2010) Estimating the sensitivity of urban surface drag to building morphology. PhD. thesis, Department of Meteorology, University of Reading, England.
- Pan Y, Follett E, Chamecki M, Nepf H (2014) Strong and weak, unsteady reconfiguration and its impact on turbulence structure within plant canopies. *Physics of Fluids* 26:105102.

- Panagiotakis E, Chrysoulakis N, Charalampopoulou V, Poursanidis D (2018) Validation of Pleiades Tri-Stereo DSM in Urban Areas. *ISPRS International Journal of Geo-Information* 7:118.
- Panofsky HA, Dutton JA (1984) *Atmospheric Turbulence: Models and Methods for Engineering Applications*. John Wiley, New York, 397 pp.
- Panofsky HA, Tennekes H, Lenschow DH, Wyngaard JC (1977) The characteristics of turbulent velocity components in the surface layer under convective conditions. *Boundary-Layer Meteorology* 11:355-361.
- Papale D, Reichstein M, Canfora E, Aubinet M, Bernhofer C, Longdoz B, Kutsch W, Rambal S, Valentini R, Vesala T, Yakir D (2006) Towards a more harmonized processing of eddy covariance CO₂ fluxes: algorithms and uncertainty estimation. *Biogeosciences Discussions* 3:961-992.
- Patino JE, Duque JC (2013) A review of regional science applications of satellite remote sensing in urban settings. *Computers, Environment and Urban Systems* 37:1-17.
- Peña A, Gryning S, Mann J, Hasager CB (2010) Length scales of the neutral wind profile over homogeneous terrain. *Journal of Applied Meteorology and Climatology* 49:792-806.
- Perko R, Raggam H, Gutjahr KH, Schardt M (2015) Advanced DTM generation from very high resolution satellite stereo images. *ISPRS annals of the photogrammetry, remote sensing and spatial information sciences* 2:165-172.
- Petrini F, Ciampoli M (2012) Performance-based wind design of tall buildings. *Structure and Infrastructure Engineering* 8:954-966.
- Rabus B, Eineder M, Roth A, Bamler R (2003) The shuttle radar topography mission—a new class of digital elevation models acquired by spaceborne radar. *ISPRS journal of photogrammetry and remote sensing* 57:241-262.
- Rafailidis S (1997) Influence of building areal density and roof shape on the wind characteristics above a town. *Boundary-Layer Meteorology* 85:255-271.
- Rannik Ü, Aubinet M, Kurbanmuradov O, Sabelfeld KK, Markkanen T, Vesala T (2000) Footprint analysis for measurements over a heterogeneous forest. *Boundary-Layer Meteorology* 97:137-66.
- Ratti C, Di Sabatino S, Britter R (2006) Urban texture analysis with image processing techniques: winds and dispersion. *Theoretical and Applied Climatology* 84:77-90.

- Ratti C, Di Sabatino S, Britter R, Brown M, Caton F, Burian S (2002) Analysis of 3-D urban databases with respect to pollution dispersion for a number of European and American cities. *Water, Air and Soil Pollution: Focus* 2:459-469.
- Raupach M (1992) Drag and drag partition on rough surfaces. *Boundary-Layer Meteorology* 60:375-395.
- Raupach M (1994) Simplified expressions for vegetation roughness length and zero-plane displacement as functions of canopy height and area index. *Boundary-Layer Meteorology* 71:211-216.
- Raupach M, Antonia R, Rajagopalan S (1991) Rough-wall turbulent boundary layers. *Applied Mechanics Reviews* 44:1-25.
- Reuter HI, Nelson A, Jarvis A (2007) An evaluation of void-filling interpolation methods for SRTM data. *International Journal of Geographical Information Science* 21:983-1008.
- Rexer M, Hirt C (2016) Evaluation of intermediate TanDEM-X digital elevation data products over Tasmania using other digital elevation models and accurate heights from the Australian National Gravity Database. *Australian Journal of Earth Sciences* 63:599-609.
- Ricci A, Kalkman I, Blocken B, Burlando M, Freda A, Repetto MP (2016) Inflow condition sensitivity in the CFD simulation of wind flow in the urban environment. 8th International Colloquium on Bluff Body Aerodynamics and Applications, Boston, Massachusetts, USA, June 7 – 11, 2016.
- Ricci A, Kalkman I, Blocken B, Burlando M, Freda A, Repetto MP (2017) Local-scale forcing effects on wind flows in an urban environment: Impact of geometrical simplifications. *Journal of Wind Engineering and Industrial Aerodynamics* 170:238-255.
- Rizzoli P, Martone M, Gonzalez C, Wecklich C, Tridon DB, Bräutigam B, Bachmann M, Schulze D, Fritz T, Huber M, Wessel B (2017) Generation and performance assessment of the global TanDEM-X digital elevation model. *ISPRS Journal of Photogrammetry and Remote Sensing* 132:119-139.
- Rodriguez E, Morris CS, Belz JE (2006) A global assessment of the SRTM performance. *Photogrammetric Engineering & Remote Sensing* 72:249-260.
- Rooney G (2001) Comparison of upwind land use and roughness length measured in the urban boundary layer. *Boundary-Layer Meteorology* 100:469-485.

- Rossi C, Gernhardt S (2013) Urban DEM generation, analysis and enhancements using TanDEM-X. *ISPRS journal of photogrammetry and remote sensing* 85:120-131.
- Rossi C, Gonzalez FR, Fritz T, Yague-Martinez N, Eineder M (2012) TanDEM-X calibrated raw DEM generation. *ISPRS Journal of Photogrammetry and Remote Sensing* 73:12-20.
- Rotach MW (1994) Determination of the zero-plane displacement in an urban environment. *Boundary-Layer Meteorology* 67:187-193.
- Rotach MW (1999) On the influence of the urban roughness sublayer on turbulence and dispersion. *Atmospheric Environment* 33:4001-8.
- Rotach MW, Vogt R, Bernhofer C, Batchvarova E, Christen A, Clappier A, Feddersen B, Gryning S-E, Martucci G, Mayer H, Mitev V, Oke TR, Parlow E, Richner H, Roth M, Roulet Y-A, Ruffieux D, Salmond JA, Schatzmann M, Vogt JA (2005) BUBBLE—an urban boundary layer meteorology project. *Theoretical and Applied Climatology* 81:231–261
- Roth M (2000) Review of atmospheric turbulence over cities. *Quarterly Journal of the Royal Meteorological Society* 126:941-990.
- Roth M, Oke TR (1995) Relative efficiencies of turbulent transfer of heat, mass, and momentum over a patchy urban surface. *Journal of the Atmospheric Sciences* 52:1863-1874.
- Roy S, Byrne J, Pickering C (2012) A systematic quantitative review of urban tree benefits, costs, and assessment methods across cities in different climatic zones. *Urban Forestry and Urban Greening* 11:351-363.
- Rudnicki M, Mitchell SJ, Novak MD (2004) Wind tunnel measurements of crown streamlining and drag relationships for three conifer species. *Canadian Journal of Forest Research* 34:666-676.
- Sadique J, Yang XI, Meneveau C, Mittal R (2017) Aerodynamic properties of rough surfaces with high aspect-ratio roughness elements: effect of aspect ratio and arrangements. *Boundary-Layer Meteorology*. 163:203-224.
- Salamanca F, Martilli A, Tewari M, Chen F (2011) A study of the urban boundary layer using different urban parameterizations and high-resolution urban canopy parameters with WRF. *Journal of Applied Meteorology and Climatology* 50:1107-28.
- Salmond JA, Tadaki M, Vardoulakis S, Arbuthnott K, Coutts A, Demuzere M, Dirks KN, Heaviside C, Lim S, Macintyre H (2016) Health and climate related ecosystem services provided by street trees in the urban environment. *Environmental Health* 15:95.

- Salmond JA, Williams D, Laing G, Kingham S, Dirks K, Longley I, Henshaw G (2013) The influence of vegetation on the horizontal and vertical distribution of pollutants in a street canyon. *Science of the Total Environment* 443:287-298.
- Savelyev SA, Taylor PA (2005) Internal boundary layers: I. Height formulae for neutral and diabatic flows. *Boundary-Layer Meteorology* 115:1-25.
- Schaudt K (1998) A new method for estimating roughness parameters and evaluating the quality of observations. *Journal of Applied Meteorology and Climatology* 37:470-476.
- Schlichting H, Gersten K (2000) *Boundary Layer Theory* (8th edn) Springer-Verlag, Berlin, 800 pp.
- Schmid HP (1997) Experimental design for flux measurements: matching scales of observations and fluxes. *Agricultural and Forest Meteorology* 87: 179–200
- Schmid HP, Oke TR (1990) A model to estimate the source area contributing to turbulent exchange in the surface layer over patchy terrain. *Quarterly Journal of the Royal Meteorological Society* 116: 965–988.
- Schmitt M, Stilla U (2014) Maximum-likelihood estimation for multi-aspect multi-baseline SAR interferometry of urban areas. *ISPRS Journal of Photogrammetry and Remote Sensing*. 87:68-77.
- Schotanus P, Nieuwstadt F, De Bruin H (1983) Temperature measurement with a sonic anemometer and its application to heat and moisture fluxes. *Boundary-Layer Meteorology* 26:81-93.
- Schreyer J, Tigges J, Lakes T, Churkina G (2014) Using airborne LiDAR and QuickBird data for modelling urban tree carbon storage and its distribution—A case study of Berlin. *Remote Sensing* 6:10636-10655.
- Schubert S, Grossman-Clarke S, Martilli A (2012) A double-canyon radiation scheme for multi-layer urban canopy models. *Boundary-Layer Meteorology* 145:439-468.
- Schuepp PH, Leclerc MY, MacPherson JI, Desjardins RL (1990) Footprint prediction of scalar fluxes from analytical solutions of the diffusion equation. *Boundary-Layer Meteorology* 50:355-373.
- Schultz M, Leitl B, Schatzmann M (2007) How rough is rough? Characterization of turbulent fluxes within and above an idealized urban roughness *Physmod 2007*, Orleans, France, pp. 69-74.

- Schultz M, Schatzmann M, Leitl B (2005) Effect of roughness inhomogeneities on the development of the urban boundary layer. *International Journal of Environment and Pollution* 25:105-117.
- Sedefian L (1980) On the vertical extrapolation of mean wind power density. *Journal of Applied Meteorology and Climatology* 19:488-493.
- Segal M, Pielke RA (1988) The extrapolation of vertical profiles of wind speed within the marine atmospheric surface layer using the p formula. *Journal of Applied Meteorology and Climatology* 27:174-181.
- Seginer I (1975) Atmospheric-stability effect on windbreak shelter and drag. *Boundary-Layer Meteorology* 8:383-400.
- Seidel DJ, Ao CO, Li K (2010) Estimating climatological planetary boundary layer heights from radiosonde observations: Comparison of methods and uncertainty analysis. *Journal of Geophysical Research: Atmospheres* 115:D16113.
- Shaw RH, Patton EG (2003) Canopy element influences on resolved-and subgrid-scale energy within a large-eddy simulation. *Agricultural and Forest Meteorology* 115:5-17.
- Shaw RH, Pereira AR (1982) Aerodynamic roughness of a plant canopy: a numerical experiment. *Agricultural Meteorology* 26:51-65.
- Shaw RH, Schumann U (1992) Large-eddy simulation of turbulent flow above and within a forest. *Boundary-Layer Meteorology* 61:47-64.
- Simiu E, Scanlan RH (1996) *Wind effects on structures*. Wiley, New York, 605 pp.
- Simpson IJ, Thurtell GW, Neumann HH, Den Hartog G, Edwards GC (1998) The validity of similarity theory in the roughness sublayer above forests. *Boundary-Layer Meteorology* 87:69-99.
- Small C, Sohn R (2015) Correlation scales of digital elevation models in developed coastal environments. *Remote Sensing of Environment* 159:80-85.
- Smith CL, Webb A, Levermore G, Lindley S, Beswick K (2011) Fine-scale spatial temperature patterns across a UK conurbation. *Climatic Change* 109:269-286.
- Sogachev A, Lloyd J (2004) Using a one-and-a-half order closure model of the atmospheric boundary layer for surface flux footprint estimation. *Boundary-Layer Meteorology* 112:467-502.

- Sorbjan Z (1989) Structure of the Atmospheric Boundary Layer. Prentice Hall, Old Tappan, 315 pp.
- Sportouche H, Tupin F, Denise L (2011) Extraction and three-dimensional reconstruction of isolated buildings in urban scenes from high-resolution optical and SAR spaceborne images. *IEEE Transactions on Geoscience and Remote Sensing* 49: 3932–3946.
- Stathopoulos T (2006) Pedestrian level winds and outdoor human comfort. *Journal of Wind Engineering and Industrial Aerodynamics* 94:769-780.
- Stevens NF, Garbeil H, Mouginis-Mark PJ (2004) NASA EOS Terra ASTER: Volcanic topographic mapping and capability. *Remote Sensing of Environment* 90:405-414.
- Stewart ID (2011) A systematic review and scientific critique of methodology in modern urban heat island literature. *International Journal of Climatology* 31:200-217.
- Stewart ID, Oke TR (2012) Local climate zones for urban temperature studies. *Bulletin of the American Meteorological Society* 93:1879-1900.
- Stilla U, Soergel U, Thoennessen U (2003) Potential and limits of InSAR data for building reconstruction in built-up areas. *ISPRS Journal of Photogrammetry and Remote Sensing* 58:113-123.
- Stovin V, Jorgensen A, Clayden A (2008) Street trees and stormwater management. *Arboricultural Journal* 30:297-310.
- Stull RB (2009) *An Introduction to Boundary Layer Meteorology* (vol 13). Springer, pp.670
- Su H, Shaw RH, Paw KT, Moeng C, Sullivan PP (1998) Turbulent statistics of neutrally stratified flow within and above a sparse forest from large-eddy simulation and field observations. *Boundary-Layer Meteorology* 88:363-397.
- Su Y, Guo Q (2014) A practical method for SRTM DEM correction over vegetated mountain areas. *ISPRS Journal of Photogrammetry and Remote Sensing* 87:216-228.
- Suter-Burri K, Gromke C, Leonard KC, Graf F (2013) Spatial patterns of aeolian sediment deposition in vegetation canopies: Observations from wind tunnel experiments using coloured sand. *Aeolian Research* 8:65-73.
- Sutton S, McKenna Neuman C (2008) Sediment entrainment to the lee of roughness elements: Effects of vortical structures. *Journal of Geophysical Research: Earth Surface* 113:F02S09.

- Tachikawa T, Kaku M, Iwasaki A, Gesch DB, Oimoen MJ, Zhang Z, Danielson JJ, Krieger T, Curtis B, Haase J (2011) ASTER global digital elevation model version 2-summary of validation results. Earth Resources Observation and Science (EROS) Center, 27 pp.
- Tallis M, Taylor G, Sinnett D, Freer-Smith P (2011) Estimating the removal of atmospheric particulate pollution by the urban tree canopy of London, under current and future environments. *Landscape and Urban Planning* 103:129-138.
- Tamura Y, Suda K, Sasaki A, Iwatani Y, Fujii K, Ishibashi R, Hibi K (2001) Simultaneous measurements of wind speed profiles at two sites using Doppler sodars. *Journal of Wind Engineering and Industrial Aerodynamics* 89:325-335.
- Tan J, Yang L, Grimmond CSB, Shi J, Gu W, Chang Y, Hu P, Sun J, Ao X, Han Z (2015) Urban integrated meteorological observations: practice and experience in Shanghai, China. *Bulletin of the American Meteorological Society* 96:85-102.
- Tanaka H, Tamura Y, Ohtake K, Nakai M, Kim YC (2012) Experimental investigation of aerodynamic forces and wind pressures acting on tall buildings with various unconventional configurations. *Journal of Wind Engineering and Industrial Aerodynamics* 107:179-191.
- Tanaka S, Sugawara H, Narita K, Yokoyama H, Misaka I, Matsushima D (2011) Zero-plane displacement height in a highly built-up area of Tokyo. *Sola* 7:93-96.
- Taranath BS (2016) Structural analysis and design of tall buildings: Steel and composite construction. CRC press, Florida, 722 pp.
- Taylor PA (1988) Turbulent wakes in the atmospheric boundary layer. In: Steffen WL, Denmead OT (eds) *Flow and Transport in the Natural Environment: Advances and Applications*. Springer, Berlin, pp 270-292.
- Tennekes H (1973) The logarithmic wind profile. *Journal of the Atmospheric Sciences* 30:234-238.
- Theurer W (1993) Dispersion of ground level emissions in complex built-up areas. PhD. thesis, Department of Architecture, University of Karlsruhe, Germany.
- Thiele A, Cadario E, Schulz K, Soergel U (2010) Analysis of gable-roofed building signature in multiaspect InSAR data. *IEEE Geoscience and Remote Sensing Letters* 7:83-87.
- Thom AS (1971) Momentum absorption by vegetation. *Quarterly Journal of the Royal Meteorological Society* 97:414-428.

- Thom AS, Stewart JB, Oliver HR, Gash JHC (1975) Comparison of aerodynamic and energy budget. *Quarterly Journal of the Royal Meteorological Society* 101:93–105.
- Tieleman HW (2008) Strong wind observations in the atmospheric surface layer. *Journal of Wind Engineering and Industrial Aerodynamics* 96:41-77.
- Tillman J (1972) The indirect determination of stability, heat and momentum fluxes in the atmospheric boundary layer from simple scalar variables during dry unstable conditions. *Journal of Applied Meteorology and Climatology* 11:783-792.
- Tiwary A, Sinnett D, Peachey C, Chalabi Z, Vardoulakis S, Fletcher T, Leonardi G, Grundy C, Azapagic A, Hutchings TR (2009) An integrated tool to assess the role of new planting in PM 10 capture and the human health benefits: a case study in London. *Environmental Pollution* 157:2645-2653.
- Toda M, Sugita M (2003) Single level turbulence measurements to determine roughness parameters of complex terrain. *Journal of Geophysical Research: Atmospheres* (1984–2012) 108: 4363.
- Tominaga Y, Stathopoulos T (2013) CFD simulation of near-field pollutant dispersion in the urban environment: A review of current modelling techniques. *Atmospheric Environment* 79:716-730.
- Tominaga Y, Stathopoulos T (2016) Ten questions concerning modeling of near-field pollutant dispersion in the built environment. *Building and Environment* 105:390-402.
- Tsuang B, Tsai J, Lin M, Chen C (2003) Determining aerodynamic roughness using tether sonde and heat flux measurements in an urban area over a complex terrain. *Atmospheric Environment* 37:1993-2003.
- United Nations (2014) *World Urbanization Prospects the 2014 Revision: Highlights*. United Nations Publications, New York. Available: <https://esa.un.org/unpd/wup/publications/files/wup2014-highlights.pdf>, accessed January 2018.
- USGS CMGP (2014) United States Geological Survey Coastal and Marine Geology Program. New York CMGP sandy 0.7m nps lidar woolpert project #73666. Available: <https://coast.noaa.gov/inventory/>, accessed March 2017.
- Van Dijk A, Moene A, De Bruin H (2004) *The principles of surface flux physics: theory, practice and description of the ECPACK library*. Wageningen University, Wageningen, The Netherlands, 99 pp.

- Van Renterghem T, Botteldooren D (2008) Numerical evaluation of sound propagating over green roofs. *Journal of Sound and Vibration* 317:781-799.
- Varquez ACG, Nakayoshi M, Kanda M (2015) The effects of highly detailed urban roughness parameters on a sea-breeze numerical simulation. *Boundary-Layer Meteorology* 154:449-469.
- Verkaik J (2000) Evaluation of two gustiness models for exposure correction calculations. *Journal of Applied Meteorology and Climatology* 39:1613-1626.
- Vesala T, Järvi L, Launiainen S, Sogachev A, Rannik Ü, Mammarella I, Siivola E, Keronen P, Rinne J, Riikonen ANU Nikinmaa E (2008) Surface–atmosphere interactions over complex urban terrain in Helsinki, Finland. *Tellus B* 60:188-199.
- Vico G, Revelli R, Porporato A (2014) Ecohydrology of street trees: design and irrigation requirements for sustainable water use. *Ecohydrology* 7:508-523.
- Vollsinger S, Mitchell SJ, Byrne KE, Novak MD, Rudnicki M (2005) Wind tunnel measurements of crown streamlining and drag relationships for several hardwood species. *Canadian Journal of Forest Research* 35:1238-1249.
- Voogt JA, Grimmond CSB (2000) Modeling surface sensible heat flux using surface radiative temperatures in a simple urban area. *Journal of Applied Meteorology and Climatology* 39:1679-1699.
- Vos PE, Maiheu B, Vankerkom J, Janssen S (2013) Improving local air quality in cities: to tree or not to tree? *Environmental pollution* 183:113-122.
- Walker GR, Mason MS, Crompton RP, Musulin RT (2016) Application of insurance modelling tools to climate change adaptation decision-making relating to the built environment. *Structure and Infrastructure Engineering*. 12:450-462.
- Walmsley JL, Taylor P, Keith T (1986) A simple model of neutrally stratified boundary-layer flow over complex terrain with surface roughness modulations (MS3DJH/3R). *Boundary-Layer Meteorology* 36:157-186.
- Walmsley JL, Woolridge D, Salmon JR (1990) Ms-Micro/3 user's guide. Technical Report ARD-90-008, Atmospheric Environment Services, Ontario, Canada, 88 pp.
- Wang K, Stathopoulos T (2007) Exposure model for wind loading of buildings. *Journal of Wind Engineering and Industrial Aerodynamics* 95:1511-1525.

- Wang W, Xu Y, Ng E, Raasch S (2018) Evaluation of satellite-derived building height extraction by CFD simulations: A case study of neighborhood-scale ventilation in Hong Kong. *Landscape and Urban Planning* 170:90-102.
- Ward HC, Evans JG, Grimmond CSB (2013) Multi-season eddy covariance observations of energy, water and carbon fluxes over a suburban area in Swindon, UK. *Atmospheric Chemistry and Physics* 13: 4645-4666.
- Ward HC, Evans JG, Grimmond CSB (2014) Multi-scale sensible heat fluxes in the suburban environment from large-aperture scintillometry and eddy covariance. *Boundary-Layer Meteorology* 152:65-89.
- Ward HC, Evans JG, Grimmond CSB (2015c) Infrared and millimetre-wave scintillometry in the suburban environment-Part 2: Large-area sensible and latent heat fluxes. *Atmospheric Measurement Techniques* 8:1407-1424.
- Ward HC, Evans JG, Grimmond CSB, Bradford J (2015b) Infrared and millimetre-wave scintillometry in the suburban environment-Part 1: Structure parameters. *Atmospheric Measurement Techniques* 8: 1385-1405.
- Ward HC, Grimmond CSB (2017) Assessing the impact of changes in surface cover, human behaviour and climate on energy partitioning across Greater London. *Landscape and Urban Planning* 165: 142-161.
- Ward HC, Kotthaus S, Grimmond CSB, BJORKEGREN A, WILKINSON M, MORRISON WTJ, EVANS JG, MORISON JIL, IAMARINO M (2015a) Effects of urban density on carbon dioxide exchanges: Observations of dense urban, suburban and woodland areas of southern England. *Environmental Pollution* 198:186-200.
- Ward HC, Kotthaus S, Järvi L, Grimmond CSB (2016) Surface Urban Energy and Water Balance Scheme (SUEWS): development and evaluation at two UK sites. *Urban Climate* 18:1-32.
- Weekes SM, Tomlin AS (2013) Evaluation of a semi-empirical model for predicting the wind energy resource relevant to small-scale wind turbines. *Renewable energy* 50:280-288.
- Wessel B (2016) TanDEM-X Ground Segment – DEM Products Specification Document. EOC, DLR, Oberpfaffenhofen, Germany, Public Document TD-GS-PS-0021, Issue 3.1. Available: <https://tandemx-science.dlr.de/>, accessed March 2017.
- Wieringa J (1986) Roughness-dependent geographical interpolation of surface wind speed averages. *Quarterly Journal of the Royal Meteorological Society* 112:867-889.

- Wieringa J (1993) Representative roughness parameters for homogeneous terrain. *Boundary-Layer Meteorology* 63:323-363.
- Wieringa J, Davenport AJ, Grimmond CSB, Oke TR (2001) New revision of Davenport roughness classification. In: *Proceedings of 3EACWE, Eindhoven, The Netherlands*, pp. 285-292.
- Willmott CJ, Matsuura K (2005) Advantages of the mean absolute error (MAE) over the root mean square error (RMSE) in assessing average model performance. *Climate Research* 30:79-82.
- Wilson JD (1985) Numerical studies of flow through a windbreak. *Journal of Wind Engineering and Industrial Aerodynamics* 21:119-154.
- Wilson JD, Flesch TK (2004) An idealized mean wind profile for the atmospheric boundary layer. *Boundary-Layer Meteorology* 110:281-299.
- Wolfe SA, Nickling WG (1993) The protective role of sparse vegetation in wind erosion. *Progress in Physical Geography* 17:50-50.
- Wood CR, Lacser A, Barlow JF, Padhra A, Belcher SE, Nemitz E, Helfter C, Famulari D, Grimmond CSB (2010) Turbulent flow at 190 m height above London during 2006–2008: a climatology and the applicability of similarity theory. *Boundary-Layer Meteorology* 137:77-96.
- Wood CR, Pauscher L, Ward H, Kotthaus S, Barlow J, Gouvea M, Lane S, Grimmond CSB (2013) Wind observations above an urban river using a new lidar technique, scintillometry and anemometry. *Science of the Total Environment* 442:527-533.
- Wyatt V, Nickling W (1997) Drag and shear stress partitioning in sparse desert creosote communities. *Canadian Journal of Earth Sciences* 34:1486-1498.
- Wyngaard J, Coté O, Izumi Y (1971) Local free convection, similarity, and the budgets of shear stress and heat flux. *Journal of the Atmospheric Sciences* 28:1171-1182.
- Xie Z, Coceal O, Castro IP (2008) Large-eddy simulation of flows over random urban-like obstacles. *Boundary-Layer Meteorology* 129:1-23.
- Xu Y, Ren C, Ma P, Ho J, Wang W, Lau KK, Lin H, Ng E (2017) Urban morphology detection and computation for urban climate research. *Landscape and Urban Planning* 167:212-224.
- Yamaguchi Y, Kahle AB, Tsu H, Kawakami T, Pniel M (1998) Overview of advanced spaceborne thermal emission and reflection radiometer (ASTER). *IEEE Transactions on Geoscience and Remote Sensing* 36:1062-1071.

- Yan WY, Shaker A, El-Ashmawy N (2015) Urban land cover classification using airborne LiDAR data: A review. *Remote Sensing of Environ* 158:295-310.
- Yang L, Meng X, Zhang X (2011) SRTM DEM and its application advances. *International Journal of Remote Sensing* 32:3875-3896.
- Yang X, Yu Y, Fan WA (2017) A method to estimate the structural parameters of windbreaks using remote sensing. *Agroforestry Systems* 91:37-49.
- Yang XI, Meneveau C (2016) Large eddy simulations and parameterisation of roughness element orientation and flow direction effects in rough wall boundary layers. *Journal of Turbulence* 17:1072-1085
- Yang XI, Sadique J, Mittal R, Meneveau C (2016) Exponential roughness layer and analytical model for turbulent boundary layer flow over rectangular-prism roughness elements. *Journal of Fluid Mechanics* 789:127-165.
- Zaki SA, Hagishima A, Tanimoto J, Ikegaya N (2011) Aerodynamic parameters of urban building arrays with random geometries. *Boundary-Layer Meteorology* 138:99-120.
- Zaki SA, Hagishima A, Tanimoto J, Mohammad AF, Razak AA (2014) Estimation of aerodynamic parameters of urban building arrays using wind tunnel measurements. *Journal of Engineering Science and Technology* 9:176-90.
- Zeng C, Wang J, Zhan W, Shi P, Gambles A (2014) An elevation difference model for building height extraction from stereo-image-derived DSMs. *International Journal of Remote Sensing* 35:7614–7630.
- Zeng P, Takahashi H (2000) A first-order closure model for the wind flow within and above vegetation canopies. *Agricultural and Forest Meteorology* 103:301-313.
- Zhang X, Zhang RR (2001) Actual ground-exposure determination and its influences in structural analysis and design. *Journal of Wind Engineering and Industrial Aerodynamics* 89:973-985.
- Zilitinkevich SS (1995) Non-local turbulent transport: pollution dispersion aspects of coherent structure of convective flows. In: Power H, Moussiopoulos N, Brebbia CA (eds) *Air Pollution III – Volume I. Air Pollution Theory and Simulation*. Computational Mechanics Publications, Boston, pp 53–60.
- Zoumakis NM (1993) Estimating the zero-plane displacement and roughness length for tall vegetation and forest canopies using semi-empirical wind profiles. *Journal of Applied Meteorology and Climatology* 32:574-579.